

# 博士論文

論文題目 **Remote Manipulation of the Binding Pocket  
of Self-Assembled Cages**

(自己組織化錯体結合ポケットの遠隔機能制御)

氏名 方 焜

Fang Yu





# Table of Contents

## Chapter 1

<b>Introduction</b> .....	1
<b>1.1 Remote Control in Natural Protein</b> .....	2
<b>1.2 What is “Remotely Control”</b> .....	6
<b>1.3 Remote Control in Synthetic Host</b> .....	6
1.3.1 Remote Substituent at the Host Framework .....	7
1.3.2 Exterior Remote Force .....	9
1.3.3 Remote Chirality on Guest or Ancillary Ligand .....	10
<b>1.4 Why Do We Need “Remote Control”</b> .....	11
<b>1.5 Designs for “Remote Control”</b> .....	13
<b>1.6 REFERENCES</b> .....	15

## Chapter 2

<b>Cavity Comparison of Self-assembled Cages</b> .....	17
<b>2.1 Introduction</b> .....	18
<b>2.2 Synthesis of Cages with Different Remote Groups</b> .....	18
<b>2.3 Cavity Comparison of Cages with Different Remote Groups</b> .....	20
<b>2.4 Conclusion</b> .....	23
<b>2.5 Experiment Section</b> .....	24
<b>2.6 REFERENCES</b> .....	59

## Chapter 3

<b>Guest-binding in Shrunken Cavities</b> .....	60
<b>3.1 Introduction</b> .....	61
<b>3.2 Guest Species</b> .....	63
<b>3.3 Fine Tuning of Remote Substituent and Guest Size</b> .....	64
<b>3.4 Conclusion</b> .....	67

<b>3.5 Experiment Section</b> .....	68
<b>3.6 REFERENCES</b> .....	96
<b>Chapter 4</b>	
<b>Guest-motion in shrunken cavities</b> .....	97
<b>4.1 Introduction</b> .....	98
<b>4.2 Low Symmetrical Single Molecule Encapsulation in the Shrunken Cavity</b> .....	100
<b>4.3 Low Symmetrical Dimer Encapsulation in the Shrunken</b> .....	103
<b>4.4 Conclusion</b> .....	106
<b>4.5 Experiment Section</b> .....	107
<b>4.6 Reference</b> .....	120
<b>Chapter 5</b>	
<b>Diels-Alder Reaction Acceleration within Shrunken Cavity</b> ..	120
<b>5.1 Introduction</b> .....	121
<b>5.2 Bimolecular Recognition</b> .....	124
<b>5.3 Diels-Alder reaction of small inert diene</b> .....	127
<b>5.4 Catalytic Diels-Alder Reaction of Anthracene Derivative</b> .....	130
<b>5.5 Conclusion</b> .....	134
<b>5.6 Experiment Section</b> .....	135
<b>5.7 REFERENCE</b> .....	137
<b>Chapter 6</b>	
<b>Bottom-Up Assembly from Helicate to Network through a Remote Binding Site</b> .....	143
<b>6.1 Introduction</b> .....	144
<b>6.2 Ligand Design and Synthesis</b> .....	145

<b>6.3 Self-Assembly of Helicate as Building Block</b> .....	145
<b>6.4 Self-assembly of Networks</b> .....	149
<b>6.5 Conclusion</b> .....	153
<b>6.6 Experimental Section</b> .....	153
<b>6.7 Reference</b> .....	154
<b>Chapter 7</b>	
<b>Summary and Perspective</b> .....	170
<b>5.1 Research Summary</b> .....	170
<b>5.2 Perspective</b> .....	173
<b>Acknowledgements</b> .....	174
<b>Publication List</b> .....	178

# Chapter 1

## Introduction

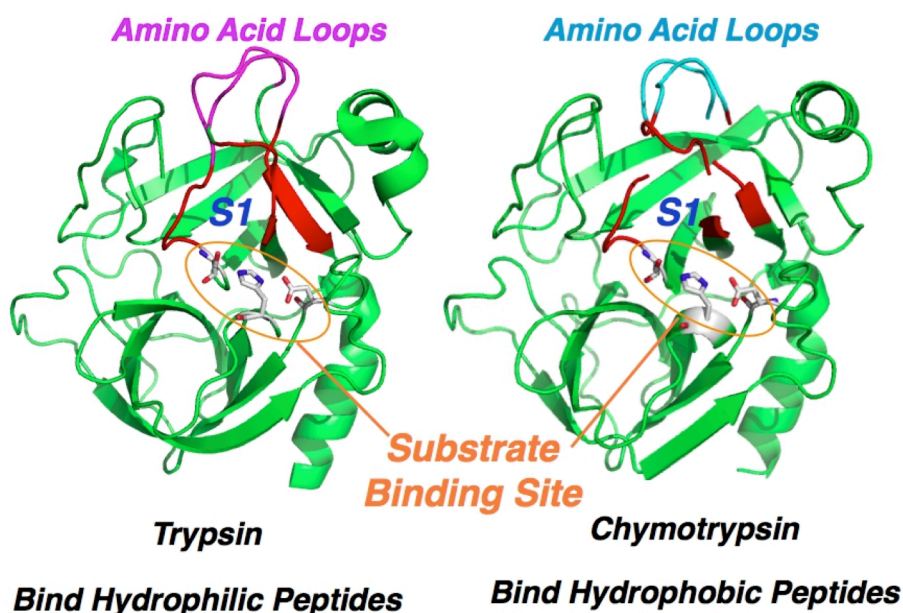
The elaborate substrate specificity in the binding pocket of enzymes is often governed by the subtle variation in amino acid residues that exist, not at the interior, but at the exterior of the pocket. Even a single amino acid difference at the exterior of the pocket makes a big difference. In this way, a small difference at a given remote site is transmitted and amplified over the entire cavity through space, resulting in fine-tuning of the characters and functionality of enzymes.

To date, there are still tremendous unknown for “Remote Control” of nature. Where is the domain factor of a natural structure for remote control? What is the criterion of the domain factor for sufficient remotely control? How does it work for small deviation in domain factor causing large functionality variation? Many biologists and protein chemists study on this field throughout several decades.

Inspired from natural system, synthetic host was designed for mimicking natural enzyme and study the enzymes' mechanism in a simplified system. However, whether the property of synthetic host can be controlled remotely has not been fully investigated. Can we conduct “Remote Control” of synthetic host? How can we “Remote Control” of synthetic host? To answer these questions, many chemists target on mimicking the “Remote Manipulating Process” by artistically designed system.

## 1.1 Remote Control in Natural Protein

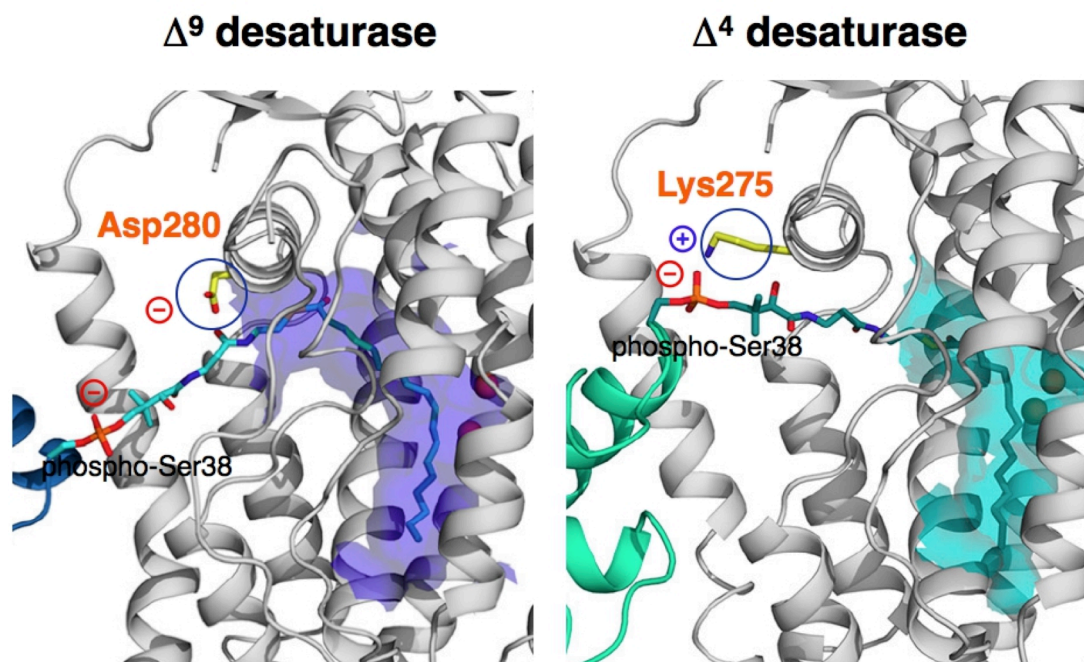
The substrate specificity of natural enzymes is often governed by the subtle variation in amino acid loops that exist, not at the interior, but at the exterior of the pocket.<sup>[1]</sup> Two similar serine proteases, trypsin and chymotrypsin (Figure 1.), share identical structure and have the same composition in “binding pockets” (S1) as well as “substrate binding site” but exhibit distinctly different substrate specificity<sup>[2]</sup> because of the difference in their “amino acid loops” (show different colors in Figure 1.) that do not touch the substrates.<sup>[3-5]</sup> For example, trypsin can only bind hydrophilic peptides, whereas chymotrypsin only favor hydrophobic peptide. The role-separation of recognition and its regulation is nature’s clever way of specific guest binding, where the specificity can be finely tuned without changing the binding pocket structure itself.



**Figure 1.** Similar structure of trypsin and chymotrypsin bearing different remote amino acid loops.

Typically, shape, size and hydrophobicity of the cavity has been tuned by exterior amino acid loops which do not directly contact with the substrates.

Because amino acid loop is consisted of several to dozens of amino acid residues, the former is rather bulky comparing single amino acid. To our surprise, substrate specificity of enzyme can even be governed by single amino acid residue that located outside the binding pocket of enzyme. For instance, castor  $\Delta 9$  and ivy  $\Delta 4$  desaturases lack distinguishable features in structure, but perform region-selective dehydrogenation

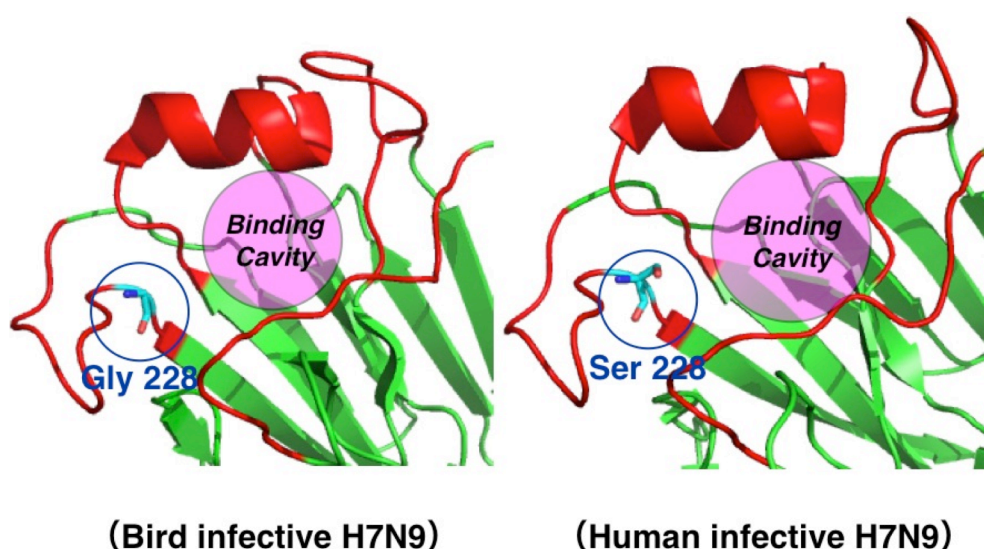


**Figure 4** Different substrate imposition depth of castor  $\Delta^9$  and ivy  $\Delta^4$  desaturases governed by single remote

of long-chain saturated fatty acids on the C9–C10 and C4–C5 positions, respectively, in the binding pocket.<sup>[6–9]</sup> Till 2007, after fully obtained the single crystals of the two protein, people have realized that the two structure have the same substrate binding pocket in size and depth. The position of the di-iron nuclear also located at the same position inside the pocket. Through mutation of the amino residues inside the substrate-binding pocket (Ala188 and Tyr189), the region-selectivity cannot be changed.<sup>[9]</sup> Longstanding researches have revealed that the dominant factor of the observed regioselectivity is Asp280 at the entrance to the pocket in the castor desaturase (Lys275 in the ivy desaturase).<sup>[9]</sup> At the entrance, electrostatic interactions of the host desaturase with acyl carrier protein dictate the insertion depth of the acyl chain in the pocket cavity, yielding dehydrogenation on the different carbon atoms adjacent to the active site in each desaturase (Figure 2.). When the remote amino residue is an Asp 280 in castor  $\Delta^9$  desaturases, the same negative charge will repel the acyl carrier (phosphor-Ser 38) and make the insertion depth of the acyl chain shallow. Because the shallow insertion depth of the acyl chain, desaturation only proceeds at C9–C10 position for castor  $\Delta^9$  desaturase. In contrast, when Lys 275 replaced Asp 280, positive charge will attract the acyl carrier (phosphor-Ser 38) much closer and insert the

acyl chain deeper into the binding pocket, yielding only C4–C5 desaturation in ivy  $\Delta 4$  desaturase. In this way, even a small difference at a given remote site is transmitted and amplified over the entire cavity through space, resulting in fine-tuning of the characters and functionality of enzymes. For desaturase, one amino residue is only thousandth of the whole protein in weight but efficiently controls the functionality of the protein.

On the other hand, avian influenza, commonly called “bird flu”, is a very infective and deadly disease for birds (Figure 3.). However, since 2000, a variety of the mutated avian influenza has cause morbidity and mortality in humans. Originally, bird flu cannot transmit to mammals, such as pig or human. Until very recent, it has been a mystery that how a mutated bird flu infect mammal and cause death to human beings. Early in 2013, after separated the newest mutant of avian influenza, know as H7N9, from bird and human body respectively, scientists elucidated that the virus mutated its amino acid substitutions locating outside the host-binding site but tuned the size, shape and hydrophobicity of the host-binding site.<sup>[10]</sup> Similar like enzyme, the host-binding site of a virus serve as a binding-pocket for hooking molecules on host. As a general rule, avian viruses initiate infection by binding to cell-surface receptor, such as glycoproteins and glycolipids, whose size is well matched for its host-binding site.<sup>[11–15]</sup> Typically, the receptor on human cell-surface is larger than normal avian receptor.<sup>[12]</sup>



**Figure 3.** Different host binding cavity of bird infective and human infective H7N9 avian influenza governed by single remote amino acid residue.

That is the reason why influenza transmission between human and avian is expected infeasible. However, under self-mutation by single amino acid in remote site (Gly 228 to Ser 228), this subtype of avian influenza (H7N9) gains enlarged host-binding site, thus switching the avian-only influenza to human-harming influenza.

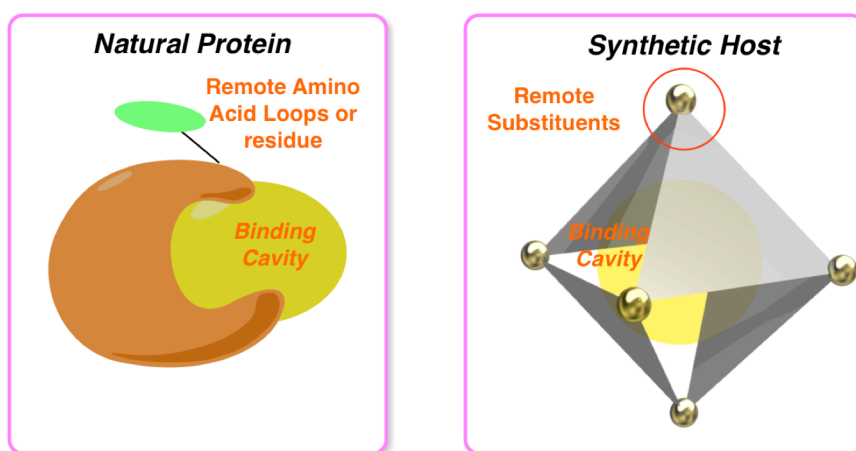
Nature conducts the “remote control” in a very subtle way. Not only amino acid loops (a combination of dozens of amino acid residues) but also single amino acid residue can govern the functionality of protein molecule. For fully understand the natural enzyme, people design synthetic host for mimicking the structure and function of enzyme. Actually synthetic host is a simplified enzyme system but maintains the core structure (framework and binding pocket) and basic function (substrate binding and catalytic property) of enzyme. By research on natural enzyme, the findings can shed light and guide the orientation of coordination chemistry. In the same way, by investigating the synthetic host, we can elucidate the fundamental rule of natural and feedback the research on natural enzyme. Reproduce the behavior and feature of natural enzyme will bridge the research between biology and chemistry. Now we realized the feature of “remote control” in natural enzyme and how does it work. Can we also “remote control” the property of synthetic host for mimicking the behavior of natural enzyme?



## 1.2 What is “Remote Control”

In natural, “remote control” means that amino loops or amino residues locate outside substrate binding pocket and do not touch substrate inside binding site but tune the function (binding-property, reactivity or region-selectivity) of the protein inside the pocket. This “remote control” sometime caused by the reformation of cavity, change of the hydrophobicity of the cavity or totally change of amino acid residue network surrounding the cavity. In some cases, bulky remote amino loops, which are consisted by several amino acid residues, play a dominant role in this behavior. In other cases, remote single amino residue is capable of doing so.

Super-molecular chemistry is a science which is aiming to construct protein-like structure and mimicking basic function of enzyme. In synthetic host, because the synthetic host with cavity is consisted of cavity-forming ligands and ancillary ligands, “remote control” defines as tuning the property of the host *via* modification on the ancillary ligand or applying some force from outside cavity without changing host framework (Figure 4).



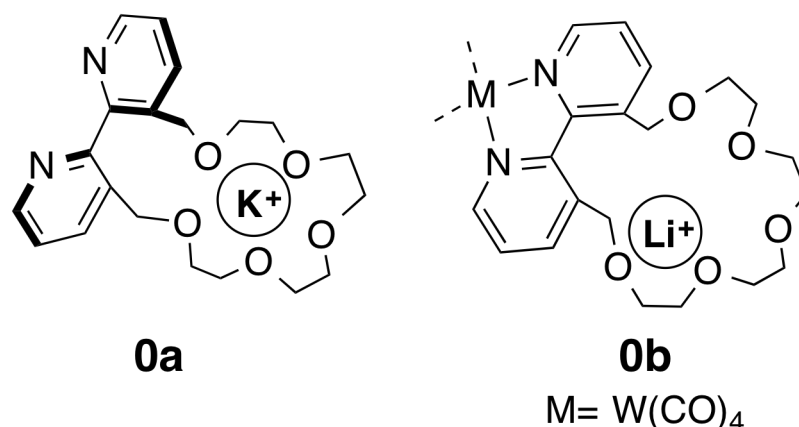
**Figure 4.** “Remote control ” by natural protein and synthetic host.

### 1.3 Remote Control in Synthetic Host

Coordination chemists designed and constructed synthetic hosts, which contain framework and cavity, for mimicking bio-chemical procedure of enzyme. The cavity of a synthetic host can bind a lot of guest species, accelerating reactions as well as developing new reactions. However, remote controlling of the host cavity is very rare and not fully interprets the natural's "Remote control" behavior yet.

#### 1.3.1 Remote Substituent at the Host Framework

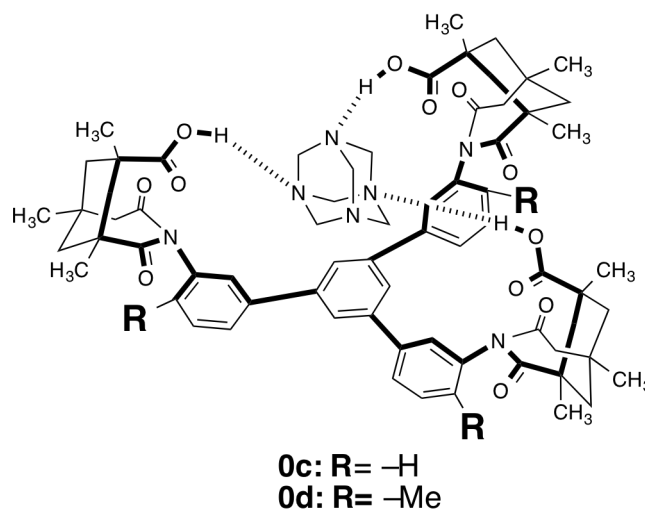
Rebek first introduced the concept of "Remote Control" to coordination chemistry and demonstrate some early examples for this study. Macrocyclic polyethers with two receptors<sup>[17]</sup>: the polyether which binds alkali metal ions and the 2,2'-bipyridyl function which binds transition metals was designed and obtained. Though some distance separates the two receptors, they are mechanically coupled in that binding at one-site forces conformational restrictions which alter receptivity at the remote site. For



**Figure 5.** Different ion binding affinity of polyether governed by remote chelate site.

instance, the polyether receptor of **0a** prefers to bind large ion ( $K^+$ ) because all the oxygen of ether can participate in binding. However, once transition metal was introduced, the geometry of the bipyridine was drawn to a plane and fixed, resulting only one side of the oxygen atoms can participate in the binding of ion. Thus, the polyether receptor of **0b** prefers to bind small ion ( $Na^+$ ) (Figure 5.).

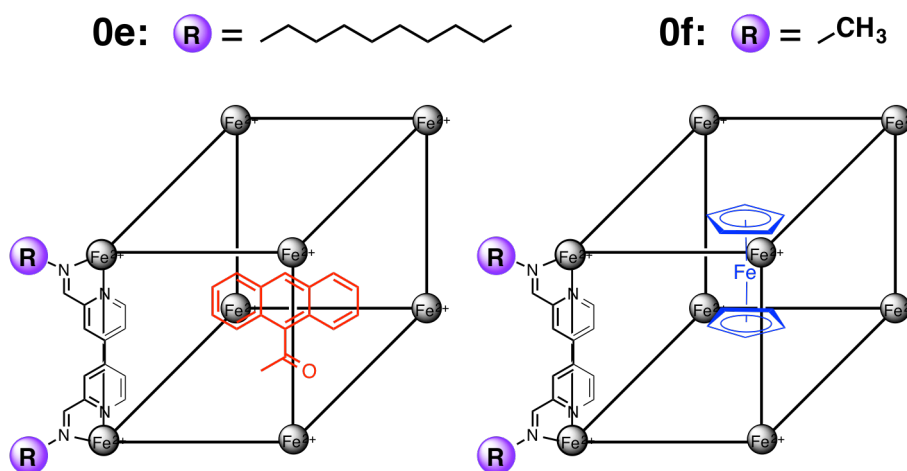
Rebek group also designed a synthetic host with hydrogen bond.<sup>[18]</sup> Once introduced a methyl group onto *ortho*-position of benzene in **0c**, the synthetic host **0d** adopt similar structure but restrict rotation. By this remote modification, binding



**Figure 6.** Different guest binding affinity tuned by substituent on ortho-position.

affinity for azadamantane of host **0d** is 3.5-fold enhancement over unmodified **0c** (Figure 6.). The author claim that the introduced *ortho*-methyl groups enforce the preorganization of the hydrogen bond donor ( $-OH$  groups) and overcome the enthalpic price by allosteric effect.

Nitschke introduced long alkyl chains onto a host framework, whose guest encapsulation property was tuned by the remote alkyl chain.<sup>[19]</sup> The different substituted aniline on subcomponent allows for alter the physicochemical properties of the cubic cage (Figure 7.). Cage **0e** containing decylaniline residues has higher solubility in hydrocarbon phases, thereby allowing encapsulation of 9-acetylanthracene. When the

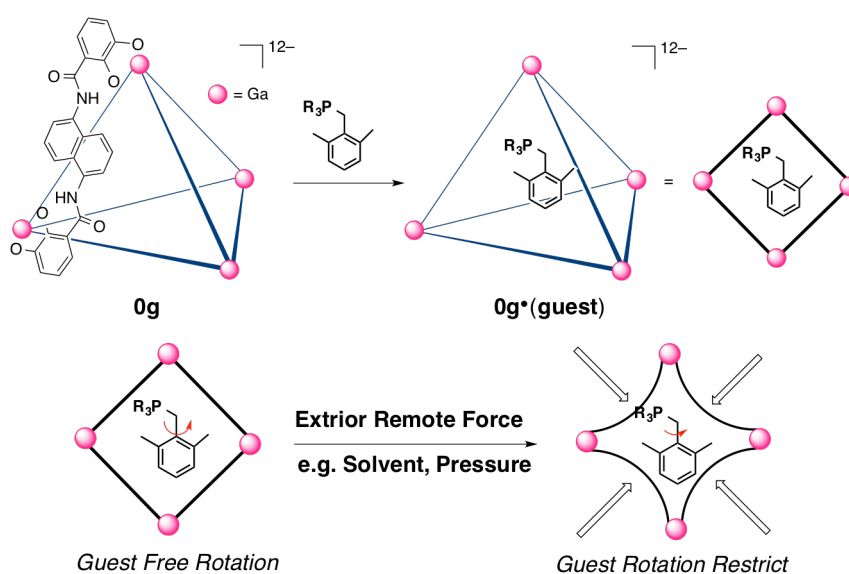


**Figure 7.** Different guest binding affinity tuned by alkane side chain.

long alkane chain is replaced by methyl, cage **0f** only dissolve in acetonitrile and can bind ferrocene. Thus, remote substituents tuned the physicochemical properties of the host and changed the guest-binding property.

### 1.3.2 Exterior Remote Force

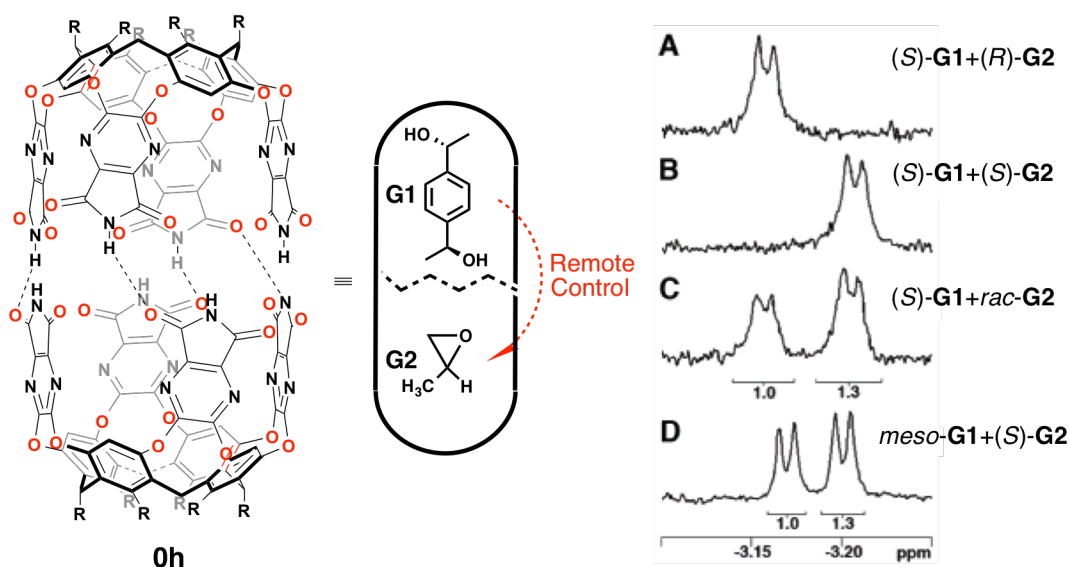
Raymond group found that motions of encapsulated guests are tuned and controlled by exterior pressure.<sup>[20]</sup> The tetrahedral and flexible host is capable of encapsulating a lot of molecules in its cavity. Once benzyltrimethyl phosphonium guest was encapsulated by cage **0g**, the free energy barrier of Ar-CH<sub>2</sub> bond rotation increases, compared with that in aqueous solution. In the contrary, when external pressure is applied to the host-guest complex in solution, the bond rotational rates for the encapsulated guests decrease. NOE distance measurements reveal shorter average host-guest distances in organic than aqueous solution. Here, organic solvent surrounding the host cavity and press the framework and make host-guest tighter packing. In a same way, external pressure also tuned the host in a similar manner. Both internal and external pressures are remote force to reduce the host cavity size or flexibility, resulting in more restricted motions for encapsulated guest molecules (Figure 8.). Changing bulk solvent or external pressure might therefore be used to tune the physical properties or reactivity of guest molecules encapsulated in a flexible supramolecular host.



**Figure 8.** Different guest binding affinity tuned by alkane side chain.

### 1.3.3 Remote Chirality on Guest or Ancillary Ligand

Unlike previous open or half open structures, a recent report from Rebek group is a full-closed hydrogen bond capsule (**0h**).<sup>[21]</sup> The inner cavity of capsule (**0h**) is quite large and can accommodate two molecules. After pre-occupied by one molecule of diol (**G1**), the capsule is restricted and offers a confined environment for accommodating another molecule (**G2**). When chiral (*S*)-**G1** was pre-occupied in the capsule, encapsulation of (*R*)-**G2** or (*S*)-**G2** shows different upfield <sup>1</sup>H NMR spectra for the methyl group of **G2**. These differences are due to the influence of both the local and remote asymmetric centers of **G1**. Thus, the cavity environment is tuned by a molecule locating in a remote site (Figure 9.). This research offers a way to judge the species of the included guest by counting the number of proton and chemical shift in NMR spectra.



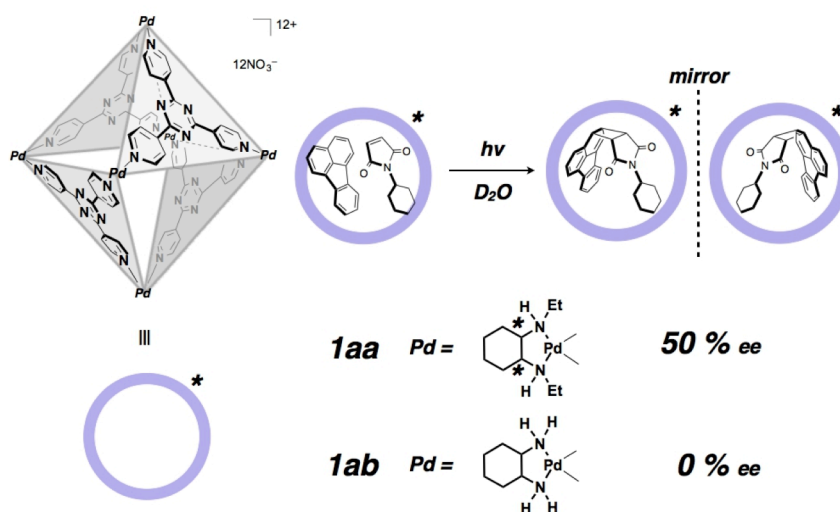
**Figure 9.** Cavity environment was tuned by molecule in a remote site. Reprinted with permission from ref. 21.

Copyright 2008 American Chemical Society.

Moreover, Fujita group is pioneer for studying synthetic host and also demonstrates the concept of “Remote Control” in an early period. Unlike previous examples, they focus on host-guest chemistry in aqueous phase. Typically, guest binding in aqueous phase is very strong due to hydrophobic effect. A lot of synthetic host has been designed and synthesized through coordination between transition metal and organic components. One of the most successful synthetic hosts is octahedral

shape hollow cage **1**.

Self-assembled hollow coordination cages **1** have nanometer-sized, large hydrophobic cavities where a variety of organic guest molecules are bound and reacted.<sup>[22]</sup> Cage **1** is consisted of ancillary *cis*-chelated ligands and cavity-forming ligands. Even a chiral center (star symbol in Figure 10.) located on the ancillary ligands, which is far from the cavity, the cavity of the cage can be controlled to have chiral environment (Figure 10.).<sup>[23]</sup> The two substrates were tightly bound inside the chiral cavity of cage **1aa**. Under UV irradiation, [2+2] photo-addition has been conducted within the cavity and generate two kinds of enantiomer in different percentage, thus moderate *ee* value was obtained. Without chiral center, cage **1ab** also proceeds the [2+2] photo-addition but only racemic product was obtained. In this case, though cavity-forming ligand is achiral, chirality can be successfully transferred from ancillary ligands and enantiomer ratio was remotely controlled. This indicates that Self-assembled hollow coordination cage **1** can be a good candidate for fully investigating “Remote Control” in the synthetic hosts.



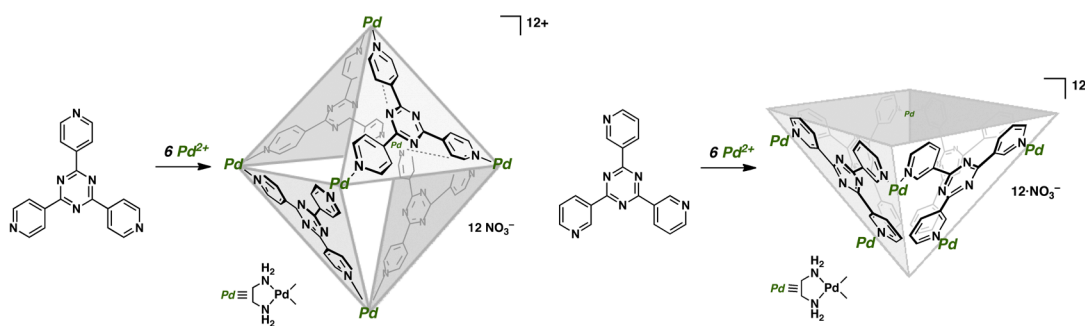
**Figure 10.** Chirality was remotely control by chiral center in remote position.

#### 1.4 Why do we need “Remote Control”

On one hand, rational design and synthesis of cavity-forming ligand is difficult and time-consuming. Structure, coordination number and physical property of the cavity-forming ligand should be considered for the designated host structure. For a new structure, we must carefully design the symmetry and geometry of the

cavity-forming ligand. And sometimes, we cannot expect the final structure. Even a small variation on cavity-forming ligand will totally change the whole structure of the synthetic host because it determines the whole structure of the host. If we modify the cavity-forming ligand, some undesired structures would be obtained through self-assembly. For example,<sup>[24]</sup> when only change the position of a nitrogen atom on the cavity-forming ligand, totally two different structures are obtained (Figure 11.).

On the other hand, changing ancillary ligand is very facile and will not change the

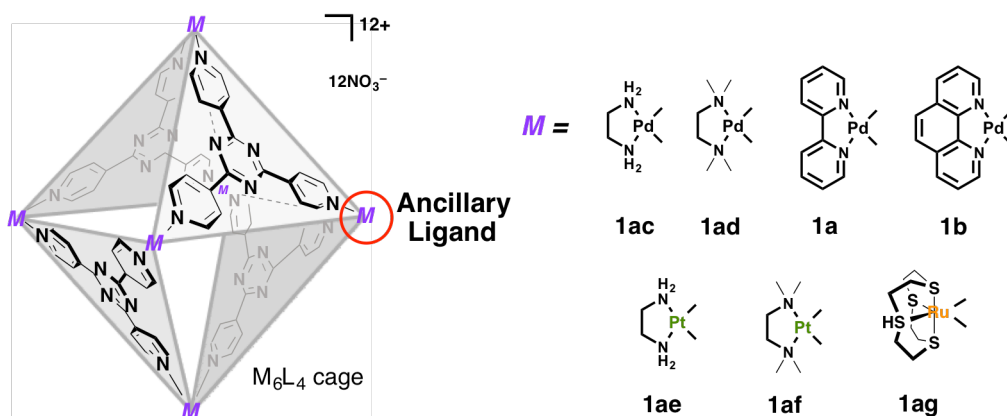


**Figure 11.** Two different structures are obtained by only changing position of one atoms.

whole structure of synthetic hosts. If we can obtain new property or functionality by just varying ancillary ligands, we can open a new way for developing new investigation by least effort. Manipulating the functionality of a synthetic host by only modifying ancillary ligands provides a good way for mimicking of the enzyme's "remote control". Because synthetic host is a simplified system for natural enzyme, investigation of synthetic host can help to understand the mechanism of the enzyme.

We have some experience for the modification on ancillary ligands (Figure 12.). For example, when we change the aliphatic organic chelate ligand (**1ac**: ethylenediamine, **1ad**: tetramethylethylenediamine) to aromatic ligand (**1a**: 2,2'-bipyridine, **1b**: 1,10-phenanthroline),<sup>[25]</sup> no significant change in the functionality of the cage regardless the decreased solubility. By replacing the Pd metal ion by Pt (**1ae** and **1af**), the M–Pyridine bond length was tuned but no difference was found for their guest binding property.<sup>[26]</sup> Even changing both metal and ancillary ligand (**1ag**), the guest binding property maintains the same.<sup>[27]</sup>

Thus we conclude that property of the cavity is normally determined only by cavity-forming ligand. However, cage **1** has potential for remotely control the property of its cavity and mimic the natural behavior.



**Figure 12.** Cage **1** with different ancillary ligands.

### 1.5 Designs for “Remote Control”

Though there are some examples for remotely controlling the functionality of synthetic host, in our concern, none of them exactly do the “Remote Control” like enzyme. Some example is open system or half-open which is not suitable for studying strong host-guest binding. Some examples totally change the chemical or physical property of the host which is not fully acceptable. More of them just show the phenomenon but do not explain why.

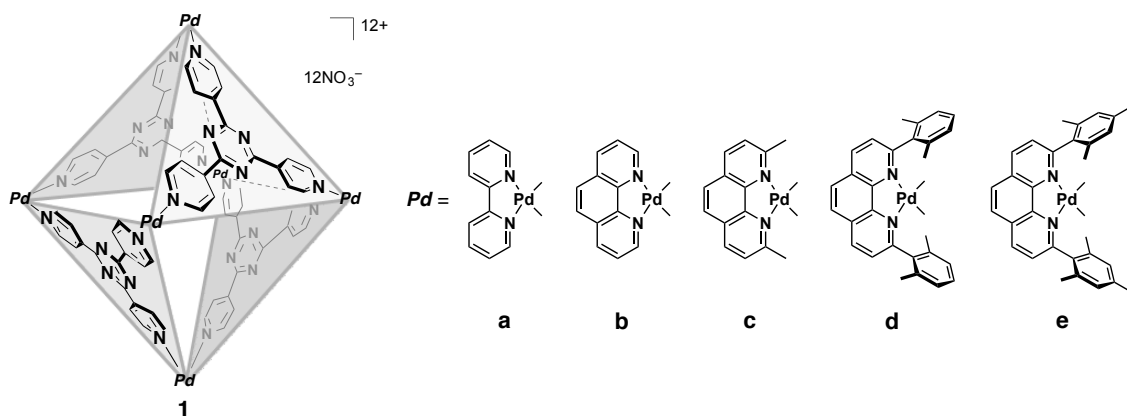
We are aiming to do reactions, which cannot proceed in conventional cavity or without cage, in the cavity modified remotely. For realizing the purpose, we modify the cage on the remote site and change the property of cavity, without changing the structure. More importantly, we want to find out the dominant factor for “Remote Control”. By this way, we can reproduce the guest recognition process similar like natural enzymes. Although previous modification on ancillary ligand do not change the property of the cavity in cage **1**, the reason was realized and specific criterion for ligand design is depicted here:

- (1) Specific interactions should be introduced between host framework and ancillary ligand. For natural enzyme, the remote amino loops or amino residues indeed affect the pocket through not direct but indirect interactions. For previous reported ancillary ligands of cage, no interaction was introduced, thus no communication was bridged.
- (2) The introduced remote substituent should not block the portal of the cavity. Because we want to investigate the guest-binding property, the entrance for the guest



molecule should be guaranteed.

(3) The modified ancillary ligand should be easily available. Because we are aiming to setup a facile way for tuning the property of a host, the ancillary should be easily synthesized or commercial available.



**Figure 13.** Ligand design of synthetic host **1**.

Self-assembled hollow coordination cages **1** is consisted of ancillary *cis*-chelated ligands and cavity-forming ligand. For ancillary ligands, a 2,9-disubstituted phenanthroline Pd complex was modified on 2,9-substituent (Figure 13). After obtained the cage, the guest-binding cavity, the guest-binding ability and motion, as well as reaction within the cavity, of cages **1a–1e** have been fully discussed in order to stress the impact of remote substituent.

## 1.6 REFERENCES

- [1] L. Hedstrom, *Chem. Rev.* **2002**, *102*, 4501.
- [2] J. J. Perona,; C. S. Craik, *Protein Sci.* **1995**, *4*, 337.
- [3] L. Hedstrom,; L. Szilagyi,; W. J. Rutter, *Science* **1992**, *255*, 1249.
- [4] L. Hedstrom,; J. J. Perona,; W. J. Rutter, *Biochemistry* **1994**, *33*, 8757.
- [5] L. Hedstrom,; S. Farr-Jones,; C. A. Kettner,; W. J. Rutter, *Biochemistry* **1994**, *33*, 8764.
- [6] K. Bloch, *Acc. Chem. Res.* **1969**, *2*, 193.
- [7] Y. Lindqvist, W. Huang, G. Schneider, J. Shanklin, *EMBO J.* **1996**, *15*, 4081.
- [8] J. E. Guy, E. Whittle, D. Kumaran, Y. Lindqvist, J. Shanklin, *J. Biol. Chem.* **2007**, *282*, 19863.
- [9] J. E. Guy, E. Whittle, M. Moche, J. Lengqvist, Y. Lindqvist, J. Shanklin, *Proc. Natl. Acad. Sci. U.S.A.* **2011**, *108*, 16594.
- [10] K. Tharakaraman, A. Jayaraman, R. Raman, K. Viswanathan, N. W. Stebbins, D. Johnson, Z. Shriver, V. Sasisekharan, R. Sasisekharan, *Cell.* **2013**, *153*, 1486.
- [11] Y. Shi, W. Zhang, F. Wang, J. Qi, Y. Wu, H. Song, F. Gao, Y. Bi, Y. Zhang, Z. Fan, C. Qin, H. Sun, J. Liu, J. Haywood, W. Liu, W. Gong, D. Wang, Y. Shu, Y. Wang, J. Yan, G. F. Gao, *Science* **2013**, *342*, 243.
- [12] H. Zhu, D. Wang, D. J. Kelvin, L. Li, Z. Zheng, S.-W. Yoon, S.-S. Wong, A. Farooqui, J. Wang, D. Banner, R. Chen, R. Zheng, J. Zhou, Y. Zhang, W. Hong, W. Dong, Q. Cai, M. H. A. Roehrl, S. S. H. Huang, A. A. Kelvin, T. Yao, B. Zhou, X. Chen, G. M. Leung, L. L. M. Poon, R. G. Webster, R. J. Webby, J. S. M. Peiris, Y. Guan, Y. Shu, *Science* **2013**, *341*, 183.
- [13] J. Zhou, D. Wang, R. Gao, B. Zhao, J. Song, X. Qi, Y. Zhang, Y. Shi, Lei Yang, W. Zhu, T. Bai, K. Qin, Y. Lan, S. Zou, J. Guo, J. Dong, L. Dong, Y. Zhang, H. Wei, X. Li, J. Lu, L. Liu, X. Zhao, X. Li, W. Huang, L. Wen, H. Bo, L. Xin, Y. Chen, C. Xu, Y. Pei, Y. Yang, X. Zhang, S. Wang, Z. Feng, J. Han, W. Yang, G. F. Gao, G. Wu, D. Li, Y. Wang, Y. Shu, *Nature* **2013**, *499*, 500.
- [14] X. Xiong, S. R. Martin, L. F. Haire, S. A. Wharton, R. S. Daniels, M. S. Bennett, J. W. McCauley, P. J. Collins, P. A. Walker, J. J. Skehel, S. J. Gamblin, *Nature* **2013**, *499*, 496.

- [15] T. Watanabe, M. Kiso, S. Fukuyama, N. Nakajima, M. Imai, S. Yamada, S. Murakami, S. Yamayoshi, K. I.-Horimoto, Y. Sakoda, E. Takashita, R. McBride, T. Noda, M. Hatta, H. Imai, D. Zhao, N. Kishida, M. Shirakura, R. P. de Vries, S. Shichinohe, M. Okamatsu, T. Tamura, Y. Tomita, N. Fujimoto, K. Goto, H. Katsura, E. Kawakami, I. Ishikawa, S. Watanabe, M. Ito, Y. S.-Tagawa, Y. Sugita, R. Uraki, R. Yamaji, A. J. Einfeld, G. Zhong, S. Fan, J. Ping, E. A. Maher, A. Hanson, Y. Uchida, T. Saito, M. Ozawa, G. Neumann, H. Kida, T. Odagiri, J. C. Paulson, H. Hasegawa, M. Tashiro, Y. Kawaoka, *Nature* **2013**, *501*, 551.
- [16] E. B. Cahoon, Y. Lindqvist, G. Schneider, J. Shanklin, *Proc. Natl. Acad. Sci. U.S.A.* **1997**, *94*, 4872.
- [17] J. Rebek, Jr., R. V. Wattlely, *J. Am. Chem. Soc.* **1980**, *102*, 4853.
- [18] N. Horiuchi, J. Huff, J. Rebek, Jr, *Tetrahedron Lett.* **1980**, *31*, 5121.
- [19] C. Browne, S. Brent, J. K. Clegg, J. R. Nitschke, *Angew. Chem. Int. Ed.* **2013**, *52*, 1944.
- [20] J. S. Mugridge, A. Zahl, R. van Eldik, R. G. Bergman, K. N. Raymond, *J. Am. Chem. Soc.* **2013**, *135*, 4299.
- [21] M. P. Schramm, P. Restorp, F. Zelder, J. Rebek, Jr., *J. Am. Chem. Soc.* **2008**, *130*, 2450.
- [22] M. Yoshizawa, J. K. Klosterman, M. Fujita, *Angew. Chem.* **2009**, *121*, 3470–3490; *Angew. Chem. Int. Ed.* **2009**, *48*, 3418.
- [23] Y. Nishioka, T. Yamaguchi, M. Kawano, M. Fujita, *J. Am. Chem. Soc.* **2008**, *130*, 8160.
- [24] M. Fujita, S.-Y. Yu, T. Kusukawa, H. Fumaki, K. Ogura, K. Yamaguchi, *Angew. Chem. Int. Ed. Engl.* **1998**, *37*, 2082.
- [25] T. Kusukawa, M. Fujita, *J. Am. Chem. Soc.* **2002**, *124*, 13576.
- [26] S. Sakamoto, M. Yoshizawa, T. Kusukawa, M. Fujita, K. Yamaguchi, *Org. Lett.*, **2001**, *3*(11), 1601.
- [27] K. Yamashita, M. Kawano, M. Fujita *Chem. Comm.* **2007**, 4102.

# Chapter 2

## Cavity comparison of self-assembled cages

The binding pockets of self-assembled coordination cages were subtly tuned by ancillary groups on the metal corners of the cage. Since the substituents on ancillary groups of the ligand hang over the cage cavity, specific interactions can be introduced. Bulky mesityl groups formed interactions and effectively shrunken cavity volume.

We report synthesis of a variety of self-assembled coordination cages **1** with *cis*-chelating phenanthroline ancillary ligands. Different substituents were introduced at 2,9-position of phenanthroline. Computational study were done for investigating how cavity volumes were affect by remote substituents. Bulky mesityl groups were proved to dramatically reduce the cavity volume of cage **1e** by 20%, comparing to the non-substituent cage **1a**. Since a variety of *cis*-chelating ligands can be employed as ancillary groups, our approach provides the most efficient and straightforward way to subtly control the binding properties of the cages.

## 2.1 Introduction

Self-assembled hollow coordination cages **1** is consisted of ancillary *cis*-chelated ligands and cavity-forming ligand.<sup>[1]</sup> We fixed the cavity-forming ligand as 2,4,6-tri(4-pyridyl)-1,3,5-triazine (TPT, **3**) and only changed *cis*-chelated ligands from bipyridine to phenanthroline derivatives (**2**). Five cages with different substituents were synthesized and characterized by NMR, ESI-MS and X-ray crystallography (Figure 1). Phenanthroline derivatives are widely used as a good building block due to its rigid framework and easy availability.<sup>[14, 15]</sup>

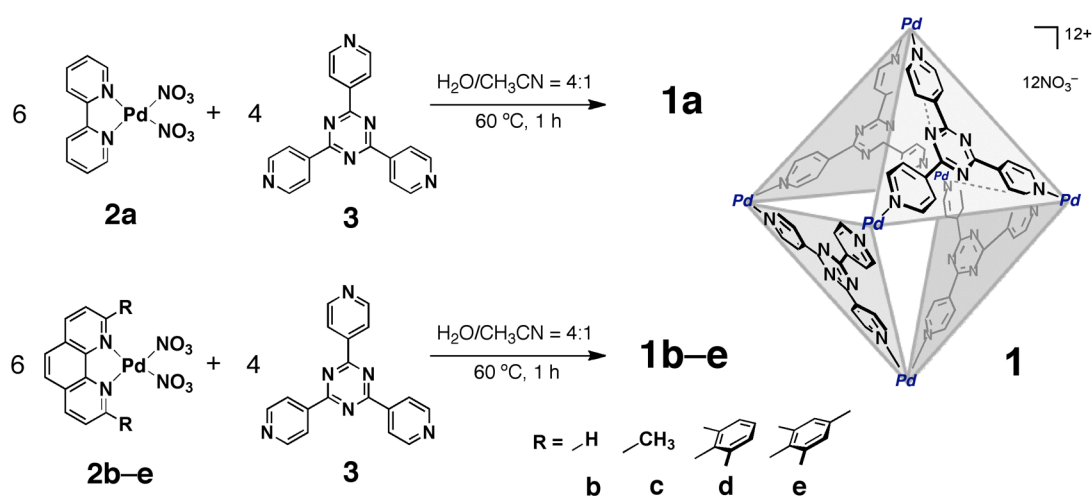


Figure 1. Self-assembly of cage **1**.

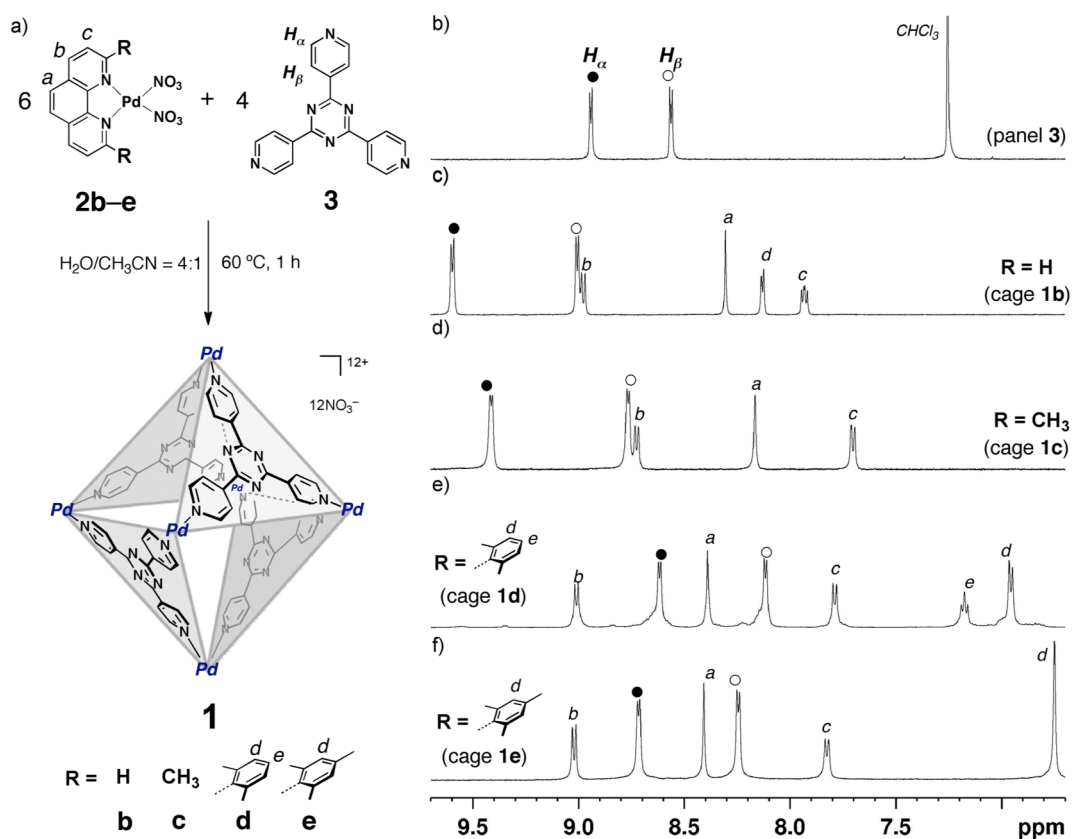
## 2.2 Synthesis of Cages with Different Remote Groups

Phenanthroline ( $R_2$ -phen)-capped cages [**1**; R = H (**1b**), Me (**1c**), 2,6-dimethylphenyl (**1d**), mesityl (**1e**)] were quantitatively self-assembled by simply mixing Pd( $R_2$ -phen)(NO<sub>3</sub>)<sub>2</sub> [**2**; R = H (**2b**), Me (**2c**), 2,6-dimethylphenyl (**2d**), mesityl (**2e**)] with 2,4,6-tri(4-pyridyl)-1,3,5-triazine (TPT, **3**) in H<sub>2</sub>O/CH<sub>3</sub>CN.<sup>[2]</sup> Bipyridine (bpy)-capped cage (**1a**) was also prepared in a similar way (Figure 1).<sup>[3]</sup> The reason of using mixed solvent is to increase the solubility of capping ligand during the self-assembly. The resulting suspension was stirred at 60 °C for 1 h. A trace amount of insoluble material was filtrated, and the clear colorless solution was evaporated to dryness to give cage **1** quantitatively as a white powder.

<sup>1</sup>H NMR spectra confirmed these new appeared signals belonging to complex **1**,

which adopt totally different pattern as cage components. DOSY NMR show single band for cage **1** to confirmed that it is a single product. Other 2D NMR measurement further confirmed the octahedral structure of cage **1**.

By comparing the  $^1\text{H}$  NMR spectra for cage **1b–e**, interesting things were found. After the pyridyl coordination on Pd(II), the pyridyl a protons (PyHa) of **3** shifted downfield for **1b** and **1c** but shifted upfield for **1d** and **1e**.<sup>[4]</sup> These different and

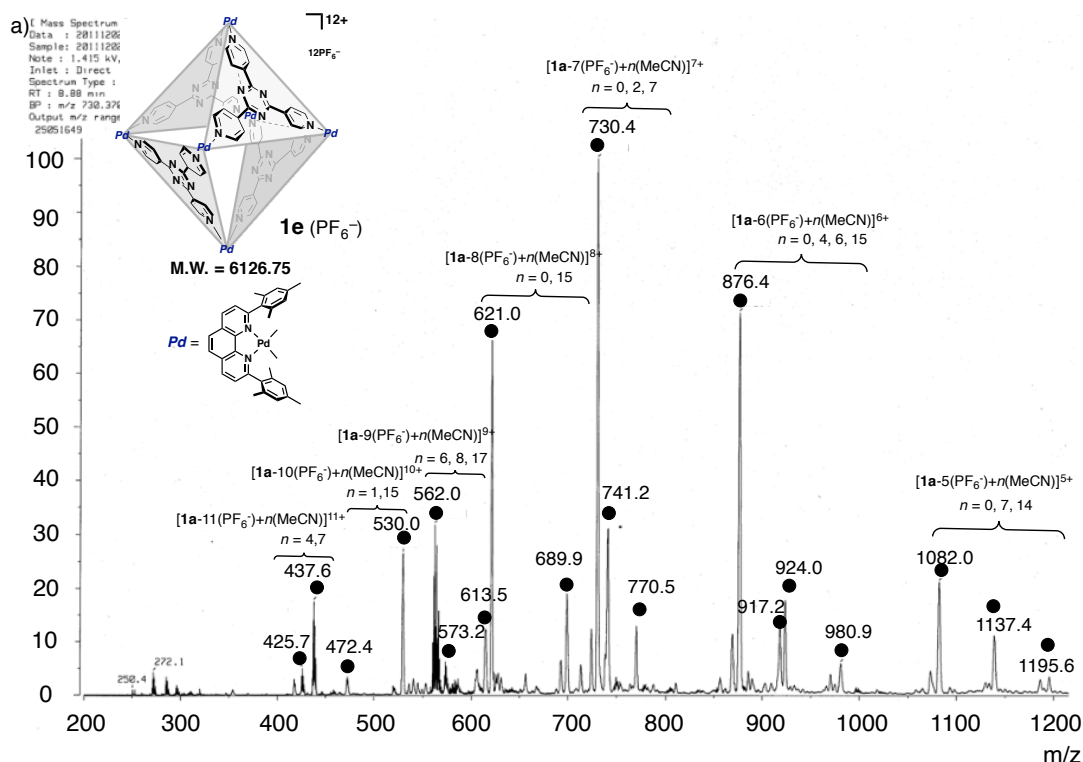


**Figure 2.** a) Self-assembly of coordination cage **1** from phenanthroline-based Pd(II) complex **1b–e** and triazine panel ligand **3**. b–f)  $^1\text{H}$  NMR spectra (500 MHz, 300 K) of the aromatic region of (b) triazine panel **3** (in  $\text{CDCl}_3$ ), (c) cage **1b** (in  $\text{D}_2\text{O}$ ), (d) cage **1c** (in  $\text{D}_2\text{O}$ ), (e) cage **1d** (in  $\text{D}_2\text{O}$ ), and (f) cage **1e** (in  $\text{D}_2\text{O}$ ). Reprinted with permission from ref. 4. Copyright 2014 John Wiley and Sons.

opposite behaviors for for **1d** and **1e** indicate a significant through-space interaction between the R pendant group of **2** and the pyridyl group of **3** (Figure 2). The cross peak between aromatic proton of **2** (*d*, *e* in **2d**; *d* in **2e**) and pyridyl proton of **3** were found by NOESY spectra, which further confirmed that the 2,9–substituents locate near the pyridyl moieties.

Through increasing the bulkiness on ancillary ligand, solubility in water were maintained due to 12 positive charges on metal ions. Chemical and thermal stability were observed almost the same for these cages. Elemental analysis and melting point were also tested and showed in the experimental part.

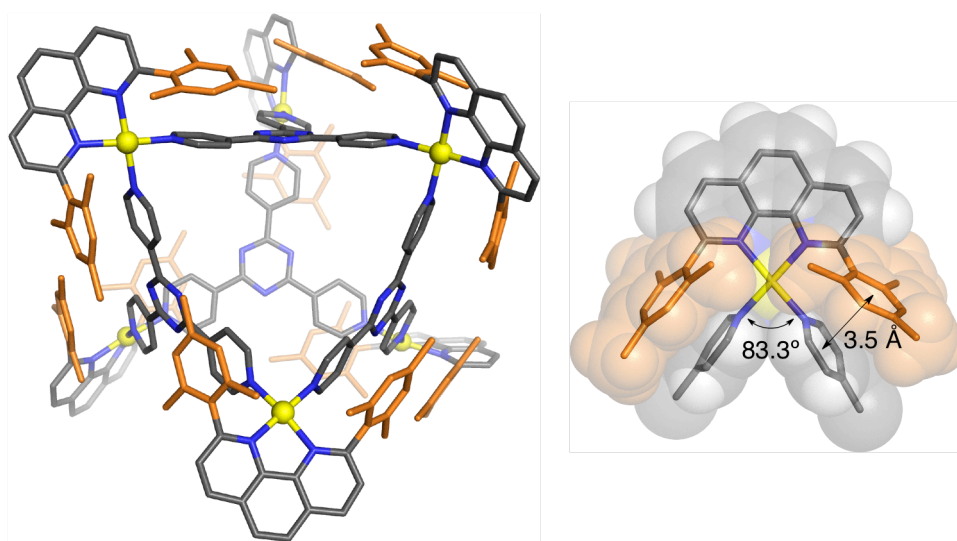
After anion exchange from  $\text{NO}_3^-$  to  $\text{PF}_6^-$  by treating aquar solution of cage **1** with  $\text{KPF}_6$ , cage **1** ( $\text{PF}_6^-$ ) was obtained as green solid. Cage **1** ( $\text{PF}_6^-$ ) easily dissolves in polar solvent acetonitrile and fully ionized under ESI-MS. Large molecular weight and charge distribution confirmed the cage is a hollow structure containing high positive charge. For example, cage **1e** shows a molecular weight of 6126.75 Da and shows positive charge from  $5^+$  to  $11^+$  (Figure 3).



**Figure 3** ESI-MS spectrum of cage **1e** with  $\text{PF}_6^-$ . Reprinted with permission from ref. 3. Copyright 2013 American Chemical Society.

## 2.3 Cavity Comparison of Cages with Different Remote Groups

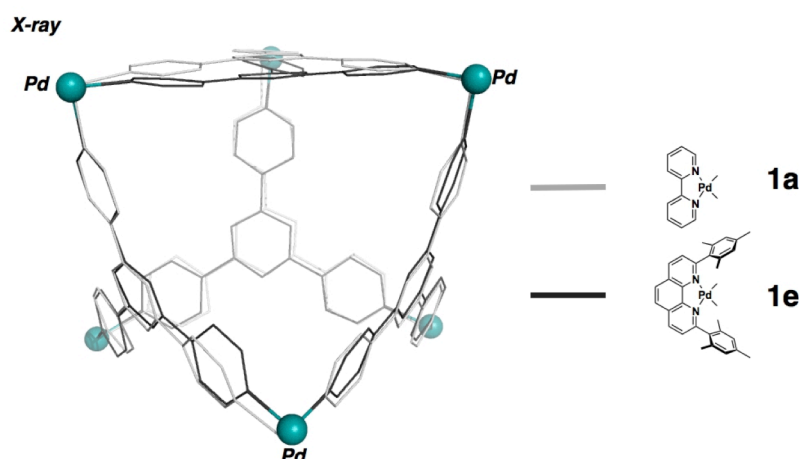
A block-shaped single crystal of **1e** ( $\text{PF}_6^-$  salt) was obtained by slow diffusion of ethanol into the acetonitrile solution at 15 °C for 4d. The structure of cage **1e** ( $\text{PF}_6^-$  salt) was unambiguously determined by a synchrotron X-ray diffraction study (Figure 4). The crystal structure shows that the two mesityl substituents in the Mes-phen ligand (**2e**) hang over the two remaining coordination sites on the Pd(II) center, narrowing the coordination bite angle. At the same time, the mesityl groups interact through space with the pyridyl groups of the triazine-cored ligand **3** of the cage at a distance of  $\sim 3.5$  Å. Due to the steric demand of the mesityl groups, the pyridine rings of **3** are tilted by  $9.4^\circ$  on average with respect to the triazine core. Most importantly, the Pd(II) ions display a distorted square planar geometry and the average N-Pd-N bite angle defined by the two 4-pyridyl nitrogen atoms on every Pd(II) ion is  $83.3^\circ$  and significantly deviates from the ideal  $90^\circ$  angle.<sup>[3]</sup>



**Figure 4.** X-ray crystal structure of cage **1e** ( $\text{PF}_6^-$  salt). For clarity, H atoms,  $\text{PF}_6^-$  counter anions, and solvent molecules have been omitted. C: gray, N: blue, Pd: yellow, mesityl group: orange. The coordination environment of the Pd(II) center is highlighted on the right with space-filling depiction in the background.

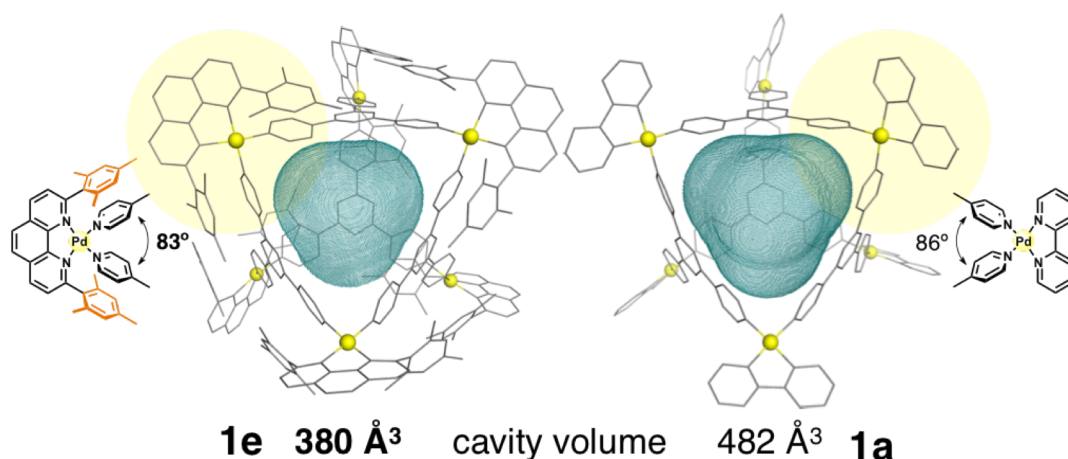
In order to study how the cavities affect by remote substituents, superposition of cages **1a** and **1e** were conducted based on their crystal structures (Figure 5). The two cannot perfectly overlap each indicate these two cavities were different.





**Figure 5.** Superposition of cages **1a** and **1e** based on X-ray single crystal structure.

For fully investigate the difference of the two cavities quantitatively, the cavity volumes of cages **1a** and **1e** were calculated by using the *VOIDOO* program<sup>[5-11]</sup> based on their crystal structures (Figure 6). A virtual sphere probe with a radius of 3.36 Å were filled into the cavity of both cages and the occupied space are measured and visualized in mesh to show the cavity volume for both cages respectively. It was found that the cavity volume of **1e** with the bulky mesityl groups (380 Å<sup>3</sup>) was dramatically reduced by ~20%, compared with that of **1a** (482 Å<sup>3</sup>) without pendant groups. Because cages **1a** (bipyridine) and **1b** (Phenanthroline) do not have pendant groups, the both cavity volumes can be regarded as the same. Indeed, superposition of cages **1a** and **1b** were conducted and show almost perfect overlap.



**Figure 6.** The central void volumes (green mesh) in cages **1a** and **1e**. Probe radius = 3.36 Å. Reprinted with permission from ref. 3. Copyright 2013 American Chemical Society.

On the other hand, in computationally optimized structures of cages **1**, due to the tiny difference of single methyl group, superposition of the cage framework between **1b** and **1c** was virtually identical and did not give any useful information. The same result was observed for comparison between cage **1d** and **1e** with tiny difference only in *para*-methyl substituents.

Thus, bulky substituent considerably reduced the cavity of cage **1e** by the smaller N-Pd-N bite angles and the deformed ligand **3** with tilted pyridine moieties. Indeed, substituent in the remote site can tailor the cavity of cage **1** by steric effect.

## 2.4 Conclusion

In summary, we prepared self-assembled cage **1a–e** with different remote pendant groups. For cage **1e** with bulky Mes-phen ancillary ligands on the Pd(II) centers, where the cavity-forming ligand and the ancillary ligand cooperatively but independently play important roles: the former forms an efficient recognition pocket and the latter tunes the recognition ability. Though not involved in the structural components of the cavity, the bulky mesityl groups hang over the cavity, reducing the effective volume and controlling the guest binding and motion. Since replacement of the ancillary ligands is straightforward, unique functions of cages **1** can be rapidly elaborated using the present strategy.

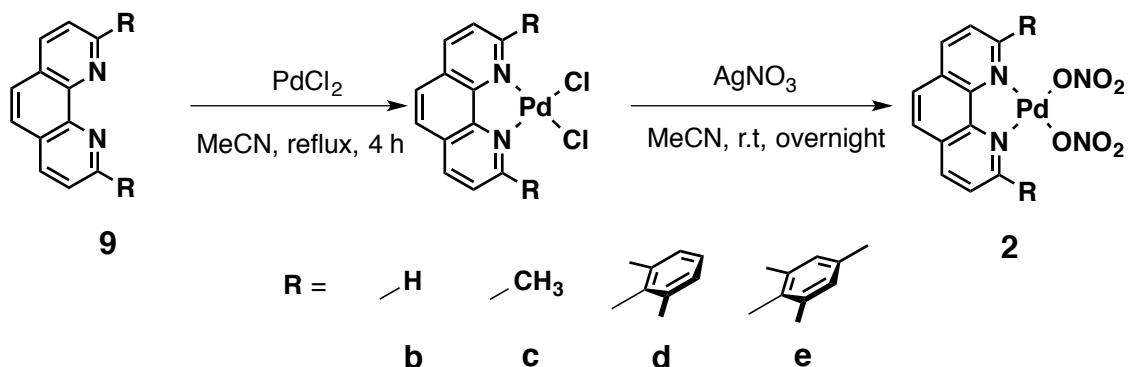
Similar like trypsin and chymotrypsin, bulky substituents (mesityl) locating far from the cavity of cage **1e** remotely controlled the cavity in size and shape, paved a way for investigating properties inside shrunken cavity.

## 2.5 Experiment Section

**Materials and Instrumentations:**  $^1\text{H}$  and other NMR spectra were recorded on a Bruker DRX-500 (500 MHz) spectrometer. TMS ( $\text{CDCl}_3$  solution) in a capillary served as an external standard ( $\delta = 0$  ppm). Melting points were determined with a Yanaco MF-500 V micro melting point apparatus. Elemental analyses were performed on a Yanaco MT-6. MALDI-TOF mass spectra were measured on an Applied Biosystem Voyager DE-STR. CSI-MS data were measured on a four-sector (BE/BE) tandem mass spectrometer (JMS-700C, JEOL) equipped with the CSI source. Diffraction measurements were made using a Bruker APEXII/CCD diffractometer equipped with a focusing mirror ( $\text{MoK}\alpha$  radiation  $\lambda = 0.71073 \text{ \AA}$ ). Solvents and reagents were purchased from TCI Co., Ltd., WAKO Pure Chemical Industries Ltd., and Sigma-Aldrich Co. Deuterated  $\text{H}_2\text{O}$  was acquired from Cambridge Isotope Laboratories, Inc. and used as supplied for the complexation reactions and NMR measurements. Bis-2,9-dimesityl-phenanthroline (**9**) was prepared according to an established method.<sup>[12, 13]</sup>

**For all the figures and tables: Reprinted with permission from ref. 3 and 4. Copyright 2013 American Chemical Society.**

## Synthesis of Pd(II) ancillary ligand **2**



## General Procedure

To a refluxing solution of PdCl<sub>2</sub> (35.5 mg, 0.20 mmol) in MeCN (15.0 mL) was added bis-2,9-dimesityl-phenanthroline (**9**; 83.2 mg, 0.20 mmol). The resulting yellowish solution was stirred at reflux for another 4 h. Then the solution was cooled down to room temperature and treated with AgNO<sub>3</sub> (67.9 mg, 0.40 mmol). A large amount of white precipitate appeared instantly, and the suspended solution was stirred at room temperature for overnight. White precipitate was filtrated, and the clear orange solution was evaporated to dryness to give **2e** as an orange crystal (104 mg, 0.16 mmol) in 81% yield. Ancillary ligand **2a–d** was prepared by a similar procedure to that of **2e**.

Physical data of **2b**: <sup>1</sup>H NMR (500 MHz, D<sub>2</sub>O) δ: 8.90 (d, *J* = 8.0 Hz, 2H), 8.56 (d, *J* = 5.5 Hz, 2H, phen), 8.18 (s, 2H), 8.02 (d-d, *J* = 8.0 Hz, 2H); <sup>13</sup>C NMR (125 MHz, D<sub>2</sub>O, 300 K) δ: 149.6 (CH), 147.3 (C), 141.4 (CH), 130.9 (C), 127.7 (CH), 125.5 (CH). m.p. = ~240 °C (decomposed). ESI-MS Calcd. for C<sub>14</sub>N<sub>3</sub>O<sub>3</sub>Pd<sup>+</sup>: *m/z* 347.96, found: 347.88. E.A. Calcd. for C<sub>12</sub>H<sub>8</sub>N<sub>4</sub>O<sub>6</sub>Pd: C, 35.10; H, 1.96; N, 13.64; Found: C, 34.99; H, 1.58; N, 13.39.

Physical data of **2c**: <sup>1</sup>H NMR (500 MHz, D<sub>2</sub>O) δ: 8.62 (d, *J* = 8.0 Hz, 2H), 8.02 (s, 2H), 7.73 (d, *J* = 8.0 Hz, 2H); <sup>13</sup>C NMR (125 MHz, D<sub>2</sub>O, 300 K) δ: 148.2 (CH), 145.3 (C), 140.1 (C), 130.2 (C), 128.7 (CH), 123.2 (CH). m.p. = ~240 °C (decomposed). ESI-MS Calcd. for C<sub>14</sub>H<sub>8</sub>N<sub>3</sub>O<sub>3</sub>Pd<sup>+</sup>: *m/z* 376.69, found: 376.61. E.A. Calcd. for C<sub>14</sub>H<sub>12</sub>N<sub>4</sub>O<sub>6</sub>Pd: C, 38.33; H, 2.76; N, 12.77; Found: C, 38.00; H, 2.55; N, 12.61.

Physical data of 2d:  $^1\text{H}$  NMR (500 MHz,  $\text{CD}_3\text{CN}$ )  $\delta$ : 8.89 (d,  $J = 8.0$  Hz, 2H, phen), 8.26 (s, 2H, phen), 7.79 (d,  $J = 8.5$  Hz, 2H, phen), 7.31 (t,  $J = 5.5$  Hz, 2H, Ph), 7.22 (d,  $J = 8.5$  Hz, 4H, Ph), 2.32 (s, 12H, Me);  $^{13}\text{C}$  NMR (125 MHz,  $\text{CD}_3\text{CN}$ , 300 K)  $\delta$ : 165.7 (C, Phen), 149.5 (C, Phen), 142.1 (CH, Phen), 141.2 (C, Mes), 137.1 (C, Mes), 135.0 (C, Mes), 131.2 (C, Phen), 130.7 (CH, Phen), 129.9 (CH, Mes), 128.8 (CH, Phen), 21.3 ( $\text{CH}_3$ , Mes), 20.9 ( $\text{CH}_3$ , Mes). m.p. =  $\sim 240$  °C (decomposed). ESI-MS Calcd. for  $\text{C}_{30}\text{H}_{28}\text{N}_3\text{O}_3\text{Pd}^+$ :  $m/z$  584.12, found: 584.31. E.A. Calcd. for  $\text{C}_{30}\text{H}_{28}\text{N}_3\text{O}_3\text{Pd}$ : C, 55.69; H, 4.36; N, 8.66; Found: C, 55.84; H, 4.72; N, 8.99.

Physical data of 2e:  $^1\text{H}$  NMR (500 MHz,  $\text{CD}_3\text{CN}$ )  $\delta$ : 8.86 (d,  $J = 8.0$  Hz, 4h, phen), 8.24 (s, 4h, phen), 7.77 (d,  $J = 8.5$  Hz, 4h, phen), 7.04 (s, 4H, Mes), 2.32 (s, 6H, Mes), 2.30 (s, 14h, Mes);  $^{13}\text{C}$  NMR (125 MHz,  $\text{CD}_3\text{CN}$ , 300 K)  $\delta$ : 165.7 (C, Phen), 149.5 (C, Phen), 142.1 (CH, Phen), 141.2 (C, Mes), 137.1 (C, Mes), 135.0 (C, Mes), 131.2 (C, Phen), 130.7 (CH, Phen), 129.9 (CH, Mes), 128.8 (CH, Phen), 21.3 ( $\text{CH}_3$ , Mes), 20.9 ( $\text{CH}_3$ , Mes). m.p. =  $\sim 240$  °C (decomposed). ESI-MS Calcd. for  $\text{C}_{30}\text{H}_{28}\text{N}_3\text{O}_3\text{Pd}^+$ :  $m/z$  584.12, found: 584.31. E.A. Calcd. for  $\text{C}_{30}\text{H}_{28}\text{N}_3\text{O}_3\text{Pd}$ : C, 55.69; H, 4.36; N, 8.66; Found: C, 55.84; H, 4.72; N, 8.99.

# NMR Spectrum

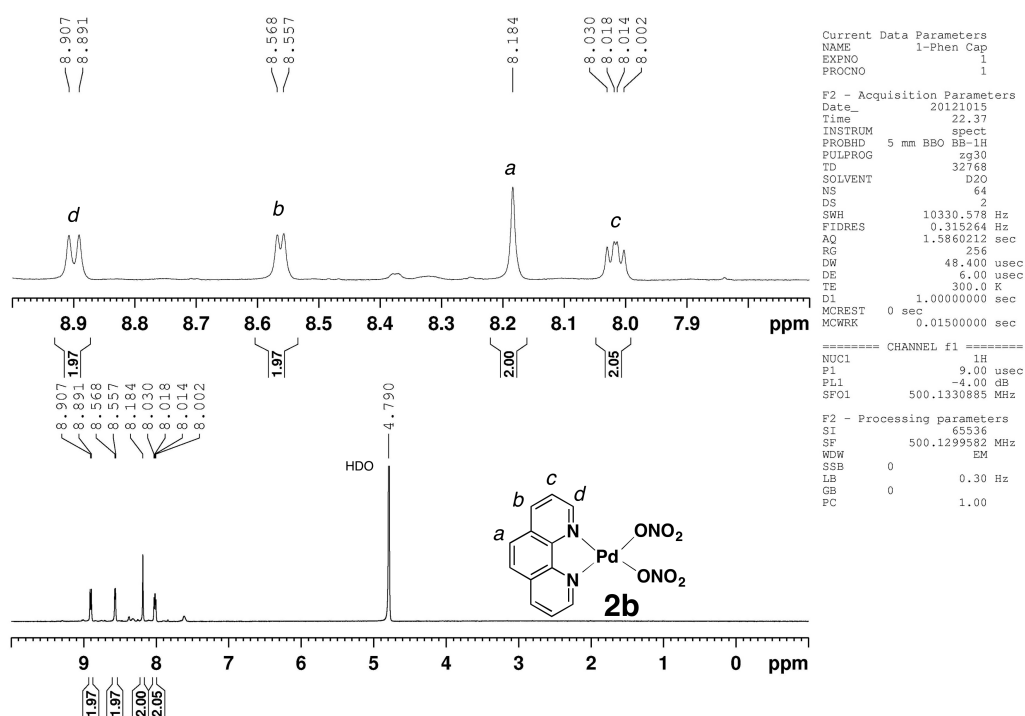


Figure S1. <sup>1</sup>H NMR spectrum (500 MHz, 300 K, CD<sub>3</sub>CN) of **2b**.

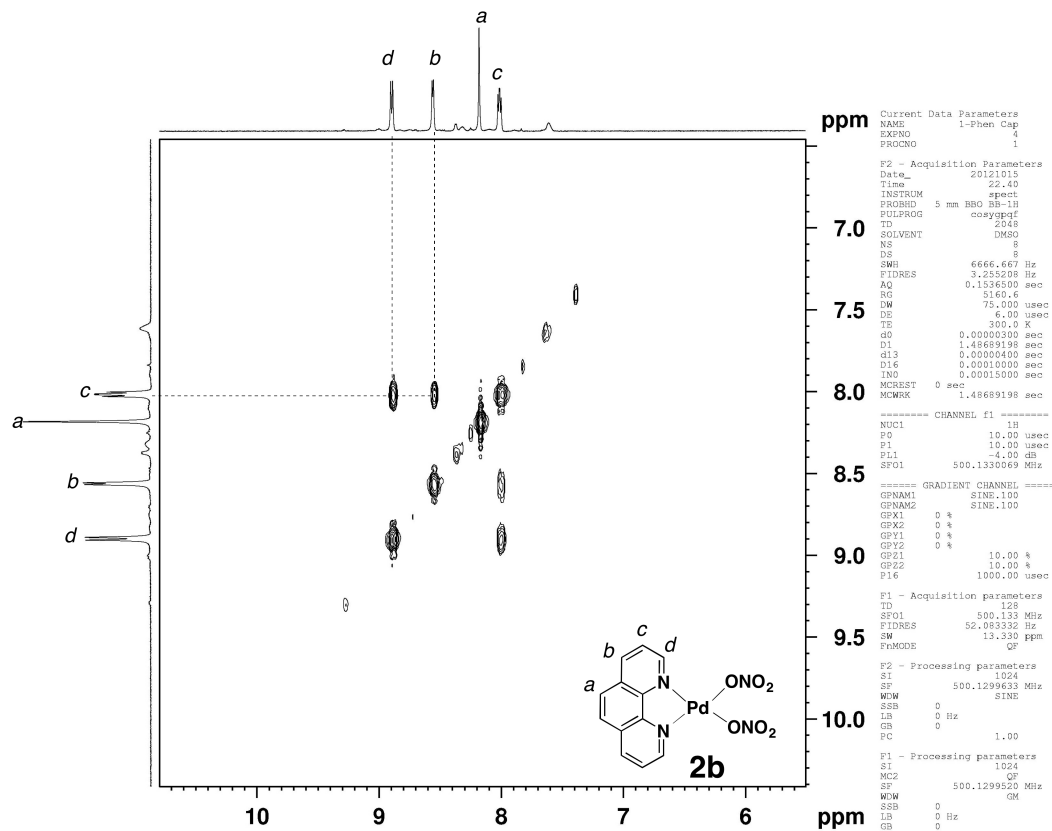


Figure S2. <sup>1</sup>H-<sup>1</sup>H COSY spectrum (500 MHz, 300 K, CD<sub>3</sub>CN) of **2b**.

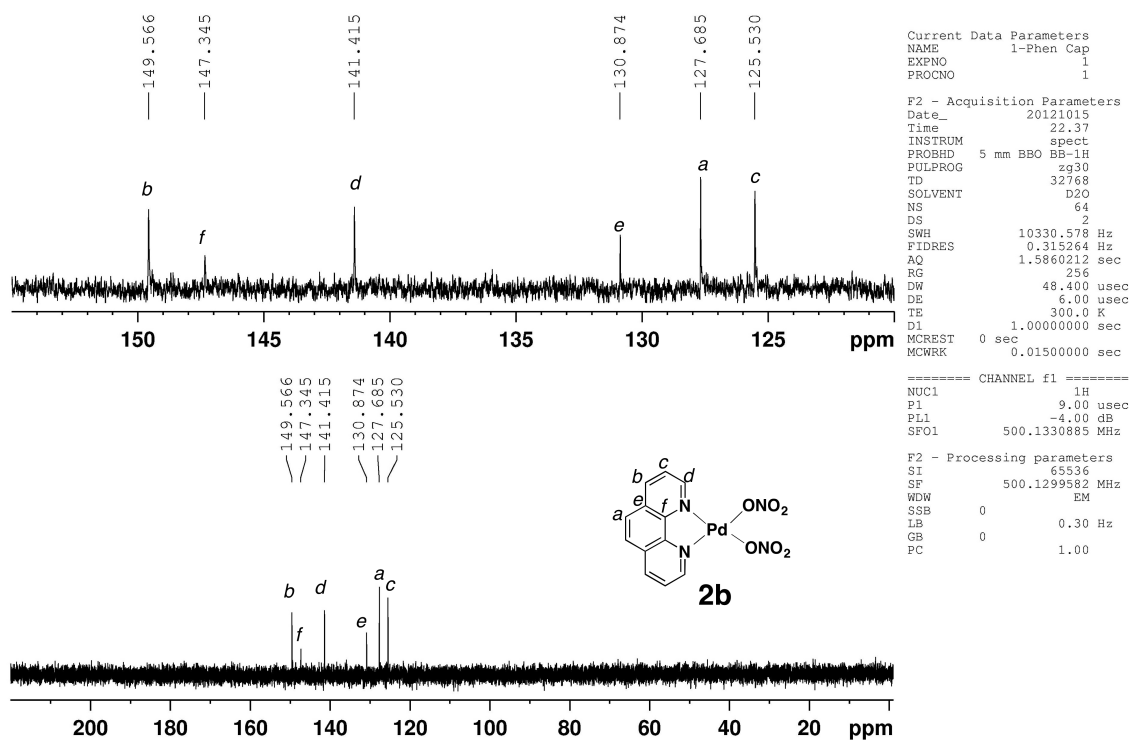


Figure S3.  $^{13}\text{C}$  NMR spectrum (125 MHz, 300 K,  $\text{CD}_3\text{CN}$ ) of **2b**.

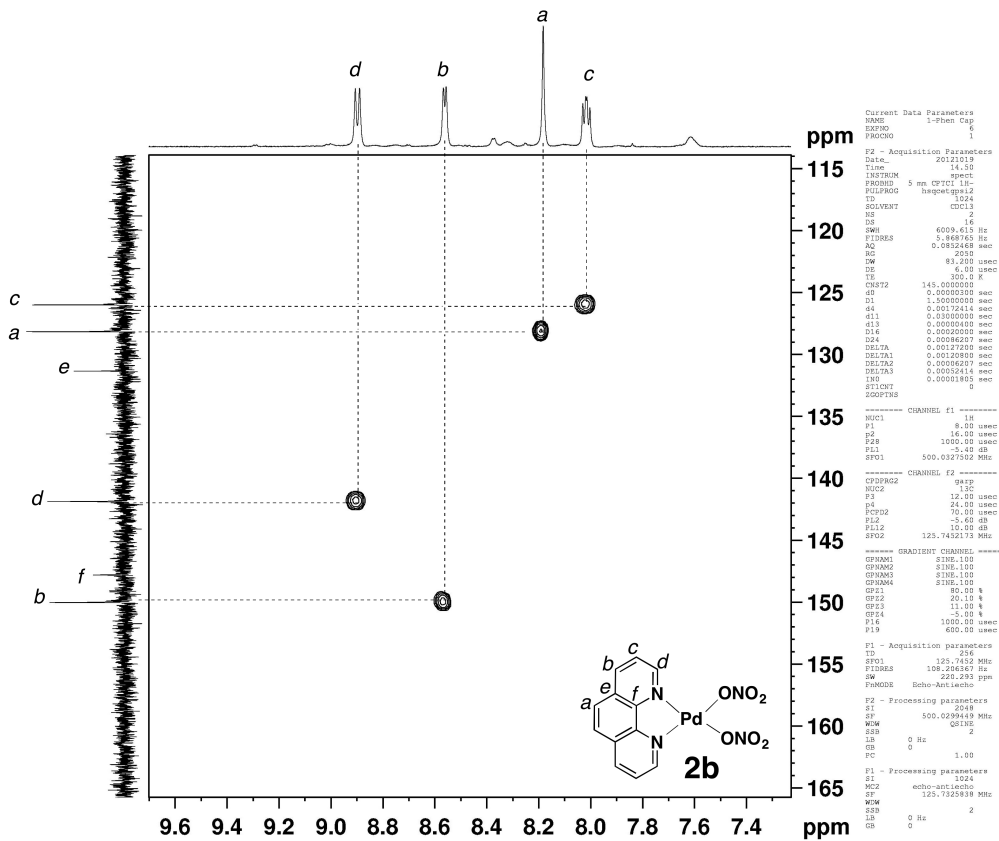


Figure S4.  $^1\text{H}$ - $^{13}\text{C}$  HSQC spectrum (500 MHz, 300 K,  $\text{CD}_3\text{CN}$ ) of **2b**.

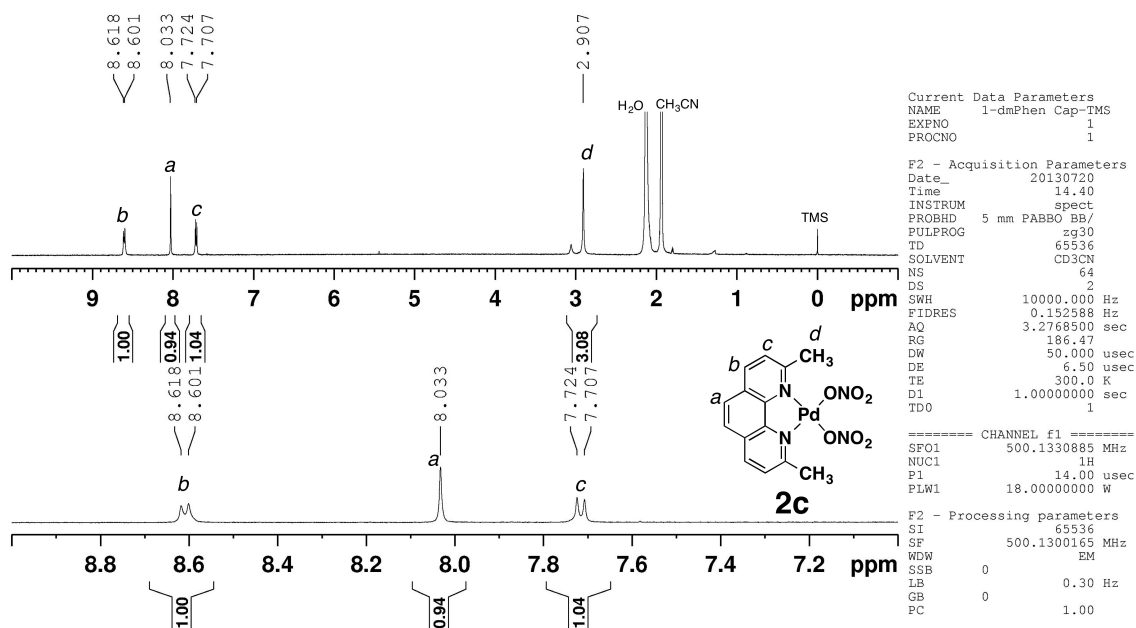


Figure S5.  $^1\text{H}$  NMR spectrum (500 MHz, 300 K,  $\text{CD}_3\text{CN}$ ) of **2c**.

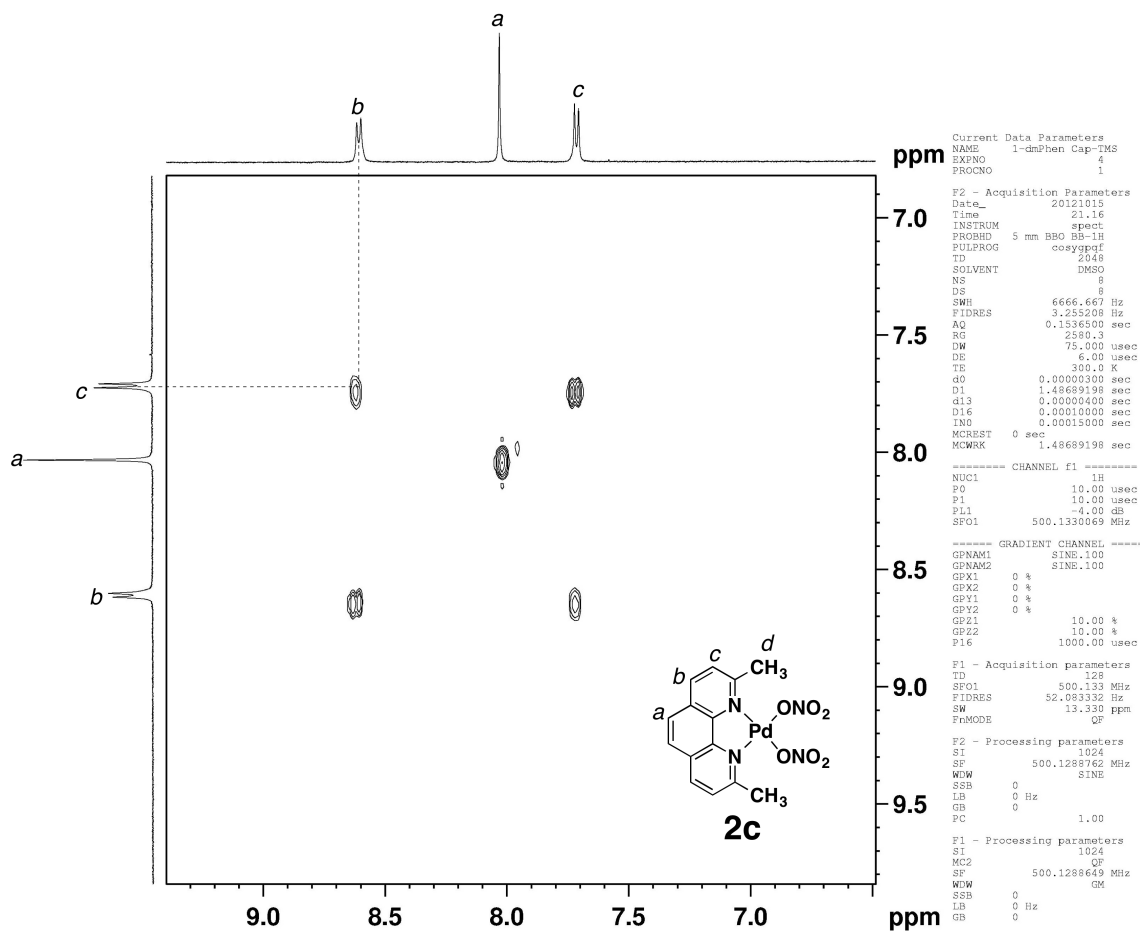


Figure S6.  $^1\text{H}$ - $^1\text{H}$  COSY spectrum (500 MHz, 300 K,  $\text{CD}_3\text{CN}$ ) of **2c**.



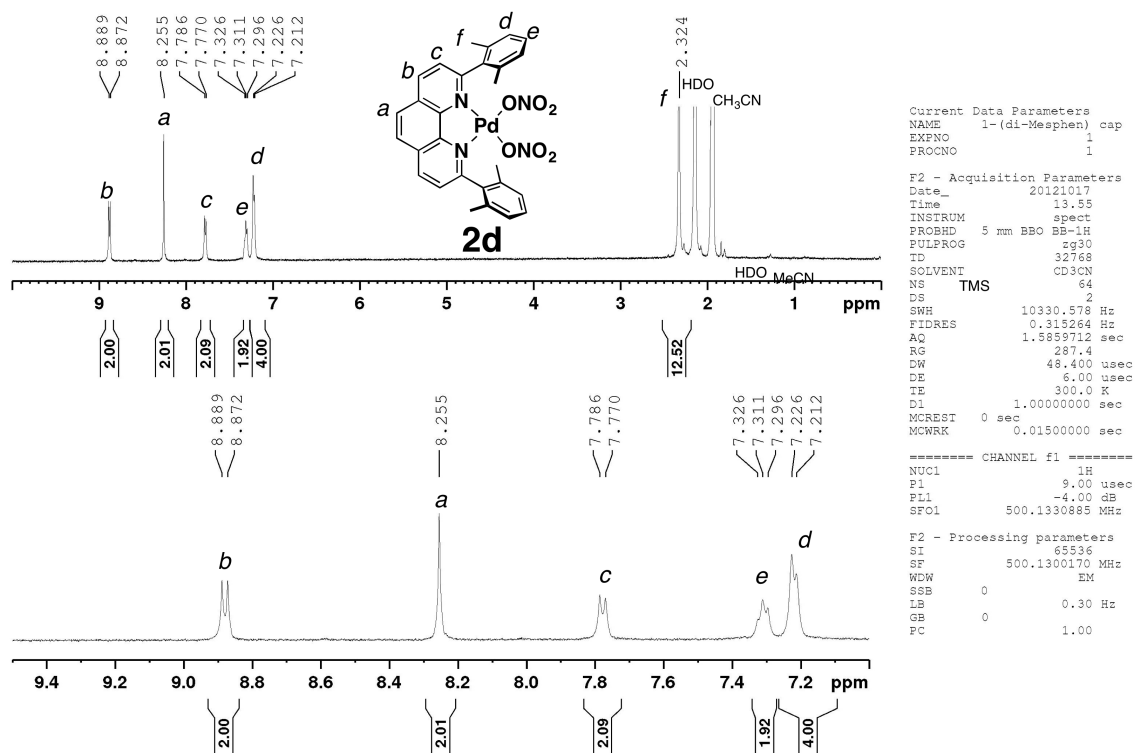


Figure S7.  $^1\text{H}$  NMR spectrum (500 MHz, 300 K,  $\text{CD}_3\text{CN}$ ) of **2d**.

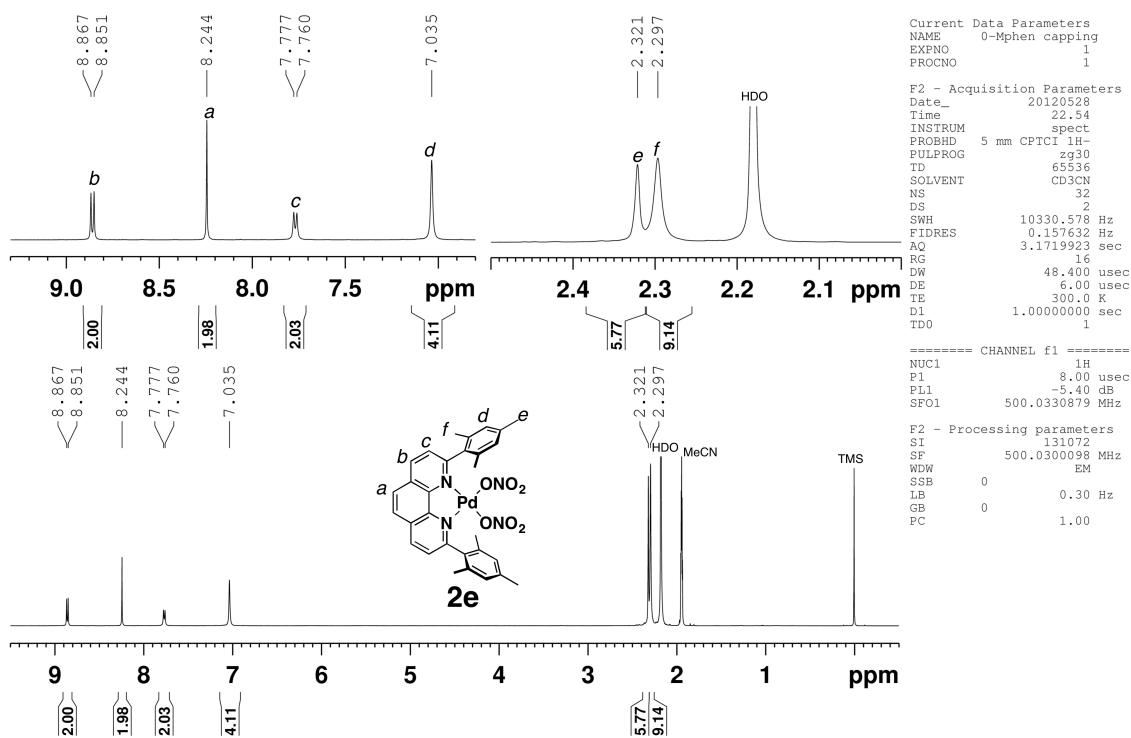


Figure S8.  $^1\text{H}$  NMR spectrum (500 MHz, 300 K,  $\text{CD}_3\text{CN}$ ) of **2e**.

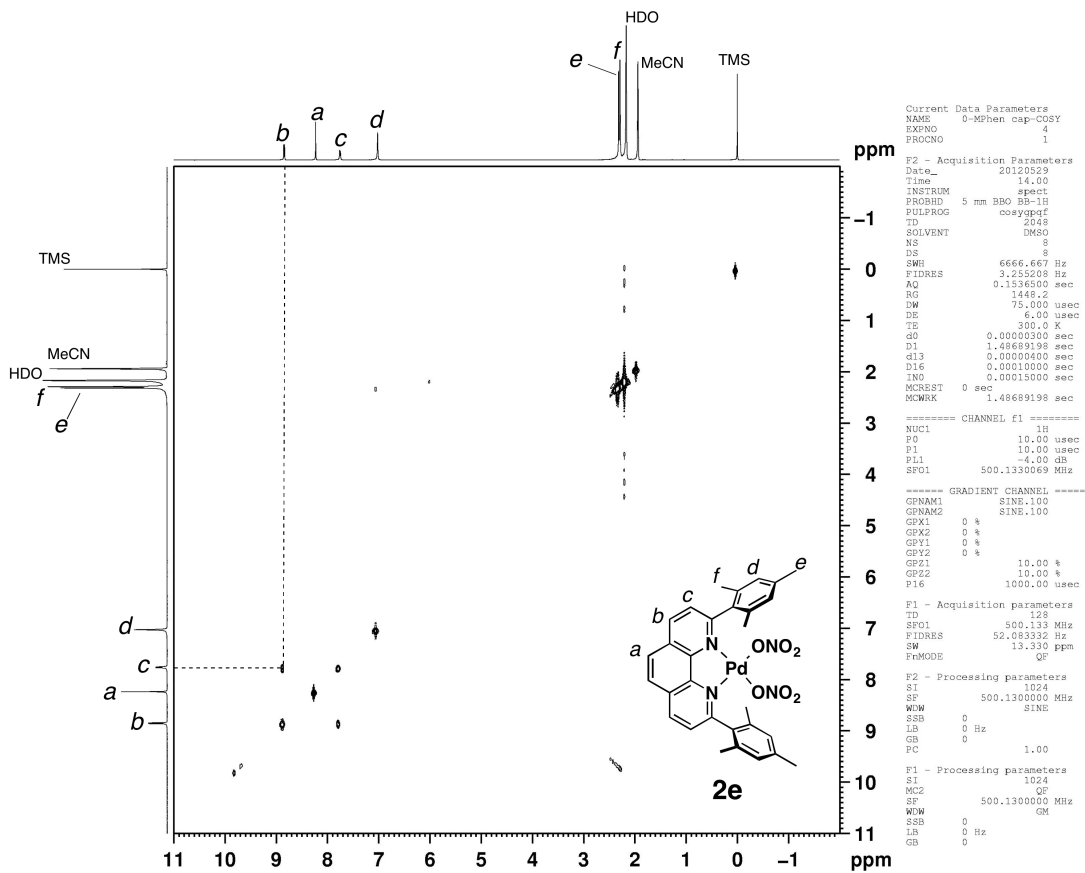


Figure S9.  $^1\text{H}$ - $^1\text{H}$  COSY spectrum (500 MHz, 300 K,  $\text{CD}_3\text{CN}$ ) of **2e**.

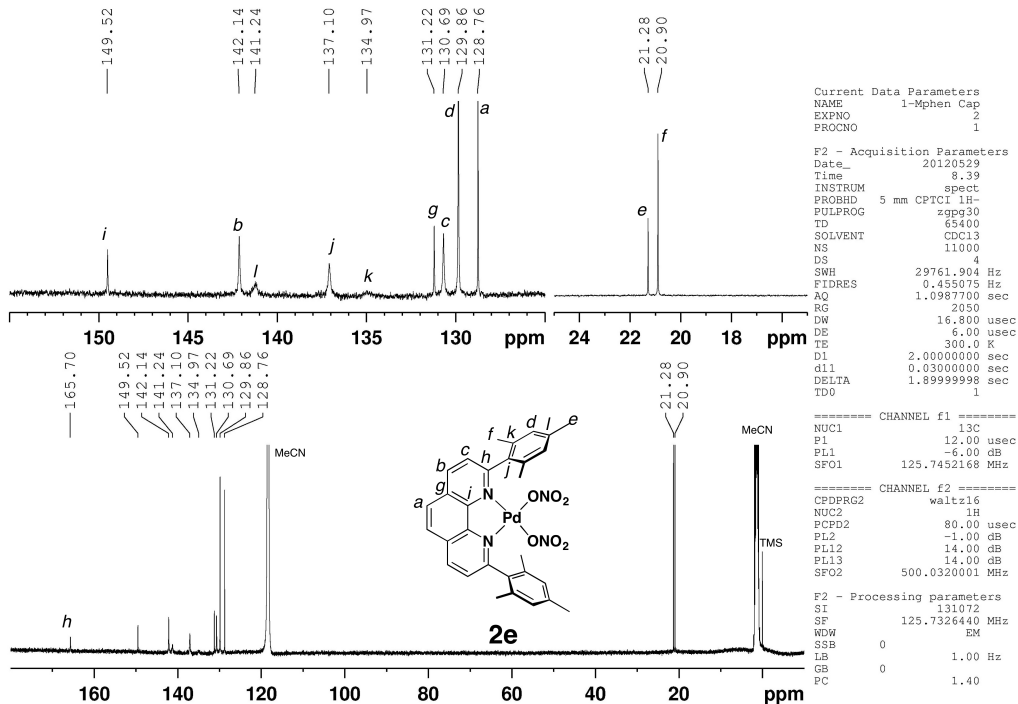


Figure S10.  $^{13}\text{C}$  NMR spectrum (125 MHz, 300 K,  $\text{CD}_3\text{CN}$ ) of **2e**.

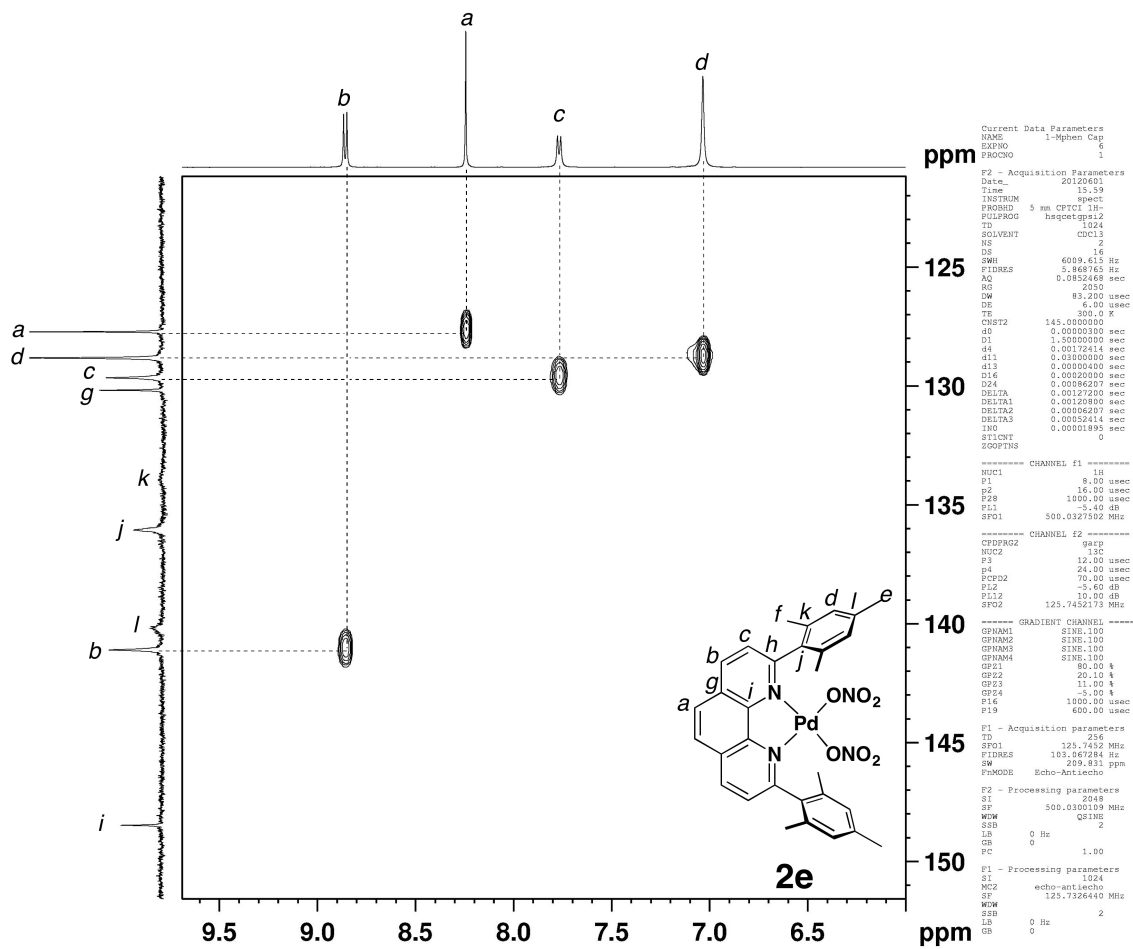
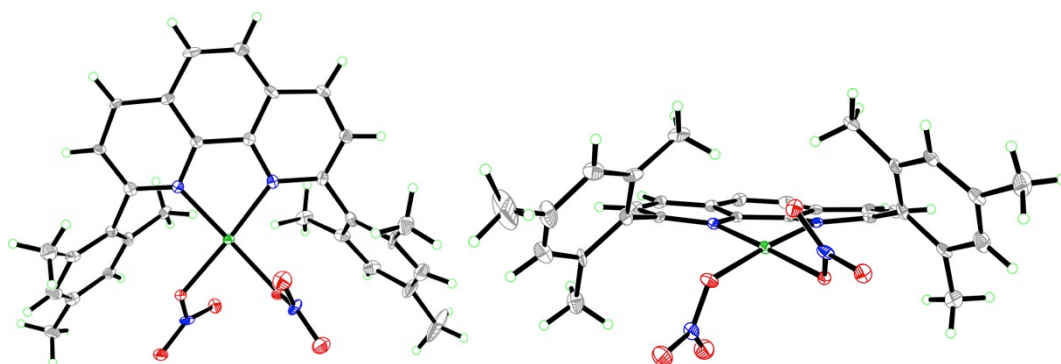


Figure S11.  $^1\text{H}$ - $^{13}\text{C}$  HSQC spectrum (500 MHz, 300 K,  $\text{CD}_3\text{CN}$ ) of **2e**.

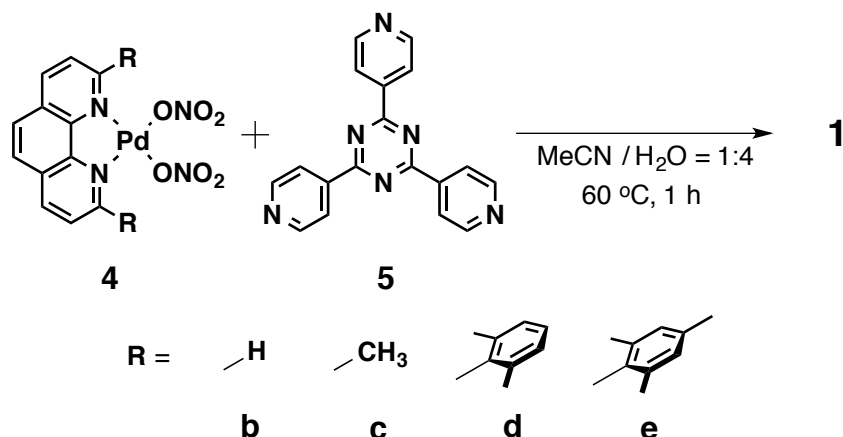
**Table S1.** Crystal data and structure refinement for **4e**.

Identification code	p1	
Empirical formula	C <sub>34</sub> H <sub>34</sub> N <sub>6</sub> O <sub>6</sub> Pd	
Formula weight	729.07	
Temperature	90(2) K	
Wavelength	0.71073 Å	
Crystal system	Triclinic	
Space group	P1	
Unit cell dimensions	a = 11.5814(11) Å	α = 71.2410(10)°.
	b = 11.7027(11) Å	β = 89.3590(10)°.
	c = 14.1322(14) Å	γ = 68.9890(10)°.
Volume	1681.3(3) Å <sup>3</sup>	
Z	2	
Density (calculated)	1.440 Mg/m <sup>3</sup>	
Absorption coefficient	0.605 mm <sup>-1</sup>	
F(000)	748	
Crystal size	0.40 x 0.18 x 0.10 mm <sup>3</sup>	
Theta range for data collection	1.53 to 24.99°.	
Index ranges	-13 ≤ h ≤ 13, -13 ≤ k ≤ 13, -16 ≤ l ≤ 16	
Reflections collected	15647	
Independent reflections	11448 [R(int) = 0.0181]	
Completeness to theta = 24.99	- 99.3 %	
Absorption correction	Semi-empirical from equivalents	
Max. and min. transmission	0.9420 and 0.7939	
Refinement method	Full-matrix least-squares on F <sup>2</sup>	
Data / restraints / parameters	11448 / 266 / 787	
Goodness-of-fit on F <sup>2</sup>	1.090	
Final R indices [I > 2σ(I)]	R1 = 0.0341, wR2 = 0.0900	
R indices (all data)	R1 = 0.0357, wR2 = 0.0919	
Absolute structure parameter	0.41(3)	
Largest diff. peak and hole	1.667 and -0.534 e.Å <sup>-3</sup>	



**Figure S12.** ORTEP drawing (30% probability ellipsoids) of **4e** (Grey: C; Blue: N; Red: O).

## Synthesis of self-assembled cages 1



[Pd(Mes-phen)](NO<sub>3</sub>)<sub>2</sub> (**2e**; 20 mg, 31 μmol) and 2,4,6-tri(4-pyridyl)-1,3,5-triazine (**3**; 6.3 mg, 20 μmol) were added in H<sub>2</sub>O-MeCN (4.0 mL, 4:1 v/v). The resulting suspension was stirred at 60 °C for 1 h. A trace amount of insoluble material was filtrated, and the clear colorless solution was evaporated to dryness to give cage **1e** quantitatively as a white powder. Cage **1a–d** was prepared by the similar procedure.

### Physical Data of Cage **1b**

<sup>1</sup>H NMR (500 MHz, D<sub>2</sub>O, 300 K) δ: 9.60 (d, *J* = 6.5 Hz, 24H, PyH<sub>a</sub>), 9.01 (d, *J* = 6.5 Hz, 12H, PyH<sub>b</sub>), 8.98 (d, *J* = 8.5 Hz, 12H, phen), 8.31 (s, 12H, phen), 8.13 (d, *J* = 5.5 Hz, 12H, phen), 7.94 (dd, *J* = 8.5 Hz, 12H, phen); <sup>13</sup>C NMR (125 MHz, D<sub>2</sub>O, 300 K) δ: 170.0 (C, triazine), 152.9 (CH, Py), 151.1 (CH, phen), 147.4 (C, Py), 146.7 (C, phen), 142.2 (CH, phen), 131.6 (C, phen), 128.5 (CH, phen), 126.9 (CH, Py), 126.5 (CH, phen). DOSY-NMR (m<sup>2</sup>/s): *D* = 1.4 × 10<sup>-10</sup>. m.p. = ~240 °C (decomposed). E.A. Calcd. for C<sub>144</sub>H<sub>96</sub>N<sub>48</sub>O<sub>36</sub>Pd<sub>6</sub>·(H<sub>2</sub>O)<sub>27</sub>: C, 41.18; H, 3.60; N, 16.01; Found: C, 41.54; H, 3.58; N, 15.81. CSI-MS (PF<sub>6</sub><sup>-</sup> salt, MeCN): *m/z* = 268.0 [**1b**+6·MeCN]<sup>12+</sup>, 298.0 [**1b**-11·PF<sub>6</sub><sup>-</sup>+4·MeCN]<sup>11+</sup>, 346.4 [**1b**-10·PF<sub>6</sub><sup>-</sup>+5·MeCN]<sup>10+</sup>, 387.4 [**1b**-9·PF<sub>6</sub><sup>-</sup>+2·MeCN]<sup>9+</sup>, 530.9 [**1b**-8·PF<sub>6</sub><sup>-</sup>+17·MeCN]<sup>8+</sup>, 533.6 [**1b**-7·PF<sub>6</sub><sup>-</sup>+MeCN]<sup>7+</sup>, 557.0 [**1b**-7·PF<sub>6</sub><sup>-</sup>+5·MeCN]<sup>7+</sup>, 592.2 [**1b**-7·PF<sub>6</sub><sup>-</sup>+11·MeCN]<sup>7+</sup>, 667.2 [**1b**-6·PF<sub>6</sub><sup>-</sup>+4·MeCN]<sup>6+</sup>, 821.4 [**1b**-5·PF<sub>6</sub><sup>-</sup>+3·MeCN]<sup>5+</sup>, 887.1 [**1b**-5·PF<sub>6</sub><sup>-</sup>+11·MeCN]<sup>5+</sup>, 1042.5 [**1b**-4·PF<sub>6</sub><sup>-</sup>+MeCN]<sup>4+</sup>.

### Physical Data of Cage **1c**

$^1\text{H}$  NMR (500 MHz,  $\text{D}_2\text{O}$ , 300 K)  $\delta$ : 9.42 (d,  $J = 5.5$  Hz, 24H,  $\text{PyH}_a$ ), 8.77 (d,  $J = 5.0$  Hz, 12H,  $\text{PyH}_b$ ), 8.73 (d,  $J = 8.5$  Hz, 12H, phen), 8.17 (s, 12H, phen), 7.71 (d,  $J = 8.0$  Hz, 12H, phen), 2.25 (s,  $\text{CH}_3$ );  $^{13}\text{C}$  NMR (125 MHz,  $\text{D}_2\text{O}$ , 300 K)  $\delta$ : 169.5 (C, triazine), 164.9 (C, phen), 153.1 (CH, Py), 148.1 (C, phen), 146.3 (C, Py), 141.1 (CH, phen), 129.6 (C, phen), 127.8 (CH, phen), 127.2 (CH, phen), 126.3 (CH, Py), 25.0 ( $\text{CH}_3$ ). DOSY-NMR ( $\text{m}^2/\text{s}$ ):  $D = 1.3 \times 10^{-10}$ . m.p. =  $\sim 240$  °C (decomposed). E.A. Calcd. for  $\text{C}_{156}\text{H}_{120}\text{N}_{48}\text{O}_{36}\text{Pd}_6 \cdot (\text{H}_2\text{O})_{24}$ : C, 43.43; H, 3.93; N, 15.59; Found: C, 43.68; H, 3.95; N, 15.46. CSI-MS ( $\text{PF}_6^-$  salt, MeCN):  $m/z = 295.7$  [ $\mathbf{1c}$ -12 $\cdot\text{PF}_6^-$ +10 $\cdot\text{MeCN}$ ] $^{12+}$ , 313.3 [ $\mathbf{1c}$ -11 $\cdot\text{PF}_6^-$ +4 $\cdot\text{MeCN}$ ] $^{11+}$ , 339.5 [ $\mathbf{1c}$ -11 $\cdot\text{PF}_6^-$ +11 $\cdot\text{MeCN}$ ] $^{11+}$ , 361.9 [ $\mathbf{1c}$ -11 $\cdot\text{PF}_6^-$ +17 $\cdot\text{MeCN}$ ] $^{11+}$ , 383.8 [ $\mathbf{1c}$ -10 $\cdot\text{PF}_6^-$ +10 $\cdot\text{MeCN}$ ] $^{10+}$ , 460.8 [ $\mathbf{1c}$ -9 $\cdot\text{PF}_6^-$ +MeCN] $^{9+}$ , 526.2 [ $\mathbf{1c}$ -8 $\cdot\text{PF}_6^-$ +12 $\cdot\text{MeCN}$ ] $^{8+}$ , 592.8 [ $\mathbf{1c}$ -7 $\cdot\text{PF}_6^-$ +7 $\cdot\text{MeCN}$ ] $^{7+}$ , 616.3 [ $\mathbf{1c}$ -7 $\cdot\text{PF}_6^-$ +11 $\cdot\text{MeCN}$ ] $^{7+}$ , 630.0 [ $\mathbf{1c}$ -7 $\cdot\text{PF}_6^-$ +13 $\cdot\text{MeCN}$ ] $^{7+}$ , 645.6 [ $\mathbf{1c}$ -7 $\cdot\text{PF}_6^-$ +16 $\cdot\text{MeCN}$ ] $^{7+}$ , 791.03 [ $\mathbf{1c}$ -6 $\cdot\text{PF}_6^-$ +18 $\cdot\text{MeCN}$ ] $^{6+}$ , 846.9 [ $\mathbf{1c}$ -5 $\cdot\text{PF}_6^-$ +2 $\cdot\text{MeCN}$ ] $^{5+}$ , 1074.3 [ $\mathbf{1c}$ -4 $\cdot\text{PF}_6^-$ +11 $\cdot\text{MeCN}$ ] $^{4+}$ .

#### *Physical Data of Cage **1d***

$^1\text{H}$  NMR (500 MHz,  $\text{D}_2\text{O}$ , 300 K)  $\delta$ : 9.01 (d,  $J = 8.5$  Hz, 12H, phen), 8.66 (d,  $J = 6.0$  Hz, 24H,  $\text{PyH}_a$ ), 8.39 (s, 12H, phen), 8.18 (d,  $J = 6.5$  Hz, 24H,  $\text{PyH}_b$ ), 8.03 (d,  $J = 8.5$  Hz, 12H, phen), 7.24 (t,  $J = 7.5$  Hz, 12H, ph), 7.01 (d,  $J = 8.0$  Hz, 24H, ph), 2.32 (s, 72H, Me);  $^{13}\text{C}$  NMR (125 MHz,  $\text{D}_2\text{O}$ )  $\delta$ : 169.7 (C, triazine), 164.4 (C, phen), 152.0 (CH, Py), 149.3 (C, phen), 144.6 (C, Py), 143.0 (CH, phen), 137.6 (C, Ph), 137.0 (C, Ph), 131.6 (C, Ph), 130.7 (C, phen), 130.5 (C, phen), 129.8 (CH, Ph), 129.2 (CH, phen), 126.1 (CH, Py), 21.8 ( $\text{CH}_3$ , Ph). DOSY-NMR ( $\text{m}^2/\text{s}$ ):  $D = 1.1 \times 10^{-10}$ . m.p. =  $\sim 250$  °C (decomposed). E.A. Calcd. for  $\text{C}_{246}\text{H}_{204}\text{F}_{72}\text{N}_{36}\text{P}_{12}\text{Pd}_6 \cdot (\text{H}_2\text{O})_{11}$ : C, 47.00; H, 3.55; N, 8.15; Found: C, 46.99; H, 3.95; N, 7.89. CSI-MS ( $\text{PF}_6^-$  salt, MeCN):  $m/z = 357.3$  [ $\mathbf{1d}$ -12 $\cdot\text{PF}_6^-$ +MeCN] $^{12+}$ , 384.7 [ $\mathbf{1d}$ -12 $\cdot\text{PF}_6^-$ +9 $\cdot\text{MeCN}$ ] $^{12+}$ , 421.7 [ $\mathbf{1d}$ -11 $\cdot\text{PF}_6^-$ +6 $\cdot\text{MeCN}$ ] $^{11+}$ , 453.7 [ $\mathbf{1d}$ -10 $\cdot\text{PF}_6^-$ +2 $\cdot\text{PF}_6^-$ ] $^{10+}$ , 490.64 [ $\mathbf{1d}$ -10 $\cdot\text{PF}_6^-$ +9 $\cdot\text{MeCN}$ ] $^{10+}$ , 533.9 [ $\mathbf{1d}$ -9 $\cdot\text{PF}_6^-$ +3 $\cdot\text{MeCN}$ ] $^{9+}$ , 556.7 [ $\mathbf{1d}$ -9 $\cdot\text{PF}_6^-$ +8 $\cdot\text{MeCN}$ ] $^{9+}$ , 593.2 [ $\mathbf{1d}$ -9 $\cdot\text{PF}_6^-$ +16 $\cdot\text{MeCN}$ ] $^{9+}$ , 629.0 [ $\mathbf{1d}$ -8 $\cdot\text{PF}_6^-$ +5 $\cdot\text{MeCN}$ ] $^{8+}$ , 695.7 [ $\mathbf{1d}$ -8 $\cdot\text{PF}_6^-$ +18 $\cdot\text{MeCN}$ ] $^{8+}$ , 733.7 [ $\mathbf{1d}$ -7 $\cdot\text{PF}_6^-$ +4 $\cdot\text{MeCN}$ ] $^{7+}$ , 821.7 [ $\mathbf{1d}$ -7 $\cdot\text{PF}_6^-$ +19 $\cdot\text{MeCN}$ ] $^{7+}$ , 887.0 [ $\mathbf{1d}$ -6 $\cdot\text{PF}_6^-$ +5 $\cdot\text{MeCN}$ ] $^{6+}$ , 900.7 [ $\mathbf{1d}$ -6 $\cdot\text{PF}_6^-$ +7 $\cdot\text{MeCN}$ ] $^{6+}$ , 948.6 [ $\mathbf{1d}$ -6 $\cdot\text{PF}_6^-$ +14 $\cdot\text{MeCN}$ ] $^{6+}$ , 1052.4 [ $\mathbf{1d}$ -5 $\cdot\text{PF}_6^-$ ] $^{5+}$ .

### Physical Data of Cage **1e**

$^1\text{H}$  NMR (500 MHz,  $\text{D}_2\text{O}$ , 300 K)  $\delta$ : 9.02 (d,  $J = 8.5$  Hz, 12H, phen), 8.71 (d,  $J = 6.0$  Hz, 24H,  $\text{PyH}_a$ ), 8.41 (s, 12H, phen), 8.24 (d,  $J = 6.5$  Hz, 24H,  $\text{PyH}_b$ ), 7.83 (d,  $J = 8.0$  Hz, 12H, phen), 6.76 (s, 24H, Mes), 2.33 (s, 36H, Me), 2.27 (s, 72H, Me);  $^{13}\text{C}$  NMR (125 MHz,  $\text{D}_2\text{O}$ )  $\delta$ : 169.3 (C, triazine), 163.9 (C, phen), 151.3 (CH, Py), 148.6 (C, phen), 144.1 (C, Py), 142.3 (CH, phen), 141.5 (C, Mes), 136.2 (C, Mes), 134.3 (C, Mes), 130.8 (C, phen), 130.0 (CH, phen), 129.7 (CH, Mes), 128.4 (CH, phen), 125.1 (CH, Py), 21.1 ( $\text{CH}_3$ , Mes), 20.8 ( $\text{CH}_3$ , Mes). DOSY-NMR ( $\text{m}^2/\text{s}$ ):  $D = 1.1 \times 10^{-10}$ . m.p. =  $\sim 250$  °C (decomposed). E.A. Calcd. for  $\text{C}_{252}\text{H}_{216}\text{N}_{48}\text{O}_{36}\text{Pd}_6 \cdot (\text{H}_2\text{O})_{22}$ : C, 54.76; H, 4.74; N, 12.16; Found: C, 54.39; H, 4.37; N, 12.50. CSI-MS ( $\text{PF}_6^-$  salt, MeCN):  $m/z = 425.7$  [**1e**-11 $\cdot\text{PF}_6^-$ +4 $\cdot\text{MeCN}$ ] $^{11+}$ , 437.6 [**1e**-11 $\cdot\text{PF}_6^-$ +7 $\cdot\text{MeCN}$ ] $^{11+}$ , 472.4 [**1e**-10 $\cdot\text{PF}_6^-$ +MeCN] $^{10+}$ , 530.0 [**1e**-10 $\cdot\text{PF}_6^-$ +15 $\cdot\text{MeCN}$ ] $^{10+}$ , 562.0 [**1e**-9 $\cdot\text{PF}_6^-$ +6 $\cdot\text{MeCN}$ ] $^{9+}$ , 573.2 [**1e**-9 $\cdot\text{PF}_6^-$ +8 $\cdot\text{MeCN}$ ] $^{9+}$ , 613.5 [**1e**-9 $\cdot\text{PF}_6^-$ +17 $\cdot\text{MeCN}$ ] $^{9+}$ , 621.0 [**1e**-8 $\cdot\text{PF}_6^-$ ] $^{8+}$ , 689.9 [**1e**-8 $\cdot\text{PF}_6^-$ +15 $\cdot\text{MeCN}$ ] $^{8+}$ , 730.4 [**1e**-7 $\cdot\text{PF}_6^-$ ] $^{7+}$ , 741.2 [**1e**-7 $\cdot\text{PF}_6^-$ +2 $\cdot\text{MeCN}$ ] $^{7+}$ , 771.5 [**1e**-7 $\cdot\text{PF}_6^-$ +7 $\cdot\text{MeCN}$ ] $^{7+}$ , 876.4 [**1e**-6 $\cdot\text{PF}_6^-$ ] $^{6+}$ , 917.2 [**1e**-6 $\cdot\text{PF}_6^-$ +6 $\cdot\text{MeCN}$ ] $^{6+}$ , 924.0 [**1e**-6 $\cdot\text{PF}_6^-$ +7 $\cdot\text{MeCN}$ ] $^{6+}$ , 980.9 [**1e**-6 $\cdot\text{PF}_6^-$ +15 $\cdot\text{MeCN}$ ] $^{6+}$ , 1082.0 [**1e**-5 $\cdot\text{PF}_6^-$ ] $^{5+}$ , 1137.4 [**1e**-5 $\cdot\text{PF}_6^-$ +7 $\cdot\text{MeCN}$ ] $^{5+}$ , 1195.6 [**1e**-5 $\cdot\text{PF}_6^-$ +14 $\cdot\text{MeCN}$ ] $^{5+}$ . Synchrotron X-ray diffraction study was carried out for cage **1e** (CCDC 911281) and the details are described in our previous paper (ref. 2).



# NMR Spectrum of self-assembled coordination cage 1

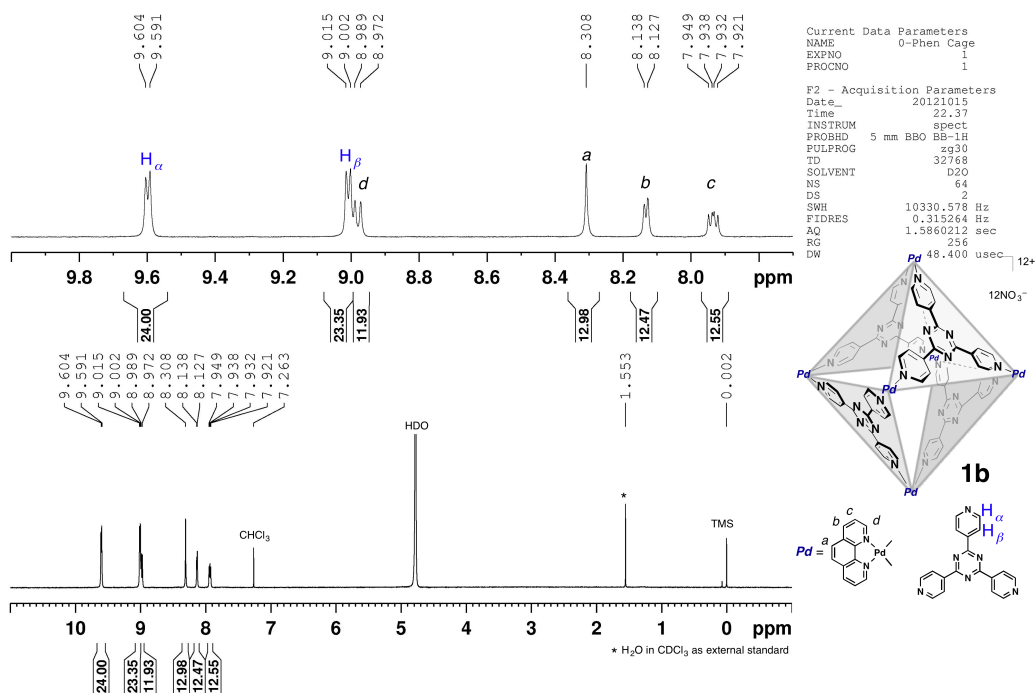


Figure S13. <sup>1</sup>H NMR spectrum (500 MHz, 300 K, D<sub>2</sub>O) of cage 1b.

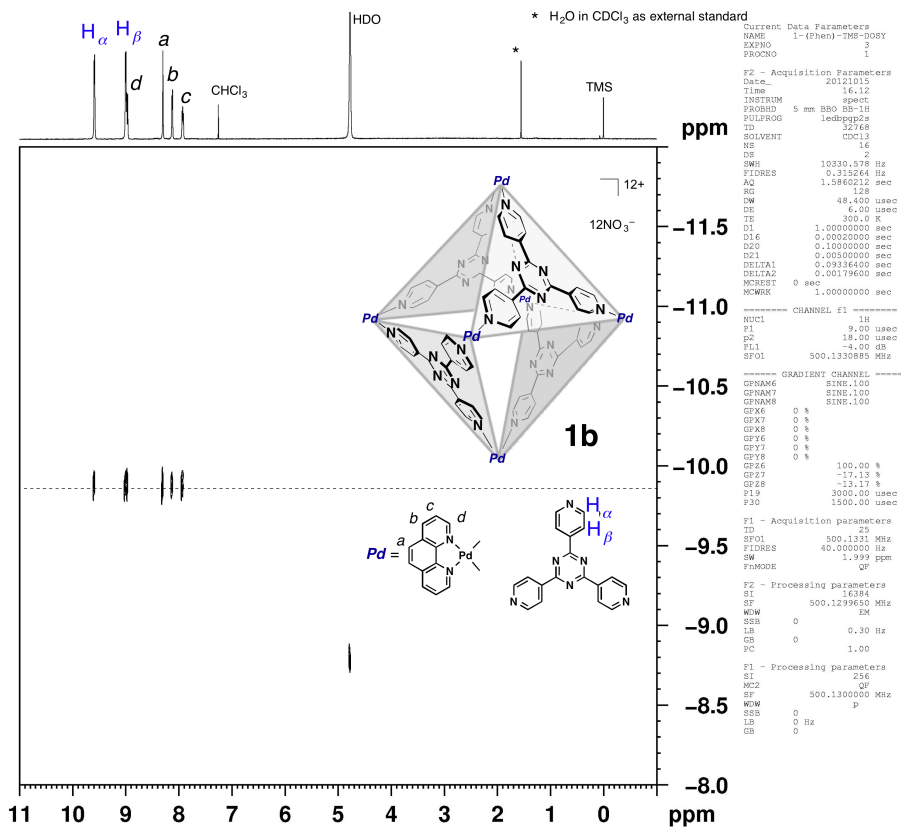


Figure S14. DOSY spectrum (500 MHz, 300 K, D<sub>2</sub>O) of cage 1b.

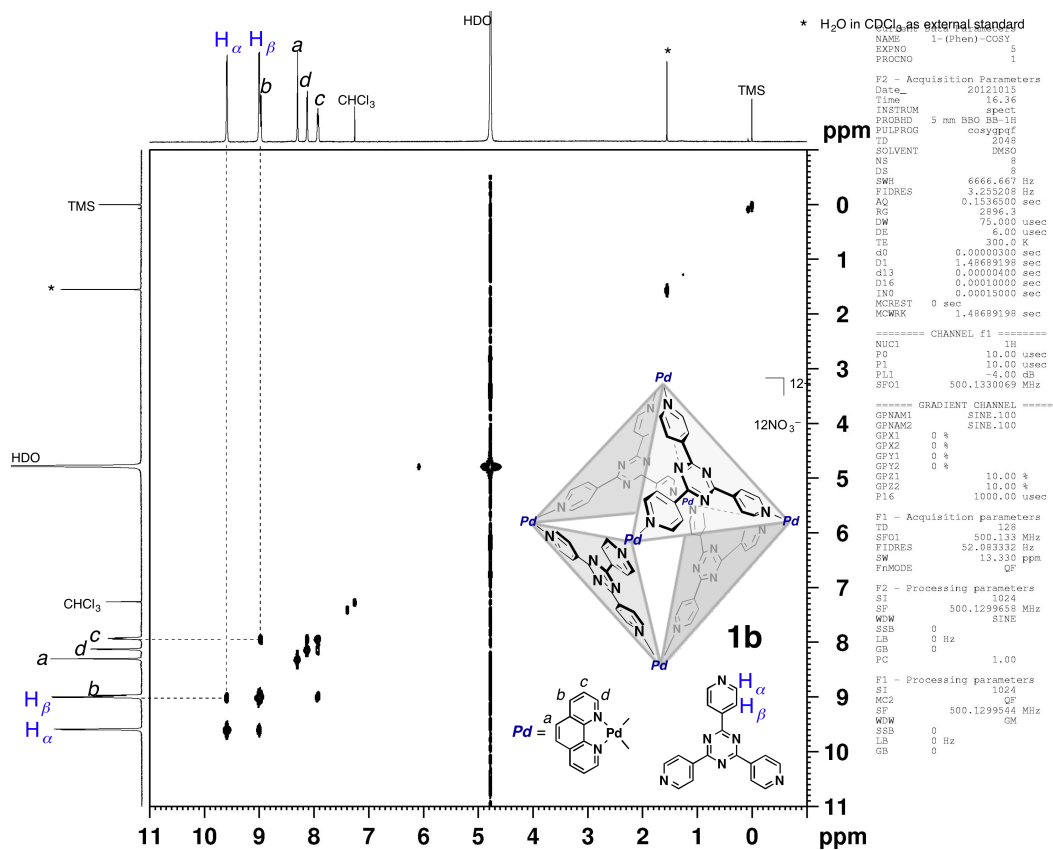


Figure S15. <sup>1</sup>H-<sup>1</sup>H COSY spectrum (500 MHz, 300 K, D<sub>2</sub>O) of cage **1b**.

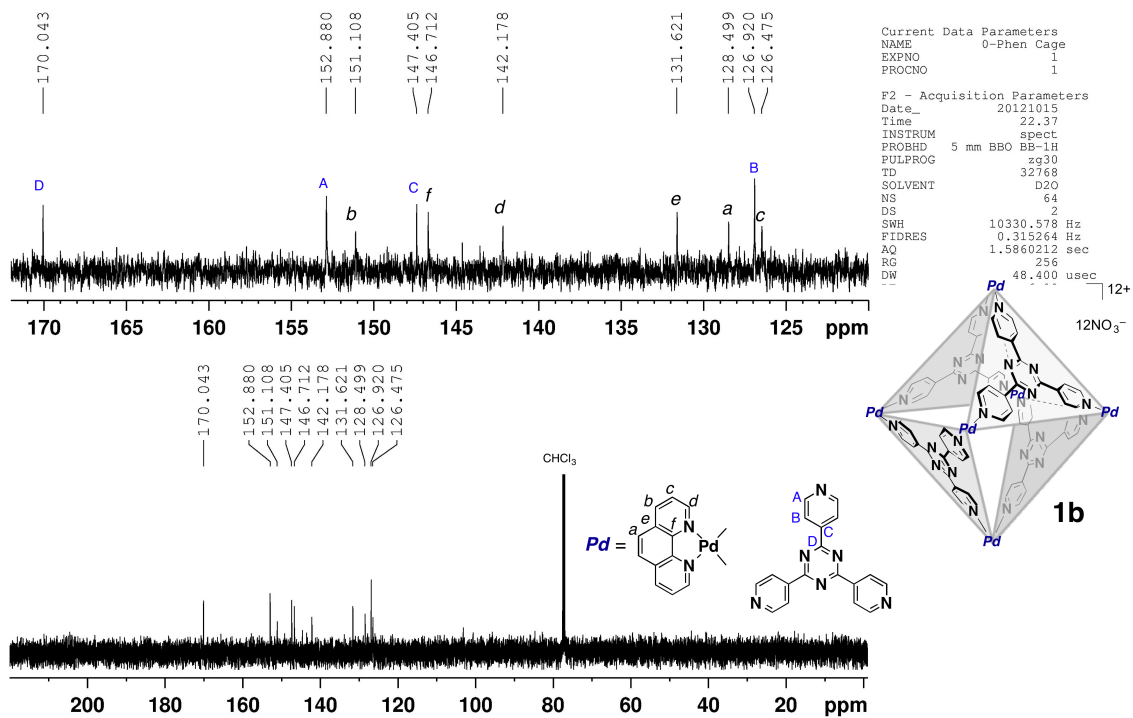


Figure S16. <sup>13</sup>C NMR spectrum (125 MHz, 300 K, D<sub>2</sub>O) of cage **1b**.

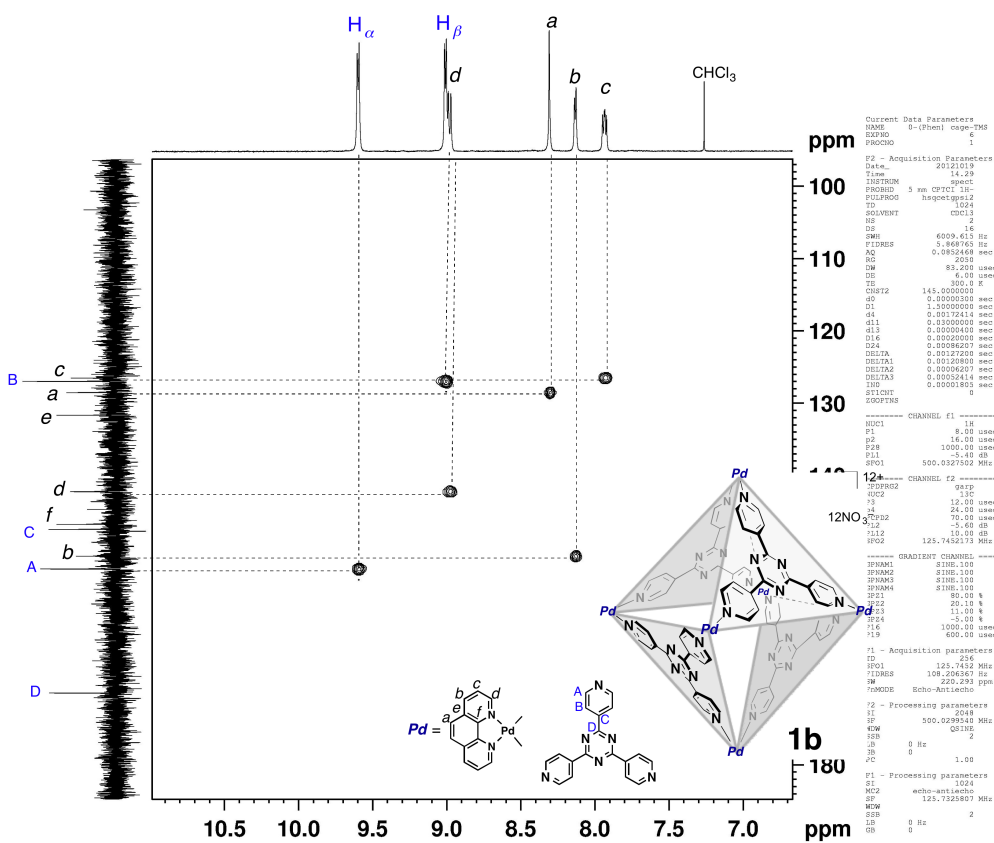


Figure S17.  $^1\text{H}$ - $^{13}\text{C}$  HSQC spectrum (125 MHz, 300 K,  $\text{D}_2\text{O}$ ) of **1b**.

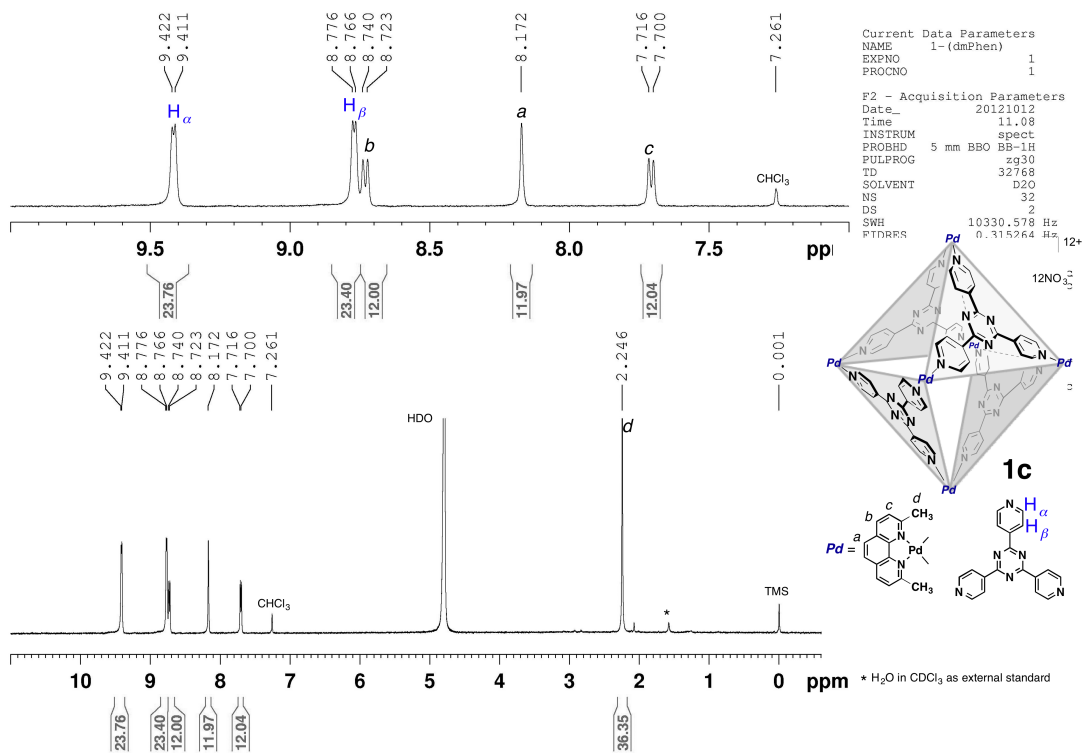


Figure S18.  $^1\text{H}$  NMR spectrum (500 MHz, 300 K,  $\text{D}_2\text{O}$ ) of cage **1c**.



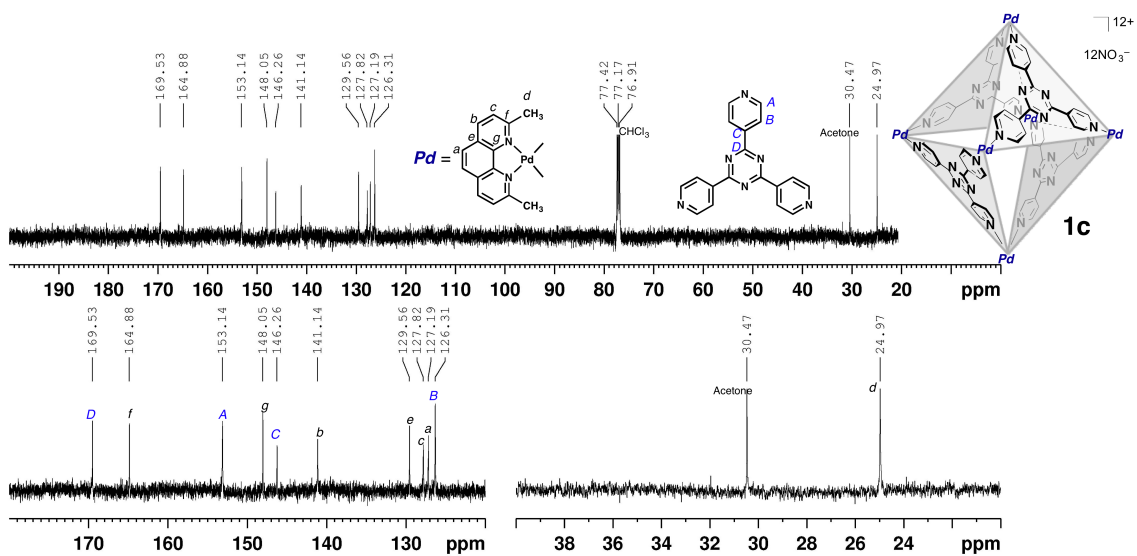


Figure S21.  $^{13}\text{C}$  NMR spectrum (125 MHz, 300 K,  $\text{D}_2\text{O}$ ) of cage **1c**.

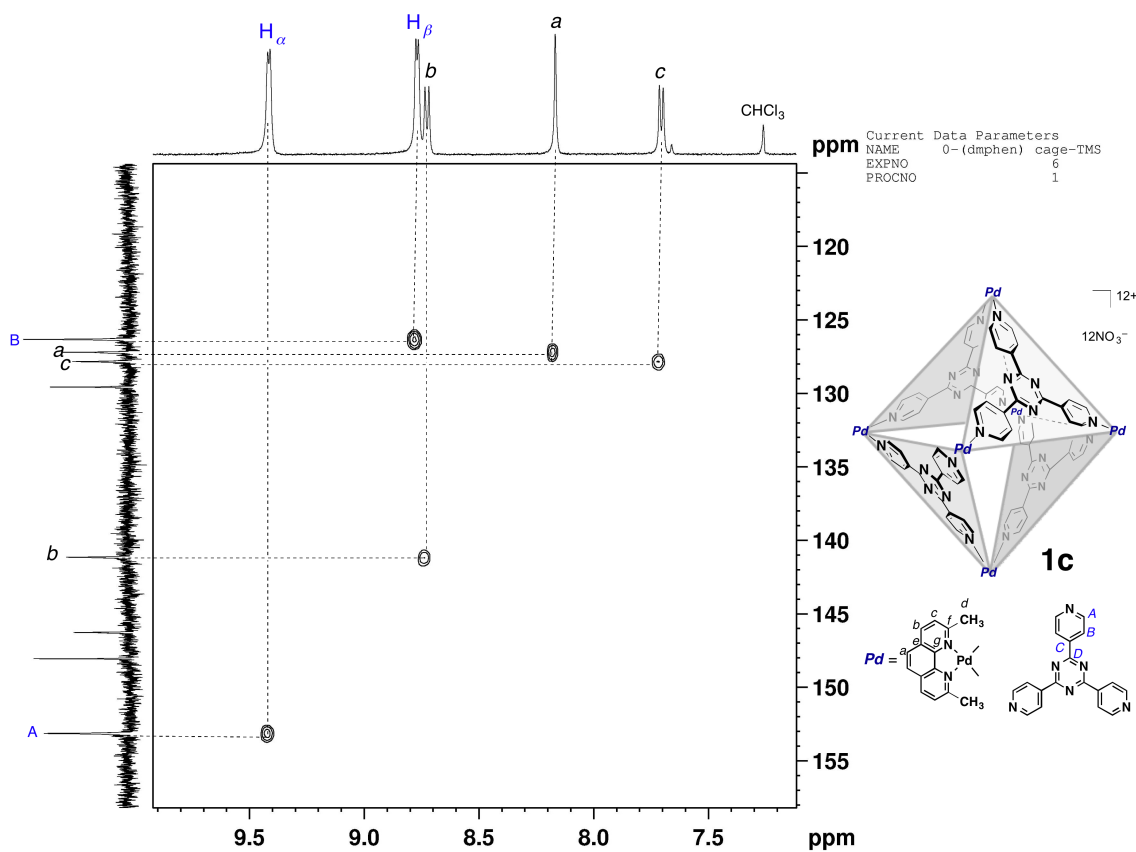


Figure S22.  $^1\text{H}$ - $^{13}\text{C}$  HSQC spectrum (500 MHz, 300 K,  $\text{D}_2\text{O}$ ) of cage **1c**.

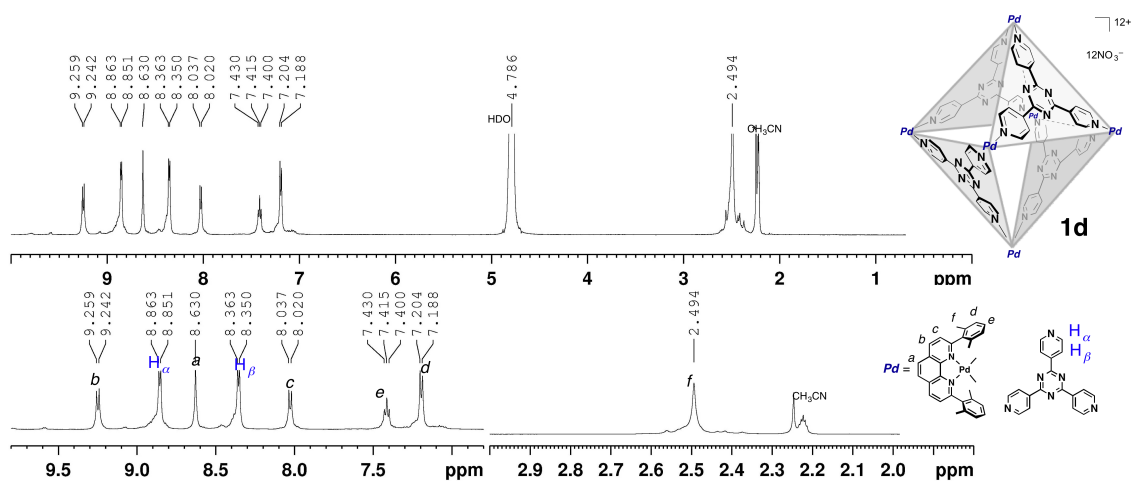


Figure S23.  $^1\text{H}$  NMR spectrum (500 MHz, 300 K,  $\text{D}_2\text{O}/\text{MeCN}$ ) of cage **1d**.

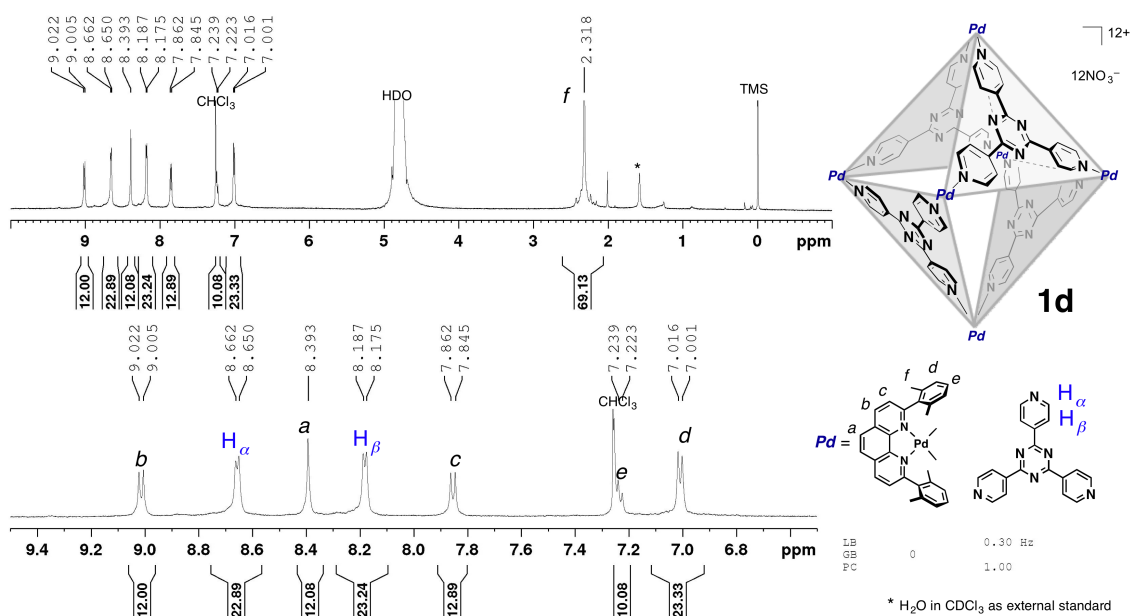


Figure S24.  $^1\text{H}$  NMR spectrum (500 MHz, 300 K,  $\text{D}_2\text{O}$ ) of cage **1d**.

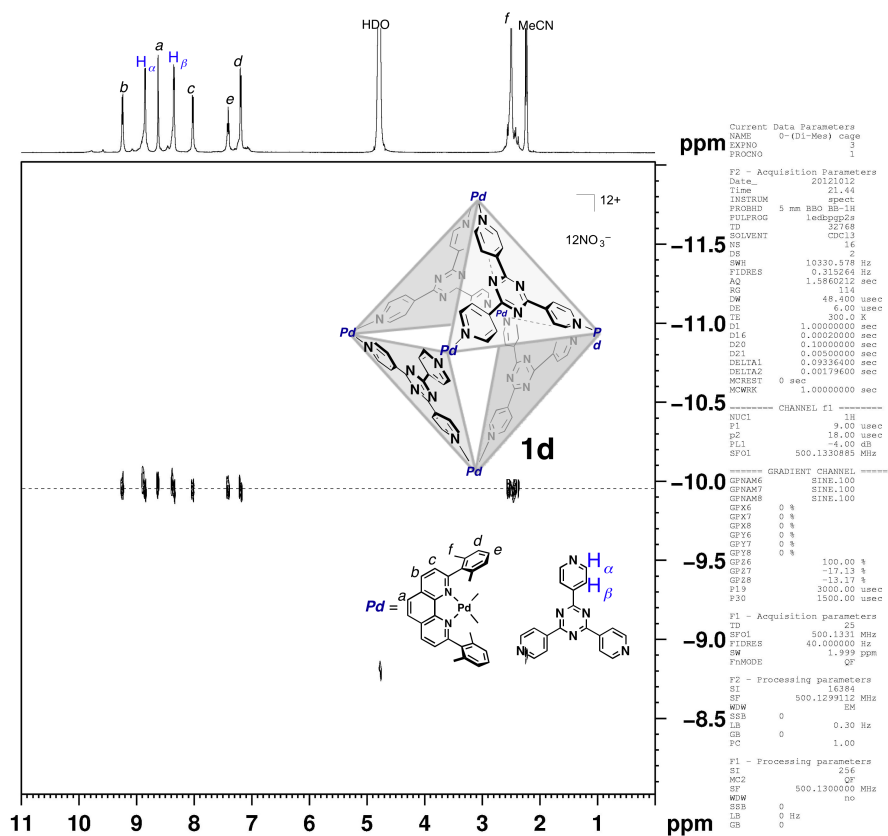


Figure S25. DOSY spectrum (500 MHz, 300 K, D<sub>2</sub>O) of cage 1d.

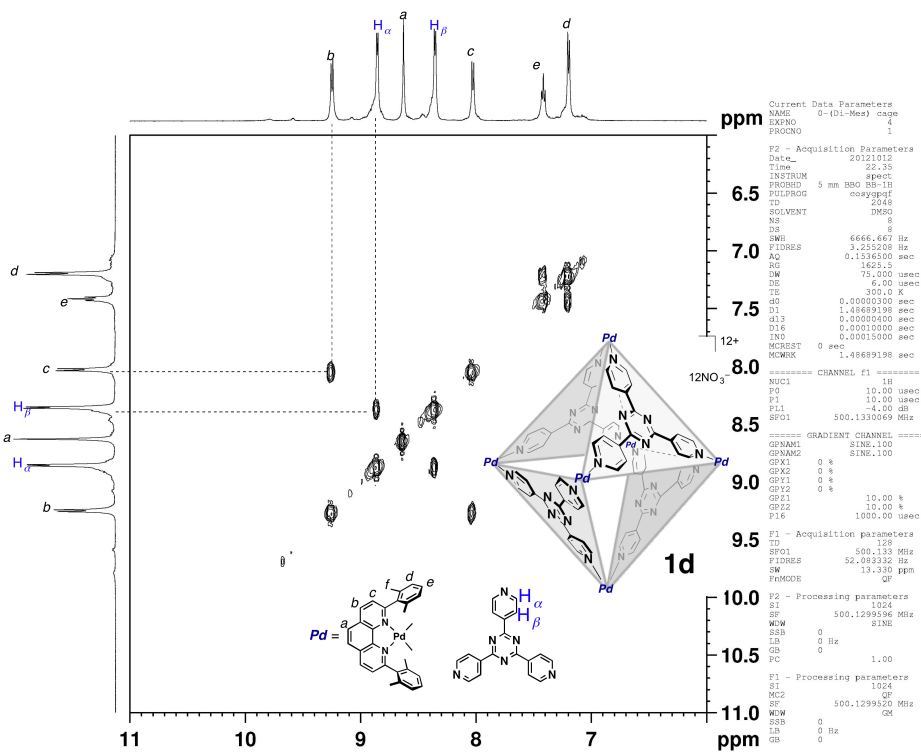


Figure S26. <sup>1</sup>H-<sup>1</sup>H COSY spectrum (500 MHz, 300 K, D<sub>2</sub>O) of cage 1d.

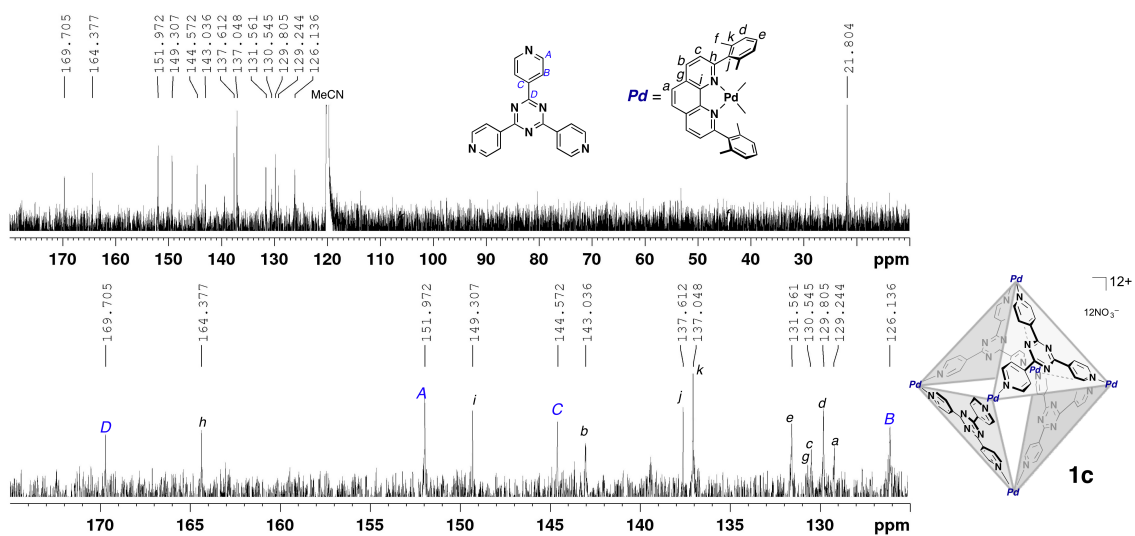


Figure S27.  $^{13}\text{C}$  NMR spectrum (125 MHz, 300 K,  $\text{D}_2\text{O}$ ) of cage **1d**.

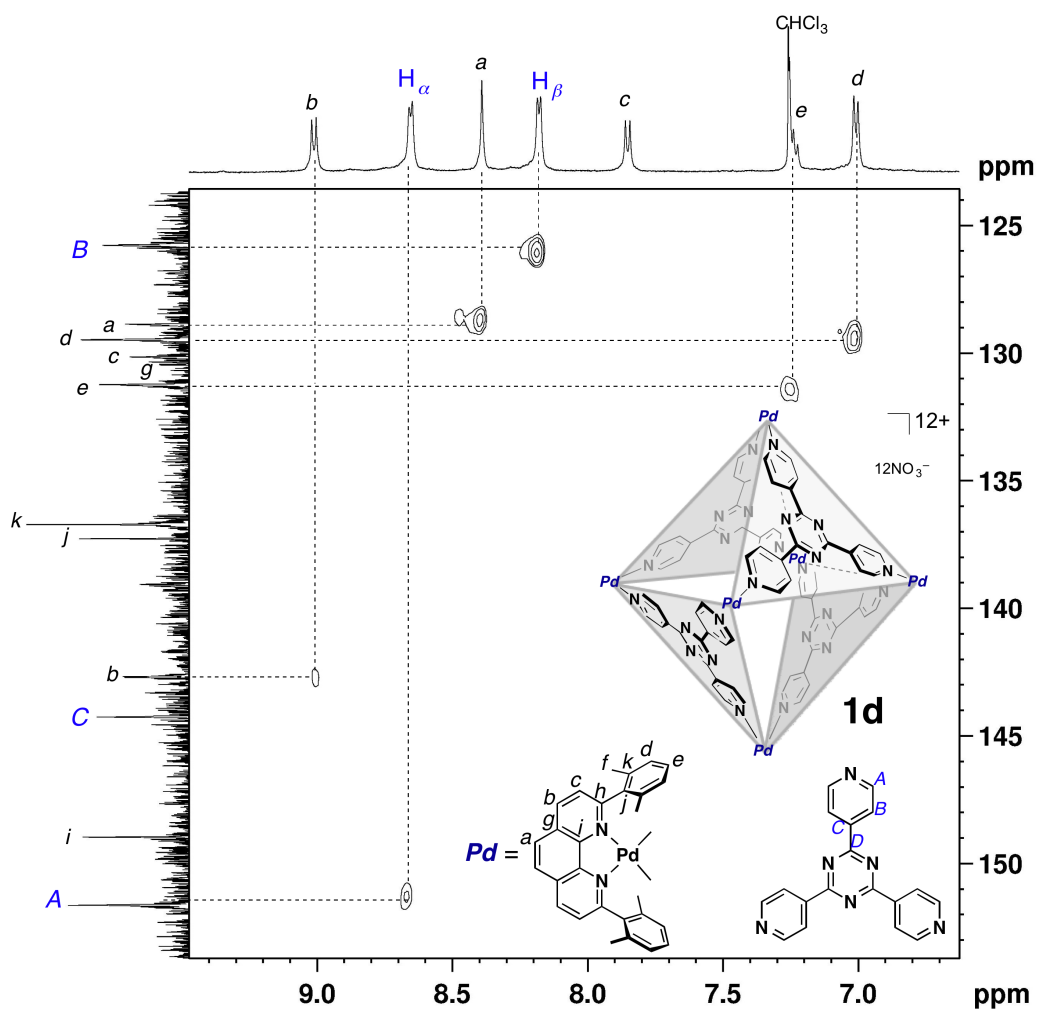


Figure S28.  $^1\text{H}$ - $^{13}\text{C}$  HSQC spectrum (500 MHz, 300 K,  $\text{D}_2\text{O}$ ) of cage **1d**.



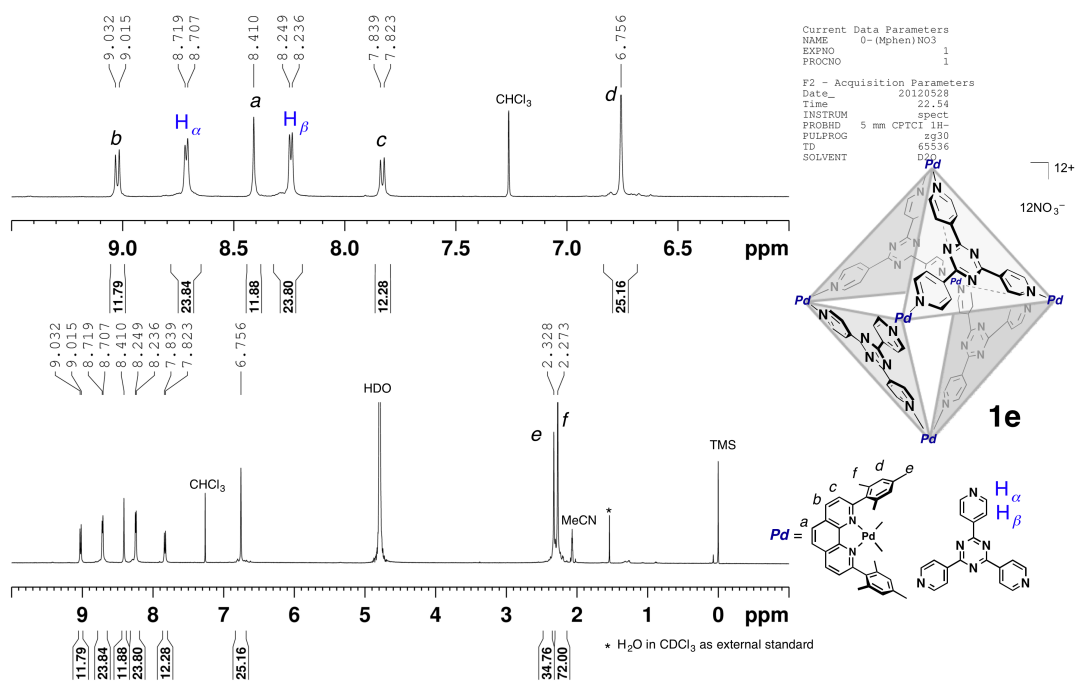


Figure S29. <sup>1</sup>H NMR spectrum (500 MHz, 300 K, D<sub>2</sub>O) of cage **1e**.

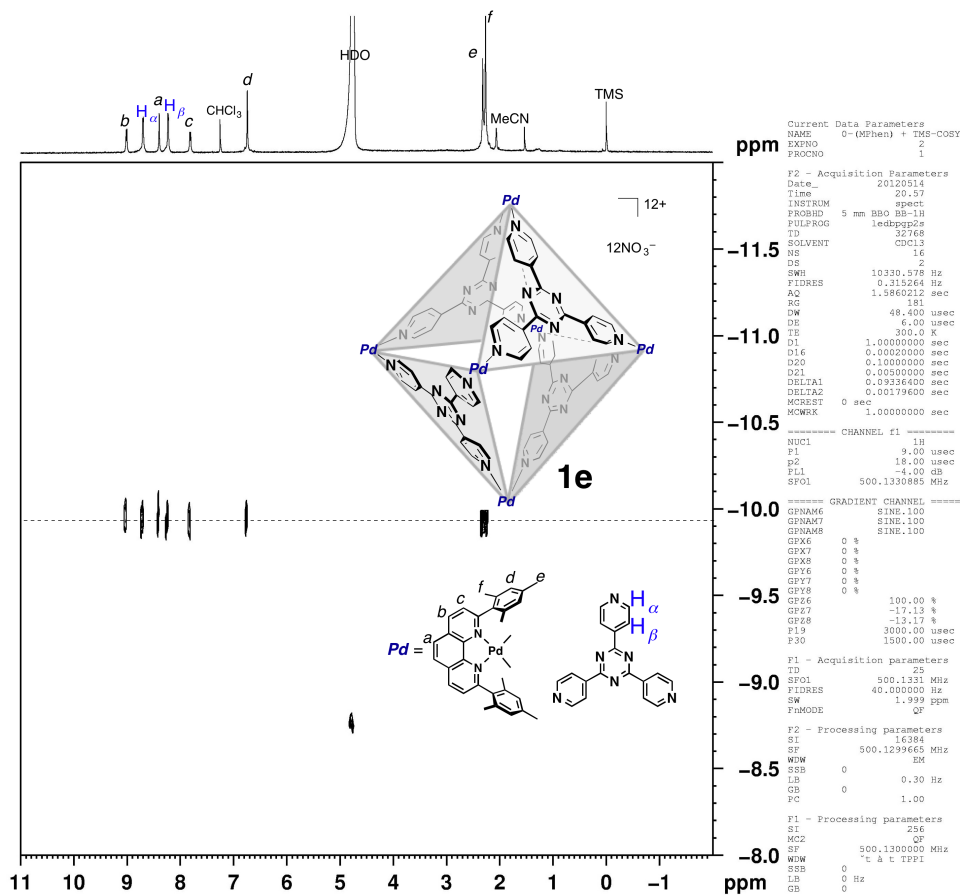


Figure S30. DOSY spectrum (500 MHz, 300 K, D<sub>2</sub>O) of cage **1e**.

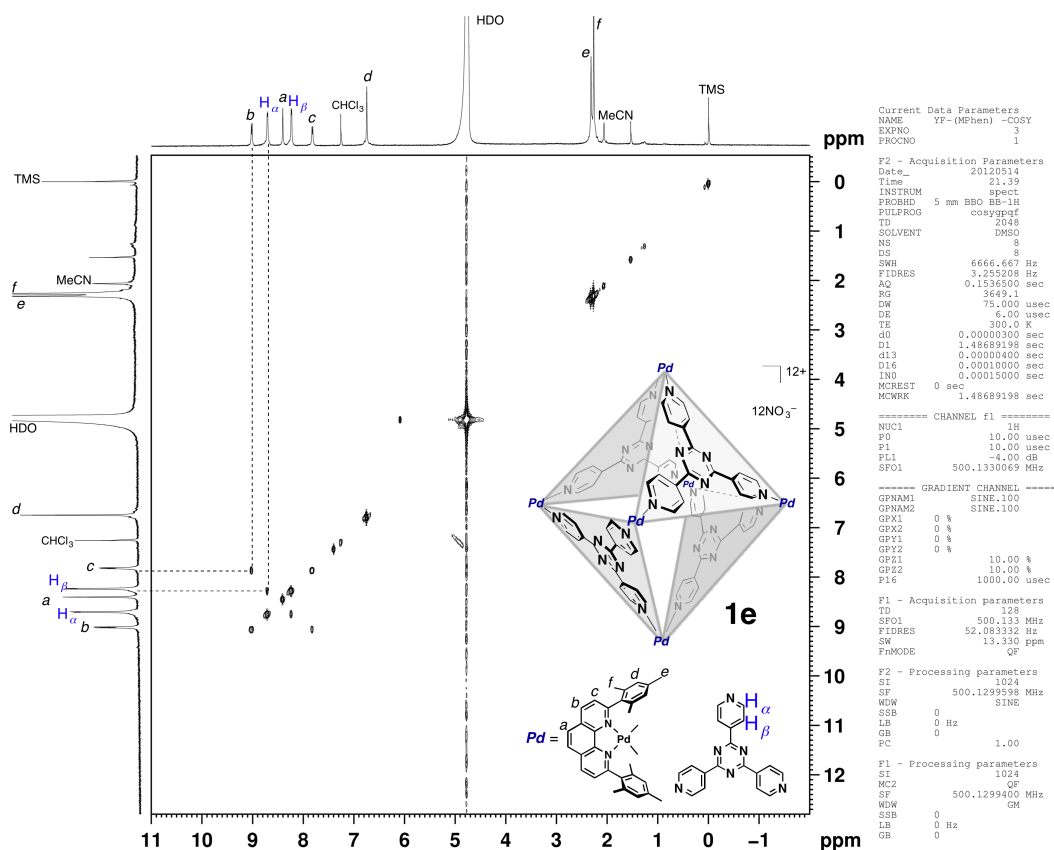


Figure S31.  $^1\text{H}$ - $^1\text{H}$  COSY spectrum (500 MHz, 300 K,  $\text{D}_2\text{O}$ ) of cage **1e**.

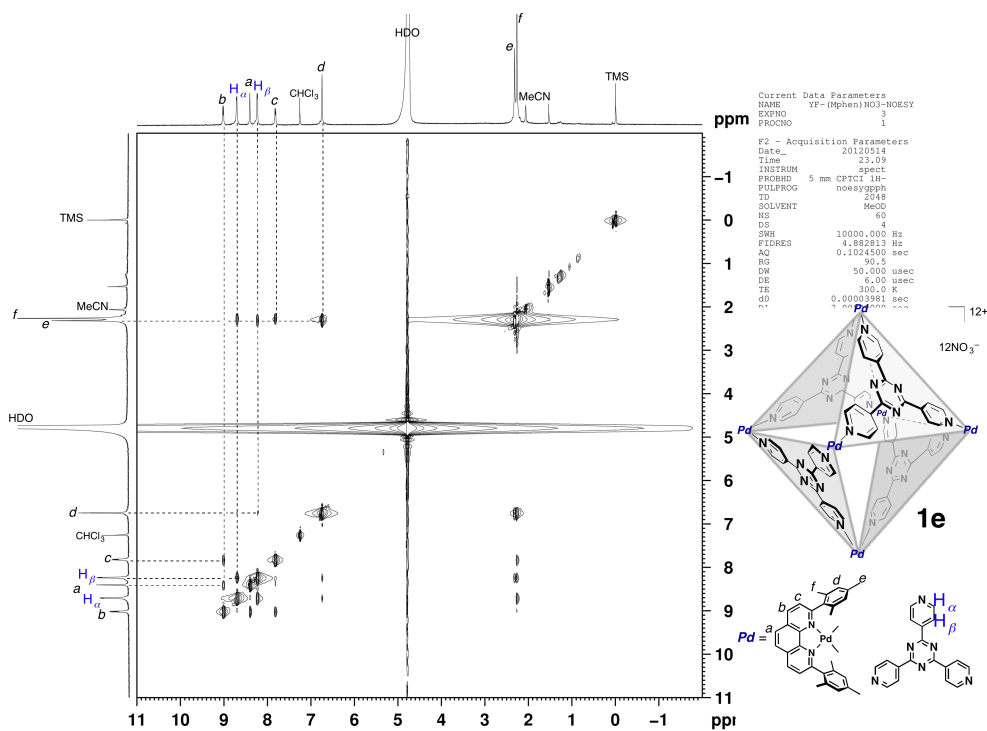


Figure S32.  $^1\text{H}$ - $^1\text{H}$  NOESY spectrum (500 MHz, 300 K,  $\text{D}_2\text{O}$ ) of cage **1e**.



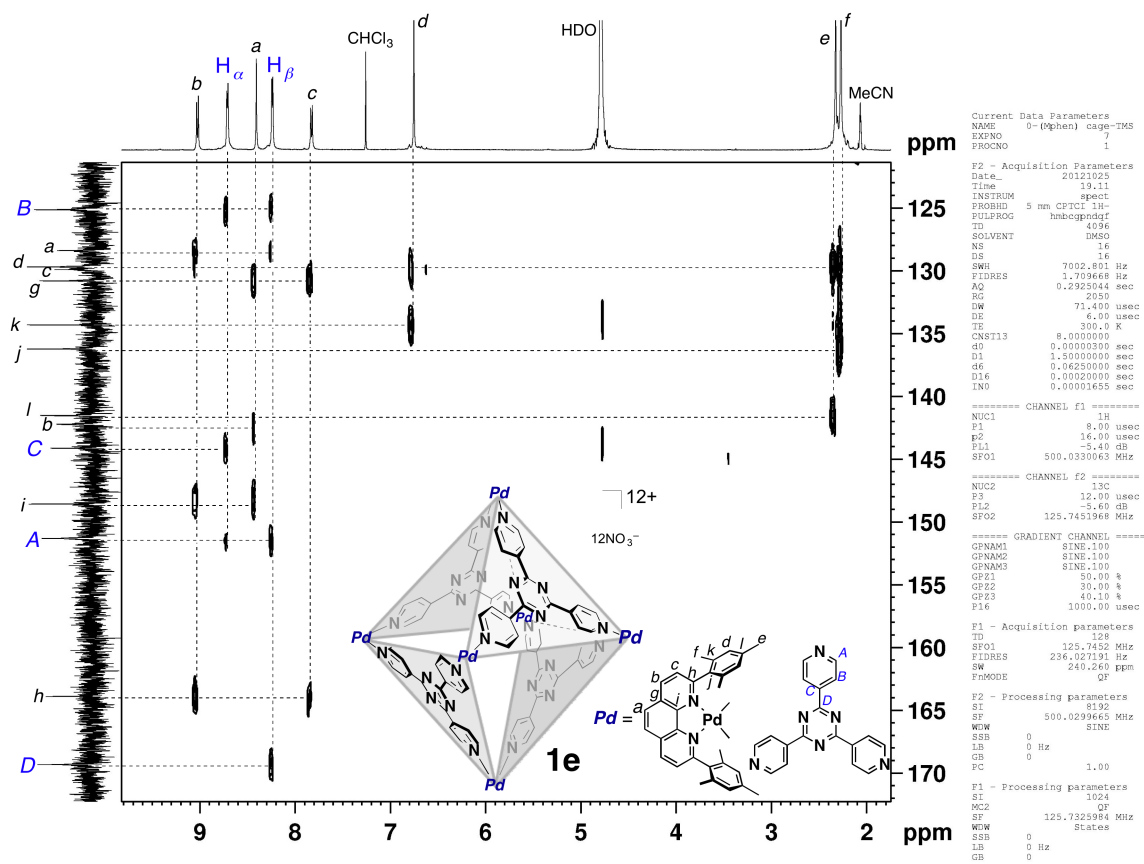
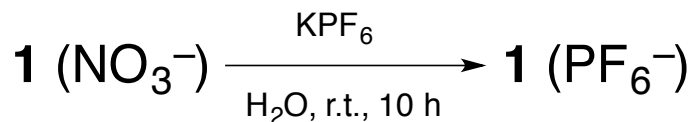


Figure S35.  $^1\text{H}$ - $^{13}\text{C}$  HMBC spectrum (500 MHz, 300 K,  $\text{D}_2\text{O}$ ) of cage **1e**.

### Counter-anion exchange from NO<sub>3</sub><sup>-</sup> (**1**) to PF<sub>6</sub><sup>-</sup> [**1** (PF<sub>6</sub><sup>-</sup>)]



To a solution of cage **1e** (26.5 mg, 5.16 μmol) in H<sub>2</sub>O (6 mL) was added a saturated aqueous solution of KPF<sub>6</sub> (10 mL). A large amount of green precipitate appeared instantly, and the suspended solution was stirred at room temperature for 10 h. Green precipitate was collected and dried to give cage **1e** (PF<sub>6</sub><sup>-</sup>) as a greenish microcrystal (31.0 mg, 5.06 μmol) in 98% yield. Other cages were prepared in the same way.

Physical data of cage **1e** (PF<sub>6</sub><sup>-</sup>): <sup>1</sup>H NMR (500 MHz, CD<sub>3</sub>CN) δ: 8.98 (d, *J* = 8.5 Hz, 14h, phen), 8.53 (d, *J* = 6.5 Hz, 24H, PyHα), 8.40 (s, 14h, phen), 8.10 (d, *J* = 6.5 Hz, 14h, PyHβ), 7.77 (d, *J* = 8.0 Hz, 14h, phen), 6.75 (s, 24H, Mes), 2.33 (s, 36H, Me), 2.21 (s, 74h, Me); <sup>13</sup>C NMR (125 MHz, CD<sub>3</sub>CN) δ: 170.0 (C, trazine), 164.9 (C, phen), 151.9 (CH, Py), 149.7 (C, Phen), 145.2 (C, Py), 142.7 (CH, phen), 142.2 (C, Mes), 136.8 (C, Mes), 134.8 (C, Mes), 131.6 (C, phen), 130.8 (CH, Phen), 130.7 (CH, Mes), 129.1 (CH, Phen), 126.0 (CH, Py), 21.8 (CH<sub>3</sub>, Mes), 21.7 (CH<sub>3</sub>, Mes). DOSY-NMR (m<sup>2</sup>/s): *D* = 1.13×10<sup>-10</sup>. E.A. Calcd. For C<sub>254</sub>H<sub>216</sub>F<sub>72</sub>N<sub>36</sub>P<sub>12</sub>Pd<sub>6</sub>(KPF<sub>6</sub>)<sub>4c</sub>, 46.60; H, 3.35; N, 7.76; Found: C, 46.90; H, 3.32; N, 7.88. CSI-MS (MeCN): *m/z* = 425.7 [**1e**-PF<sub>6</sub>+4·MeCN]<sup>11+</sup>, 437.6 [**1e**-PF<sub>6</sub>+7·MeCN]<sup>11+</sup>, 472.4 [**1e**-2·PF<sub>6</sub>+1·MeCN]<sup>10+</sup>, 530.0 [**1e**-2·PF<sub>6</sub>+15·MeCN]<sup>10+</sup>, 562.0 [**1e**-3·PF<sub>6</sub>+6·MeCN]<sup>9+</sup>, 573.2 [**1e**-3·PF<sub>6</sub>+8·MeCN]<sup>9+</sup>, 613.5 [**1e**-3·PF<sub>6</sub>+17·MeCN]<sup>9+</sup>, 621.0 [**1e**-4·PF<sub>6</sub>+0·MeCN]<sup>8+</sup>, 689.9 [**1e**-4·PF<sub>6</sub>+15·MeCN]<sup>8+</sup>, 730.4 [**1e**-5·PF<sub>6</sub>+0·MeCN]<sup>7+</sup>, 741.2 [**1e**-5·PF<sub>6</sub>+2·MeCN]<sup>7+</sup>, 771.5 [**1e**-5·PF<sub>6</sub>+7·MeCN]<sup>7+</sup>, 876.4 [**1e**-6·PF<sub>6</sub>+0·MeCN]<sup>6+</sup>, 917.2 [**1e**-6·PF<sub>6</sub>+6·MeCN]<sup>6+</sup>, 924.0 [**1e**-6·PF<sub>6</sub>+7·MeCN]<sup>6+</sup>, 980.9 [**1e**-6·PF<sub>6</sub>+15·MeCN]<sup>6+</sup>, 1082.0 [**1e**-7·PF<sub>6</sub>+0·MeCN]<sup>5+</sup>, 1137.4 [**1e**-7·PF<sub>6</sub>+7·MeCN]<sup>5+</sup>, 1195.6 [**1e**-7·PF<sub>6</sub>+14·MeCN]<sup>5+</sup>.

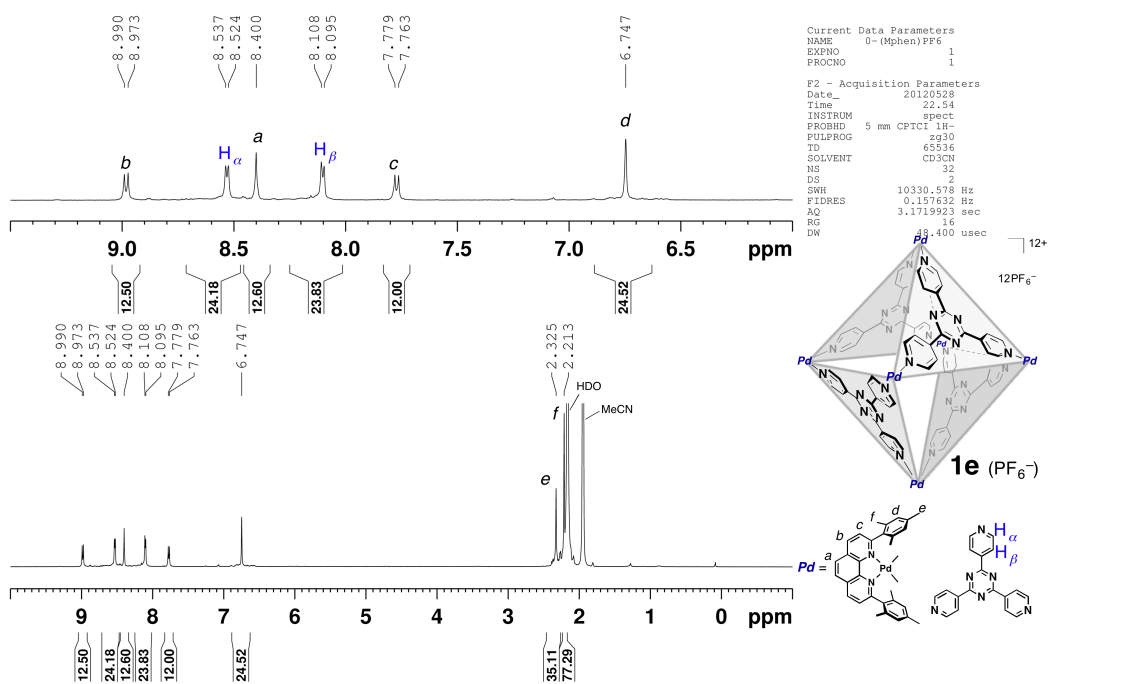


Figure S36.  $^1H$  NMR spectrum (500 MHz, 300 K,  $CD_3CN$ ) of cage **1e** ( $PF_6^-$ ).

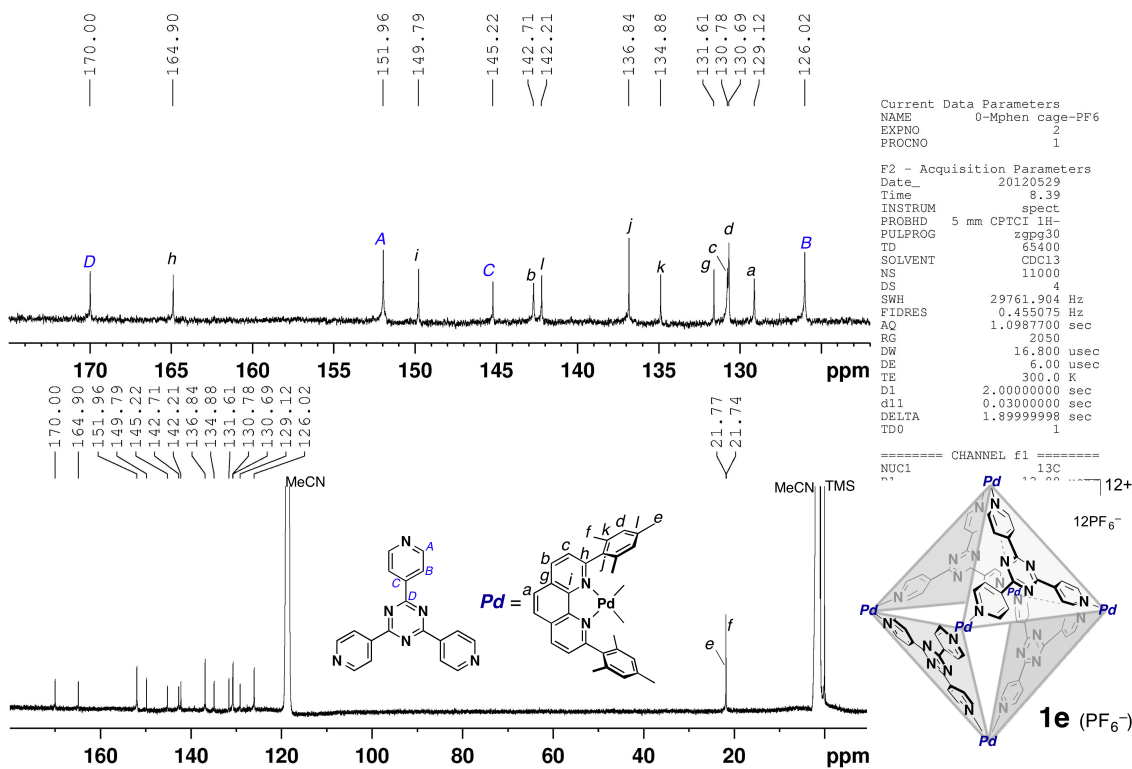


Figure S37.  $^{13}C$  NMR spectrum (125 MHz, 300 K,  $CD_3CN$ ) of cage **1e** ( $PF_6^-$ ).

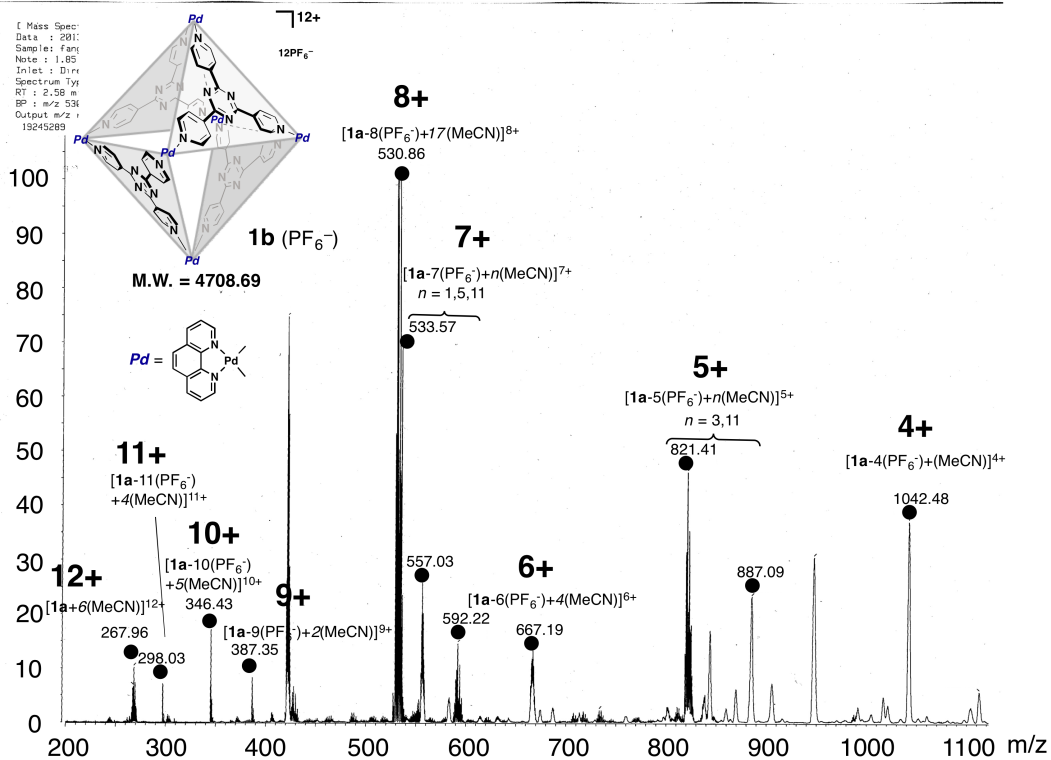


Figure S38. ESI-MS spectrum of cage **1b** ( $\text{PF}_6^-$ ).

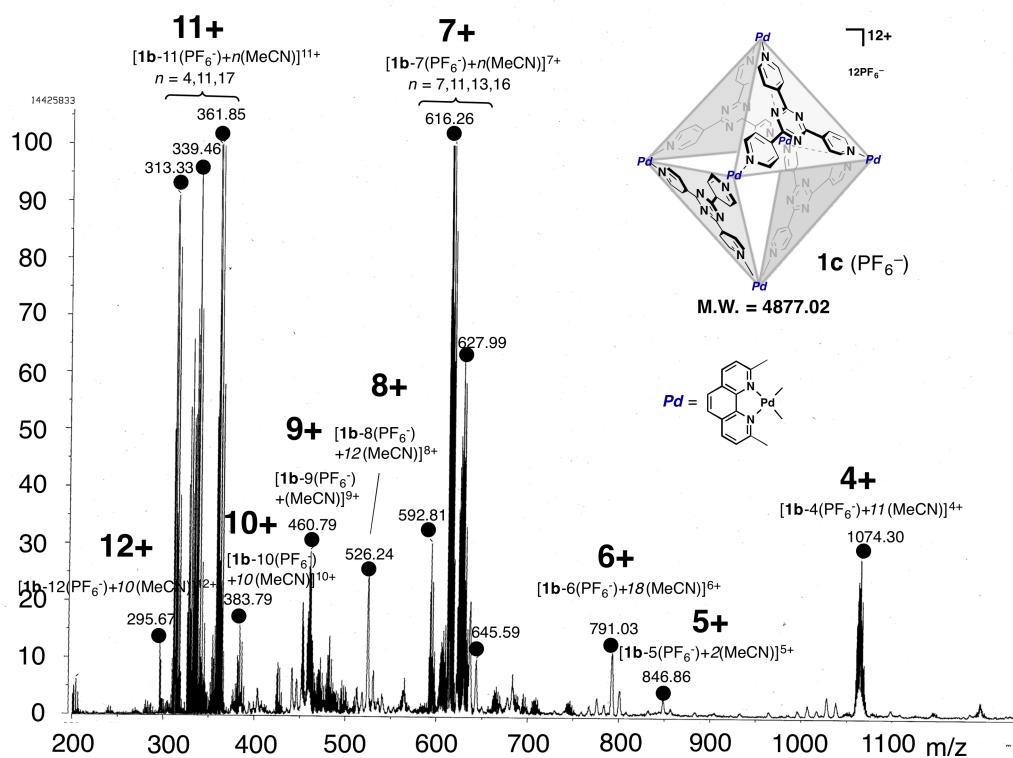


Figure S39. ESI-MS spectrum of cage **1c** ( $\text{PF}_6^-$ ).

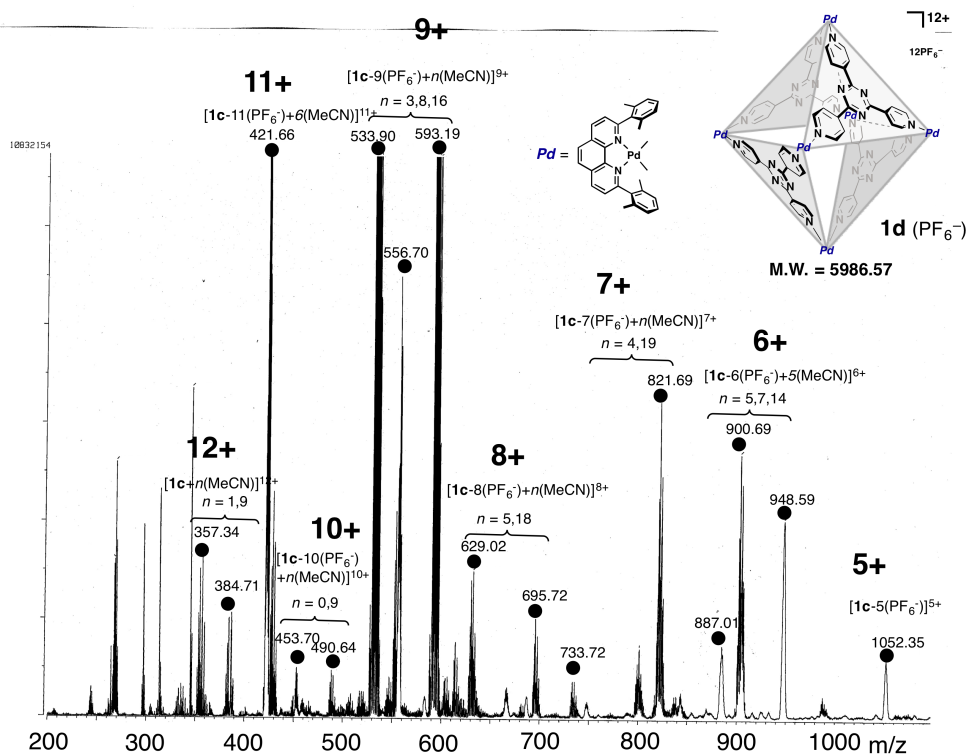


Figure S40. ESI-MS spectrum of cage **1d** ( $\text{PF}_6^-$ ).

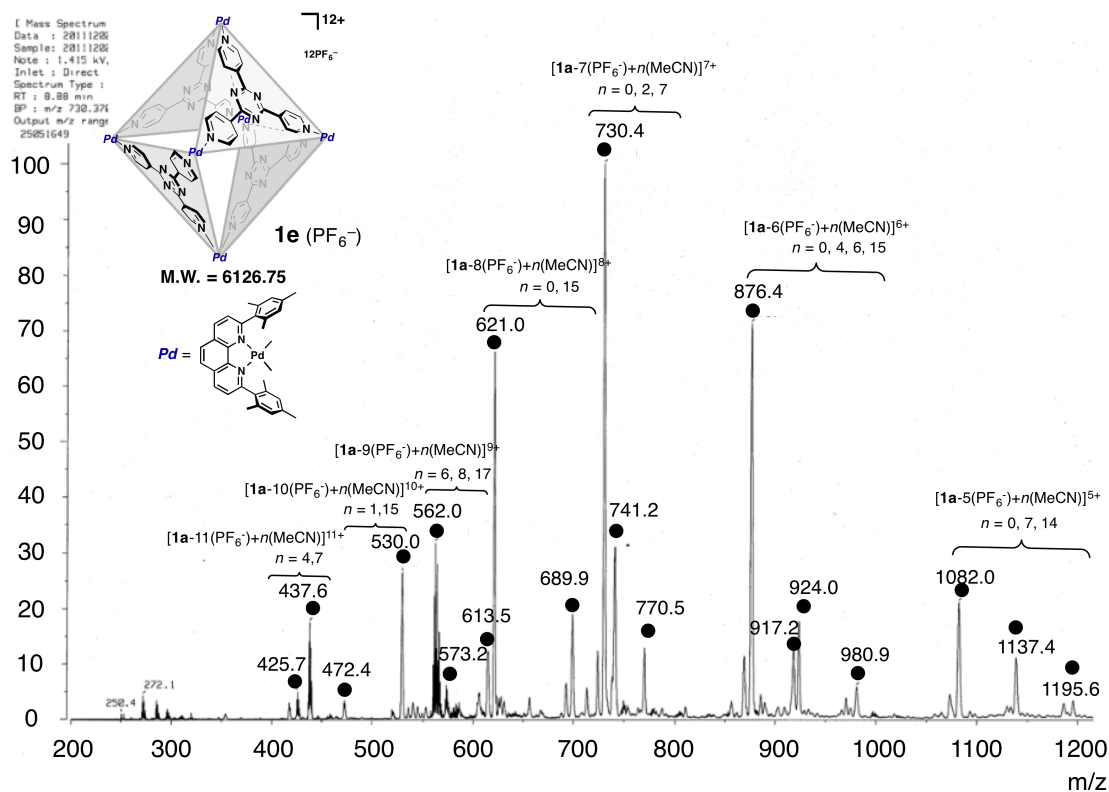
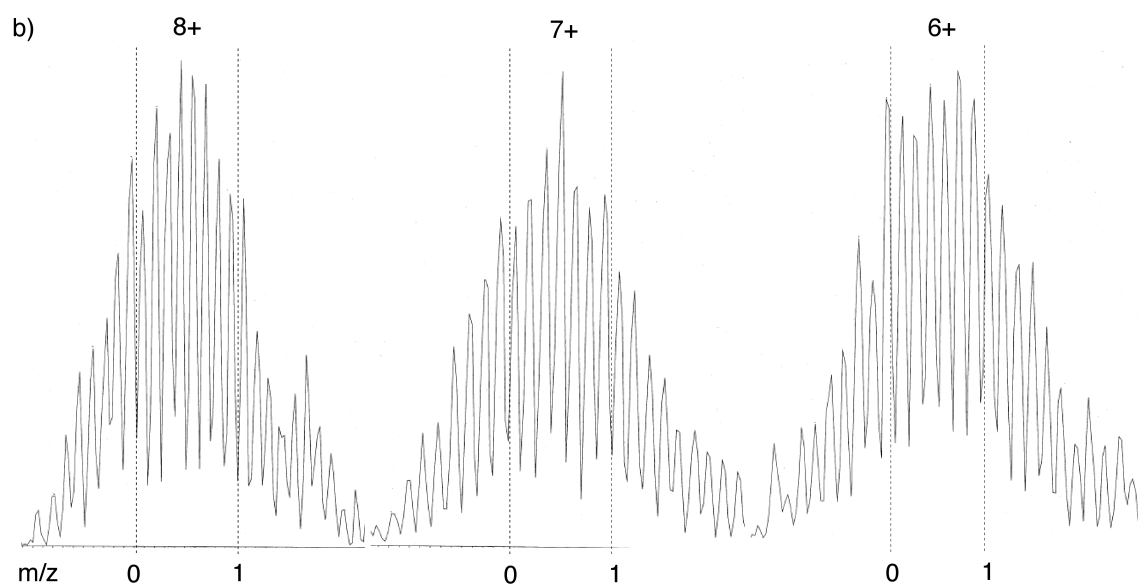


Figure S41. ESI-MS spectrum of cage **1e** ( $\text{PF}_6^-$ ).

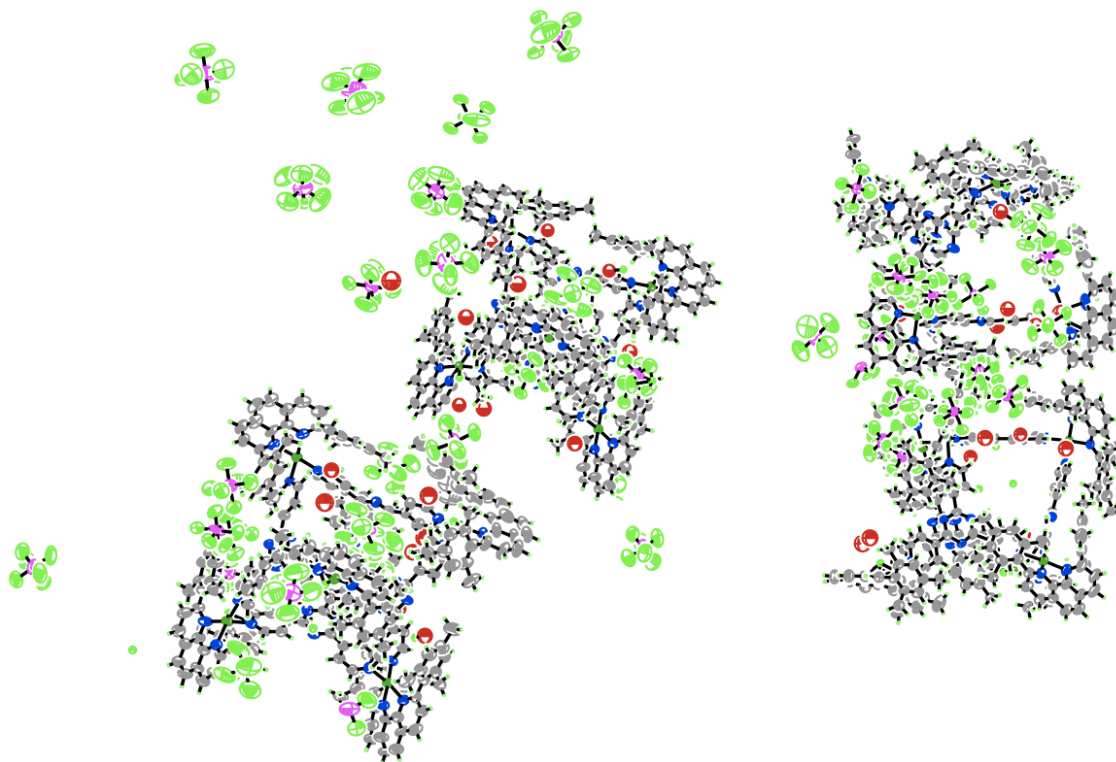




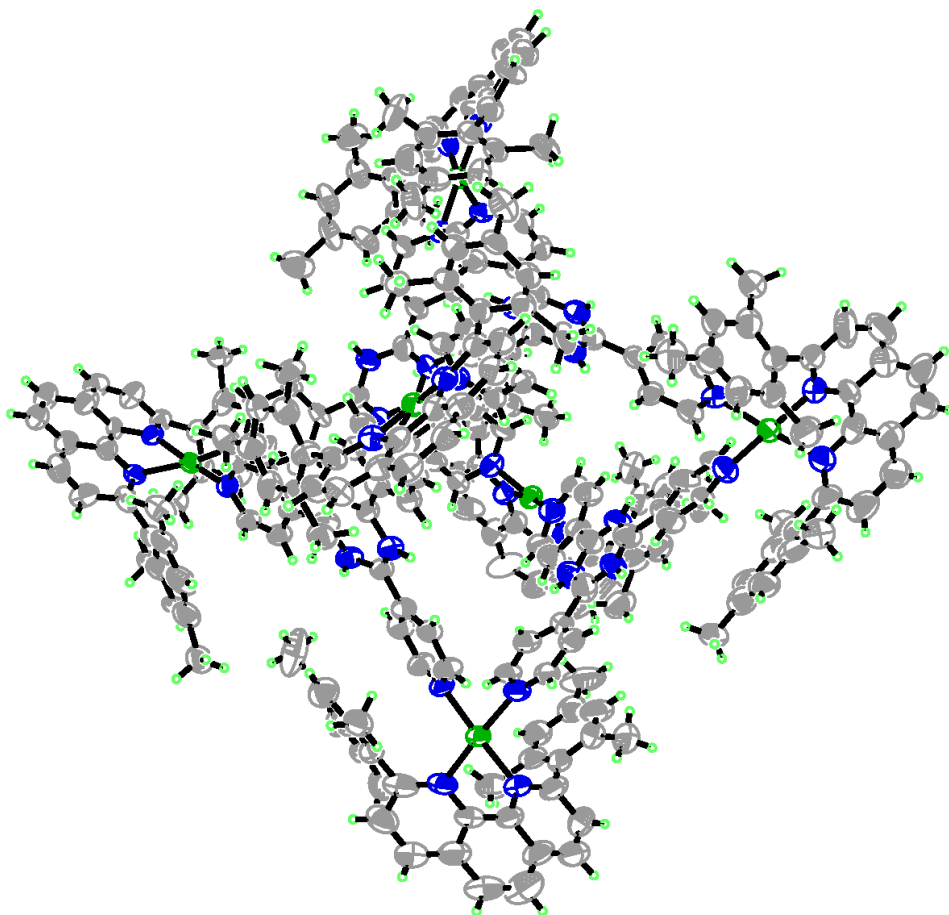
**Figure S42.** Isotope patterns of cage **1e** ( $\text{PF}_6^-$ ).



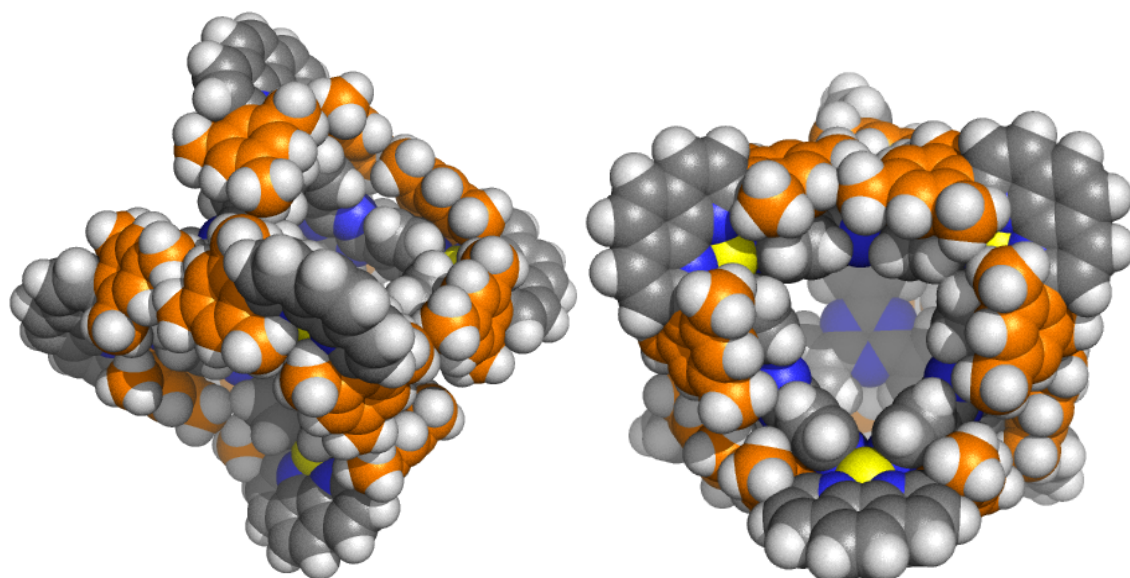
Crystal size 0.10 x 0.04 x 0.04 mm<sup>3</sup>  
Theta range for data collection 0.57 to 26.04°.  
Index ranges -45<=h<=45, -77<=k<=77, -47<=l<=47  
Reflections collected 557706  
Independent reflections 152706 [R(int) = 0.0748]  
Completeness to theta = 26.04° 92.9 %  
Absorption correction Semi-empirical from equivalents  
Max. and min. transmission 0.9756 and 0.9405  
Refinement method Full-matrix least-squares on F<sup>2</sup>  
Data / restraints / parameters 152706 / 8282 / 13399  
Goodness-of-fit on F<sup>2</sup> 1.882  
Final R indices [I>2sigma(I)] R1 = 0.1638, wR2 = 0.4344  
R indices (all data) R1 = 0.1880, wR2 = 0.4531  
Largest diff. peak and hole 2.423 and -1.943 e.Å<sup>-3</sup>



**Figure S43.** ORTEP drawing (30% probability ellipsoids) of cage **1e** with PF<sub>6</sub><sup>-</sup> and oxygen atoms.



**Figure S44.** Selected crystal structure of **1e** ( $\text{PF}_6^-$ ) (ORTEP view, 30% probability ellipsoids)



**Figure S45.** A space-filling depiction of the crystal structure of cage **1e** ( $\text{PF}_6^-$ ) (view from side, left; view from portal, right).

### **Details for a void volume calculation (by *VOIDOO* program)**

In order to estimate the central void volume of cages **1**, *VOIDOO* calculations based on the crystal structures were performed. Due to the large portals of the cage, a default virtual probe with radius of 1.4 Å is not suitable. Finally, we employed a virtual probe with radius of 3.36 Å to calculate a reasonable central cavity volume for each cage. The following parameters were modified for the calculations:

Maximum number of detection cycles: 30

Maximum number of volume-refinement cycles: 30

Minimum size of secondary grid: 1

Grid for plot files: 0.1

Primary grid spacing: 0.1

## 2.6 REFERENCES

- [1] M. Fujita, D. Oguro, M. Miyazawa, H. Oka, K. Yamaguchi, K. Ogura, *Nature* **1995**, 378, 469.
- [2] Y. Fang, T. Murase, S. Sota, M. Fujita, *J. Am. Chem. Soc.* **2013**, 135, 613.
- [3] T. Kusukawa, M. Fujita, *J. Am. Chem. Soc.* **2002**, 124, 13576.
- [4] M. Yoshizawa, J. K. Klosterman, M. Fujita, *Angew. Chem., Int. Ed.* **2009**, 48, 3418.
- [5] R. A. Bilbeisi, J. K. Clegg, N. Elgrishi, X. D. Hatten, M. Devillard, B. Breiner, P. Mal, J. R. Nitschke, *J. Am. Chem. Soc.* **2012**, 134, 5110.
- [6] I. A. Riddell, M. M. J. Smulders, J. K. Clegg, Y. R. Hristova, B. Breiner, J. D. Thoburn, J. R. Nitschke, *Nat. Chem.* **2012**, 4, 751.
- [7] Y. R. Hristova, M. M. J. Smulders, J. K. Clegg, B. Breiner, J. R. Nitschke, *Chem. Sci.* **2011**, 2, 638.
- [8] J. S. Mugridge, R. G. Bergman, K. N. Raymond, *J. Am. Chem. Soc.* **2010**, 132, 16256.
- [9] J. S. Mugridge, R. G. Bergman, K. N. Raymond, *J. Am. Chem. Soc.* **2011**, 133, 11205.
- [10] M. D. Pluth, R. G. Bergman, K. N. Raymond, *J. Am. Chem. Soc.* **2007**, 129, 94720.
- [11] J. K. Clegg, F. Li, K. A. Jolliffe, G. V. Meehan, L. F. Lindoy, *Chem. Commun.* **2011**, 47, 6042.
- [12] V. Kalsani, H. Ammon, F. Jackel, J. P. Rabe, M. Schmittel, *Chem. Eur. J.* **2004**, 10, 5481.
- [13] M. Schmittel, U. Luning, M. Meder, A. Ganz, C. Michel, M. Herderich, *Heterocycl. Commun.* **1997**, 3, 493.
- [14] S. De, K. Mahata, M. Schmittel, *Chem. Soc. Rev.* **2010**, 39, 1555;
- [15] M. L. Saha, S. De, S. Pramanik, M. Schmittel, *Chem. Soc. Rev.* **2013**, 42, 6860.
- M. Yoshizawa, J. K. Klosterman, M. Fujita, *Angew. Chem., Int. Ed.* **2009**, 48, 3418.

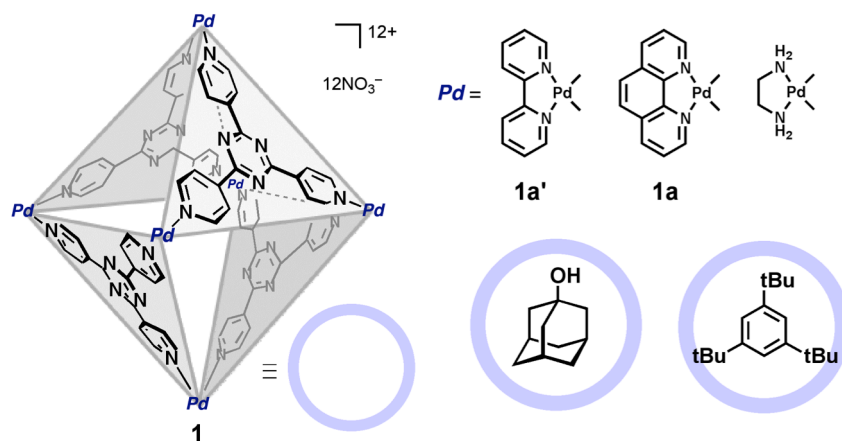
# Chapter 3

## Guest-binding in shrunken cavities

The binding properties of a self-assembled coordination cage **1a–e** were compared by encapsulation of various guest molecules. Because the cages with pendant groups have modified cavities in shape and size, guest-binding properties were found totally different from unmodified cages. Different cavities prefer different species of guest in size, shape and rigidity. The cavities of the cage were proved to be very sensitive for guest species and size. Moreover, even a single methyl difference in ancillary ligand results in big difference in guest binding. A minor difference in size of rigid guest also results in difference in inclusion yield.

### 3.1 Introduction

A variety of organic molecules have been encapsulated by self-assembled coordination cage **1**. For example, both cage **1a'** and **1a** can encapsulate adamantanol, 1,3,5-tritertbutylbenzene and other guests. Changing the aromatic capping ligand to aliphatic, such as ethylenediamine, also does not change the guest-binding property (Figure 1).<sup>[1-5]</sup>



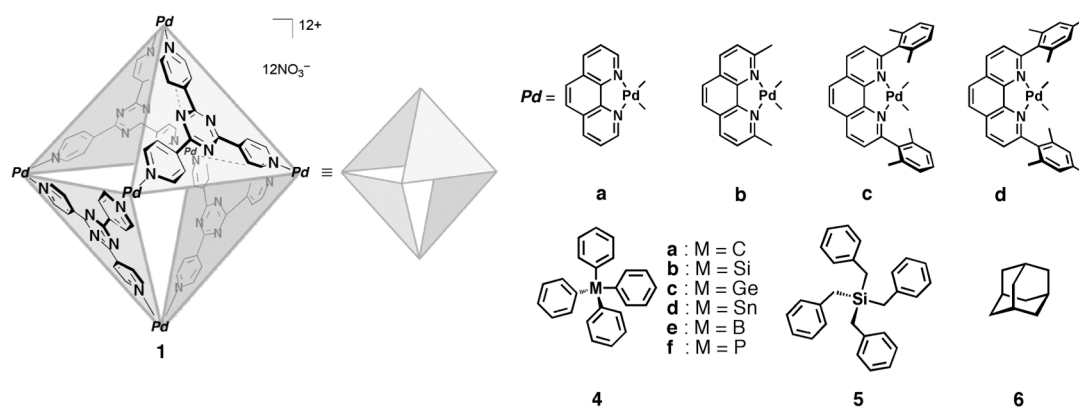
**Figure 1.** Self-assembled coordination cages **1**.

In this chapter, guest encapsulation of cages with different remote substituents was fully investigated (Figure 2). Because the cavities of these cages were tuned in size and shape due to the remote substituents, different guest-binding properties were expected. Then dominant factor of tuning guest species can be found out.

According to our concern, both electronic property and steric property of the guest were proved to be crucial for guest binding by self-assembled coordination cage **1**. For electronic property, the anionic, neutral or cationic guests always show totally different binding abilities. For steric factor, the shape and size of the guest sometimes show subtle difference in guest-binding. Here, three typical guest species were selected (Figure 2). Firstly, a large size but flexible tetrabenzylsilane (**5**) was introduced. Because this guest is flexible, it can shrink or extend itself to adapt the cavity environment. Second one is a medium-sized but rigid tetrahedral molecules  $\text{Ph}_4\text{M}$  (**4**,  $\text{M} = \text{C}, \text{Si}, \text{Ge}, \text{Sn}$ ). When central atoms were changed from C to Sn, the molecules maintains their tetrahedral shape and slighted increase their bulkiness (362–394 Å<sup>3</sup>). Finally, small and rigid adamantane (**6**) was used. Different from previous two species, four molecules of adamantane aggregated in the cage in previous reports



and each adamantane occupied a window of the octahedral cage.

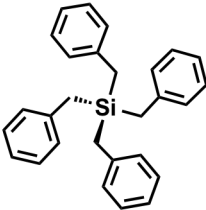
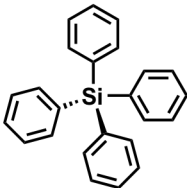



**Figure 2.** Self-assembled coordination cage **1b–e**. Three guest species **4–6**.

### 3.2 Guest Species

Firstly, guest-binding comparison between cage **1b** and **1e** was conducted. Because of lacking the remote substituents, cage **1a** and **1b** was regarded as sharing the same cavity volume, which make them the same guest-binding property in previous study. Here, cage **1b** represents ordinary cavity without modification and cage **1e** represents the most shrunken cavity. When an excess amount of insoluble guest **4b**, **5** and **6** (10 eq. for cage **1**) was suspended in a D<sub>2</sub>O solution (0.5 mL) of cages **1** (0.5 μmol; 1 mM) and the resulting solution was stirred at 80 °C for 4 h, the solution color

Table 1. Inclusion yields of host-guest complex<sup>a</sup>.

			
<b>1b</b>	73 %	0 %	65 % <sup>b</sup>
<b>1e</b>	99 %	75 %	0 %

<sup>a</sup> Encapsulation conditions: cage **1** and guest (10 equiv) in D<sub>2</sub>O (1.0 mM) at 80 °C for 4 h. <sup>b</sup> Four molecules were encapsulated.

turned from colorless to pale yellow. After removal of residual guest by filtration, <sup>1</sup>H NMR confirmed the formation of inclusion complexes in different yields. The guest species was totally different for the two cages (Table 1).

For flexible tetrabenzylsilane (**5**), Cage **1e** with the shrunken cavity encapsulated tetrabenzylsilane more efficiently, compared to unmodified cage **1b**. Although the flexible guest **5** can shrink or extent itself to adapt the cavity environment, shrunken cavity was proved to be more suitable for it, thus inclusion yield of **1e•5** (99%) is higher than **1b•5** (73%).

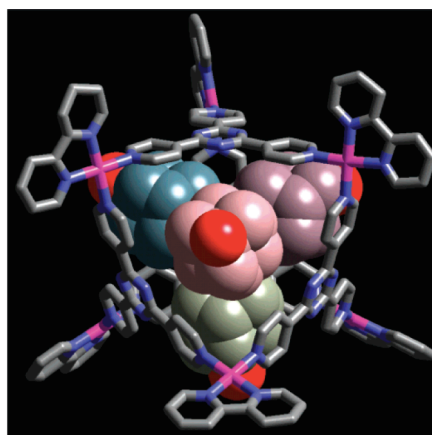


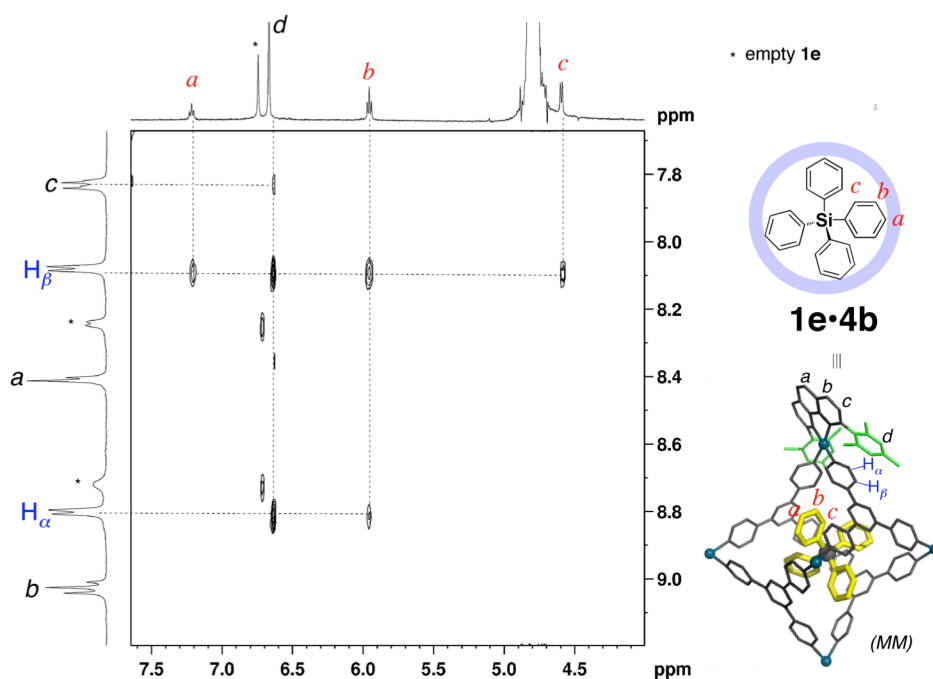
Figure 3. X-ray of inclusion complex **1a•(adamantanol)<sub>4</sub>**. Reprinted with permission from ref. 4. Copyright 2002 American Chemical Society.

For rigid tetraphenylsilane (**4b**), surprisingly, no inclusion complex **1b•4b** was found while inclusion complex **1e•4b** was formed in high yield (75%). A plausible explanation is that such rigid small molecule **4b** only tightly binds with shrunken cavity of cage **1e**, whereas large cavity of cage **1b** cannot stabilize it.

For the smallest guest adamantane **6**, situation was reversed. No guest encapsulation for **1e** was found while inclusion complex **1b•(6)<sub>4</sub>** was formed in moderate yield (65%). From X-ray single crystal of inclusion complex **1a•(adamantanol)<sub>4</sub>**, four molecules of adamantanol was encapsulated and each molecule occupied a window of the octahedral cage (Figure 3).<sup>[4]</sup> Inclusion complex **1b•(6)<sub>4</sub>** was expected to adopt the same pattern due to the analogue structures in host (**1a** and **1b**) and guest (adamantanol and adamantane). Cage **1e** has shrunken cavity volume and modified window and made its cavity unfavorable for guest **6**.

### 3.3 Fine Tuning of Remote Substituent and Guest Size

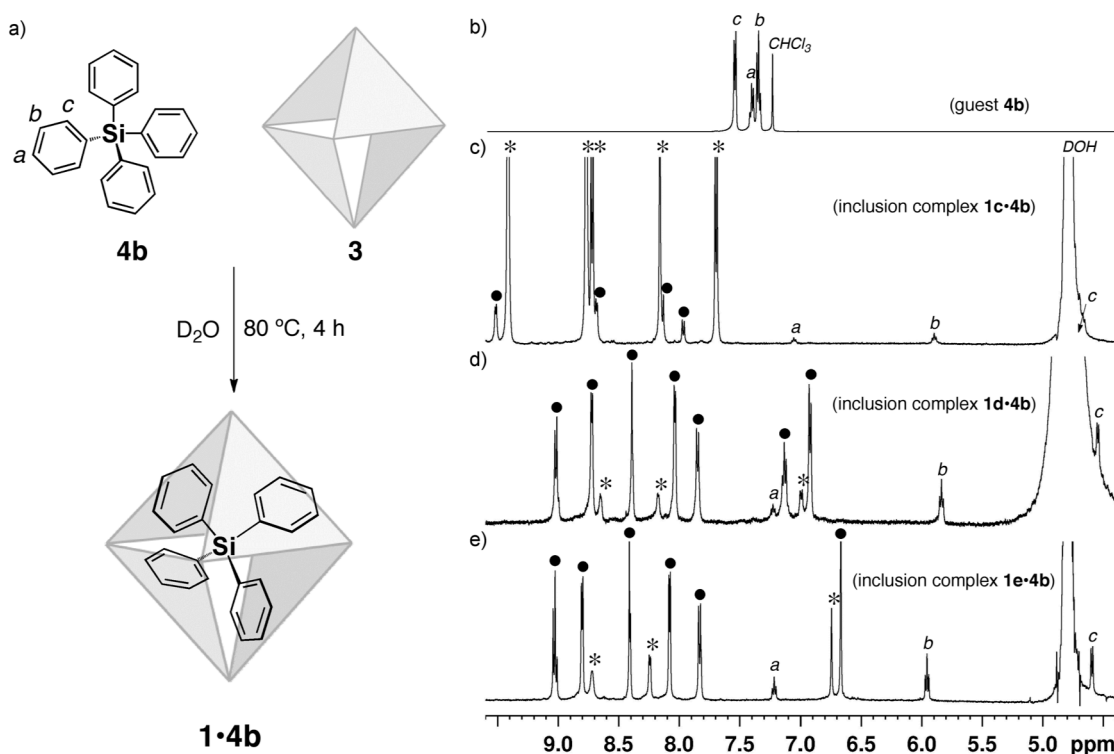
Great interest was attached for encapsulating rigid guest **4b** and its analogues. Combining NMR measurement and molecular modeling of inclusion complex **1e•4b**, guest **4b** was located at the center of the cavity of cage **1e**, pointing four phenyl groups



**Figure 4.** NOESY spectrum and modeling structure of inclusion complex **1e•4b**. Reprinted with permission from ref. 6. Copyright 2013 American Chemical Society.

at the cage portals. This indicated that such rigid molecule could act as a probe molecule for detecting the central void of the cavity (Figure 4).<sup>[6]</sup>

Firstly, to experimentally show the impact of the R pendant groups on the cage cavity, rigid tetrahedral guests **4b** (374 Å<sup>3</sup>) were employed to perform the guest encapsulation into cages **1**. When an excess amount of insoluble guest **4b** (10 eq. for cage **1**) was suspended in a D<sub>2</sub>O solution (0.5 mL) of cages **1** (0.5 μmol; 1 mM) and the resulting solution was stirred at 80 °C for 4 h, the solution color turned from colorless to pale yellow. After removal of residual guest by filtration, <sup>1</sup>H NMR confirmed the formation of inclusion complexes in different yields.<sup>[7]</sup> The inclusion yields were quite sensitive depending on the remote substituents of the cage (Figure 5).



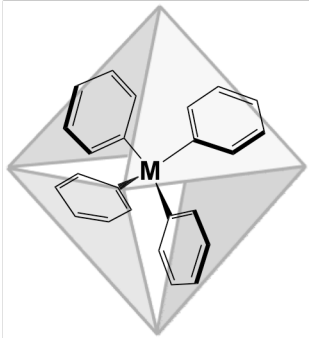
**Figure 5.** a) Encapsulation of tetraphenylsilane (**4b**) into cage **1** in D<sub>2</sub>O. b–e) <sup>1</sup>H NMR spectra (500 MHz, 300 K) of (b) guest **4b** (in CDCl<sub>3</sub>), (c) inclusion complex **1c•4b** (in D<sub>2</sub>O), (d) inclusion complex **1d•4b** (in D<sub>2</sub>O), and (e) inclusion complex **1e•4b** (in D<sub>2</sub>O). The black circle (•) and asterisk (\*) denote resonances of inclusion complex **1•4b** and empty cage **1**, respectively. Reprinted with permission from ref. 7. Copyright 2014 John Wiley and Sons.

As described in the last section, inclusion complex **1b•4b** was not found. Introduction of methyl groups at the 2,9-positions allowed cage **1c** to accommodate

tetrahedral guests **4b** (yield 76%), whose signals underwent upfield-shift. When bulky substituents (2,6-dimethylphenyl and mesityl) attached to cage **1d** and **1e** respective, inclusion yield of **1d•4b** and **1e•4b** was dramatically improved (76% and 75%, respectively) and included guest signals were highly upfield shifted (−3.0 ppm). Here, the methyl substituents slightly reformed and shrunken the cavity of cage **1c**, making it accommodating guest **4b** with low inclusion yield. Bulky 2,6-dimethylphenyl and mesityl substituents considerably shrunken the cavities of cages cage **1d** and **1e**, leading to tight binding of **4b**.

On the other hand, guest size can be easily tuned by varying central atoms from B, C, Si, P, Ge to Sn (355–394 Å<sup>3</sup>). When an excess amount of insoluble guest **4a–f** (10 eq. for cage **1**) was suspended in a D<sub>2</sub>O solution (0.5 mL) of cages **1** (0.5 μmol; 1 mM) and the resulting solution was stirred at 80 °C for 4 h, the solution color turned from colorless to pale yellow. After removal of residual guest by filtration, <sup>1</sup>H NMR confirmed the formation of inclusion complexes in different yields. Again, the inclusion yields were quite sensitive to the guest (Table 2).

**Table 2.** Inclusion yields of rigid tetrahedral Ph<sub>4</sub>M guests **4a–f** within cages **1**.

Inclusion complex <sup>[a]</sup>	Guest		Inclusion yield (%) <sup>[c]</sup>			
	<b>4</b>	size (Å <sup>3</sup> ) <sup>[b]</sup>	<b>1b</b>	<b>1c</b>	<b>1d</b>	<b>1e</b>
	M = C ( <b>4a</b> )	361.50	0	11	55	56
	M = Si ( <b>4b</b> )	374.46	0	11	76	75
	M = Ge ( <b>4c</b> )	382.73	0	12	40	43
	M = Sn ( <b>4d</b> )	393.75	0	18	39	38
	M = B ( <b>4e</b> ) <sup>[d]</sup>	355.28	>99	>99	>99	>99
	M = P ( <b>4f</b> ) <sup>[e]</sup>	378.30	0	0	0	0

[a] Conditions: cage **1** and guest **4** (10 equiv) in D<sub>2</sub>O (1.0 mM) at 80 °C for 4 h unless otherwise noted. Excess guest was removed by filtration before NMR measurements. [b] van der Waals volumes calculated from structure optimized using SPARTAN'10 with MP2 using both a 6-31G\* and a larger 6-311+G\*\* basis set. [c] NMR yields. [d] Na<sup>+</sup>[Ph<sub>4</sub>B]<sup>−</sup>. Guest encapsulation was performed at room temperature. [e] [Ph<sub>4</sub>P]<sup>+</sup>PF<sub>6</sub><sup>−</sup>. Reprinted with permission from ref. 7. Copyright 2014 John Wiley and Sons.

The difference between cages **1b** and **1c** is merely the methyl substituent on the phenanthroline ancillary ligand that is far from the actual guest-binding site. But, the methyl substituent plays a critical role in the guest encapsulation. Cage **1b** showed no guest-binding affinity due to its too large cavity to hold such a small molecule. However, cage **1c** readily binds guest **1** in a manner of increasing inclusion yield with the growing size of the guests. Based on the result of the growing inclusion yield of **1c•4**, it is suggested that the methyl substituent slightly pushes the cage framework inward to shrink the cavity to enable the preferable holding of larger guest, such as **4d**. For example, when the largest Ph<sub>4</sub>Sn (**4d**) was employed in place of Ph<sub>4</sub>Si (**4b**), the inclusion yield within cage **1c** slightly increased from 11% to 18%, whereas those within cages **1d** and **1e** significantly decreased from three-quarters (75%) to a half (~40%). Actually, lack of the p-methyl group of the mesityl substituent seems not to change the strong  $\pi$ - $\pi$  interactions with aromatic panel of the cage framework; the encapsulation yield of **4** in cage **1d** was almost the same as that in cage **1e**. Interestingly, the inclusion yields of **1d•4** and **1e•4** highly depend on the size of the guest molecules. Medium sized tetraphenylsilane **4b** (374 Å<sup>3</sup>) was the best-fit guest for cage **1d** and **1e**. If the guest molecule is too small (**4b**, 362 Å<sup>3</sup>), inclusion yield for **1d•4a** and **1e•4a** drop down to ~55% due to guest escape. In contrast, if the guest molecule is too large (**4d**, 394 Å<sup>3</sup>), inclusion yield for **1d•4d** and **1e•4d** also drop down to ~40% due to the difficulty in encapsulation. These crucial phenomenon characterized the shrunken degree of the cavities depended on the remote substituents.

One more thing to mention: in host-guest interactions, their size complementarity does not always matter; the outer positive charges (total 12+) on the Pd(II) centers of cages **1** play a critical role for encapsulating charged guest molecules in water. Water-soluble tetraphenylborate anion **4e** was accommodated quantitatively within all the cages at room temperature. In contrast, water-soluble tetraphenylphosphonium cation **4f** was not accommodated at all due to electrostatic repulsion, despite the fact that the size and shape of **4f** are almost the same as those of **4b**.

### **3.4 Conclusion**

This chapter is included that guest species of self-assembled coordination cages can be remotely and finely tuned by remote substituents. Because the cavity volumes

of self-assembled coordination cages were reduced by substituents of the phenanthroline ancillary ligand without directly modifying the inside cavity, cages show totally different guest-binding properties. More importantly, the presence or absence of one methyl group, which is particularly located far from the guest-binding site, proved to be dominating for binding guest molecules.

A tiny difference in remote site makes a big difference in artificial host–guest systems. By judicious design of the ancillary ligand on the metal corner of the cage furnishes a way for finely tuning chemical transformations inside the cage without changing the components of the cage framework.

### **3.5 Experiment Section**

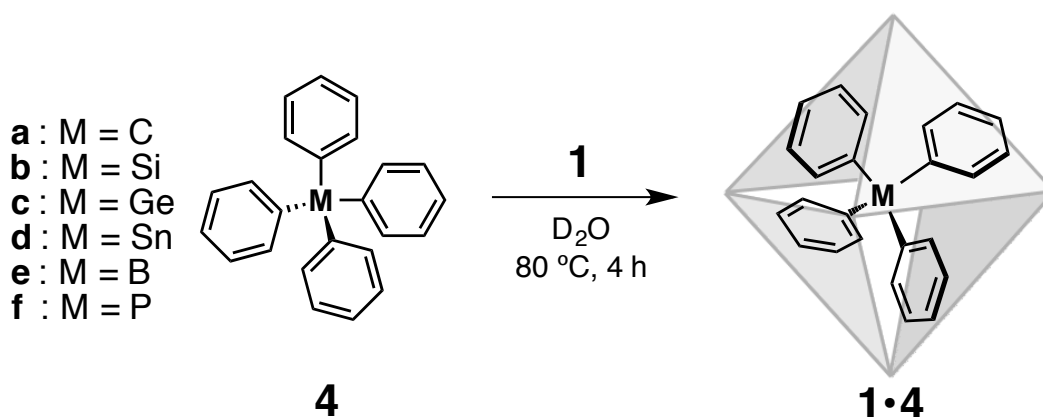
#### **Materials and Instrumentations:**

<sup>1</sup>H and other NMR spectra were recorded on a Bruker DRX-500 (500 MHz) spectrometer. TMS (CDCl<sub>3</sub> solution) in a capillary served as an external standard ( $\delta = 0$  ppm). Melting points were determined with a Yanaco MF-500 V micro melting point apparatus. Elemental analyses were performed on a Yanaco MT-6. MALDI-TOF mass spectra were measured on an Applied Biosystem Voyager DE-STR. CSI-MS data were measured on a four-sector (BE/BE) tandem mass spectrometer (JMS-700C, JEOL) equipped with the CSI source. Diffraction measurements were made using a Bruker APEXII/CCD diffractometer equipped with a focusing mirror (MoK $\alpha$  radiation  $\lambda = 0.71073$  Å). Solvents and reagents were purchased from TCI Co., Ltd., WAKO Pure Chemical Industries Ltd., and Sigma-Aldrich Co. Deuterated H<sub>2</sub>O was acquired from Cambridge Isotope Laboratories, Inc. and used as supplied for the complexation reactions and NMR measurements.

For figures and tables: Reprinted with permission from ref. 6 and 7. Copyright 2014 John Wiley and Sons. Copyright 2013 American Chemical Society.



## General Procedure for Encapsulation of Guests 4a–h into Cages 1



When an excess amount of **4** (10 eq. for cage **1**) was suspended in a D<sub>2</sub>O solution (0.5 mL) of cages **1** (0.5 μmol; 1 mM) and the resulting solution was stirred at 80 °C for 4 h, the solution color turned from colorless to pale yellow. After removal of residual guest **4** by filtration, <sup>1</sup>H NMR confirmed the formation of inclusion complexes **1•4** in different yields. In the case of guest **4e**, guest encapsulation was performed at room temperature.

### *Physical Data of Inclusion Complex 1b•4e*

<sup>1</sup>H NMR (500 MHz, D<sub>2</sub>O, 300 K) δ: 9.35 (d, *J* = 5.0 Hz, 24H, **1b**), 8.76 (d, *J* = 8.5 Hz, 12H, **1b**), 8.65 (d, *J* = 4.5 Hz, 24H, **1b**), 8.05 (s, 12H, **1b**), 7.89 (d, *J* = 4.5 Hz, 12H, **1b**), 7.66 (dd, *J* = 8.5 Hz, 14h, **1a**), 6.46 (t, *J* = 7.3 Hz, 4H, **4e**), 5.62 (t, *J* = 7.8 Hz, 8H, **4e**), 4.96 (d, *J* = 7.5 Hz, 8H, **4e**), Yield: quant.

### *Physical Data of Inclusion Complex 1b•4g*

<sup>1</sup>H NMR (500 MHz, D<sub>2</sub>O, 300 K) δ: 9.67 (d, *J* = 5.0 Hz, 24H, **1b**), 8.99 (d, *J* = 8.5 Hz, 12H, **1b**), 8.93 (d, *J* = 4.5 Hz, 24H, **1b**), 8.31 (s, 12H, **1b**), 8.22 (d, *J* = 4.5 Hz, 12H, **1b**), 7.94 (dd, *J* = 8.5 Hz, 12H, **1b**), 7.14 (d, *J* = 7.0 Hz, 4h, **4g**), 6.10 (t, *J* = 8.0 Hz, 4H, **4g**), 5.50 (d, *J* = 8.0 Hz, 4H, **4g**), 4.97 (d, *J* = 9.5 Hz, 4H, **4g**), 4.72 (d, *J* = 7.5 Hz, 4H, **4g**), Yield: quant.

*Physical Data of Inclusion Complex **1c•4a***

<sup>1</sup>H NMR (500 MHz, D<sub>2</sub>O, 300 K) δ: 9.52 (d, *J* = 6.5 Hz, 24H, **1c**), 8.73 (d, *J* = 8.5 Hz, 12H, **1c**), 8.68 (d, *J* = 6.5 Hz, 24H, **1c**), 8.16 (s, 12H, **1c**), 7.70 (d, *J* = 8.5 Hz, 12H, **1c**), 7.06 (d, *J* = 7.3 Hz, 4H, **4a**), 5.91 (t, *J* = 7.8 Hz, 8H, **4a**), 4.84 (d, *J* = 8.0 Hz, 8H, **4a**), 2.24 (s, 36H, **1c**), Yield: 11%.

*Physical Data of Inclusion Complex **1c•4b***

<sup>1</sup>H NMR (500 MHz, D<sub>2</sub>O, 300 K) δ: 9.50 (d, *J* = 6.5 Hz, 24H, **1c**), 8.71 (d, *J* = 8.5 Hz, 12H, **1c**), 8.67 (d, *J* = 6.5 Hz, 24H, **1c**), 8.12 (s, 12H, **1c**), 7.69 (d, *J* = 8.5 Hz, 12H, **1c**), 7.05 (t, *J* = 7.3 Hz, 4H, **4b**), 5.90 (t, *J* = 7.8 Hz, 8H, **4b**), 4.90–4.65 (d, *J* = 7.5 Hz, 8H, **4b**, overlapped with HDO), 2.23 (s, 36H, **1c**), Yield: 11%.

*Physical Data of Inclusion Complex **1c•4c***

<sup>1</sup>H NMR (500 MHz, D<sub>2</sub>O, 300 K) δ: 9.52 (d, *J* = 6.5 Hz, 24H, **1c**), 8.72 (d, *J* = 8.5 Hz, 12H, **1c**), 8.64 (d, *J* = 6.5 Hz, 24H, **1c**), 8.16 (s, 12H, **1c**), 7.70 (d, *J* = 8.5 Hz, 12H, **1c**), 7.39 (t, *J* = 7.3 Hz, 4H, **4c**), 6.26 (t, *J* = 7.8 Hz, 8H, **4c**), 5.50 (d, *J* = 7.5 Hz, 8H, **4c**), 2.24 (s, 36H, **1c**), Yield: 12%.

*Physical Data of Inclusion Complex **1c•4d***

<sup>1</sup>H NMR (500 MHz, D<sub>2</sub>O, 300 K) δ: 9.51 (d, *J* = 6.5 Hz, 24H, **1c**), 8.72 (d, *J* = 8.5 Hz, 12H, **1c**), 8.62 (d, *J* = 6.5 Hz, 24H, **1c**), 8.16 (s, 12H, **1c**), 7.69 (d, *J* = 8.5 Hz, 12H, **1c**), 7.44 (t, *J* = 7.3 Hz, 4H, **4d**), 6.44 (t, *J* = 7.8 Hz, 8H, **4d**), 5.17 (d, *J* = 7.5 Hz, 8H, **4d**), 2.24 (s, 36H, **1c**), Yield: 18%.

*Physical Data of Inclusion Complex **1c•4e***

<sup>1</sup>H NMR (500 MHz, D<sub>2</sub>O, 300 K) δ: 9.31 (d, *J* = 6.5 Hz, 24H, **1c**), 8.58 (d, *J* = 8.5 Hz, 12H, **1c**), 8.53 (d, *J* = 6.5 Hz, 24H, **1c**), 8.02 (s, 12H, **1c**), 7.55 (d, *J* = 8.5 Hz, 12H, **1c**), 6.47 (t, *J* = 7.3 Hz, 4H, **4e**), 5.47 (t, *J* = 7.8 Hz, 8H, **4e**), 4.69 (d, *J* = 7.5 Hz, 8H, **4e**), 2.11 (s, 36H, **1c**), Yield: quant.

*Physical Data of Inclusion Complex **1c•4g***

<sup>1</sup>H NMR (500 MHz, D<sub>2</sub>O, 300 K) δ: 9.55–9.54 (m, 24H, **1c**), 8.75 (d, *J* = 8.5 Hz, 12H, **1c**), 8.70–8.50 (m, 24H, **1c**), 8.19 (s, 12H, **1c**), 7.72 (d, *J* = 8.5 Hz, 12H, **1c**), 7.09 (t, *J* = 7.0 Hz, 4h, **4g**), 5.98 (t, *J* = 8.0 Hz, 4H, **4g**), 5.38 (d, *J* = 8.0 Hz, 4H, **4g**), 4.67 (d, *J* = 9.5 Hz, 4H, **4g**), 4.52 (d, *J* = 7.5 Hz, 4H, **4g**), 2.31 (s, 36H, **1c**), Yield: quant.

*Physical Data of Inclusion Complex **1c•4h***

<sup>1</sup>H NMR (500 MHz, D<sub>2</sub>O, 300 K) δ: 9.43–9.38 (m, 24H, **1c**), 8.57 (d, *J* = 8.5 Hz, 12H, **1c**), 8.70–8.50 (m, 24H, **1c**), 8.02 (s, 12H, **1c**), 7.55 (d, *J* = 8.5 Hz, 12H, **1c**), 6.97 (t, *J* = 7.5 Hz, 4h, **4h**), 5.87 (t, *J* = 8.0 Hz, 4H, **4h**), 5.19 (d, *J* = 10.0 Hz, 4H, **4h**), 4.52 (d, *J* = 8.0 Hz, 4H, **4h**), 4.45 (d, *J* = 6.5 Hz, 4H, **4h**), 3.76 (s, 6H, **4h**), 2.09 (s, 36H, **1c**), Yield: 33%.

*Physical Data of Inclusion Complex **1d•4a***

<sup>1</sup>H NMR (500 MHz, D<sub>2</sub>O, 300 K) δ: 9.03–9.00 (m, 12H, **1d**), 8.72 (d, *J* = 7.0 Hz, 24H, **1d**), 8.40–8.38 (m, 12H, **1d**), 8.09 (d, *J* = 6.0 Hz, 24H, **1d**), 7.87–7.84 (m, 12H, **1d**), 7.14 (t, *J* = 8.8 Hz, 12H, **1d**), 6.93 (d, *J* = 9.5 Hz, 24H, **1d**), 6.75 (t, *J* = 7.3 Hz, 4H, **4a**), 5.49 (t, *J* = 7.8 Hz, 4H, **4a**), 4.11 (d, *J* = 7.5 Hz, 8H, **4a**), 2.30–2.20 (m, 72H, **1d**). Yield: 55%.

*Physical Data of Inclusion Complex **1d•4b***

<sup>1</sup>H NMR (500 MHz, D<sub>2</sub>O, 300 K) δ: 9.02 (d, *J* = 7.3 Hz, 12H, **1d**), 8.72 (d, *J* = 7.0 Hz, 24H, **1d**), 8.39 (s, 12H, **1d**), 8.09 (d, *J* = 6.0 Hz, 24H, **1d**), 7.86 (d, *J* = 7.0 Hz, 12H, **1d**), 7.13 (t, *J* = 8.8 Hz, 12H, **1d**), 7.10 (t, *J* = 7.3 Hz, 4H, **4b**), 6.92 (d, *J* = 9.5 Hz, 24H, **1d**), 5.84 (t, *J* = 7.8 Hz, 8H, **4b**), 4.55 (d, *J* = 7.5 Hz, 8H, **4b**), 2.30–2.20 (m, 72H, **1d**). Yield: 76%.

*Physical Data of Inclusion Complex **1d•4c***

<sup>1</sup>H NMR (500 MHz, D<sub>2</sub>O, 300 K) δ: 9.07–9.04 (m, 12H, **1d**), 8.75 (d, *J* = 7.0 Hz, 24H, **1d**), 8.43 (s, 12H, **1d**), 8.04 (d, *J* = 6.0 Hz, 24H, **1d**), 7.88 (d, *J* = 7.0 Hz, 12H, **1d**), 7.16 (t, *J* = 8.8 Hz, 12H, **1d**), 7.15 (t, *J* = 7.3 Hz, 4H, **4c**), 6.96 (d, *J* = 9.5 Hz, 24H, **1c**), 5.91 (t, *J* = 7.8 Hz, 8H, **4c**), 4.54 (d, *J* = 7.5 Hz, 8H, **4c**), 2.33–2.20 (m, 72H, **1d**). Yield: 40%.

*Physical Data of Inclusion Complex **1d•4d***

<sup>1</sup>H NMR (500 MHz, D<sub>2</sub>O, 300 K) δ: 8.96–8.93 (m, 12H, **1d**), 8.64 (d, *J* = 7.0 Hz, 24H, **1d**), 8.31 (s, 12H, **1d**), 7.91 (d, *J* = 6.0 Hz, 24H, **1d**), 7.77 (d, *J* = 7.0 Hz, 12H, **1d**), 7.12 (t, *J* = 7.3 Hz, 4H, **4d**), 7.06 (t, *J* = 8.8 Hz, 12H, **1d**), 6.85 (d, *J* = 9.5 Hz, 24H, **1d**), 6.01 (t, *J* = 7.8 Hz, 8H, **4d**), 4.53 (d, *J* = 7.5 Hz, 8H, **4d**), 2.23–2.14 (m, 74h, **1d**). Yield: 39%.

*Physical Data of Inclusion Complex **1d•4e***

<sup>1</sup>H NMR (500 MHz, D<sub>2</sub>O, 300 K) δ: 8.96–8.93 (m, 12H, **1d**), 8.56 (d, *J* = 8.5 Hz, 24H, **1d**), 8.27 (s, 12H, **1d**), 7.93 (d, *J* = 8.5 Hz, 24H, **1d**), 7.73 (d, *J* = 8.5 Hz, 12H, **1d**), 7.04 (t, *J* = 8.8 Hz, 12H, **1d**), 6.81 (d, *J* = 8.0 Hz, 24H, **1d**), 6.19 (t, *J* = 8.5 Hz, 4H, **4e**), 5.81 (t, *J* = 8.0 Hz, 4H, **4e**), 4.27 (d, *J* = 7.5 Hz, 8H, **4e**), 2.23–2.00 (m, 72H, **1d**). Yield: quant.

*Physical Data of Inclusion Complex **1d•4g***

<sup>1</sup>H NMR (500 MHz, D<sub>2</sub>O, 300 K) δ: 8.89 (d, *J* = 8.0 Hz, 12H, **1d**), 8.63–8.58 (m, 24H, **1d**), 8.26 (s, 12H, **1d**), 8.00–7.95 (m, 24H, **1d**), 7.74 (d, *J* = 8.0 Hz, 12H, **1d**), 7.10–7.00 (m, 12H, **1d**), 6.82–6.81 (m, 24H, **1d**), 6.62 (t, *J* = 7.0 Hz, 4h, **4g**), 5.41 (t, *J* = 8.0 Hz, 4H, **4g**), 5.11 (d, *J* = 9.0 Hz, 4H, **4g**), 3.96 (d, *J* = 8.0 Hz, 4H, **4g**), 3.80 (d, *J* = 9.5 Hz, 4H, **4g**), 2.17–2.14 (m, 72H, **1d**). Yield: quant.

*Physical Data of Inclusion Complex **1d•4h***

<sup>1</sup>H NMR (500 MHz, D<sub>2</sub>O, 300 K) δ: 8.89 (br, 12, **1d**), 8.73–8.50 (m, 24H, **1d**), 8.26 (s, 12, **1d**), 8.05–7.90 (m, 24H, **1d**), 7.75–7.72 (m, 12H, **1d**), 6.86–6.60 (m, 36H, **1d**), 6.05 (t, *J* = 7.0 Hz, 4h, **4h**), 5.59 (t, *J* = 8.0 Hz, 4H, **4h**), 4.93 (d, *J* = 9.0 Hz, 4H, **4h**), 3.97 (d, *J* = 8.0 Hz, 4H, **4h**), 3.85 (d, *J* = 9.5 Hz, 4H, **4h**), 3.52 (s, 6H, **4h**), 2.31–1.78 (m, 72H, **1d**). Yield: 50%.

*Physical Data of Inclusion Complex **1e•4a***

<sup>1</sup>H NMR (500 MHz, D<sub>2</sub>O, 300 K) δ: 9.04 (d, *J* = 8.5 Hz, 12H, **1e**), 8.80 (d, *J* = 6.0 Hz, 24H, **1e**), 8.42 (s, 12H, **1e**), 8.14 (d, *J* = 6.5 Hz, 24H, **1e**), 7.83 (d, *J* = 8.5 Hz, 12H, **1e**), 6.87 (t, *J* = 7.3 Hz, 4H, **4a**), 6.68 (s, 24H, **1e**), 5.62 (t, *J* = 7.8 Hz, 4H, **4a**), 4.15 (d, *J* = 7.5 Hz, 8H, **4a**), 2.28 (s, 36H, Mes, **1e**), 2.24 (s, 72H, Mes, **1e**). Yield: 56%.

*Physical Data of Inclusion Complex **1e•4b***

<sup>1</sup>H NMR (500 MHz, D<sub>2</sub>O, 300 K) δ: 9.03 (d, *J* = 8.5 Hz, 12H, **1e**), 8.80 (d, *J* = 6.0 Hz, 24H, **1e**), 8.41 (s, 12H, **1e**), 8.08 (d, *J* = 6.5 Hz, 24H, **1e**), 7.83 (d, *J* = 8.5 Hz, 12H, **1e**), 7.22 (t, *J* = 7.3 Hz, 4H, **4b**), 6.67 (s, 24H, **1e**), 5.96 (t, *J* = 7.8 Hz, 8H, **4b**), 4.59 (d, *J* = 7.5 Hz, 8H, **4b**), 2.23 (s, 36H, Mes, **1e**), 2.22 (s, 72H, Mes, **1e**). Yield: 75%.

*Physical Data of Inclusion Complex **1e•4c***

<sup>1</sup>H NMR (500 MHz, D<sub>2</sub>O, 300 K) δ: 9.03 (d, *J* = 8.5 Hz, 12H, **1e**), 8.80 (d, *J* = 6.0 Hz, 24H, **1e**), 8.42 (s, 12H, **1e**), 8.07 (d, *J* = 6.5 Hz, 24H, **1e**), 7.84 (d, *J* = 8.5 Hz, 12H, **1e**), 7.23 (t, *J* = 7.3 Hz, 4H, **4c**), 6.68 (s, 24H, **1e**), 6.02 (t, *J* = 7.8 Hz, 8H, **4c**), 4.75 (d, *J* = 7.5 Hz, 8H, **4c**), 2.27 (s, 36H, Mes, **1e**), 2.25 (s, 72H, Mes, **1e**). Yield: 43%.

*Physical Data of Inclusion Complex **1e•4d***

<sup>1</sup>H NMR (500 MHz, D<sub>2</sub>O, 300 K) δ: 9.02 (d, *J* = 8.5 Hz, 12H, **1e**), 8.80 (d, *J* = 6.0 Hz, 24H, **1e**), 8.40 (s, 12H, **1e**), 8.04 (d, *J* = 6.5 Hz, 24H, **1e**), 7.82 (d, *J* = 8.5 Hz, 12H, **1e**), 7.29 (t, *J* = 7.3 Hz, 4H, **4d**), 6.67 (s, 24H, **1e**), 6.22 (t, *J* = 7.8 Hz, 8H, **4d**), 4.79 (d, *J* =

7.5 Hz, 8H, **4d**, overlapped with HDO), 2.26 (s, 36H, Mes, **1e**), 2.22 (s, 74h, Mes, **1e**).  
Yield: 38%.

*Physical Data of Inclusion Complex **1e•4e***

<sup>1</sup>H NMR (500 MHz, D<sub>2</sub>O, 300 K) δ: 9.02 (d, *J* = 8.5 Hz, 12H, **1e**), 8.74 (d, *J* = 6.0 Hz, 24H, **1e**), 8.39 (s, 12H, **1e**), 8.09 (d, *J* = 6.5 Hz, 24H, **1e**), 7.82 (d, *J* = 8.5 Hz, 12H, **1e**), 6.63 (s, 24H, **1e**), 6.40 (t, *J* = 7.3 Hz, 4H, **4e**), 5.19 (t, *J* = 7.8 Hz, 8H, **4e**), 4.40 (d, *J* = 7.5 Hz, 8H, **4e**), 2.24–2.21 (m, 108H, Mes, **1e**). Yield: quant.

*Physical Data of Inclusion Complex **1e•4g***

<sup>1</sup>H NMR (500 MHz, D<sub>2</sub>O, 300 K) δ: 9.04 (d, *J* = 8.0 Hz, 12H, **1e**), 8.82–8.78 (m, 24H, **1e**), 8.41 (s, 12H, **1e**), 8.14–8.13 (m, 24H, **1e**), 7.85 (d, *J* = 8.0 Hz, 12H, **1e**), 6.86 (t, *J* = 7.5 Hz, 4h, **4g**), 6.68 (d, *J* = 8.0 Hz, 12H, **1e**), 5.66 (t, *J* = 7.3 Hz, 4H, **4g**), 5.10 (d, *J* = 9.0 Hz, 4H, **4g**), 4.12 (d, *J* = 7.0 Hz, 4H, **4g**), 3.97 (d, *J* = 9.0 Hz, 4H, **4g**), 2.25–2.22 (m, 108H, Mes, **1e**). Yield: quant.

*Physical Data of Inclusion Complex **1e•4h***

<sup>1</sup>H NMR (500 MHz, D<sub>2</sub>O, 300 K) δ: 9.02 (t, *J* = 8.0 Hz, 12H, **1e**), 8.84–8.80 (m, 24H, **1e**), 8.40–8.39 (m, 12H, **1e**), 8.12–8.11 (m, 24H, **1e**), 7.84–7.81 (m, *J* = 8.0 Hz, 12H, **1e**), 6.93 (t, *J* = 7.5 Hz, 4h, **4h**), 6.60–6.62 (m, *J* = 8.0 Hz, 24H, **1e**), 5.73 (t, *J* = 7.3 Hz, 4H, **4h**), 5.20 (d, *J* = 9.0 Hz, 4H, **4h**), 4.13 (d, *J* = 7.0 Hz, 4H, **4h**), 4.06 (d, *J* = 9.0 Hz, 4H, **4h**), 3.78 (s, 6H, **4h**), 2.30–2.20 (m, 108H, Mes, **1e**). Yield: 51%.

## NMR spectrum for inclusion complex 1•4

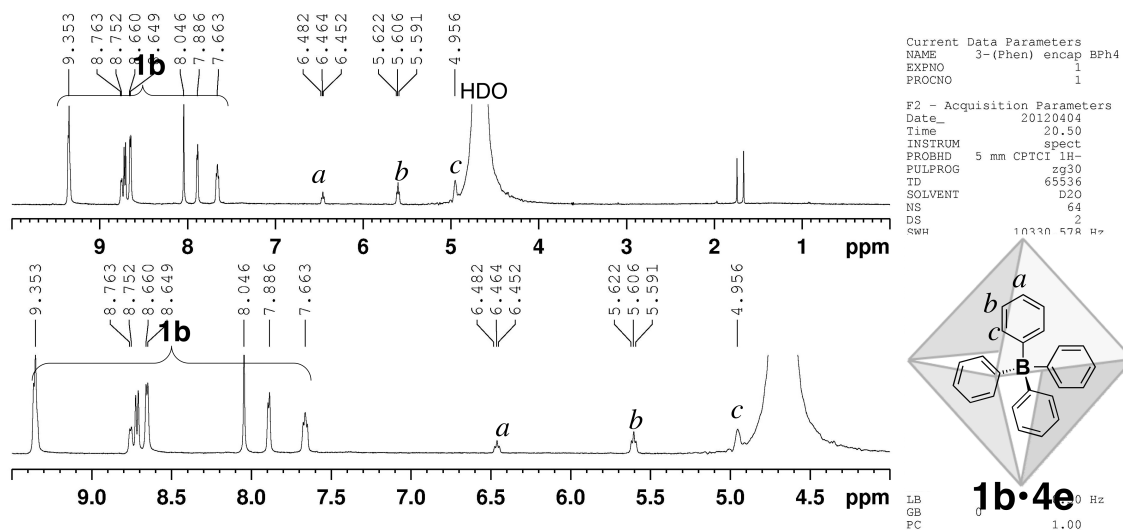


Figure S1.  $^1\text{H}$  NMR spectrum (500 MHz,  $\text{D}_2\text{O}$ , 300 K) of inclusion complex  $1\mathbf{b}\cdot 4\mathbf{e}$ .

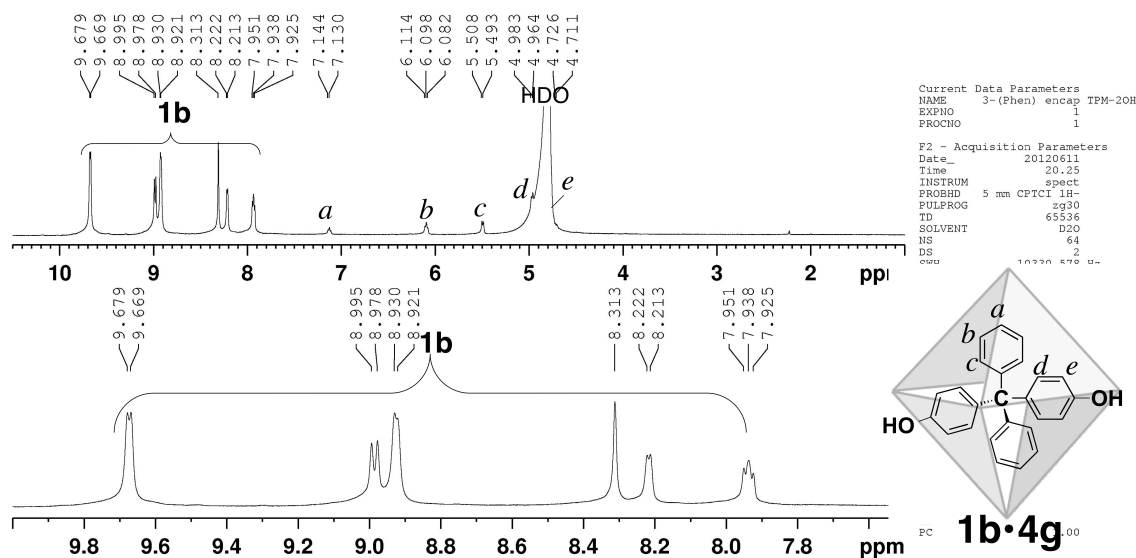


Figure S2.  $^1\text{H}$  NMR spectrum (500 MHz,  $\text{D}_2\text{O}$ , 300 K) of inclusion complex  $1\mathbf{b}\cdot 4\mathbf{g}$ .

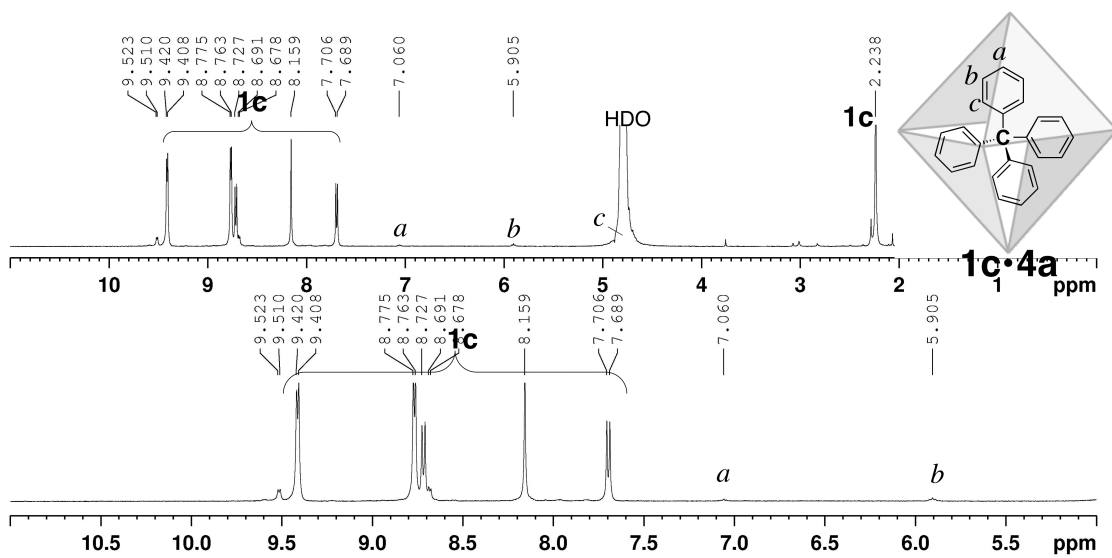


Figure S3.  $^1\text{H}$  NMR spectrum (500 MHz,  $\text{D}_2\text{O}$ , 300 K) of inclusion complex  $1\text{c}\cdot 4\text{a}$ .

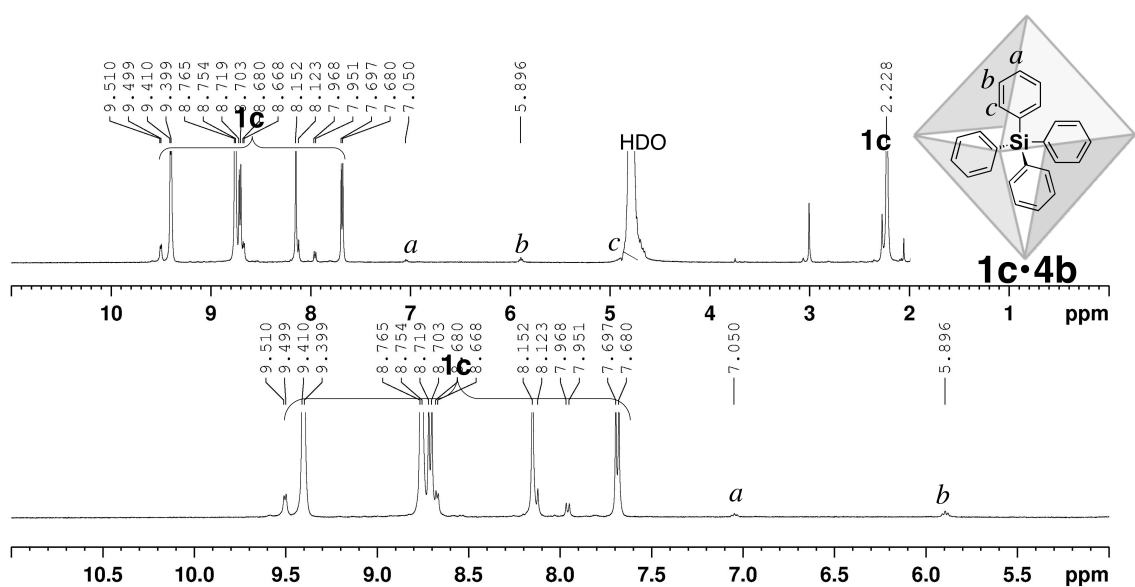


Figure S4.  $^1\text{H}$  NMR spectrum (500 MHz,  $\text{D}_2\text{O}$ , 300 K) of inclusion complex  $1\text{c}\cdot 4\text{b}$ .



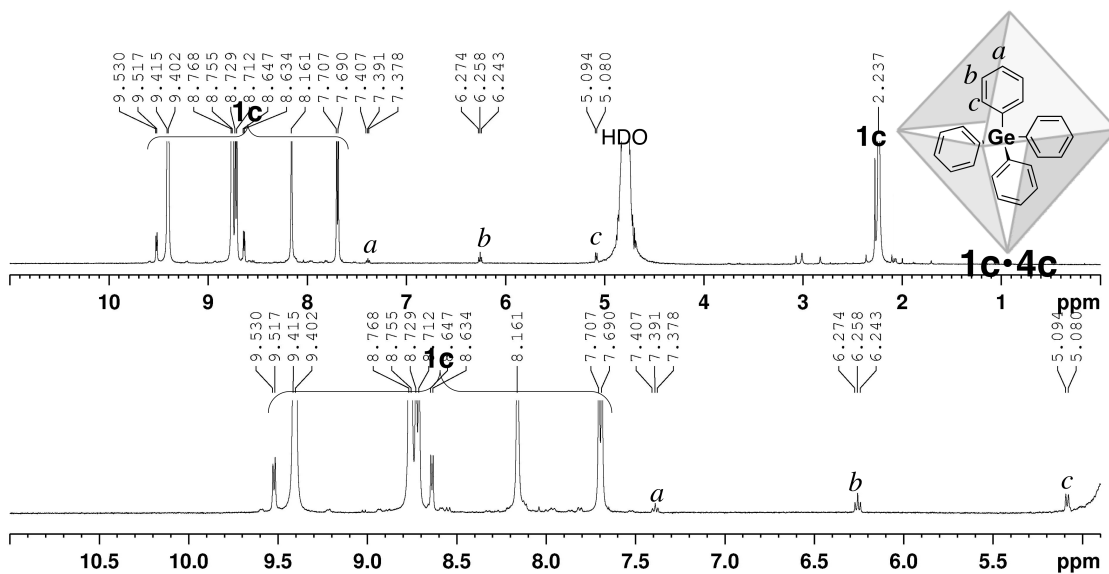


Figure S5.  $^1\text{H}$  NMR spectrum (500 MHz,  $\text{D}_2\text{O}$ , 300 K) of inclusion complex  $1\text{c}\cdot 4\text{c}$ .

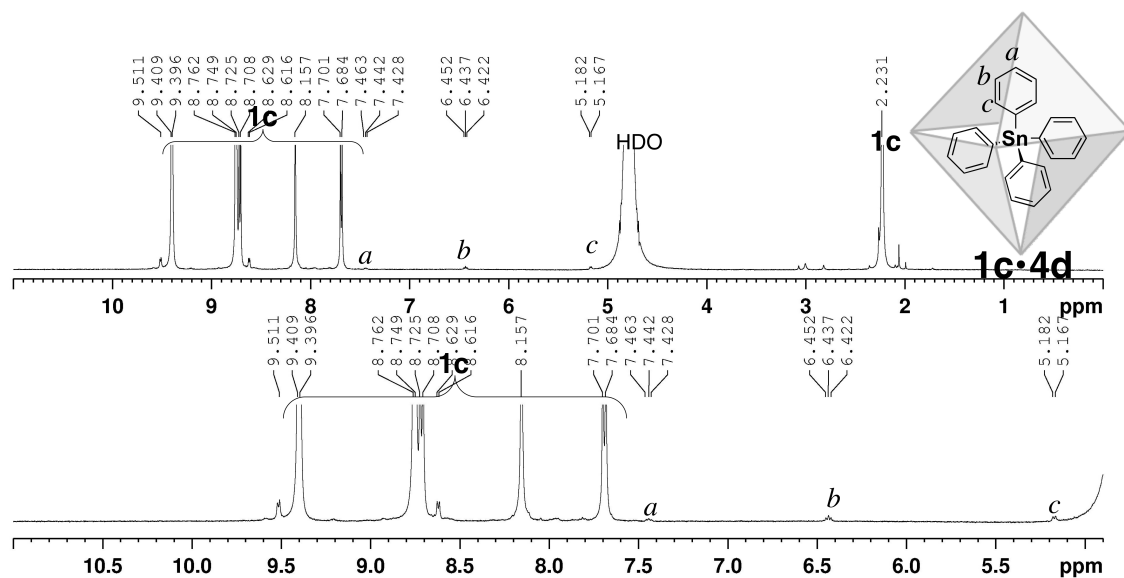


Figure S6.  $^1\text{H}$  NMR spectrum (500 MHz,  $\text{D}_2\text{O}$ , 300 K) of inclusion complex  $1\text{c}\cdot 4\text{d}$ .

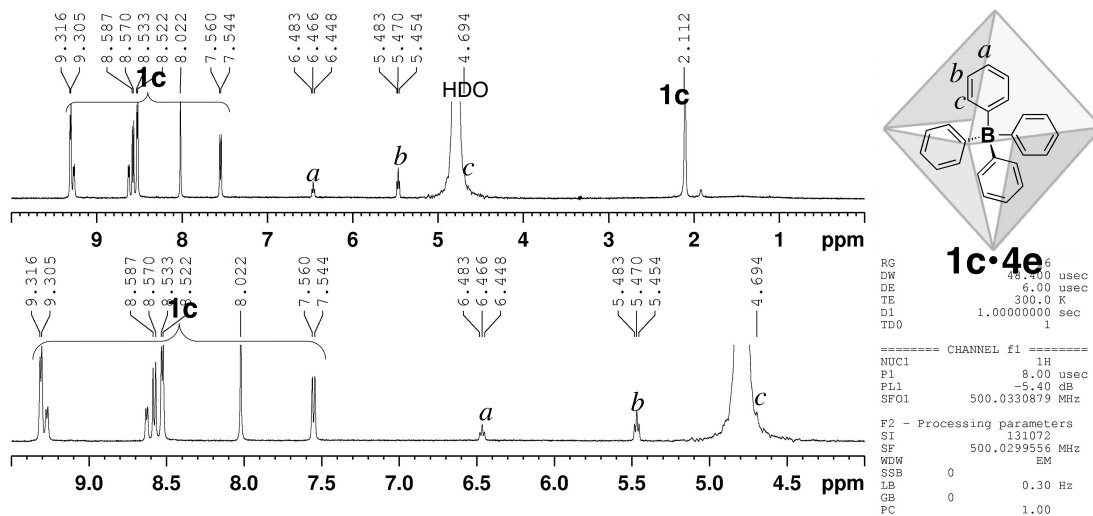


Figure S7.  $^1\text{H}$  NMR spectrum (500 MHz,  $\text{D}_2\text{O}$ , 300 K) of inclusion complex  $1\text{c}\cdot 4\text{e}$ .

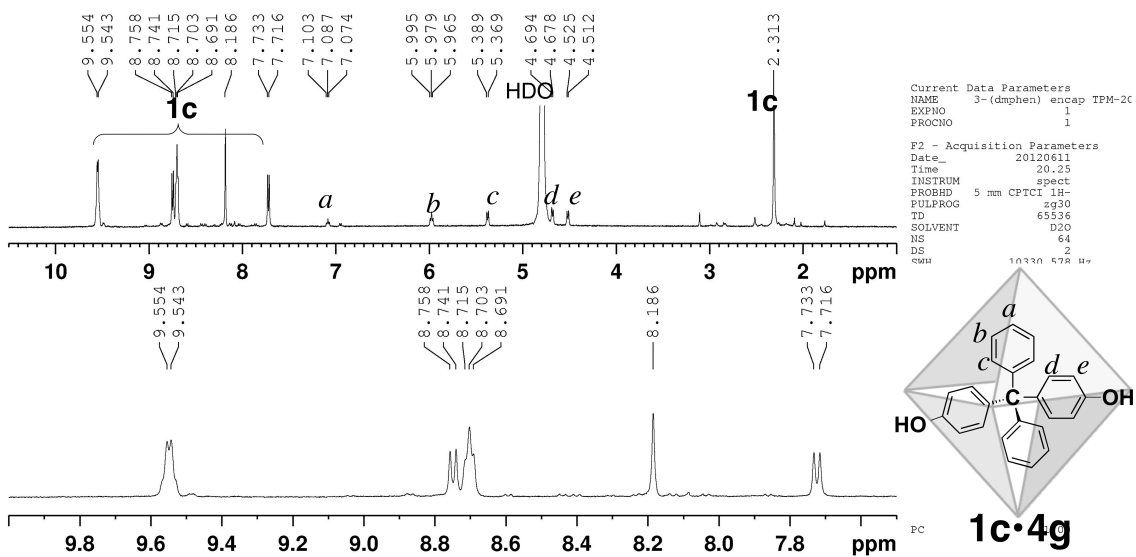


Figure S8.  $^1\text{H}$  NMR spectrum (500 MHz,  $\text{D}_2\text{O}$ , 300 K) of inclusion complex  $1\text{c}\cdot 4\text{g}$ .

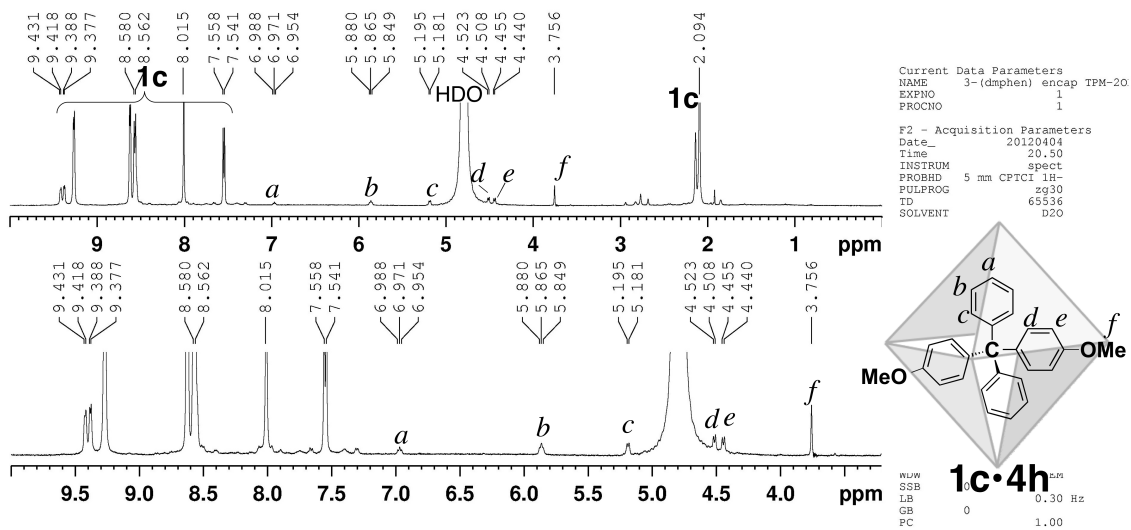


Figure S9.  $^1\text{H}$  NMR spectrum (500 MHz,  $\text{D}_2\text{O}$ , 300 K) of inclusion complex  $1\text{c}\cdot 4\text{h}$ .

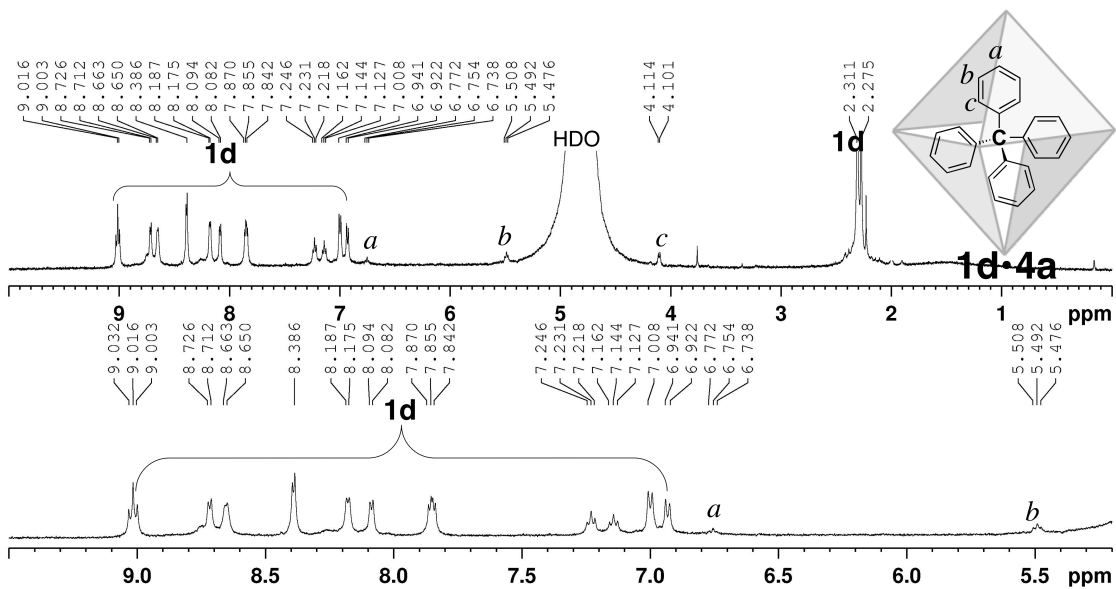


Figure S10.  $^1\text{H}$  NMR spectrum (500 MHz,  $\text{D}_2\text{O}$ , 300 K) of inclusion complex  $1\text{d}\cdot 4\text{a}$ .

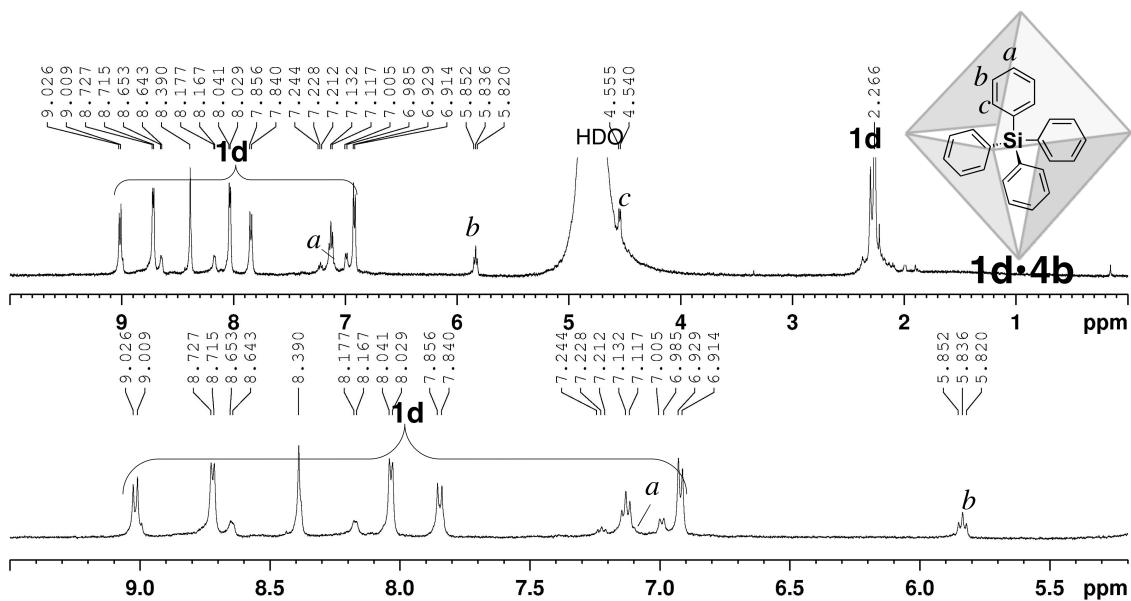


Figure S11.  $^1\text{H}$  NMR spectrum (500 MHz,  $\text{D}_2\text{O}$ , 300 K) of inclusion complex  $1\text{d}\cdot 4\text{b}$ .

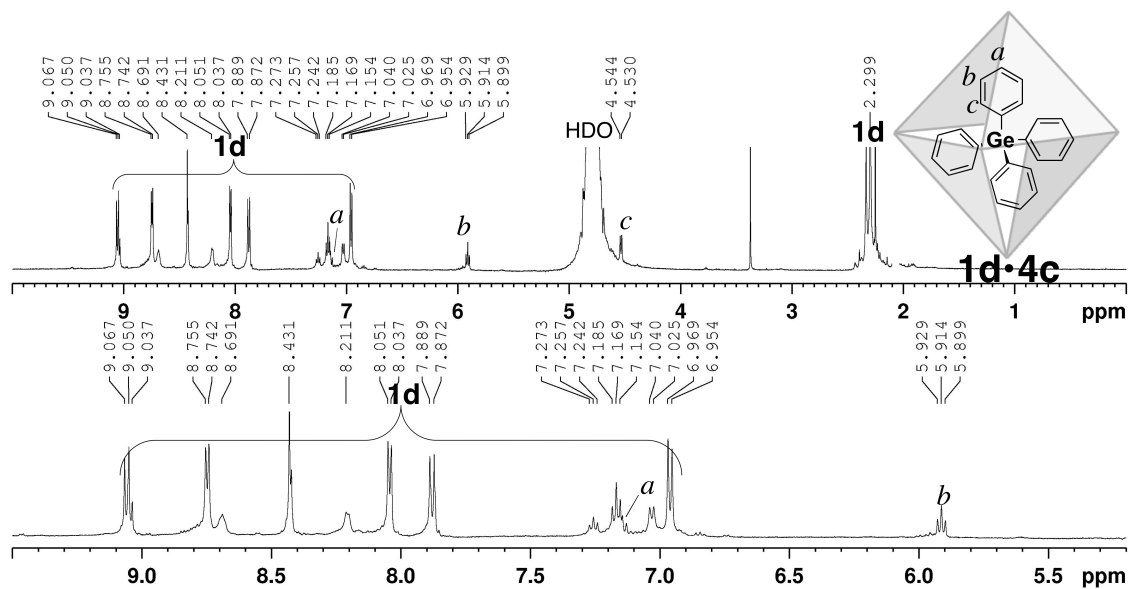


Figure S12.  $^1\text{H}$  NMR spectrum (500 MHz,  $\text{D}_2\text{O}$ , 300 K) of inclusion complex  $1\text{d}\cdot 4\text{c}$ .

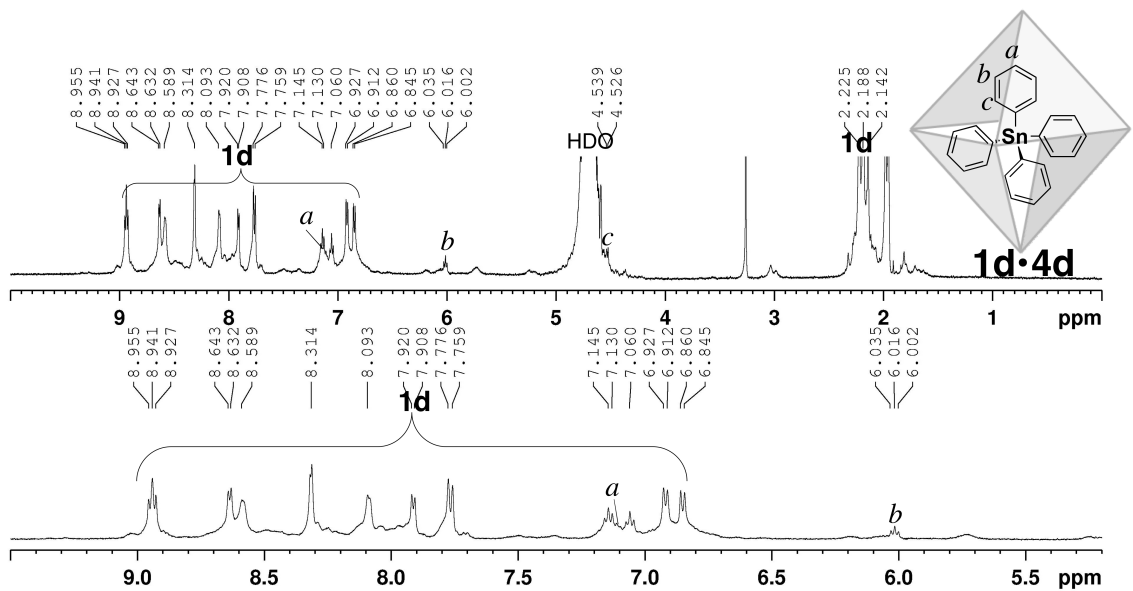


Figure S13.  $^1\text{H}$  NMR spectrum (500 MHz,  $\text{D}_2\text{O}$ , 300 K) of inclusion complex  $1\text{d}\cdot 4\text{d}$ .

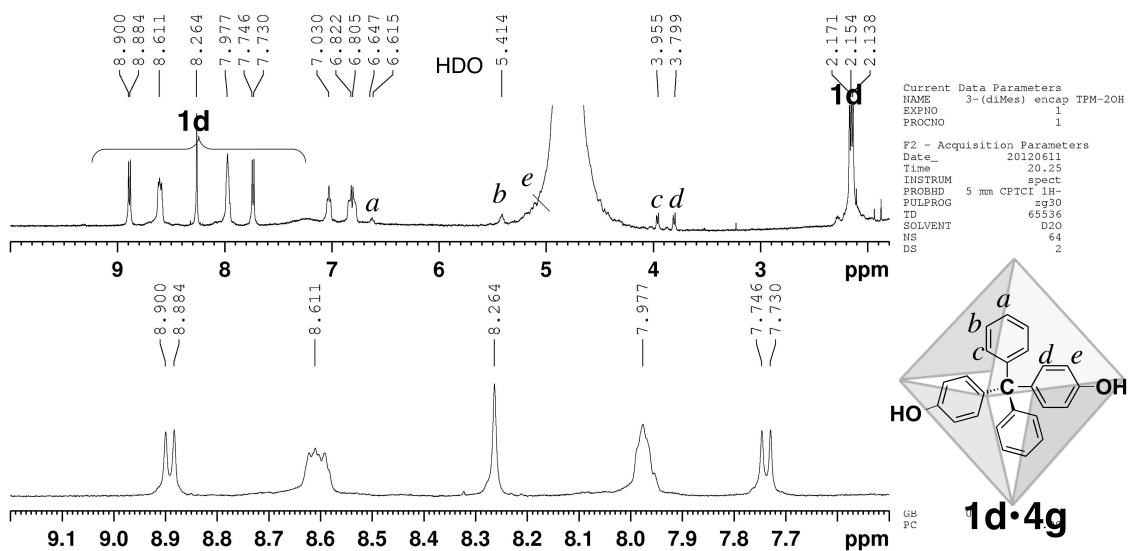


Figure S14.  $^1\text{H}$  NMR spectrum (500 MHz,  $\text{D}_2\text{O}$ , 300 K) of inclusion complex  $1\text{d}\cdot 4\text{g}$ .

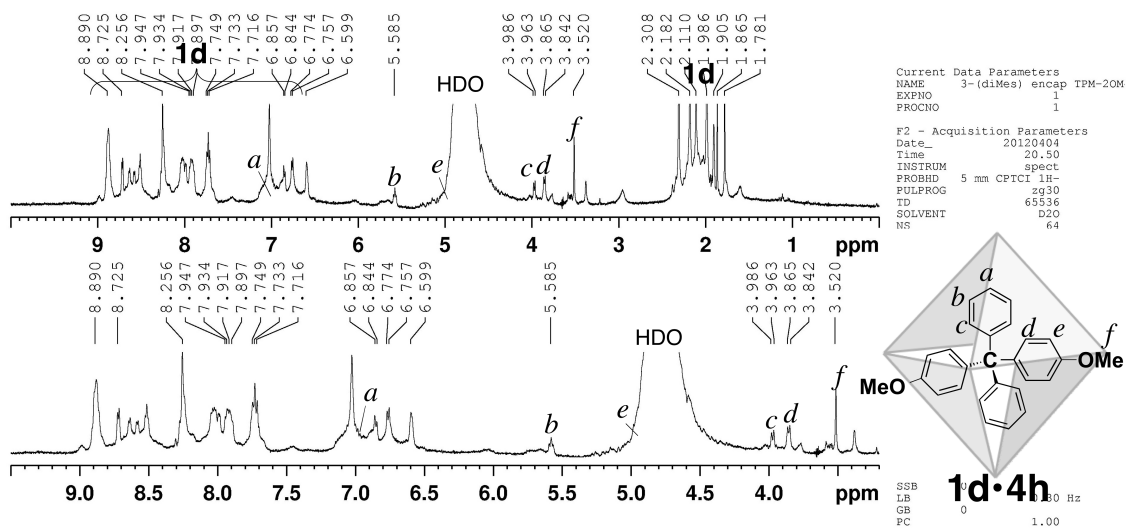


Figure S15.  $^1\text{H}$  NMR spectrum (500 MHz,  $\text{D}_2\text{O}$ , 300 K) of inclusion complex **1d•4h**.

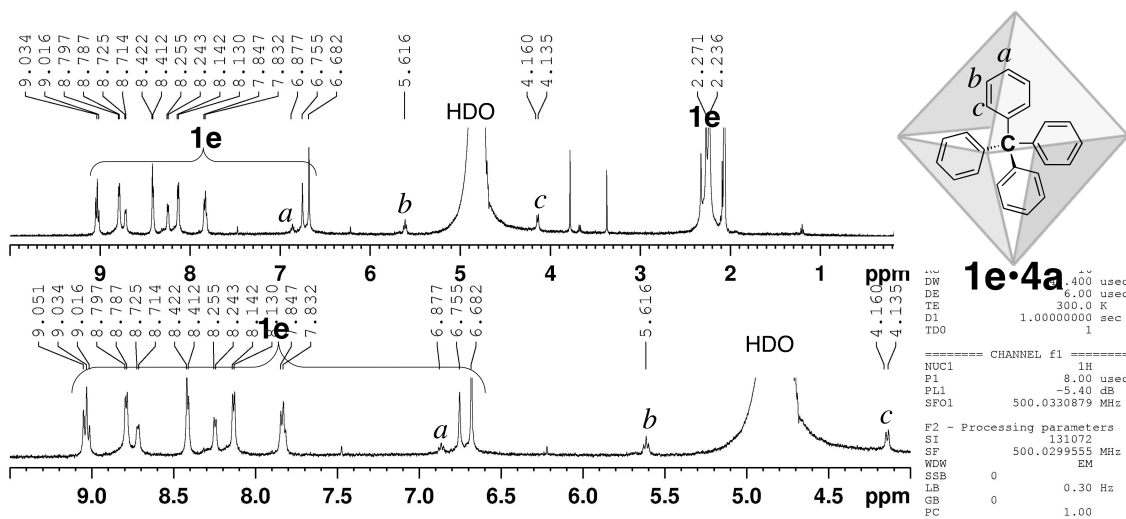


Figure S16.  $^1\text{H}$  NMR spectrum (500 MHz,  $\text{D}_2\text{O}$ , 300 K) of inclusion complex **1e•4a**.

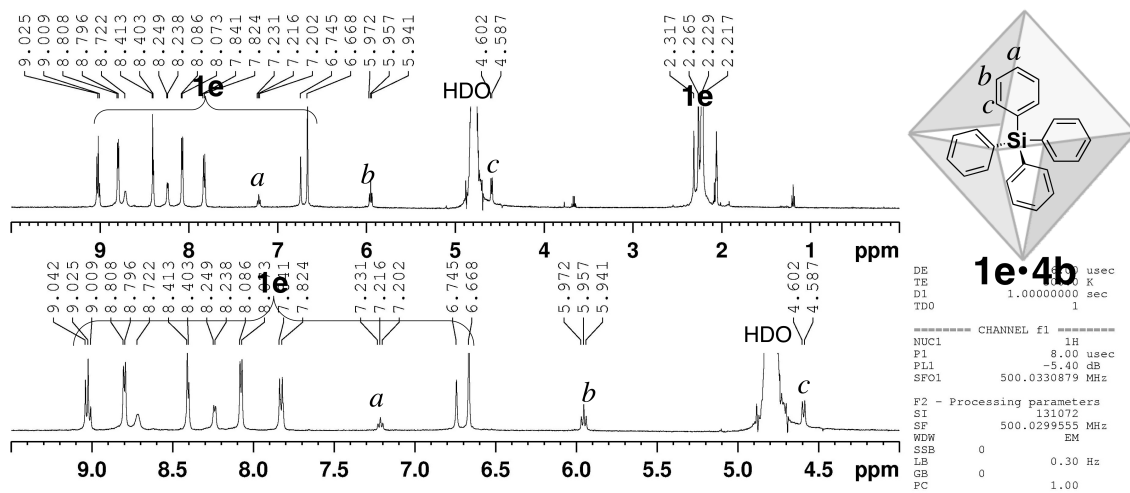


Figure S17.  $^1\text{H}$  NMR spectrum (500 MHz,  $\text{D}_2\text{O}$ , 300 K) of inclusion complex  $1\text{e}\cdot 4\text{b}$ .

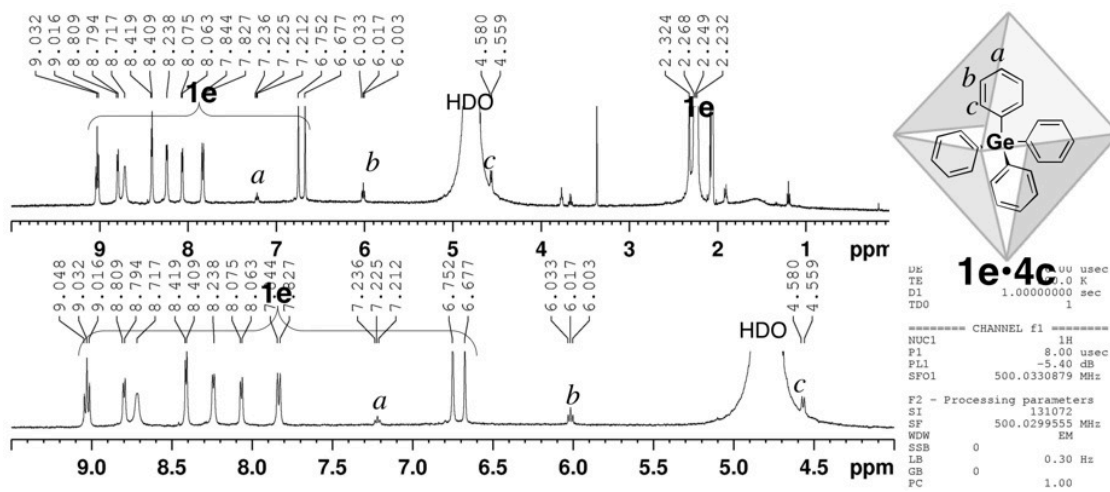


Figure S18.  $^1\text{H}$  NMR spectrum (500 MHz,  $\text{D}_2\text{O}$ , 300 K) of inclusion complex  $1\text{e}\cdot 4\text{c}$ .

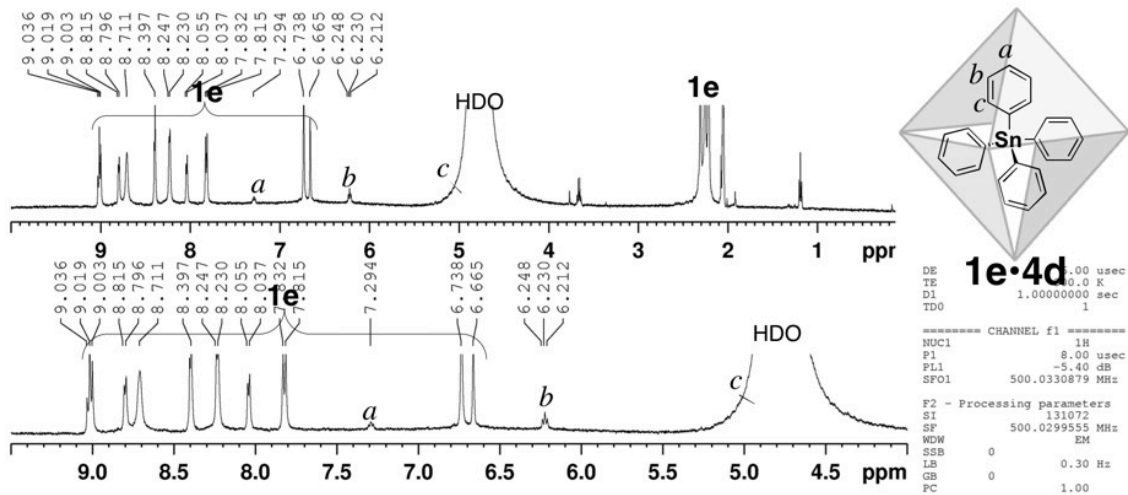


Figure S19.  $^1\text{H}$  NMR spectrum (500 MHz,  $\text{D}_2\text{O}$ , 300 K) of inclusion complex  $1\text{e}\cdot 4\text{d}$ .

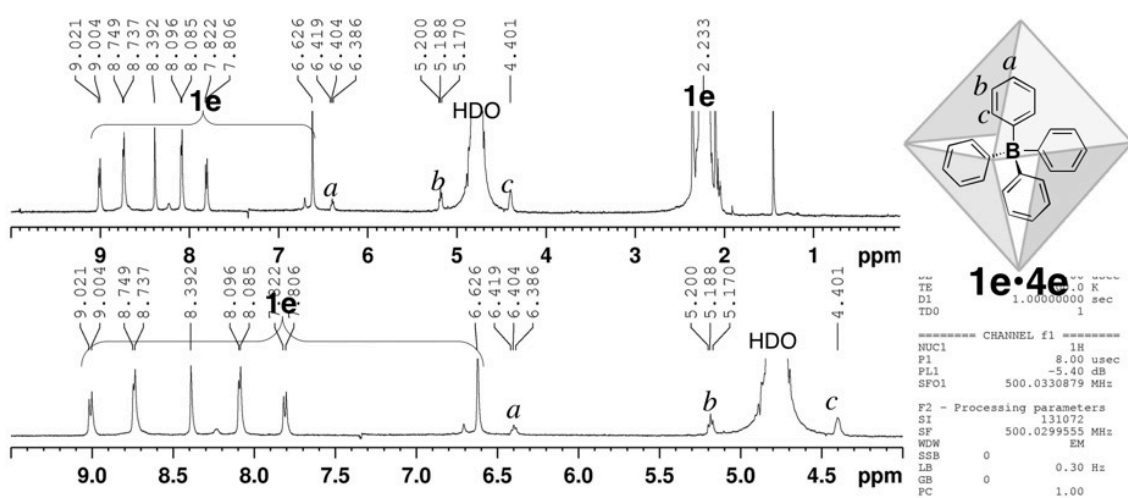


Figure S20.  $^1\text{H}$  NMR spectrum (500 MHz,  $\text{D}_2\text{O}$ , 300 K) of inclusion complex  $1\text{e}\cdot 4\text{e}$ .



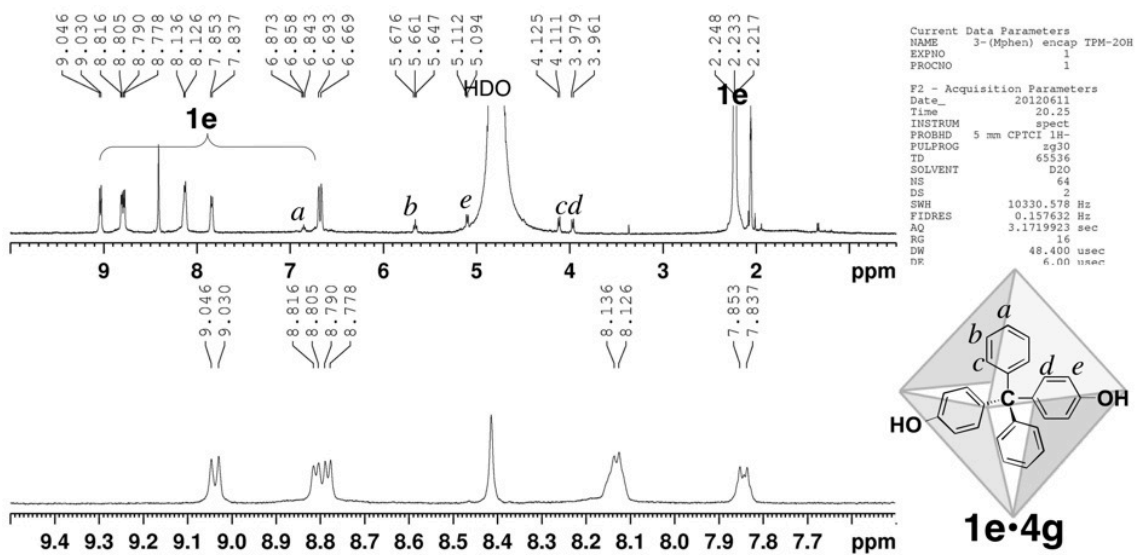


Figure S21. <sup>1</sup>H NMR spectrum (500 MHz, D<sub>2</sub>O, 300 K) of inclusion complex 1e•4g.

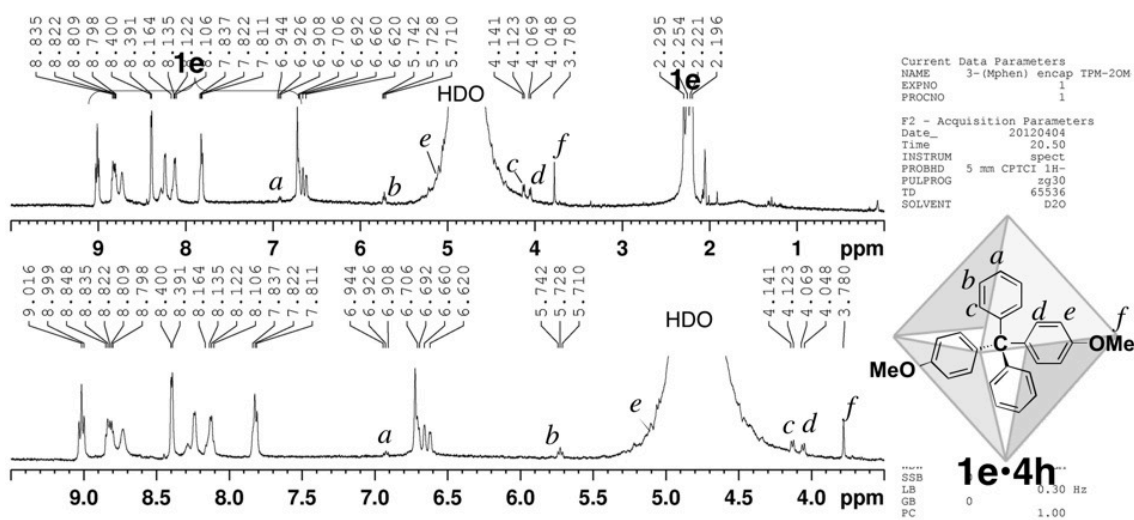


Figure S22.  $^1\text{H}$  NMR spectrum (500 MHz,  $\text{D}_2\text{O}$ , 300 K) of inclusion complex **1e•4h**.

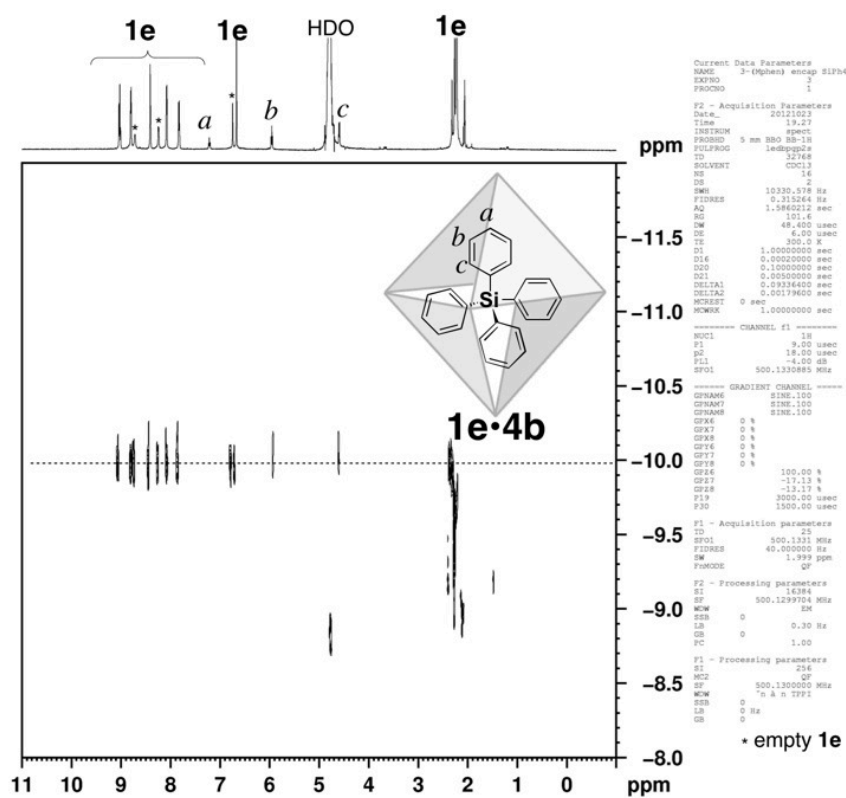


Figure S23. DOSY spectrum (500 MHz,  $\text{D}_2\text{O}$ , 300 K) of inclusion complex **1e•4b**.

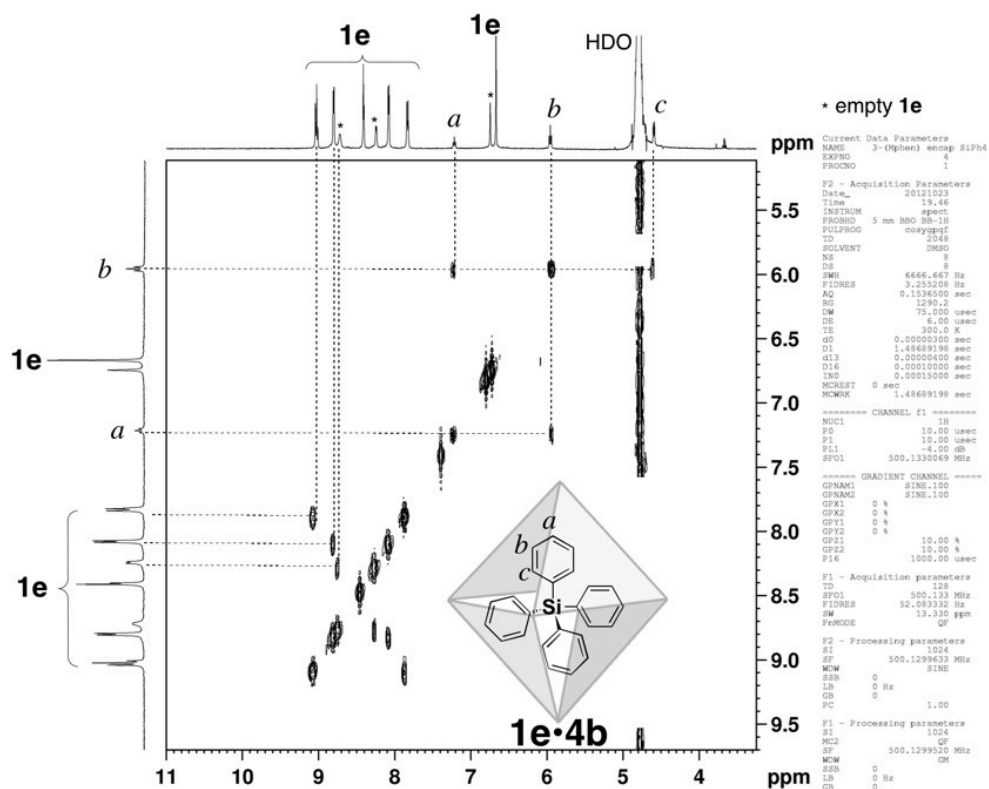


Figure S24.  $^1\text{H}$ - $^1\text{H}$  COSY spectrum (500 MHz,  $\text{D}_2\text{O}$ , 300 K) of inclusion complex  $1\text{e}\cdot 4\text{b}$ .

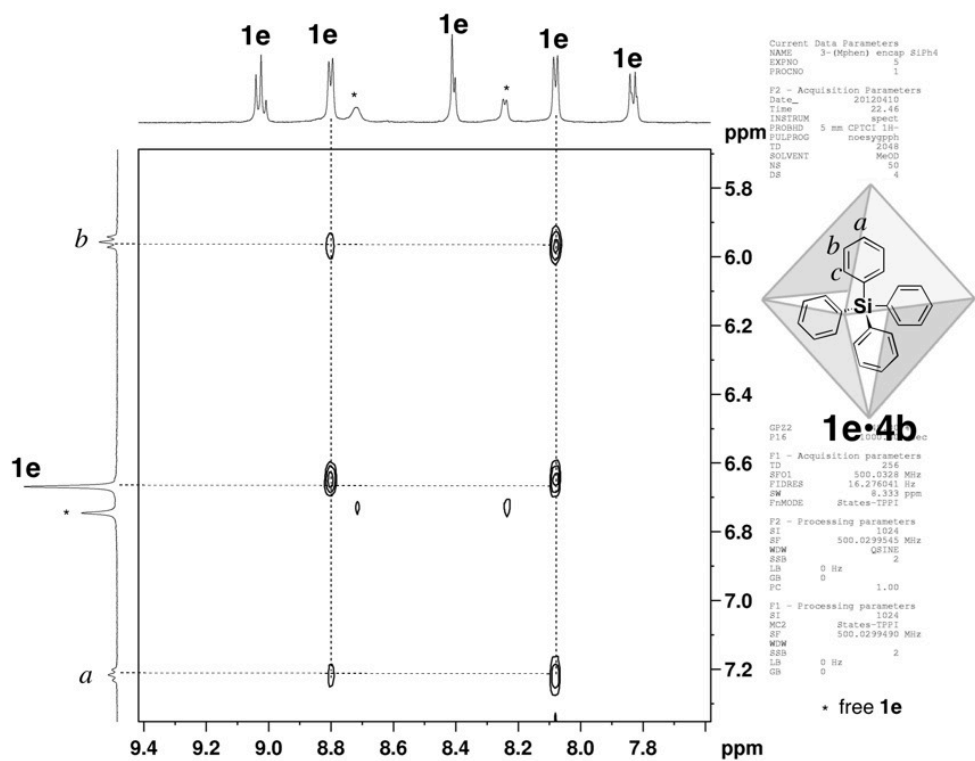


Figure S25.  $^1\text{H}$ - $^1\text{H}$  NOESY spectrum (500 MHz,  $\text{D}_2\text{O}$ , 300 K) of inclusion complex  $1\text{e}\cdot 4\text{b}$ .

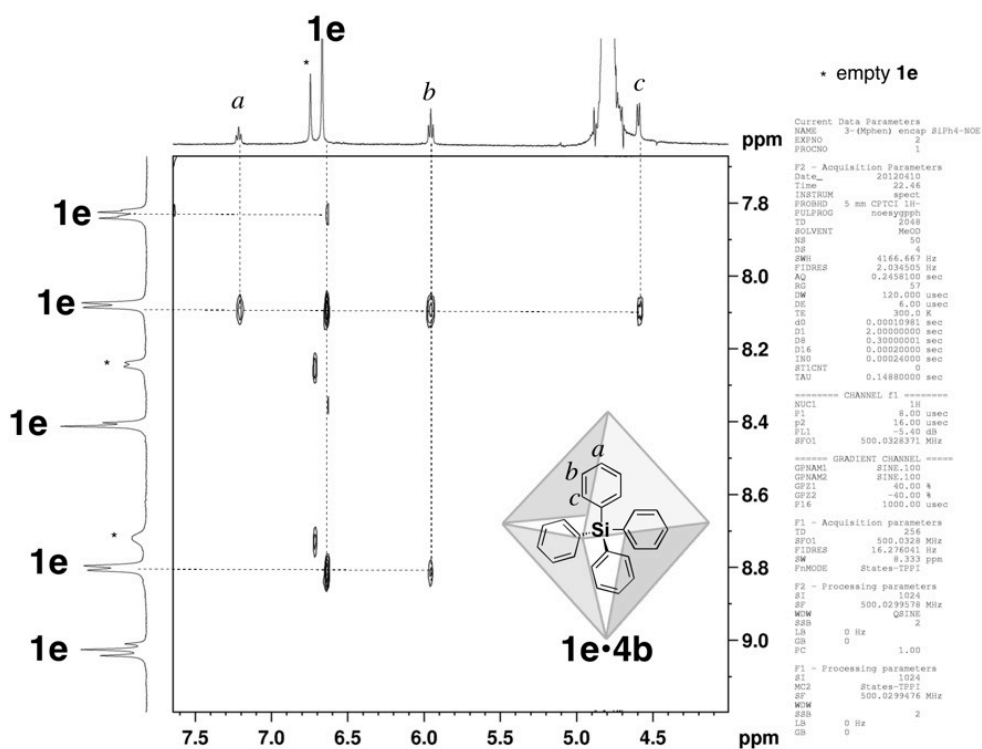
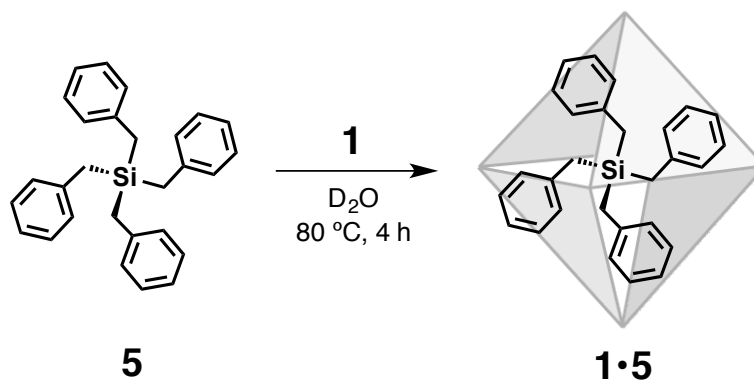


Figure S26.  $^1\text{H}$ - $^1\text{H}$  NOESY spectrum (500 MHz,  $\text{D}_2\text{O}$ , 300 K) of inclusion complex  $1\text{e}\cdot 4\text{b}$ .

### General Procedure for Encapsulation of Guests **5** into Cages **1**



When an excess amount of **5** (10 eq. for cage **1**) was suspended in a  $\text{D}_2\text{O}$  solution (0.5 mL) of cages **1** ( $0.5\text{ }\mu\text{mol}$ ; 1 mM) and the resulting solution was stirred at  $80\text{ }^\circ\text{C}$  for 4 h, the solution color turned from colorless to pale yellow. After removal of residual guest **5** by filtration,  $^1\text{H}$  NMR confirmed the formation of inclusion complexes **1•5** in different yields.

*Physical Data of Inclusion Complex 1b•5*

<sup>1</sup>H NMR (500 MHz, D<sub>2</sub>O, 300 K) δ: 9.71 (d, *J* = 6.5 Hz, 24H, **1b**), 9.00–8.97 (d, 12h, **1b**), 8.92 (d, *J* = 6.5 Hz, 24H, **1b**), 8.05 (s, 12h, **1b**), 8.19 (d, *J* = 5.0 Hz, 12h, **1b**), 7.92 (dd, *J* = 8.5 Hz, 12h, **1b**), 7.09 (t, *J* = 7.3 Hz, 4H, **5**), 6.60 (t, *J* = 7.8 Hz, 8H, **5**), 4.79 (d, 8H, overlapped by HDO, **5**), 0.03 (s, 8H, **5**), Yield: 85%.

*Physical Data of Inclusion Complex 1c•5*

<sup>1</sup>H NMR (500 MHz, D<sub>2</sub>O, 300 K) δ: 9.54 (d, *J* = 6.5 Hz, 24H, **1c**), 8.76–8.67 (m, 36h, **1c**), 8.15 (s, 12h, **1c**), 7.69 (d, *J* = 5.0 Hz, 12h, **1c**), 7.09 (t, *J* = 7.3 Hz, 4H, **5**), 6.63 (t, *J* = 7.8 Hz, 8H, **5**), 4.61 (d, 8H, *J* = 7.8 Hz, **5**), 2.25 (s, 24H, **1c**), 0.38 (s, 8H, **5**), Yield: 90%.

*Physical Data of Inclusion Complex 1d•5*

<sup>1</sup>H NMR (500 MHz, D<sub>2</sub>O, 300 K) δ: 9.02 (d, *J* = 8.0 Hz, 12H, **1d**), 8.73 (d, *J* = 5.5 Hz, 24h, **1d**), 8.38 (s, 12H, **1d**), 8.04 (d, *J* = 5.5 Hz, 24h, **1d**), 7.85 (d, *J* = 8.5 Hz, 12h, **1d**), 7.16 (t, *J* = 7.5 Hz, 12H, **1d**), 7.05 (t, *J* = 7.3 Hz, 4H, **5**), 6.95 (d, *J* = 8.0 Hz, 24H, **1d**), 6.57 (t, *J* = 7.8 Hz, 8H, **5**), 4.33 (d, *J* = 7.5 Hz, 8H, **5**), 2.27 (s, 72H, **1d**), -1.12 (s, 12H, **5**), Yield: quant.

*Physical Data of Inclusion Complex 1e•5*

<sup>1</sup>H NMR (500 MHz, D<sub>2</sub>O, 300 K) δ: 9.04 (d, *J* = 8.0 Hz, 12H, **1e**), 8.84 (d, *J* = 5.5 Hz, 24h, **1e**), 8.42 (s, 12H, **1e**), 8.08 (d, *J* = 5.5 Hz, 24h, **1e**), 7.85 (d, *J* = 8.5 Hz, 12h, **1e**), 7.14 (t, *J* = 7.3 Hz, 4H, **5**), 6.71 (s, 24H, **1e**), 6.65 (t, *J* = 7.8 Hz, 8H, **5**), 4.33 (d, *J* = 7.5 Hz, 8H, **5**), 2.26–2.24 (m, 108H, **1e**), -1.04 (s, 12H, **5**), Yield: quant.

### NMR spectrum for inclusion complex **1•5**

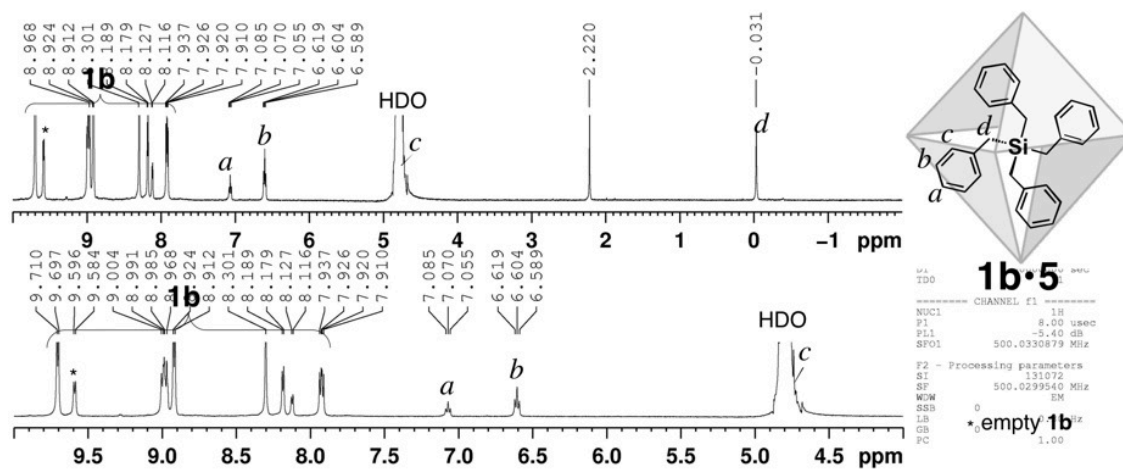


Figure S27. <sup>1</sup>H NMR spectrum (500 MHz, D<sub>2</sub>O, 300 K) of inclusion complex **1b•5**.

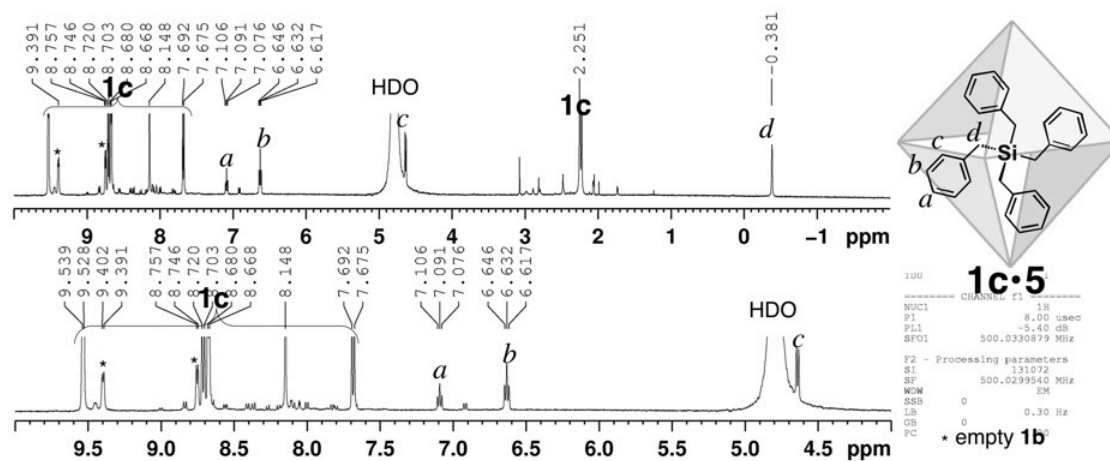


Figure S28. <sup>1</sup>H NMR spectrum (500 MHz, D<sub>2</sub>O, 300 K) of inclusion complex **1c•5**.

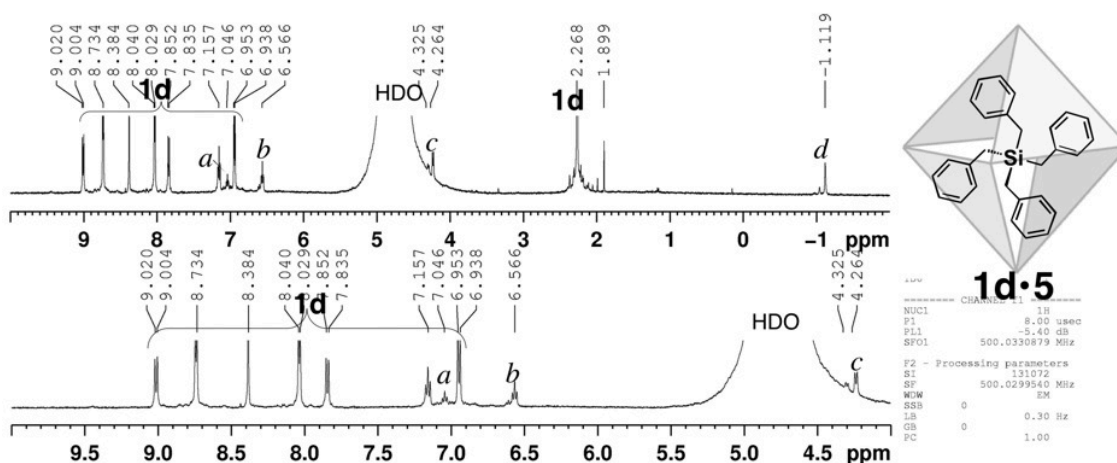


Figure S29.  $^1\text{H}$  NMR spectrum (500 MHz,  $\text{D}_2\text{O}$ , 300 K) of inclusion complex  $1\text{d}\cdot 5$ .

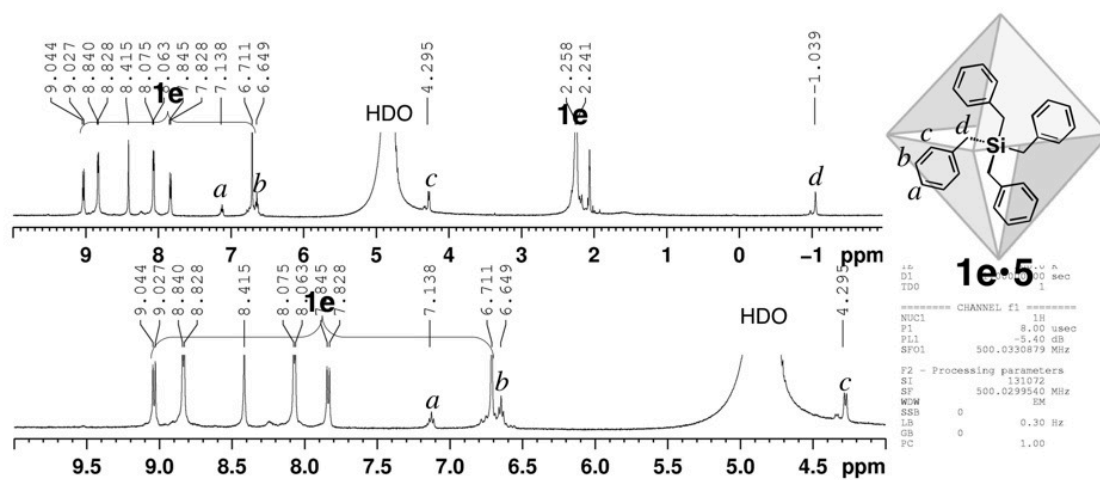
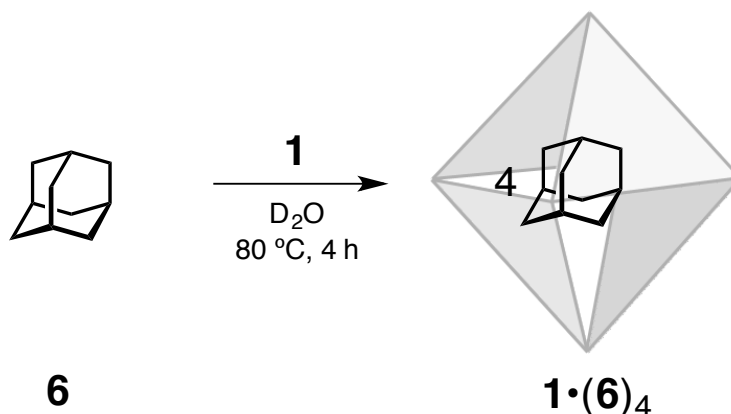


Figure S30.  $^1\text{H}$  NMR spectrum (500 MHz,  $\text{D}_2\text{O}$ , 300 K) of inclusion complex  $1\text{e}\cdot 5$ .

## General Procedure for Encapsulation of Guests **6** into Cages **1**



When an excess amount of adamantane (**6**; 10 eq. for cage **1**) was suspended in a  $D_2O$  solution (0.5 mL) of cage **1** (0.5  $\mu\text{mol}$ ; 1 mM) and the resulting solution was stirred at  $80\text{ }^\circ\text{C}$  for 4 h, the solution color turned from colorless to pale yellow. After removal of residual guest **6** by filtration,  $^1\text{H}$  NMR confirmed the formation of inclusion complex **1a•(6)<sub>4</sub>**, **1b•(6)<sub>4</sub>** and **1c•(6)<sub>4</sub>** in different yield. No encapsulation was observed for cage **1d** or **1e**.

### *Physical Data of Inclusion Complex **1a•(6)<sub>4</sub>***

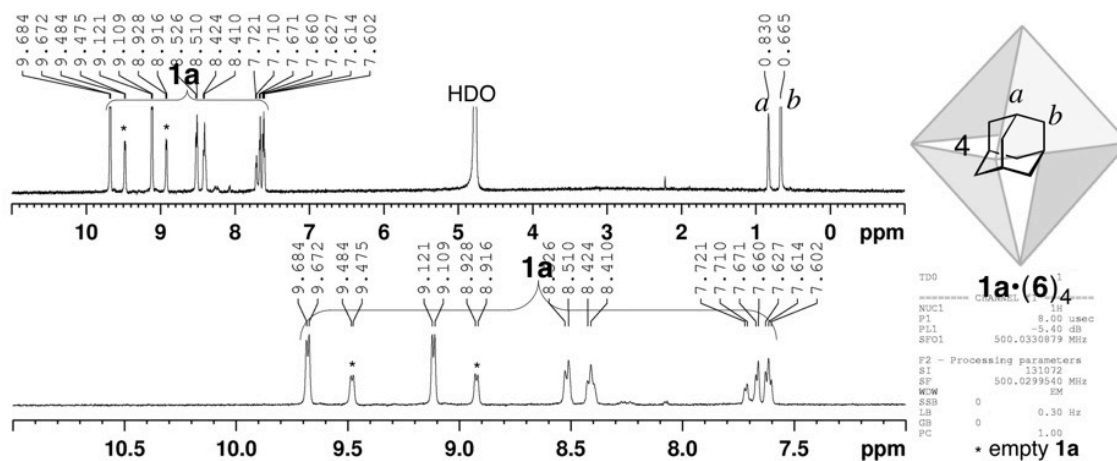
$^1\text{H}$  NMR (500 MHz,  $D_2O$ , 300 K)  $\delta$ : 9.68 (d,  $J = 6.0$  Hz, 24H, **1a**), 9.11 (d,  $J = 6.0$  Hz, 24H, **1a**), 8.53–8.41 (m, 24h, **1a**), 7.72–7.60 (m, 24h, **1a**), 0.83 (s, 16H, **6**), 0.67 (s, 48H, **6**). Yield: 59%.

### *Physical Data of Inclusion Complex **1b•(6)<sub>4</sub>***

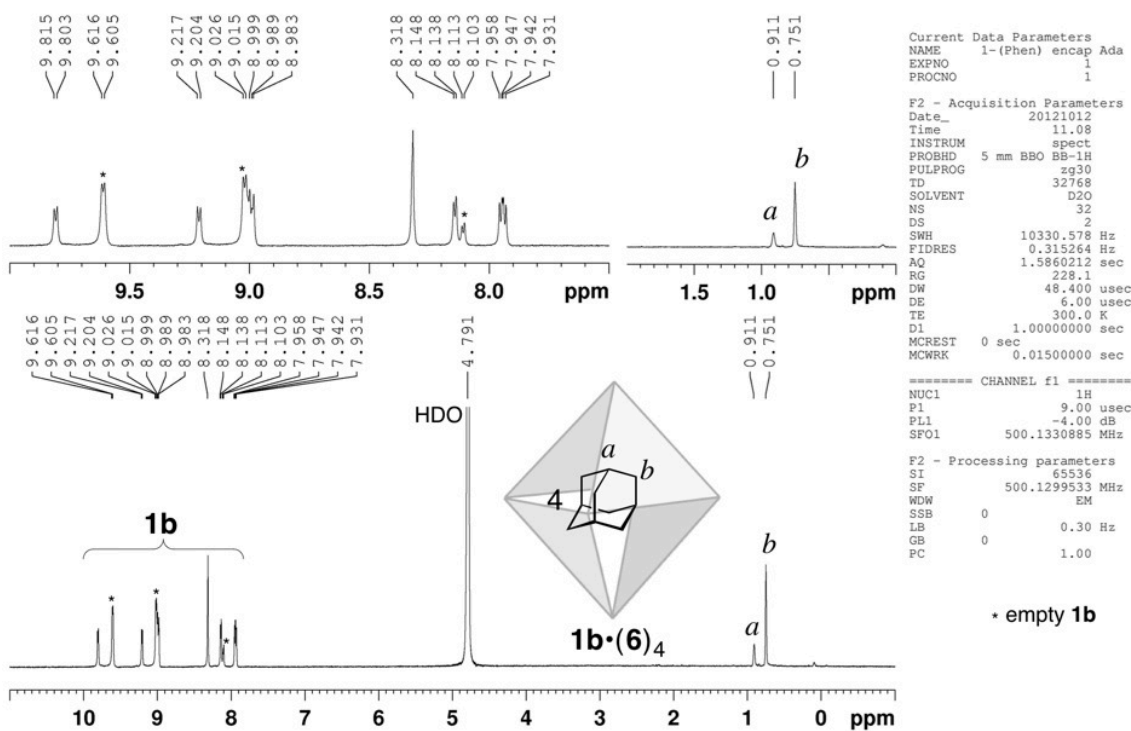
$^1\text{H}$  NMR (500 MHz,  $D_2O$ , 300 K)  $\delta$ : 9.81 (d,  $J = 6.0$  Hz, 24H, **1b**), 9.21 (d,  $J = 6.0$  Hz, 24H, **1b**), 8.99 (d,  $J = 8.0$  Hz, 14h, **1b**), 8.32 (s, 14h, **1a**), 8.14 (d,  $J = 5.0$  Hz, 14h, **1b**), 7.94 (d-d,  $J = 8.0$  Hz, 14h, **1b**), 0.91 (s, 16H, **6**), 0.75 (s, 48H, **6**). Yield: 59%.



**NMR spectrum for inclusion complex  $1\cdot(6)_4$**



**Figure S31.**  $^1\text{H}$  NMR spectrum (500 MHz,  $\text{D}_2\text{O}$ , 300 K) of inclusion complex  $1\mathbf{b}\cdot(6)_4$ .



**Figure S32.**  $^1\text{H}$  NMR spectrum (500 MHz,  $\text{D}_2\text{O}$ , 300 K) of inclusion complex  $1\mathbf{b}\cdot(6)_4$ .

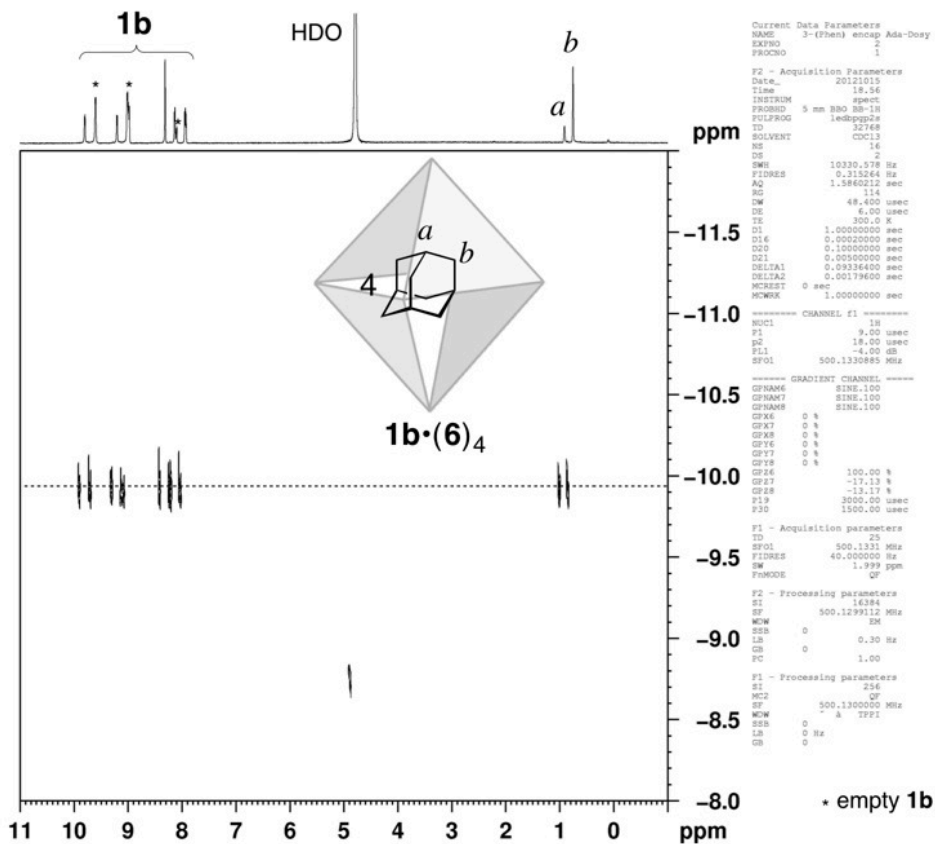


Figure S33. DOSY spectrum (500 MHz, D<sub>2</sub>O, 300 K) of inclusion complex **1b•(6)<sub>4</sub>**.

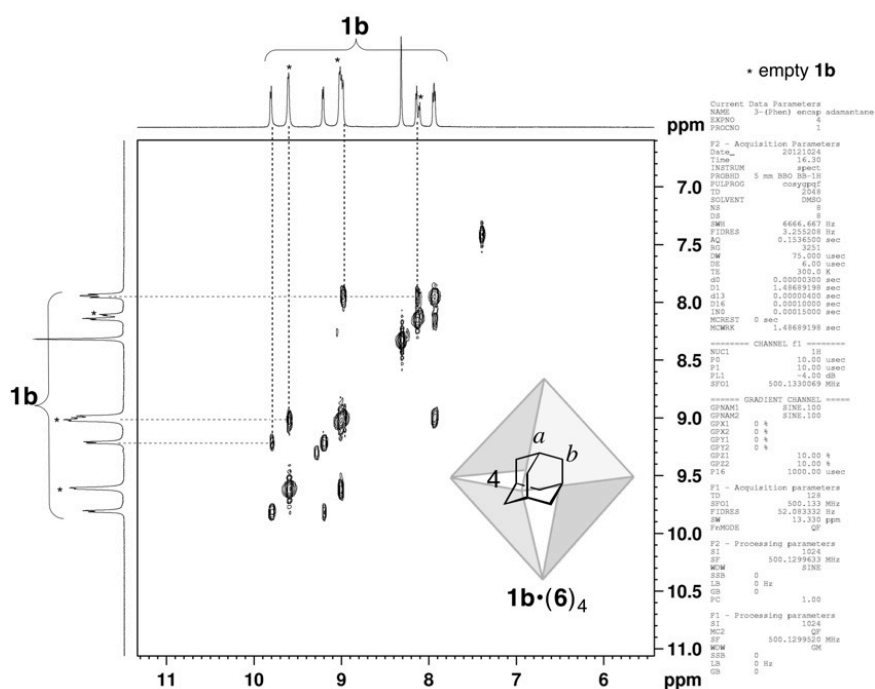


Figure S34. COSY spectrum (500 MHz, D<sub>2</sub>O, 300 K) of inclusion complex **1b•(6)<sub>4</sub>**.

### 3.6 REFERENCES

- [1] M. Yoshizawa, J. K. Klosterman, M. Fujita, *Angew. Chem., Int. Ed.* **2009**, *48*, 3418.
- [2] T. Kusukawa, M. Fujita, *Angew. Chem., Int. Ed.* **1998**, *37*, 3142.
- [3] T. Kusukawa, M. Yoshizawa, M. Fujita, *Angew. Chem., Int. Ed.* **2001**, *40*, 1879.
- [4] T. Kusukawa, M. Fujita, *J. Am. Chem. Soc.* **2002**, *124*, 13576.
- [5] S. Sakamoto, M. Yoshizawa, T. Kusukawa, M. Fujita, K. Yamaguchi, *Org. Lett.* **2001**, *3*(11), 1601.
- [6] Y. Fang, T. Murase, S. Sota, M. Fujita, *J. Am. Chem. Soc.* **2013**, *135*, 613.
- [7] Y. Fang, T. Murase, M. Fujita, *Chem. Asian J.* **2014**, *in press*, DOI: 10.1002/asia.201301642

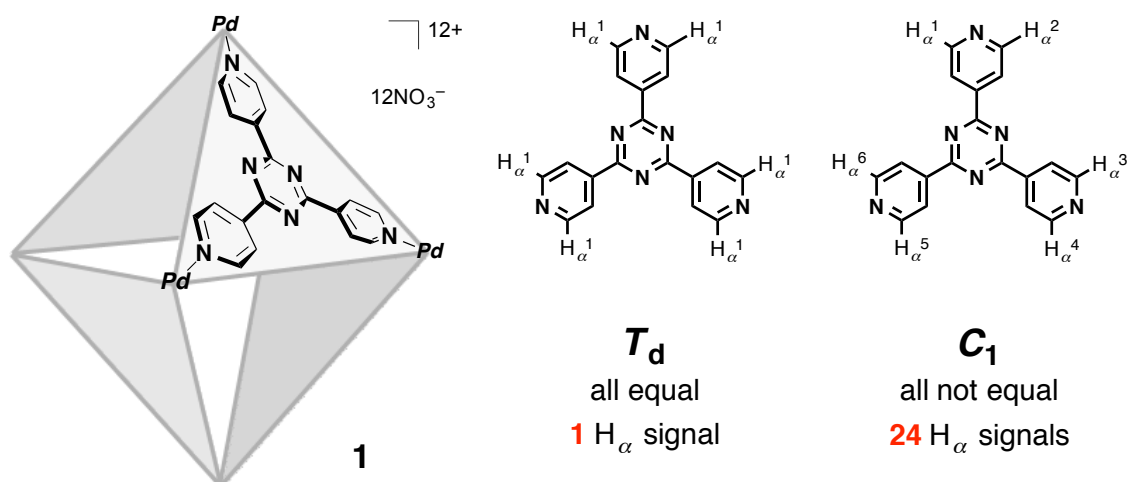
# Chapter 4

## Guest-motion in shrunken cavities

Besides guest-binding, guest mobility largely depends on the cavity volumes of hosts **1**. We employed several low symmetrical guest molecules to investigate guest motion with the cavities with or without modification. With increasing the bulkiness of the pendant groups, the cavity volumes of cages were expected shrunken stereo-wisely, thus the restraint of guest motion was gradually enhanced, probably due to the step-wisely decreasing of cavity volume enabling the host-guest tightly packing. Although not involved in the framework of the cage and not touch the guest, the *para*-methyl groups dictate guest motion and sufficiently freeze the guest motion at high temperature during NMR time scale.

## 4.1 Introduction

Conformational geometry and free motion of the enclathrated molecules are restricted within the confined interior space of hollow synthetic host.<sup>[1-3]</sup> Investigation of the inclusion geometry of guest molecules is of great importance because molecules in a specific geometry or aggregation are expected to show unique properties and reactivities which do not appear when they are in bulk solution. On the other hand, information on the geometry of guests can be read out by the spectroscopic analysis of host frameworks that provide the host and the guest communicating with each other through specific host-guest interactions. Several reports have dealt with the conformational analysis of guests by the observation of host frameworks.<sup>[4-12]</sup> However, the observed spectra of the hosts are often not sufficiently simple to analyze details.

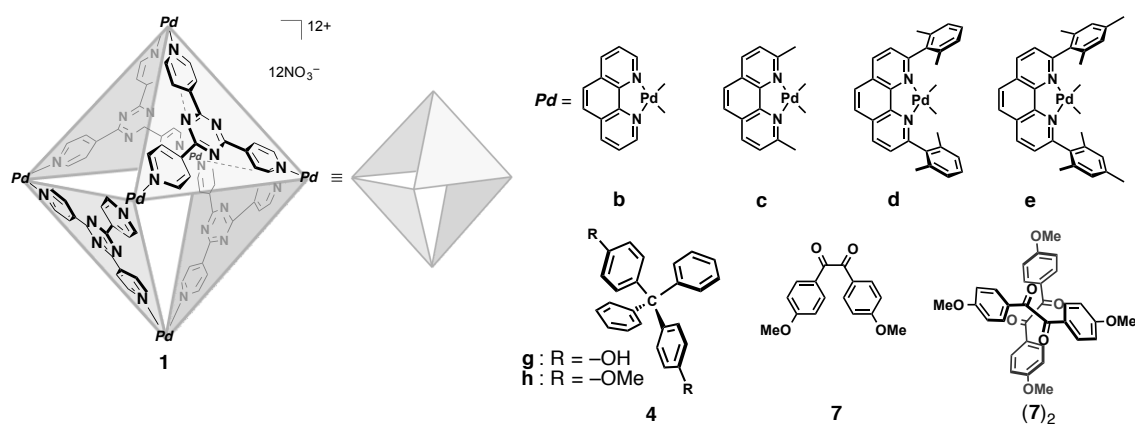


**Figure 1.** Different number of pyridine ortho-protons when cages adopting different symmetry.

Coordination nanocage **1** has been shown to strongly bind a variety of neutral substrates within its nanosized cavity.<sup>[13-15]</sup> We obtained several cages (**1b-e**) with different remote substituents. Previous chapters showed the guest-binding property are totally different. However, the symmetry of all these empty cages is the same. For example, due to the high symmetry of cage **1** ( $T_d$ ), the twelve pyridine rings in **1** are all equivalent, and the NMR spectrum of the empty cage displays only a set of pyridine protons for all these cages (Figure 1). Typically, when the cage accommodates guest molecule(s) with lower symmetry the  $T_d$  symmetry of the cage is desymmetrized and the symmetry of the entity follows that of the guest(s) if the cage and the guest(s)

strongly interact. For instance, if the guest has  $C_1$  symmetry then six pyridine ortho-protons ( $\text{PyH}_a$ ) on one panel ligand (**3**) become inequivalent and each four panel ligands also become different. As a result, 24 independent protons of pyridine ortho-position ( $\text{PyH}_a$ ) should be observed in the  $^1\text{H}$  NMR spectrum (Figure 1).

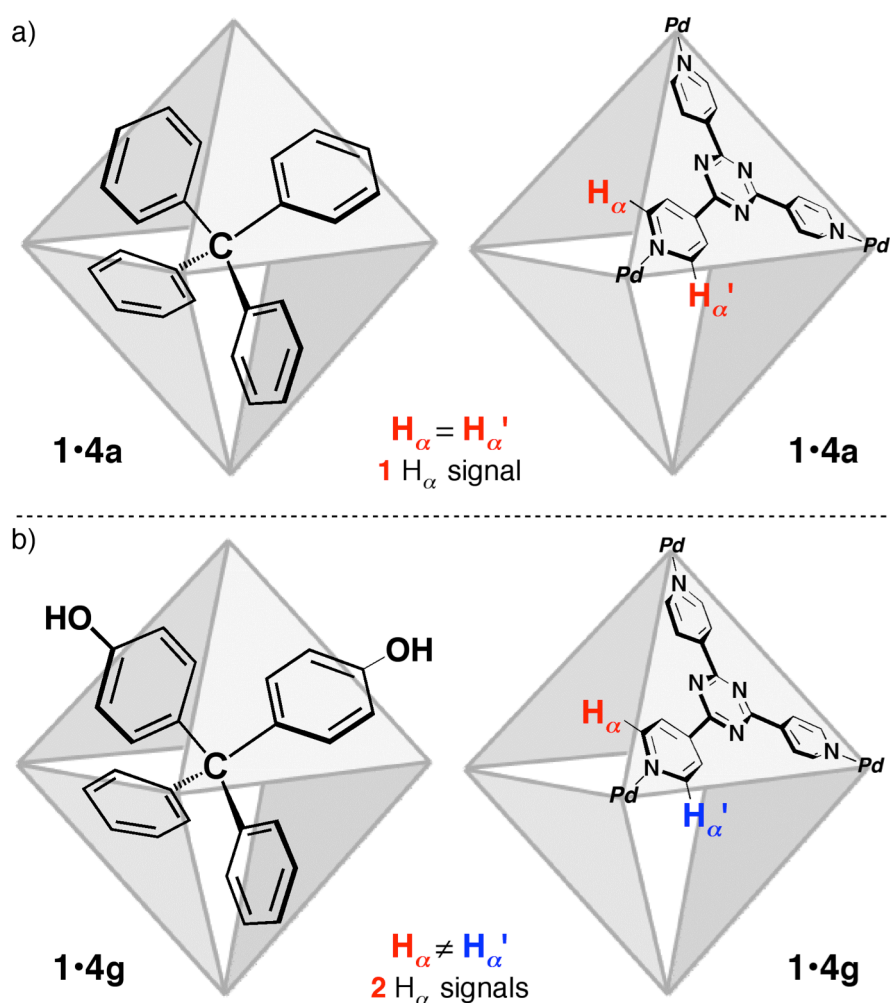
In previous chapters, when small and high symmetrical guest were used, inclusion complexes shown the same two signals for pyridine ring as empty cage due to the free rotation of pyridine moieties. In this chapter, relative large and low symmetrical guest were used to investigate whether guest motion can be tuned by remote substituents (Figure 2).



**Figure 2.** Self-assembled coordination cage **1b–e**. Guest **4**, **7** and its dimer **(7)<sub>2</sub>**.

## 4.2 Low symmetrical single molecule encapsulation in the shrunken cavity

In  $^1\text{H}$  NMR spectrum, after encapsulated the  $T$  symmetrical guest **4a–f**, the cage maintained the same signals as empty cage because the high symmetry of the guest is the same as the cage. Hence, a more suitable low symmetrical guest probe is necessary to distinguish the guest motion and discuss the impact of substituent groups of the cages.



**Figure 3.** Chemical environments of  $\text{PyH}_\alpha$  protons of inclusion complexes a) **1·4a** and b) **1·4g**.

Since guest **4** can also be modified in para-position of the phenyl groups without changing the skeleton structure and core size of the guest. Therefore, we next employed lower  $C_{2v}$ -symmetric guests **4g** and **4h** to expect symmetry reduction of the cage after guest encapsulation through strong host–guest interactions.

Ideally, two species of PyH<sub>a</sub> protons should be observed for inclusion complex **1•4g** (or **1•4h**) due to the desymmetrization of the cage when included low symmetrical guest. This phenomenon can be explained by the change of chemical environment of PyH<sub>a</sub> protons. As shown in Figure 3, cage **1** has four portals and each was surrounded by six PyH<sub>a</sub> protons. For inclusion complex **1•4a**, each portals of the cage **1** are equal where the same phenyl moiety located. Therefore, only one set of PyH<sub>a</sub> protons was observed for all inclusion complex **1•4a**, regardless their remote substituents. In the contrary, for inclusion complex **1•4g**, there are two types of cage portals of which phenyl and phenol groups occupied half respectively. Therefore, two sets of PyH<sub>a</sub> protons should be observed for inclusion complex **1•4g**. However, if host-guest are not tightly packed, one signal or broaden signals of PyH<sub>a</sub> protons could be obtained due to free rotation of pyridine moieties were not restrained.

Actually, in contrast to **4a**, the terminal –OH groups of **4g** enabled the quantitative guest encapsulation in all the cages. The hydrophilic –OH groups extend out from the cage cavity in inclusion complex **1•4g**. Presumably, electrostatic attractions between cationic cage **1** and deprotonated anionic **4g** stabilize the inclusion complex in water. As in the case of **4h**, when the –OH groups were replaced by –OMe, guest was encapsulated within cages **1c–e** in lower yield but no longer encapsulated within cage **1b** (Table 1).

Table 1. Inclusion yield of host-guest complex **1•4**<sup>a</sup>

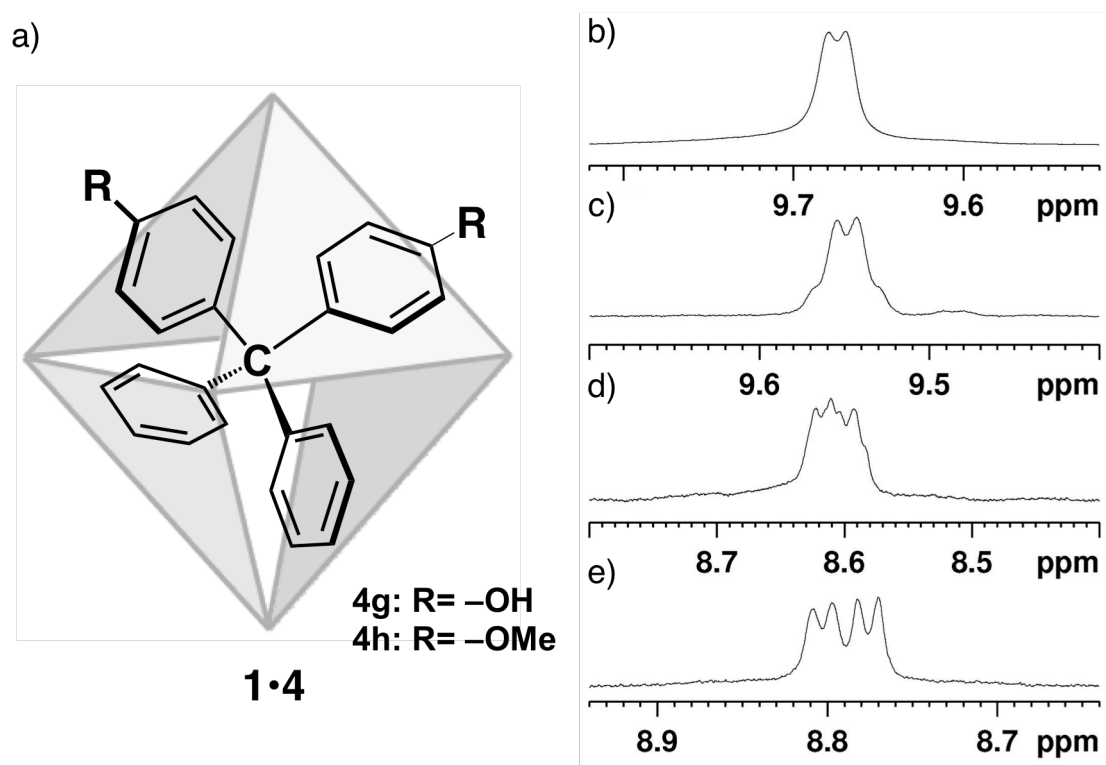
Cage	Inclusion yield (%)			
	<b>1b</b>	<b>1c</b>	<b>1d</b>	<b>1e</b>
<b>1</b>	>99	>99	>99	>99
<b>4g</b>	50	50	34	00

<sup>a</sup> Encapsulation conditions: cage **1** and guest (10 equiv) in D<sub>2</sub>O (1.0 mM) at 80 °C for 4 h.

Although C<sub>2v</sub>-symmetric guest **4g** was encapsulated within all the T<sub>d</sub>-symmetric cages **1**, the NMR signal behaviors of the cages were totally different. With increasing



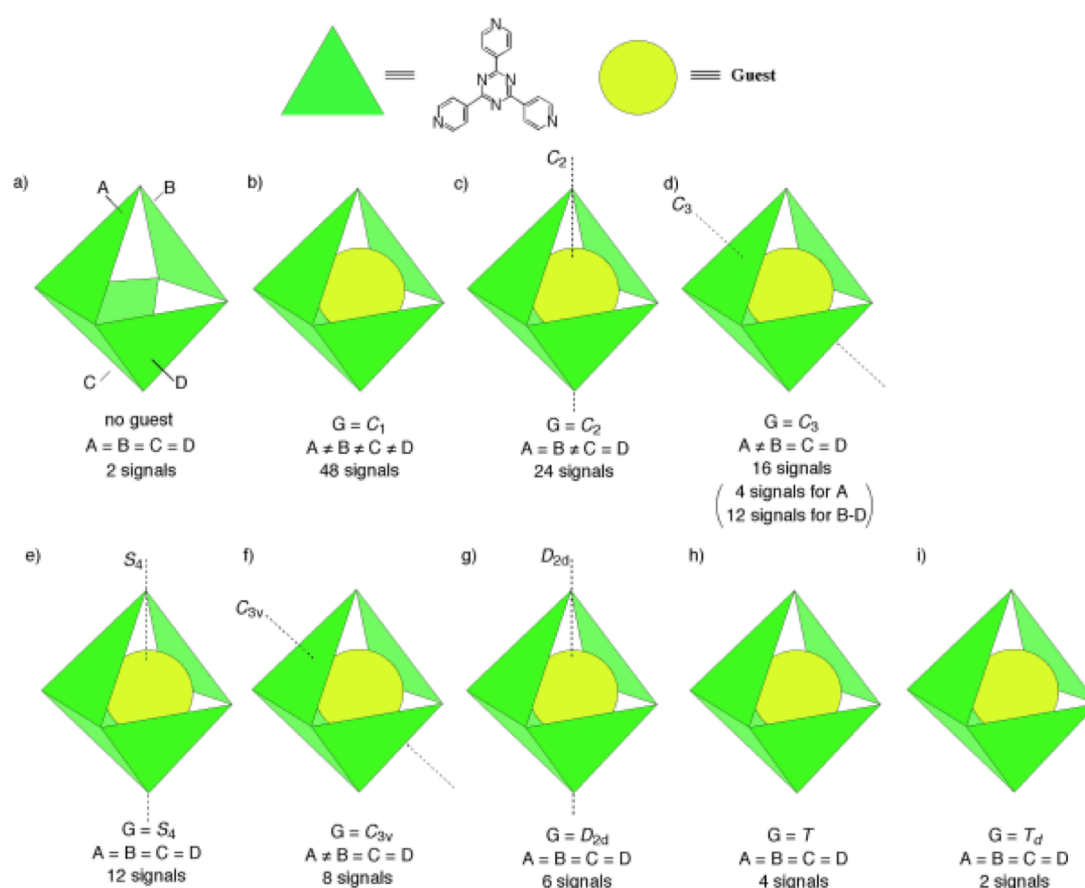
the bulkiness of the remote substituents in cages **1**, the PyH<sub>a</sub> signal of **3** was gradually split and finally doubled in inclusion complex **1e•4g**, indicating that the rotation of the pyridyl moieties got slower in the NMR time scale (Figure 4b–e). This phenomenon is attributed to the close packing of **4g** within the cage **1e** and supports the gradual shrinkage of the cage cavity from **1b** to **1e**. It is surprise to us that even a tiny difference (*para*-methyl) on remote groups show distinguished NMR spectra for cage **1d** and **1e**. Guest encapsulation cannot distinguish the cage **1d** and **1e** but guest motion can. This indicates that investigation on guest motion inside cavity offers a way for finding a minor difference in synthetic host.



**Figure 4.** a) Inclusion complexes **1•4g** and **1•4h** and b)–f) <sup>1</sup>H NMR spectra (500 MHz, D<sub>2</sub>O, 300 K) of the PyH<sub>a</sub> of (b) **1b•4g**, (c) **1c•4g**, (d) **1d•4g**, and (e) **1e•4g**. Reprinted with permission from ref. 17. Copyright 2014 John Wiley and Sons.

### 4.3 Low symmetrical dimer encapsulation in the shrunken

If the guest is bulky and host-guest interaction is enough strong, the split pattern of the host can be mathematically calculated and empirically expected because the maximum number of pyridine protons highly depends on guest symmetry. Figure 5 summarizes the relationship between the guest symmetry and the maximum number of pyridine protons which should appear in the NMR spectra.<sup>[1]</sup> Thus, we can learn



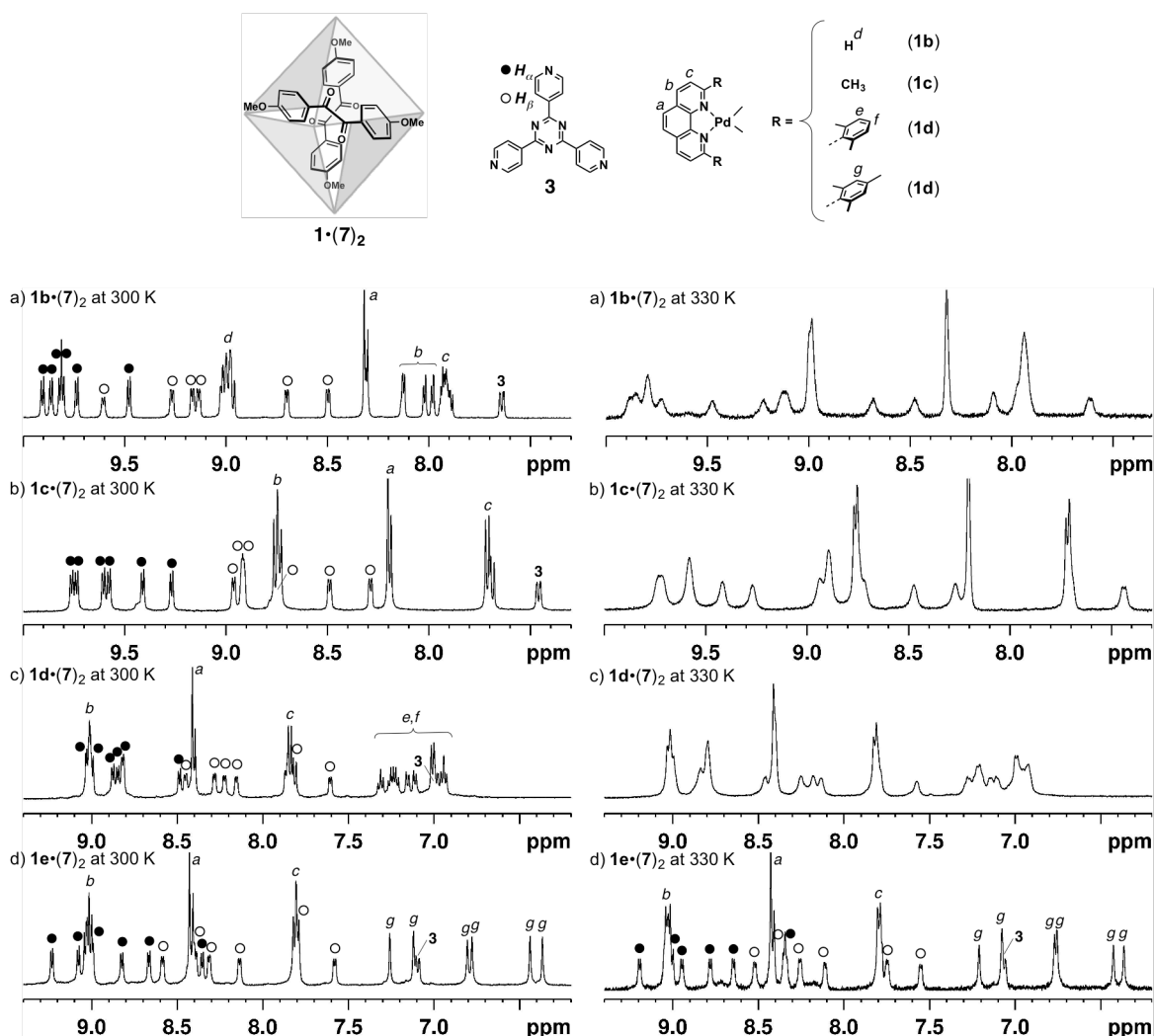
**Figure 5.** The relationship between the guest symmetry and the maximum number of pyridine protons which should appear in the NMR spectra. Reprinted with permission from ref. 1. Copyright 2011 John Wiley and Sons.

whether guests are firmly accommodated in the cavity or not by judging from the NMR spectra. The analysis of the symmetry by NMR spectroscopic analysis also elucidates the dynamic motion of included guests. Recently, we have showed some discussions

on some examples of probing the guest geometry by NMR analysis of the host symmetry, where all predicted structures have been confirmed by X-ray analyses.<sup>[16]</sup>

Cage **1d** and **1e** shared almost identical guest-binding affinity in many cases but were distinguished by encapsulating guest **4g**, although the only difference is just *para*-methyl groups. This finding suggests that investigation of guest motion offers a unique way for distinguish two similar synthetic host even only have a small variation in the remote site. In this section, we selected a rather bulky guest **7**.<sup>[11,2]</sup>

The 1:2 complexation of cage **1** with 4,4'-dimethoxydibenzoyl (**7**) provides a fine model for investigating in the cavities with different size.<sup>[17]</sup> The 1:2 inclusion



**Figure 6.** VT-<sup>1</sup>H NMR spectra (500 MHz, D<sub>2</sub>O) of (a) inclusion complex **1b**•(**7**)<sub>2</sub>, (b) inclusion complex **1c**•(**7**)<sub>2</sub>, (c) inclusion complex **1d**•(**7**)<sub>2</sub> and (d) inclusion complex **1e**•(**7**)<sub>2</sub>. Measurement temperature: (left) 300 K, (right) 330 K. Reprinted with permission from ref. 17. Copyright 2014 John Wiley and Sons.

complex **1**•(**7**)<sub>2</sub> was easily prepared by suspending excess amount of **7** (10 eq. for cage **1**) in a solution of **1** in D<sub>2</sub>O (5.3 mm, 0.5 mL), and stirring the mixture at 25 °C for 1 h, the solution color turned from colorless to pale yellow. After removal of residual guest **7** by filtration, <sup>1</sup>H NMR confirmed the formation of inclusion complexes **1**•(**7**)<sub>2</sub> in quantitative yields.

At room temperature (300 K), the pyridine protons of all the host were split into six pairs: six PyH<sub>a</sub> protons and six PyH<sub>b</sub> protons (Figure 6a–d, left column). This observation suggested the desymmetrization of the host into an *S*<sub>4</sub> symmetric entity with 12 inequivalent protons on triazine panel **3** are all equivalent but each ligand possesses no symmetry element. This observation also well matched the predicted split pattern of host according to low symmetrical guest. Well-separated and clear-split host signals for cage **1b–e** indicate that the included guest dimer (**7**)<sub>2</sub> is fixed within all the originally *T*<sub>d</sub>-symmetric cage **1** at low temperature.

Situation was changed when elevating the NMR experiment temperament. With increasing the measurement temperature to 330 K, the NMR signals of cages **1b–d** were gradually broadened and the fixed geometry of dimer (**7**)<sub>2</sub> was relieved. However, the NMR signals of cage **1e** remained intact and sharp, indicating that the guest motions were still restricted in the shrunken cavity even at high temperature. The only difference between cages **1d** and **1e** is the *para*-methyl group of the aromatic substituent on the phenanthroline ancillary ligand. Again, the single methyl group difference, **1d** and **1e**, plays a critical role in the guest motions.

## 4.4 Conclusion

Therefore, mere a *p*-methyl group further shrunken the cage cavity and tuned the guest motion property. Thus, again, the impact of the methyl substituent was experimentally observed.

This chapter is included that guest motions of self-assembled coordination cages can be remotely and finely tuned by remote substituents. Because the cavity volumes of self-assembled coordination cages were gradually reduced by increasing the size of substituents on the phenanthroline ancillary ligands, cages show enhancing abilities for restraining guest motion inside the cavities. More importantly, the presence or absence of *para*-methyl group, which is particularly located far from the guest-binding site, governed guest motions inside the cavities.

Again, a tiny difference in remote site makes a big difference in artificial host-guest systems. Through careful investigation of guest motion which is governed by remote substituents, the relationship between guest mobility and host cavity size was elucidated. We envision that cage with most shrunken cavity will provide a excellent confined inner space for tuning reactivates for specific reactions.

## 4.5 Experiment Section

### General Procedure for Encapsulation of Inclusion Complexes $\mathbf{1}\cdot(\mathbf{7})_2$ :

(For figures and tables: Reprinted with permission from ref. 16 and 17. Copyright 2014 John Wiley and Sons. Copyright 2013 American Chemical Society.)

When an excess amount of **7** (10 eq. for cage **1**) was suspended in a D<sub>2</sub>O solution (0.5 mL) of cages **1** (0.5 μmol; 1 mM) and the resulting solution was stirred at 25°C for 1 h, the solution color turned from colorless to pale yellow. After removal of residual guest **7** by filtration, <sup>1</sup>H NMR confirmed the formation of inclusion complexes  $\mathbf{1}\cdot(\mathbf{7})_2$  in quantitative yields.

#### *Physical Data of Inclusion Complex $\mathbf{1b}\cdot(\mathbf{7})_2$*

<sup>1</sup>H NMR (500 MHz, D<sub>2</sub>O, 300 K) δ: 9.92 (d, *J* = 6.0 Hz, 4H, PyH<sub>a</sub>, **1b**), 9.86 (d, *J* = 6.0 Hz, 4H, PyH<sub>a</sub>, **1b**), 9.83 (d, *J* = 6.0 Hz, 4H, PyH<sub>a</sub>, **1b**), 9.80 (d, *J* = 6.0 Hz, 4H, PyH<sub>a</sub>, **1b**), 9.74 (d, *J* = 6.0 Hz, 4H, PyH<sub>a</sub>, **1b**), 9.61 (d, *J* = 6.0 Hz, 4H, PyH<sub>b</sub>, **1b**), 9.48 (d, *J* = 6.0 Hz, 4H, PyH<sub>a</sub>, **1b**), 9.27 (d, *J* = 6.0 Hz, 4H, PyH<sub>b</sub>, **1b**), 9.17 (d, *J* = 6.0 Hz, 4H, PyH<sub>b</sub>, **1b**), 9.14 (d, *J* = 6.0 Hz, 4H, PyH<sub>b</sub>, **1b**), 9.03–8.97 (m, 12H, phen, **1b**), 8.71 (d, *J* = 6.0 Hz, 4H, PyH<sub>b</sub>, **1b**), 8.50 (d, *J* = 6.0 Hz, 4H, PyH<sub>b</sub>, **1b**), 8.31–8.12 (m, 12H, phen, **1b**), 8.13–8.12 (m, 12H, phen, **1b**), 8.03 (d, *J* = 6.0 Hz, 4H, phen, **1b**), 7.99 (d, *J* = 6.0 Hz, 4H, phen, **1b**), 7.94–7.89 (m, 12H, phen, **1b**), 7.65 (d, *J* = 9.0 Hz, 4H, **7**), 5.78 (d, *J* = 9.0 Hz, 4H, **7**), 4.16 (d, *J* = 9.0 Hz, 4H, **7**), 3.63 (d, *J* = 9.0 Hz, 4H, **7**), 2.88 (s, 12H, **7**).  
Yield: quant.

#### *Physical Data of Inclusion Complex $\mathbf{1c}\cdot(\mathbf{7})_2$*

<sup>1</sup>H NMR (500 MHz, D<sub>2</sub>O, 300 K) δ: 9.76 (d, *J* = 6.0 Hz, 4H, PyH<sub>a</sub>, **1c**), 9.74 (d, *J* = 6.0 Hz, 4H, PyH<sub>a</sub>, **1c**), 9.60 (d, *J* = 6.0 Hz, 4H, PyH<sub>a</sub>, **1c**), 9.58 (d, *J* = 6.0 Hz, 4H, PyH<sub>a</sub>, **1c**), 9.41 (d, *J* = 6.0 Hz, 4H, PyH<sub>a</sub>, **1c**), 9.27 (d, *J* = 6.0 Hz, 4H, PyH<sub>a</sub>, **1c**), 8.96 (d, *J* = 6.0 Hz, 4H, PyH<sub>b</sub>, **1c**), 8.92–8.89 (m, 8H, PyH<sub>b</sub>, **1c**), 8.73 (d, *J* = 6.0 Hz, 4H, overlap, PyH<sub>b</sub>, **1c**), 8.77–8.73 (m, 12H, phen, **1c**), 8.49 (d, *J* = 6.0 Hz, 4H, PyH<sub>b</sub>, **1c**), 8.29 (d, *J* = 6.0 Hz, 4H, PyH<sub>b</sub>, **1c**), 8.20–8.19 (m, 12H, phen, **1c**), 7.72–7.68 (m, *J* = 4.5 Hz, 12H, phen,

**1c**), 7.46 (d,  $J = 9.0$  Hz, 4H, **7**), 5.63 (d,  $J = 9.0$  Hz, 4H, **7**), 3.88 (d,  $J = 9.0$  Hz, 4H, **7**), 3.39 (d,  $J = 9.0$  Hz, 4H, **7**), 2.64 (s, 12H, **7**) 2.26–2.16 (m, 36H, **1c**). Yield: quant.

*Physical Data of Inclusion Complex **1d**•(7)<sub>2</sub>*

<sup>1</sup>H NMR (500 MHz, D<sub>2</sub>O, 300 K)  $\delta$ : 9.03 (d,  $J = 6.0$  Hz, 4H, PyH<sub>a</sub>, **1d**), 9.02–9.00 (m, 12H, phen, **1d**), 8.99 (d,  $J = 6.0$  Hz, 4H, PyH<sub>a</sub>, **1d**), 8.88 (d,  $J = 6.0$  Hz, 4H, PyH<sub>a</sub>, **1d**), 8.85 (d,  $J = 6.0$  Hz, 4H, PyH<sub>a</sub>, **1d**), 8.82 (d,  $J = 6.0$  Hz, 4H, PyH<sub>a</sub>, **1d**), 8.49 (d,  $J = 6.0$  Hz, 4H, PyH<sub>a</sub>, **1d**), 8.45 (d,  $J = 6.0$  Hz, 4H, PyH<sub>b</sub>, **1d**), 8.41–8.40 (m, 12H, phen, **1d**), 8.29 (d,  $J = 6.0$  Hz, 4H, PyH<sub>b</sub>, **1d**), 8.23 (d,  $J = 6.0$  Hz, 4H, PyH<sub>b</sub>, **1d**), 8.15 (d,  $J = 6.0$  Hz, 4H, PyH<sub>b</sub>, **1d**), 7.85–7.82 (m, 12H, phen, **1d**), 7.81 (d,  $J = 6.0$  Hz, 4H, PyH<sub>b</sub>, **1d**), 7.61 (d,  $J = 6.0$  Hz, 4H, PyH<sub>b</sub>, **1d**), 7.33–6.93 (m, 36H, ph, **1d**), 7.02 (d,  $J = 9.0$  Hz, 4H, **7**), 5.00 (d,  $J = 9.0$  Hz, 4H, **7**), 3.33 (d,  $J = 9.0$  Hz, 4H, **7**), 2.84 (d,  $J = 9.0$  Hz, 4H, **7**), 2.82–2.25 (m, 72H, Me, **1d**), 2.20 (s, 12H, **7**). Yield: quant.

*Physical Data of Inclusion Complex **1e**•(7)<sub>2</sub>*

<sup>1</sup>H NMR (500 MHz, D<sub>2</sub>O, 300 K)  $\delta$ : 9.23 (d,  $J = 6.0$  Hz, 4H, PyH<sub>a</sub>, **1e**), 9.08 (d,  $J = 6.0$  Hz, 4H, PyH<sub>a</sub>, **1e**), 9.04–8.98 (m, 12H, phen, **1e**), 9.00 (d,  $J = 6.0$  Hz, 4H, PyH<sub>a</sub>, **1e**), 8.83 (d,  $J = 6.0$  Hz, 4H, PyH<sub>a</sub>, **1e**), 8.67 (d,  $J = 6.0$  Hz, 4H, PyH<sub>a</sub>, **1e**), 8.59 (d,  $J = 6.0$  Hz, 4H, PyH<sub>b</sub>, **1e**), 8.43–8.41 (m, 12H, phen, **1e**), 8.39 (d,  $J = 6.0$  Hz, 4H, PyH<sub>b</sub>, **1e**), 8.36 (d,  $J = 6.0$  Hz, 4H, PyH<sub>a</sub>, **1e**), 8.32 (d,  $J = 6.0$  Hz, 4H, PyH<sub>b</sub>, **1e**), 8.14 (d,  $J = 6.0$  Hz, 4H, PyH<sub>b</sub>, **1e**), 7.82–7.79 (m, 12H, phen, **1e**), 7.79 (d,  $J = 6.0$  Hz, 4H, PyH<sub>b</sub>, **1e**), 7.58 (d,  $J = 6.0$  Hz, 4H, PyH<sub>b</sub>, **1e**), 7.26 (s, 4H, Mes, **1e**), 7.12 (s, 4H, Mes, **1e**), 7.11 (d,  $J = 9.0$  Hz, 4H, **7**), 6.81 (s, 4H, Mes, **1e**), 6.78 (s, 4H, Mes, **1e**), 6.44 (s, 4H, Mes, **1e**), 6.37 (s, 4H, Mes, **1e**), 5.09 (d,  $J = 9.0$  Hz, 4H, **7**), 3.37 (d,  $J = 9.0$  Hz, 4H, **7**), 2.87 (d,  $J = 9.0$  Hz, 4H, **7**), 2.74 (s, 18H, Me, **1e**), 2.51 (s, 18H, Me, **1e**), 2.42 (s, 18H, Me, **1e**), 2.40 (s, 18H, Me, **1e**), 2.23 (s, 12H, **7**), 2.01 (s, 18H, Me, **1e**), 1.97 (s, 18H, Me, **1e**). Yield: quant.

NMR spectrum for inclusion complex  $1\cdot(7)_2$ :

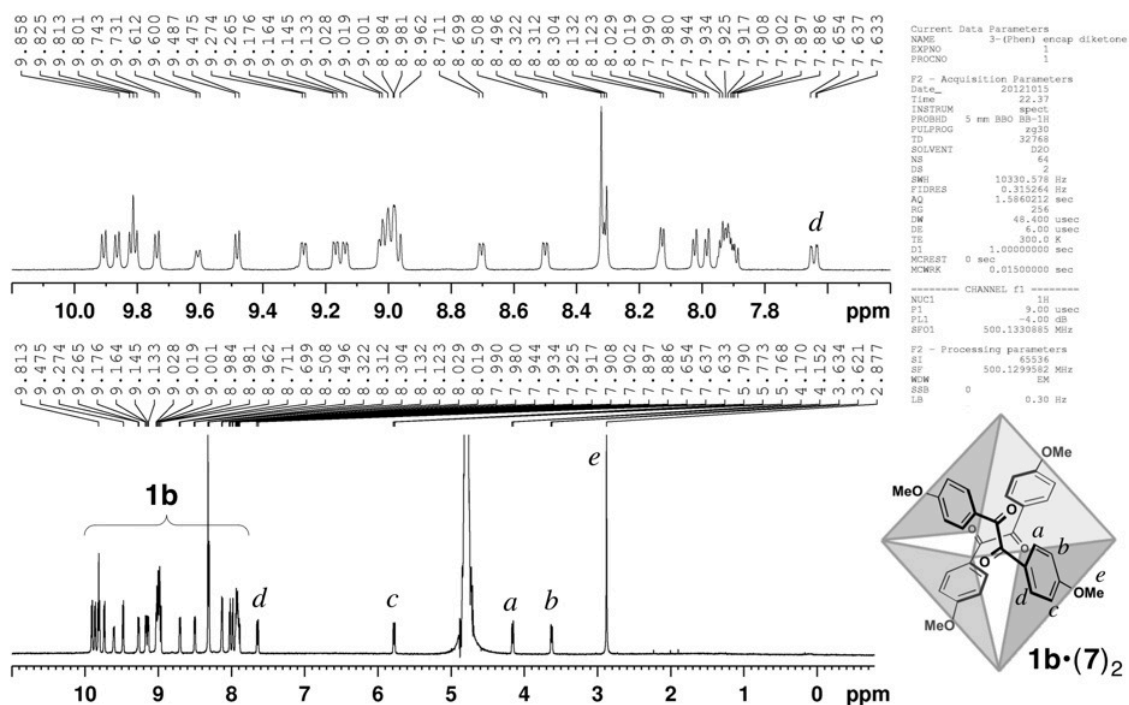


Figure S1.  $^1\text{H}$  NMR spectrum (500 MHz,  $\text{D}_2\text{O}$ , 300 K) of inclusion complex  $1\text{b}\cdot(7)_2$ .

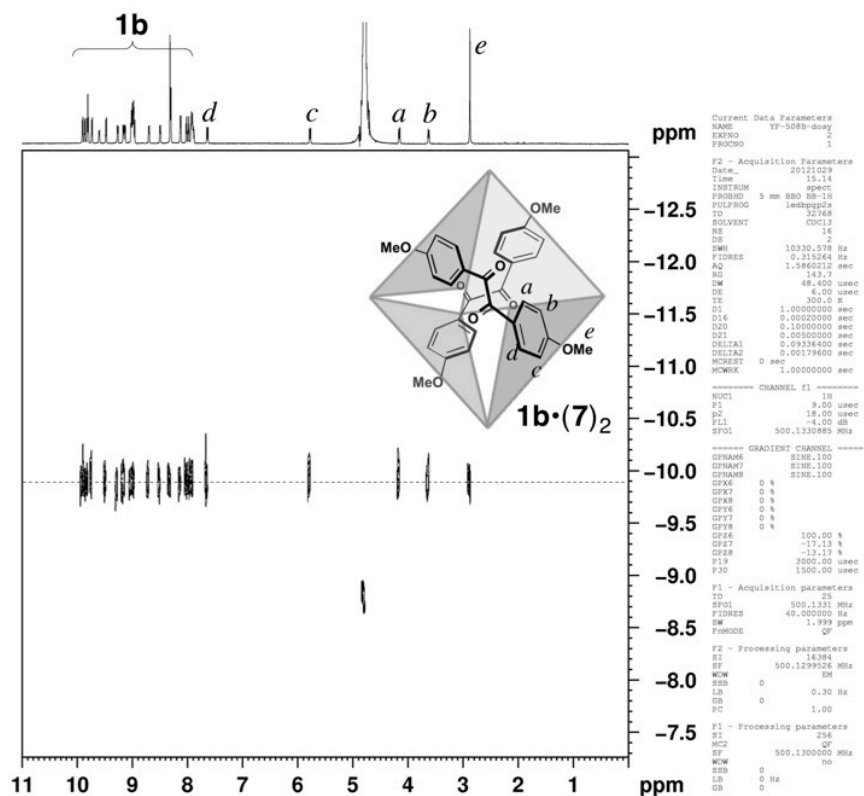


Figure S2. DOSY spectrum (500 MHz,  $\text{D}_2\text{O}$ , 300 K) of inclusion complex  $1\text{b}\cdot(7)_2$ .



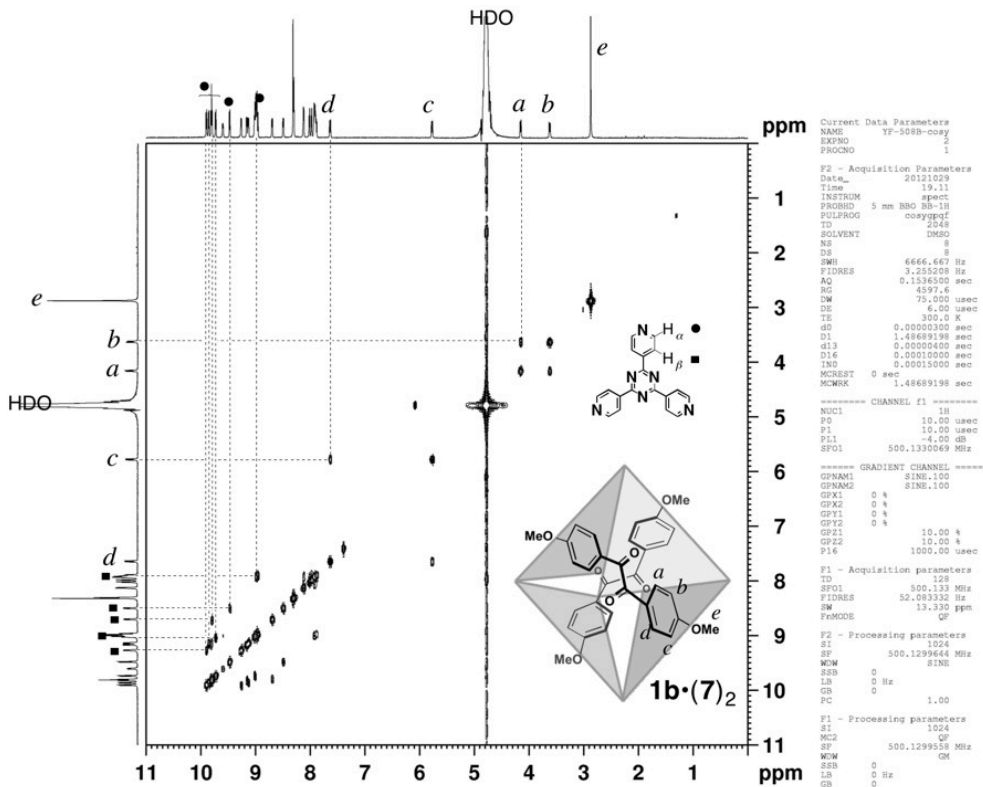


Figure S3.  $^1\text{H}$ - $^1\text{H}$  COSY spectrum (500 MHz,  $\text{D}_2\text{O}$ , 300 K) of inclusion complex  $1\mathbf{b}\cdot(7)_2$ .

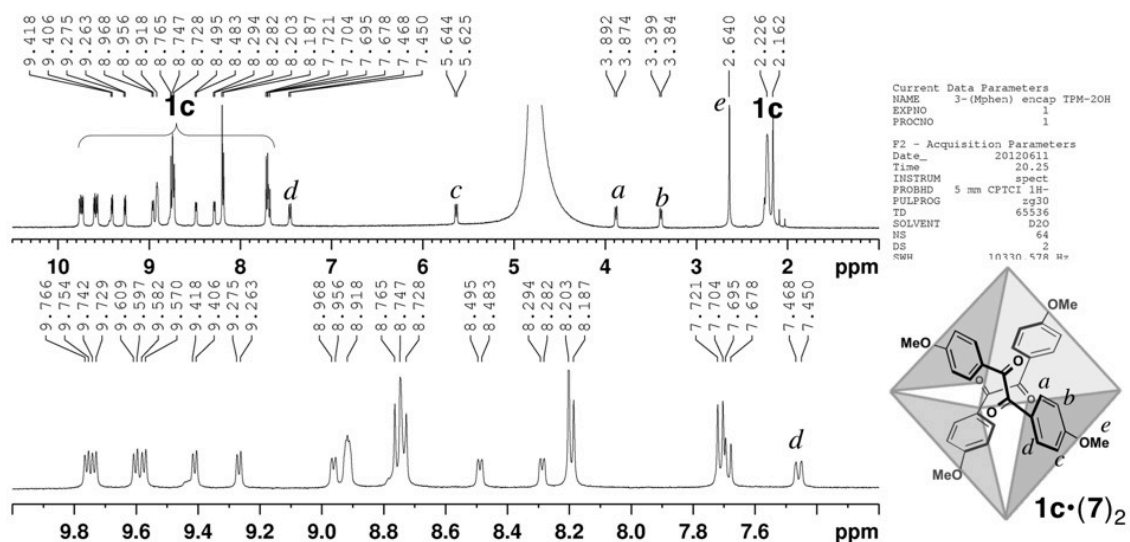
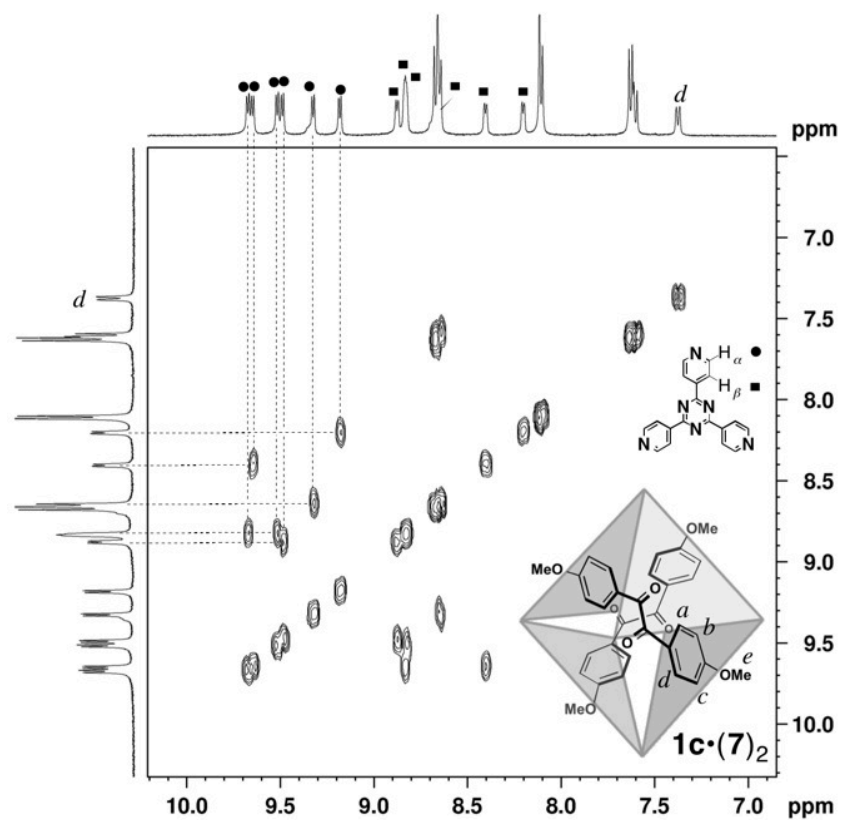
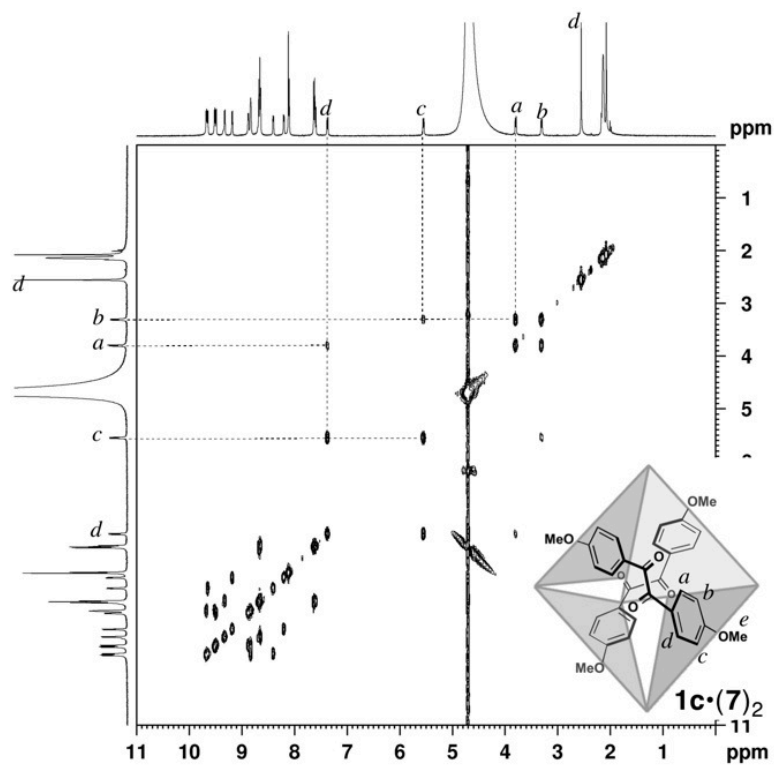


Figure S4.  $^1\text{H}$  NMR spectrum (500 MHz,  $\text{D}_2\text{O}$ , 300 K) of inclusion complex  $1\mathbf{c}\cdot(7)_2$ .



**Figure S5.**  $^1\text{H}$ - $^1\text{H}$  COSY spectrum (500 MHz,  $\text{D}_2\text{O}$ , 300 K) of inclusion complex  $1\text{c}\cdot(7)_2$ .



**Figure S6.**  $^1\text{H}$ - $^1\text{H}$  COSY spectrum (500 MHz,  $\text{D}_2\text{O}$ , 300 K) of inclusion complex  $1\text{c}\cdot(7)_2$ .

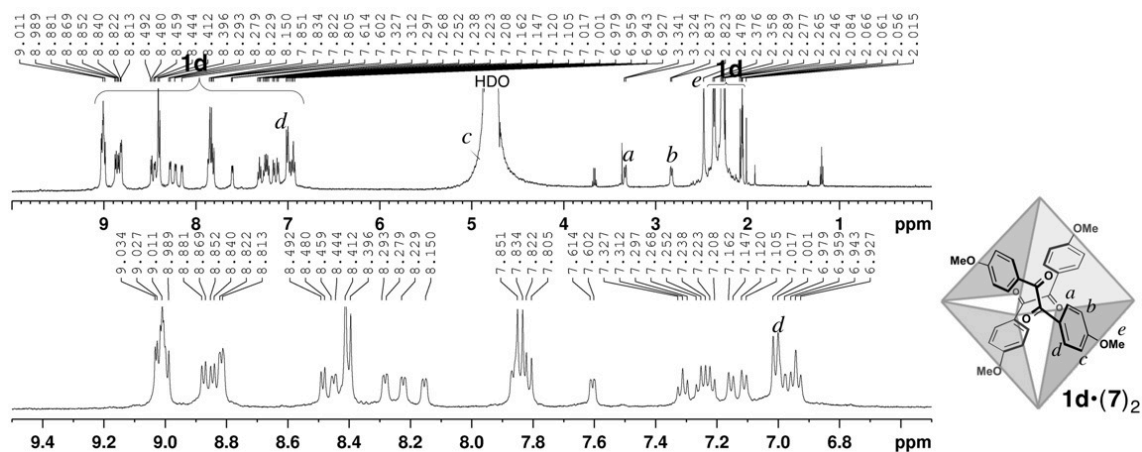


Figure S7.  $^1\text{H}$  NMR spectrum (500 MHz,  $\text{D}_2\text{O}$ , 300 K) of inclusion complex  $1\text{d}\cdot(7)_2$ .

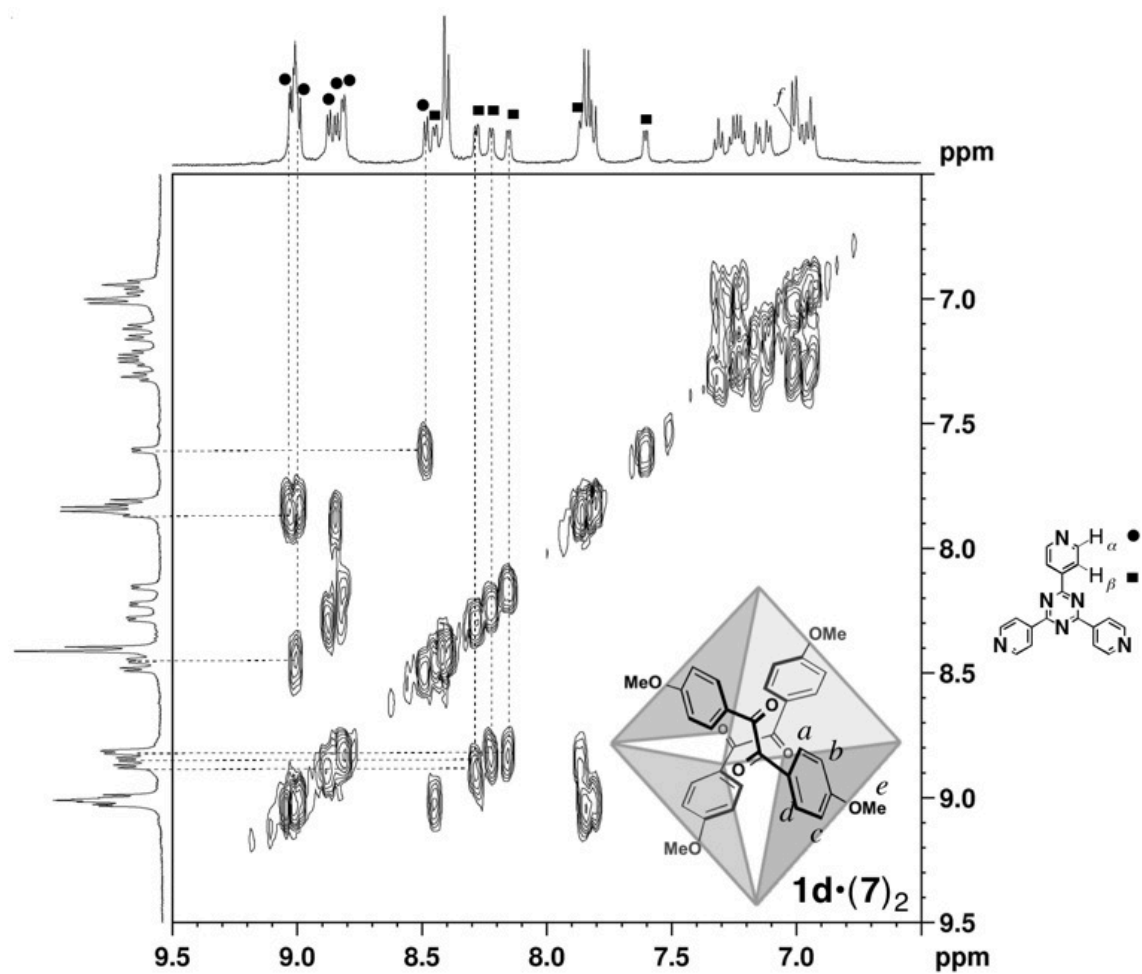


Figure S8.  $^1\text{H}$ - $^1\text{H}$  COSY spectrum (500 MHz,  $\text{D}_2\text{O}$ , 300 K) of inclusion complex  $1\text{d}\cdot(7)_2$ .

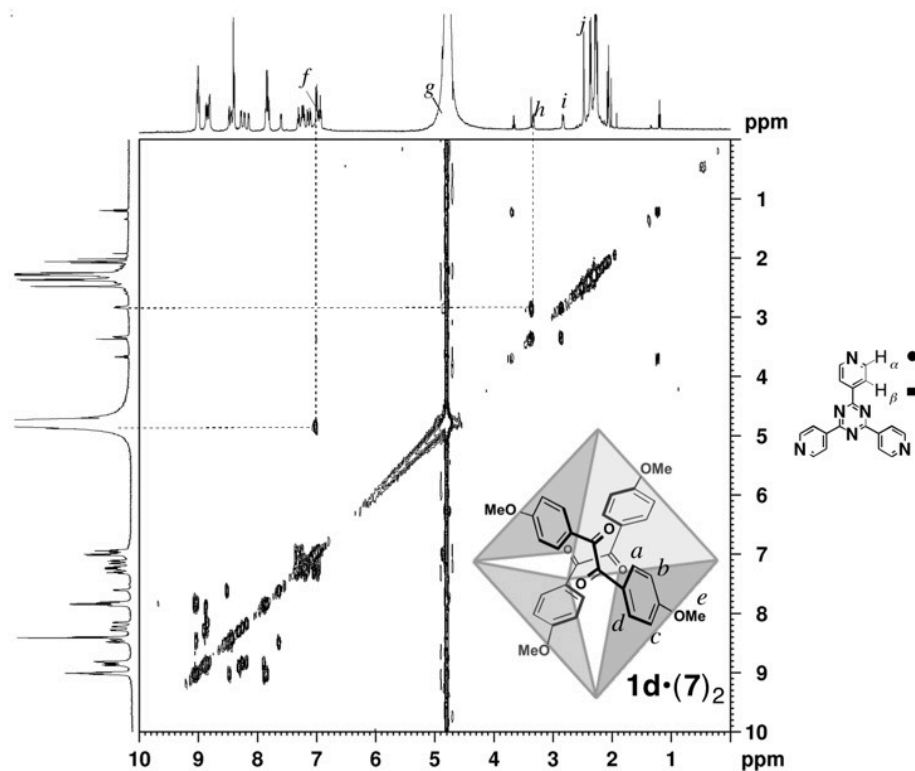


Figure S9.  $^1\text{H}$ - $^1\text{H}$  COSY spectrum (500 MHz,  $\text{D}_2\text{O}$ , 300 K) of inclusion complex  $1\text{d}\cdot(7)_2$ .

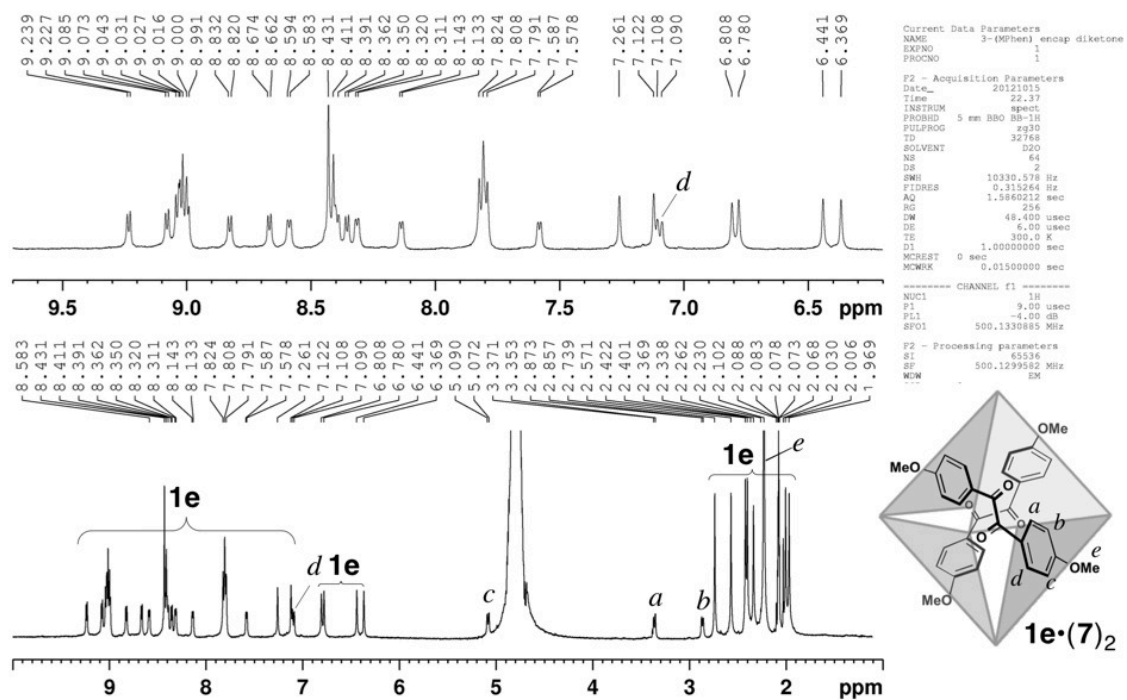


Figure S10.  $^1\text{H}$  NMR spectrum (500 MHz,  $\text{D}_2\text{O}$ , 300 K) of inclusion complex  $1\text{e}\cdot(7)_2$ .

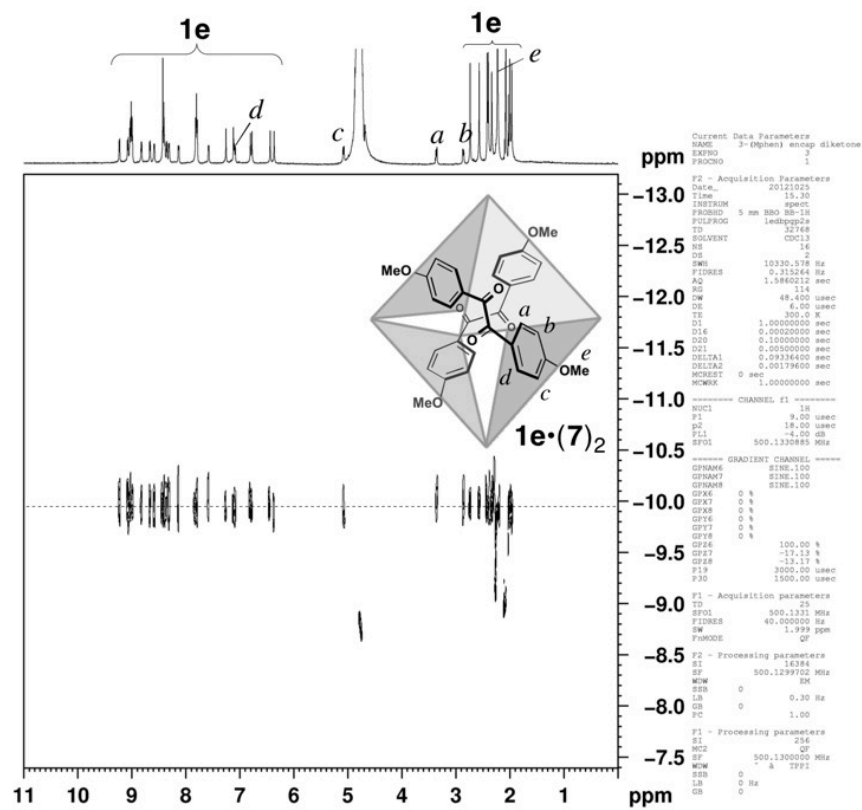


Figure S11. DOSY spectrum (500 MHz, D<sub>2</sub>O, 300 K) of inclusion complex **1e•(7)<sub>2</sub>**.

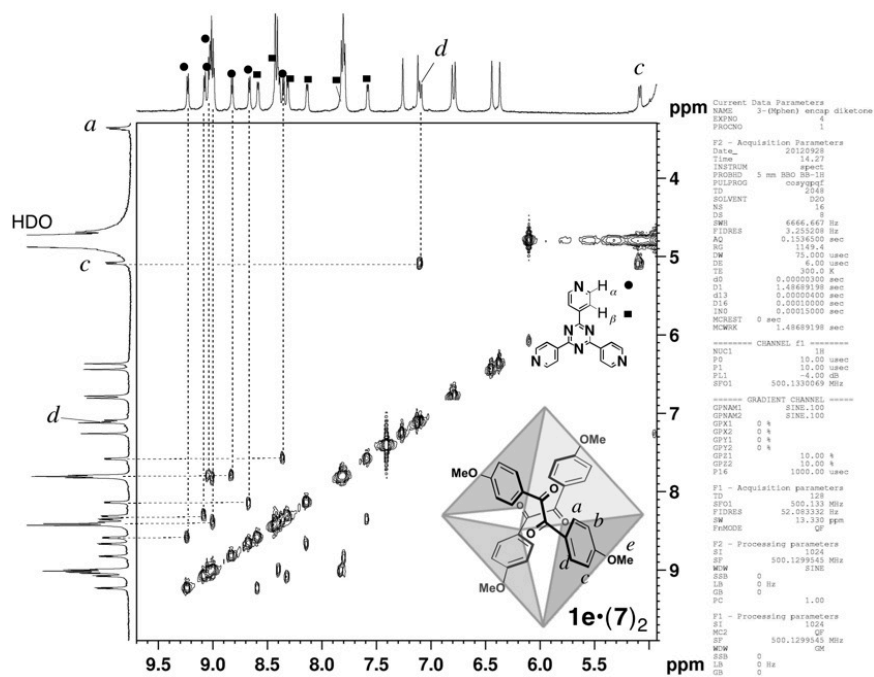


Figure S12. <sup>1</sup>H-<sup>1</sup>H COSY spectrum (500 MHz, D<sub>2</sub>O, 300 K) of inclusion complex **1e•(7)<sub>2</sub>**.

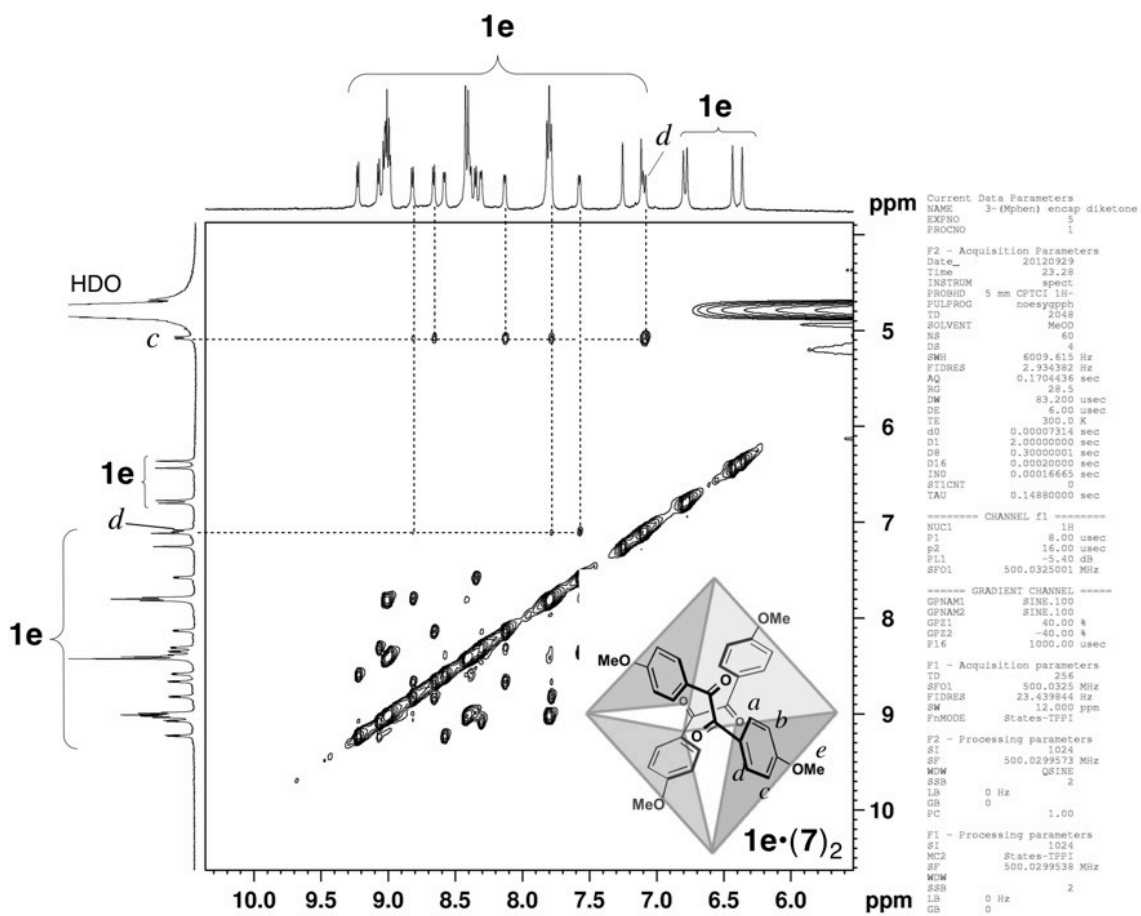
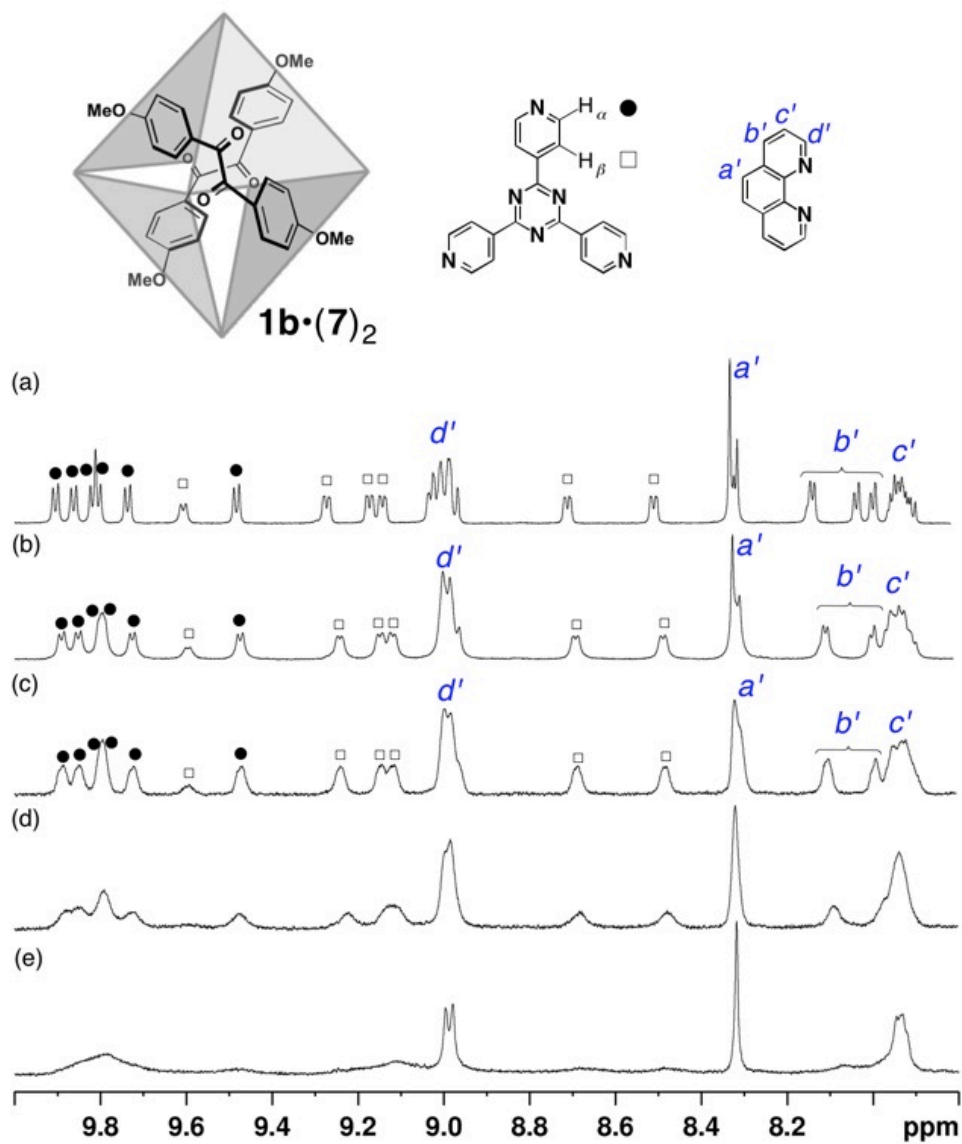


Figure S13.  $^1\text{H}$ - $^1\text{H}$  NOESY spectrum (500 MHz,  $\text{D}_2\text{O}$ , 300 K) of inclusion complex  $1\mathbf{e}\cdot(7)_2$ .

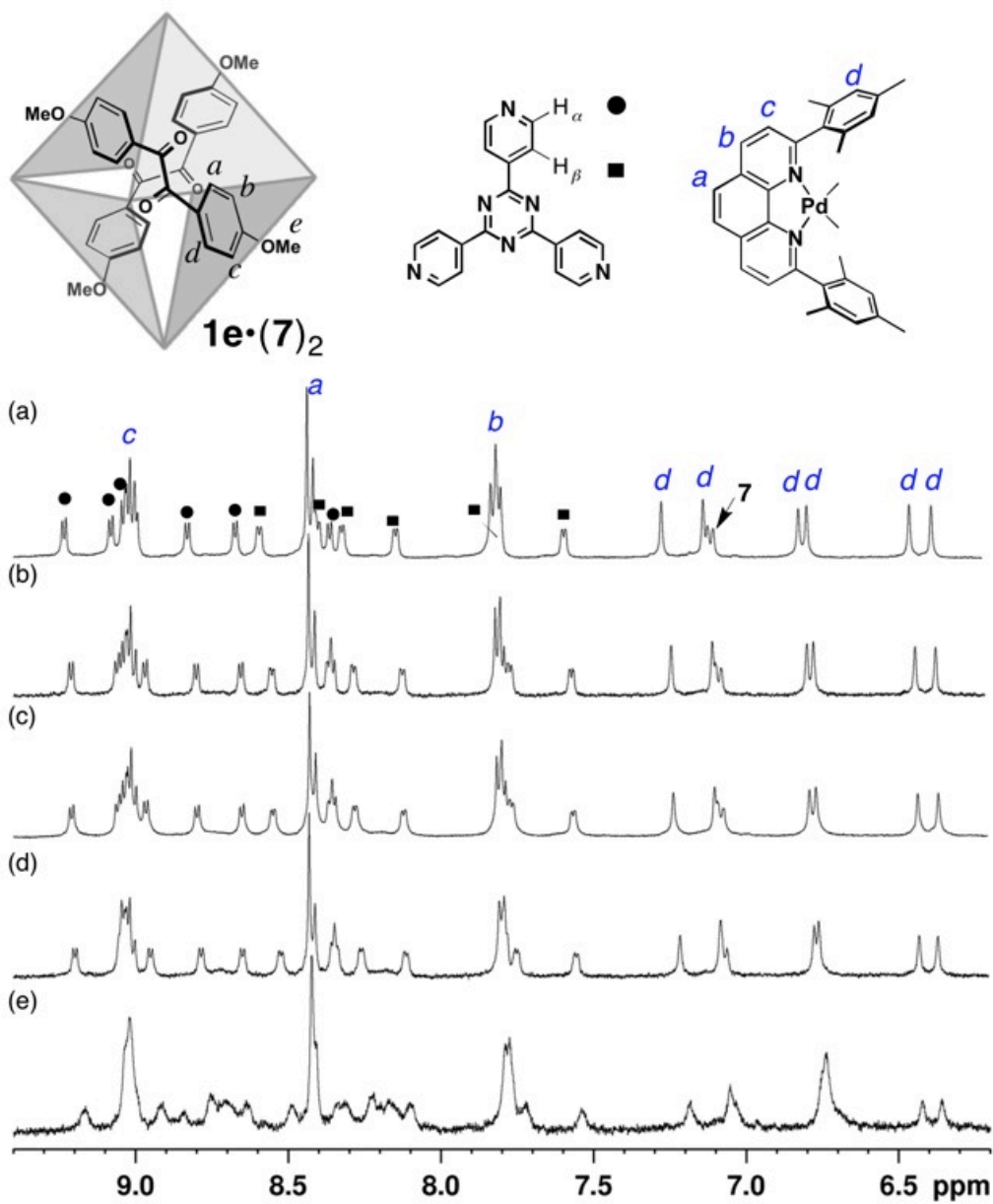
### **VT-NMR study for inclusion complex $1\cdot(7)_2$ :**

After formation of inclusion complex  $1\cdot(7)_2$ ,  $D_2O$  solution of the inclusion complex was put into a NMR tube for various temperatures NMR experiment. The temperature was varied from 300 K to 340 K. At every recorded temperature, we carefully adjusted the shim current. The  $^1H$  NMR spectra of the aromatic region for both inclusion complexes are shown below. For inclusion complex  $1\cdot(7)_2$ , the protons on the pyridine rings of the host framework split to 12 signals. Inclusion complex  $1b\cdot(7)_2$  and  $1e\cdot(7)_2$  show identical split pattern in low temperature and sharp contrast in high temperatures.



**Figure S14.** VT-NMR spectra of inclusion complex  $1b \cdot (7)_2$  at (a) 300 K, (b) 315 K, (c) 320 K, (d) 330 K, and (e) 340 K. Reprinted with permission from ref. 16. Copyright 2013 American Chemical Society.





**Figure S15.** VT-NMR spectra of inclusion complex  $1e \cdot (7)_2$  at (a) 300 K, (b) 315 K, (c) 320 K, (d) 330 K, and (e) 340 K. Reprinted with permission from ref. 3. Copyright 2013 American Chemical Society.

## 4.6 REFERENCES

- [1] T. Kusukawa,; M. Yoshizawa,; M. Fujita, *Angew. Chem. Int. Ed.* **2001**, *40*, 1879.
- [2] T. Kusukawa,; M. Fujita, *J. Am. Chem. Soc.* **2002**, *124*, 13576.
- [3] D. J. Cram, J. M. Cram, *Container Molecules and Their Guests*, Royal Society of Chemistry, Cambridge, **1994**.
- [4] P. Timmerman, W. Verboom, F. C. J. M. van Veggel, J. P. M. van Duynhoven, D.N. Reinhoudt, *Angew. Chem.* **1994**, *106*, 2437; *Angew. Chem. Int. Ed. Engl.* **1994**, *33*, 2345.
- [5] A. M. A. van Wageningen, P. Timmerman, J. P. M. van Duynhoven, W. Verboom, F. C. M. van Veggel, D. N. Reinhoudt, *Chem. Eur. J.* **1997**, *3*, 639.
- [6] J. R. Fraser, B. Borecka, J. Trotter, J. C. Sherman, *J. Org. Chem.* **1995**, *60*, 1207.
- [7] J. C. Sherman, C. B. Knobler, D. J. Cram, *J. Am. Chem. Soc.* **1991**, *113*, 2194 .
- [8] R. G. Chapman, J. C. Sherman, *J. Org. Chem.* **2000**, *65*, 513.
- [9] T. Heinz, D. M. Rudkevich, J. Rebek, Jr., *Nature* **1998**, *394*, 764.
- [10] T. Heinz, D. M. Rudkevich, J. Rebek, Jr., *Angew. Chem.* **1999**, *111*, 1206; *Angew. Chem. Int. Ed.* **1999**, *38*, 1136.
- [11] S. Ma, D. M. Rudkevich, J. Rebek, Jr., *Angew. Chem.* **1999**, *111*, 2761; *Angew. Chem. Int. Ed.* **1999**, *38*, 2600.
- [12] F. C. Tucci, D.M. Rudkevich, J. Rebek, Jr., *J. Am. Chem. Soc.* **1999**, *121*, 4928.
- [13] M. Fujita, D. Oguro, M. Miyazawa, H. Oka, K. Yamaguchi, K. Ogura, *Nature* **1995**, *378*, 469.
- [14] T. Kusukawa, M. Fujita, *Angew. Chem.* **1998**, *110*, 3327; *Angew. Chem. Int. Ed.* **1998**, *37*, 3142.
- [15] T. Kusukawa, M. Fujita, *J. Am. Chem. Soc.* **1999**, *121*, 1397.
- [16] Y. Fang, T. Murase, S. Sota, M. Fujita, *J. Am. Chem. Soc.* **2013**, *135*, 613.
- [17] Y. Fang, T. Murase, M. Fujita, *Chem. Asian J.* **2014**, *in press*, DOI: 10.1002/asia.201301642

# Chapter 5

## Diels-Alder Reaction Acceleration within Shrunken Cavity

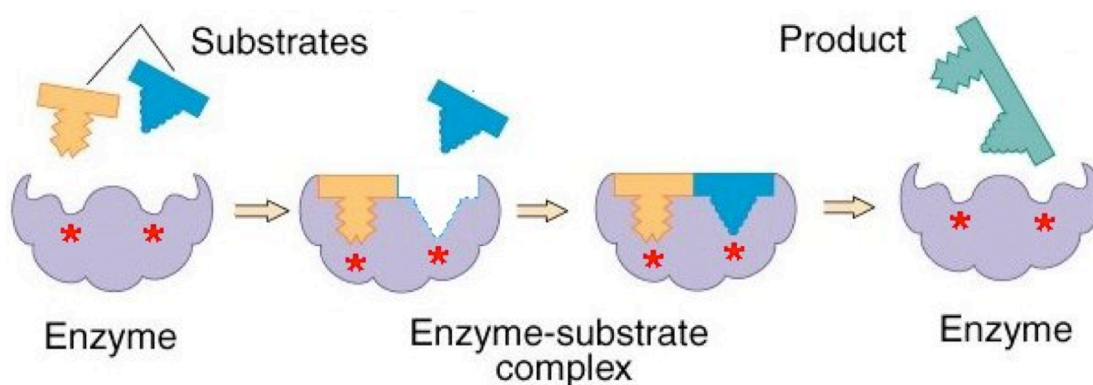
The binding pocket of enzymes is so elastic that can bind a variety of substrate by “induced fit”. The suitable orientation of the bound substrates accelerated the reaction. In many cases, the reaction was promoted by enzyme in a catalytic way.

Synthetic host has robust guest-binding cavity where guests are bound and react. However, the rigidity of the cavity limits to create a suitable reaction environment for guests in different size and species. On the other hand, similar binding affinity for substrates and products stop the synthetic host for using as a catalyst.

The shrunken cavity shows totally different guest-binding property comparing with conventional cavity due to its reduced cavity volume. The smaller cavity may accelerate some small substrates that cannot proceed reaction in conventional cavity. More importantly, as the shrunken cavity is very sensitive for guest size, it may have potential for distinguishing substrates and products, thus a catalytic reaction may proceed by shrunken cavity.

## 5.1 Introduction

In the large and much complicated substrate binding pockets of enzymes, the substrates are forced into specific orientations that favor designated reaction pathways and react much efficient.<sup>[1, 2]</sup> The elastic enzyme pocket can accommodate lots of substrates in different size and shape through “induced fit” (Figure 1). Comparing to



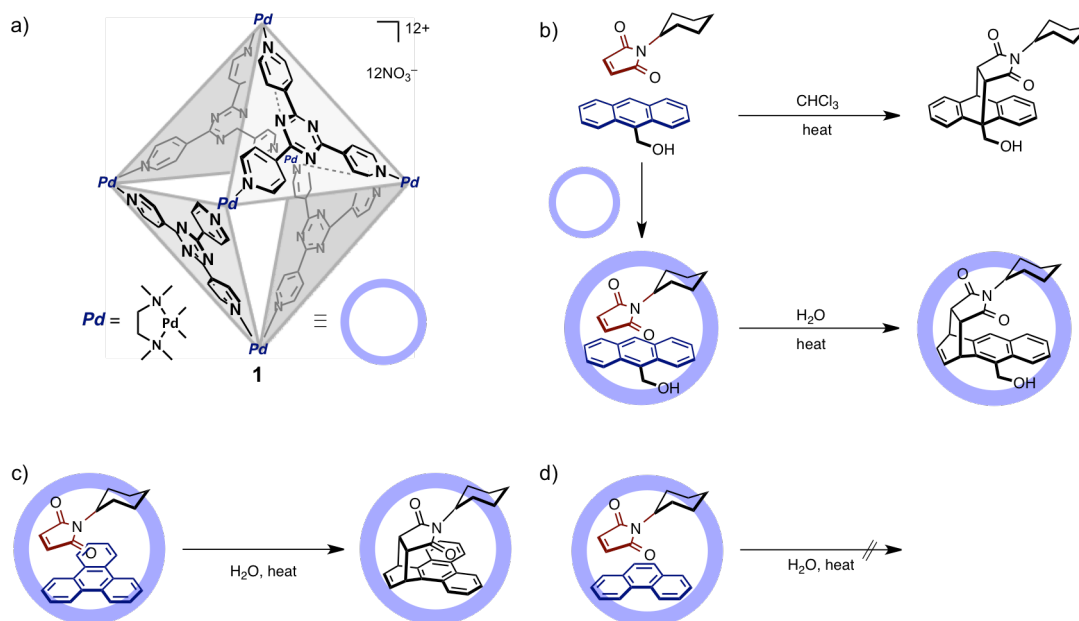
**Figure 1.** “Inducted fit” of natural enzyme.

enzyme’s pocket, guest binding pockets of synthetic host is smaller and more simplified, which allow us to study the mechanism by mimicking the behavior of natural enzymes. In the past decade, a lot of chemists have made significant progress in designing synthetic hosts for emulating enzymatic pockets.<sup>[3, 4]</sup> However, unlike the flexible pockets of natural enzymes, the rigid synthetic hosts usually adopt shape persistent cavities. Lacking of natural enzyme’s “induced fit”, the synthetic host is either not capable of encapsulating small guests, or binding the small guest in a “wrong pre-organization” inside the relative large cavity, thus no reaction proceed. For proceeding reaction for a small substrate, a newly designed small cavity is required.

Moreover, enzymes catalyzed the reactions by smoothly release the products from the pockets as soon as they were produced. In contrast, catalytic turnover has been inhibited because the hosts bind products as effectively as reactants. For example, in earlier reports by Sanders,<sup>[5]</sup> Rebek,<sup>[6, 7]</sup> and our group,<sup>[8]</sup> the Diels-Alder and related cycloadditions are significantly accelerated in synthetic pockets, but the product inhibition prevents the reactions from showing turnover. For catalytic reactions by self-assembled hosts, there have appeared only a few examples, including the aza-Cope

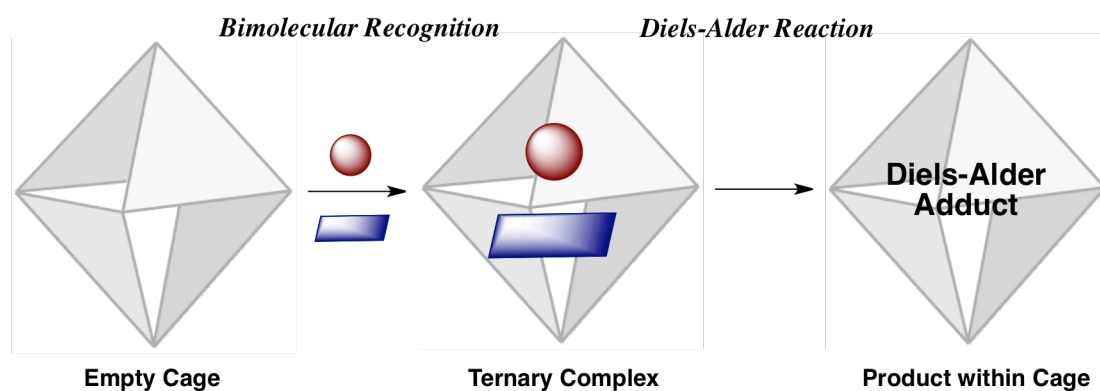
rearrangement,<sup>[9]</sup> epoxidation,<sup>[10]</sup> and the Diels-Alder.<sup>[11]</sup> In order to conduct the reaction in a catalytic fashion, a newly designed cavity containing discriminating cavity environment for substrates and product is necessary.

Among various potential excellent synthetic hosts for accelerating reactions, the cavity of  $M_6L_4$  cages creates almost neat conditions, where not only the substrate concentration is increased but also pre-organization of substrates reduces the high entropic cost for bimolecular reactions (Figure 2a). For example, within the confined cavity of  $M_6L_4$  cage **1**, Diels-Alder reaction of anthracene derivatives proceeds at a unusual 1,4-position (Figure 2b).<sup>[12]</sup> Furthermore, the cavity of  $M_6L_4$  cage **1** was shown to efficiently promote the Diels-Alder reaction of aromatic molecules, such as perylene and triphenylene, which are inert under ordinary thermal conditions (Figure 2c).<sup>[13]</sup> However, the above-mentioned problems also exist for such confined cavity. If the size of aromatic molecules is decreased, no reaction proceeds even within the cavity (Figure 2d). On the other hand, the cage is not capable of conducting a catalytic reaction because the product was found tightly packed inside the cavity. As a solution, the cage with shrunken cavity is introduced for Diels-Alder reaction. Because the shrunken cavity is modified in size and shape, it is expected to show different reactivity for small aromatic molecules and different binding affinity for substrates and products.



**Figure 2.** a)  $M_6L_4$  self-assembled cage **1**. b) regio-selectivity of Diels-Alder reaction within cage **1**. c) activation of inert diene for Diels-Alder reaction by cage **1**. d) no reaction for small inert diene.

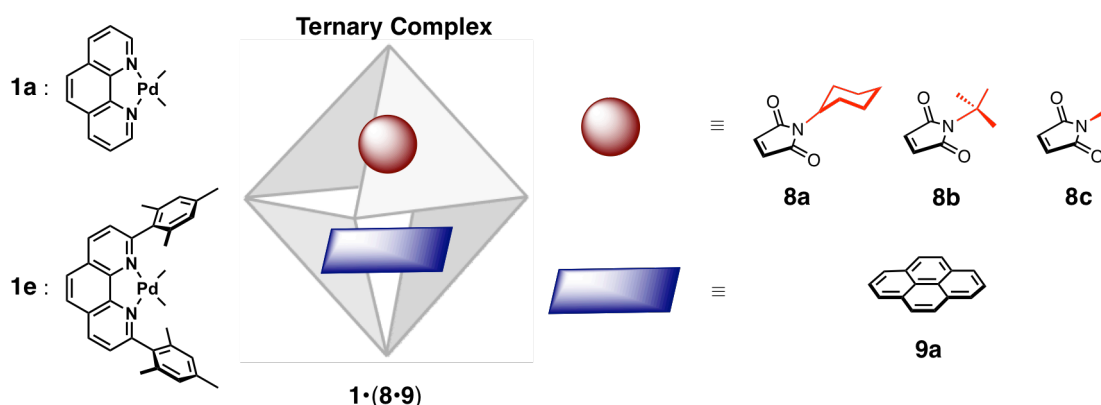
In this chapter, we firstly investigated the bimolecular recognition by cage with shrunken cavity. After finding a suitable guest pair for panel guest and spherical guest, we introduced diene as panel guest and study the Diels-Alder reaction inside the cavity (Scheme 1).



**Scheme 1.** Bimolecular reaction and Diels-Alder reaction by cage 1.

## 5.2 Bimolecular Recognition

Ternary complexes are described as host–guest assemblies in which a host includes two different guest molecules.<sup>[14-16]</sup> Due to entropic disadvantages, the formation of stable ternary complexes is relatively unusual unless there is a specific interaction between the two guests, such as charge transfer, electrostatic, or hydrogen bonding interactions.<sup>[17-21]</sup> Long ago, our group have previously reported that a large cavity of self-assembled  $M_6L_4$  cage (**1**) can accommodate a pair of two hydrophobic guests, which do not particularly interact with each other.<sup>[22]</sup> The most suitable combination for the pair formation is proved to be a large aromatic molecule and a round-shaped medium-sized molecule. By selecting and designing the shape and size of the guest molecules, either [2+2] photoadditions<sup>[23, 24]</sup> or [2+4] Diels–Alder<sup>[25-27]</sup> additions are efficiently promoted from pairs of relatively unreactive substrates.

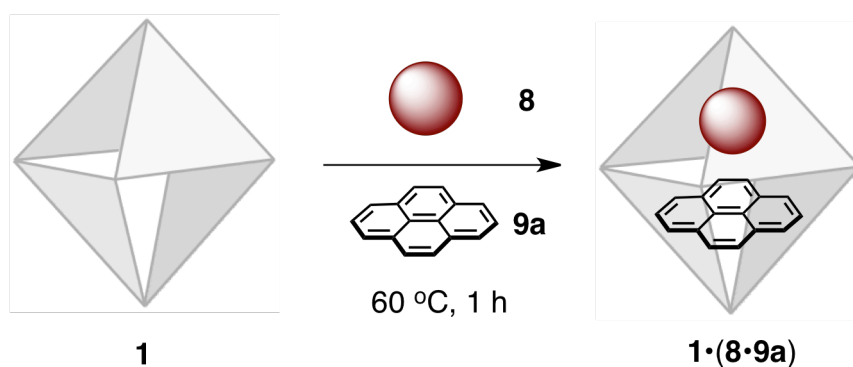


**Figure 3.** Ternary complex and different guest pairs.


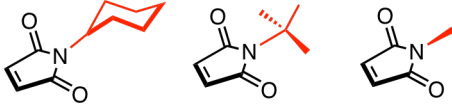
In the above chapters (Chapter 3 and 4), we showed that cage with shrunken cavity show totally different guest binding and guest-motion property for single molecule or homo-molecules. We suspect that the bimolecular recognition will also be different. For screening the best guest pair, we first chose pyrene as the panel aromatic molecule. Then we tuned the substituents on the N atom of round-shape maleimide molecules (Figure 3).

When a suspension of **8a** and **9a** (10-fold excess each) in a D<sub>2</sub>O solution of cage **1** (1 mM) was stirred for 1 h at 60 °C, the color of the solution turned red (Scheme 2). Ternary complex **1a·(8a·9a)** was obtained in 83% NMR yield. In contrast, cage **1e** only bind one molecule of **9a** and formed inclusion complex **1e·9a** in 100% NMR yield, probably due to the remaining space of **1e·9a** is not enough for guest **8a**. When **8a** was replaced by smaller **8b**, ternary complex **1·(8b·9a)** was observed for both cages in 80% and 80% NMR yield, respectively. Further decreasing the size of maleimide (**8c**, *N*-methylmaleimide) maintained the formation of ternary complex **1·(8c·9a)** for both cages but harmed the bimolecular binding affinity for cage **1e** (Table 1). Similar like single molecule encapsulation by cage **1e**, shrunken cavity also show high sensitivity for the size of guest even in the bimolecular recognition.

**Scheme 2.** Procedure for bimolecular recognition of cage **1**.



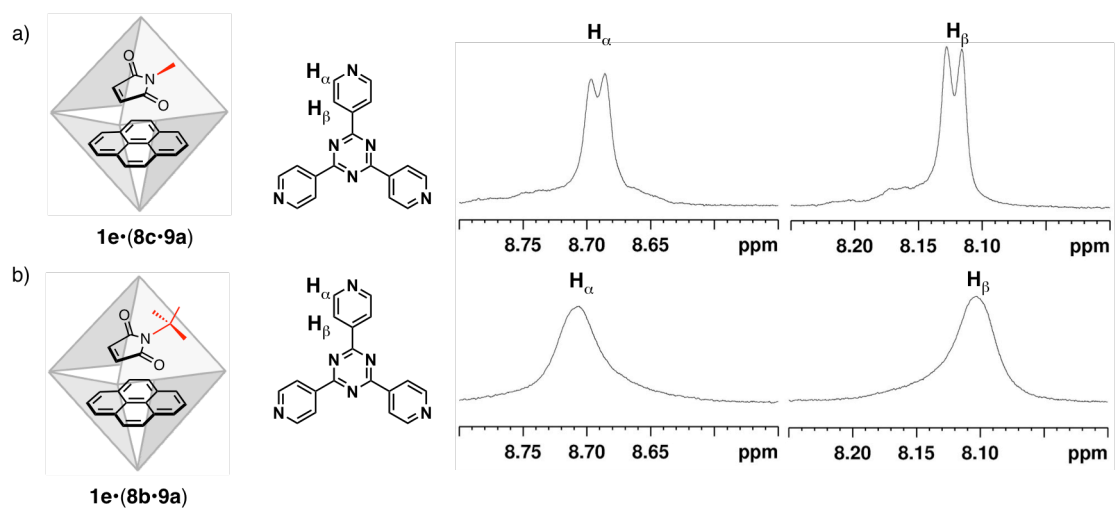
**Table 1.** NMR yields of ternary complex of cage **1**.

Ternary Complex				
		<b>8a</b>	<b>8b</b>	<b>8c</b>
<b>1a·(8·9a)</b>		83%	80%	81%
<b>1e·(8·9a)</b>		0%	80%	69%

On the other hand, the host signals of **1e·(8b·9a)** turned sever broad, while **1a·(8b·9a)** maintain sharp. No broad signals were observed for **1e·(8c·9a)**. Broad signals were only observed for guest pair (**8b·9a**) inside cage **1e** indicated that guest pair was tightly packed within shrunken cavity of cage **1e** (Figure 4). Normally, tightly packed guest pair can make effective use of the cavity and usually show high reactivity

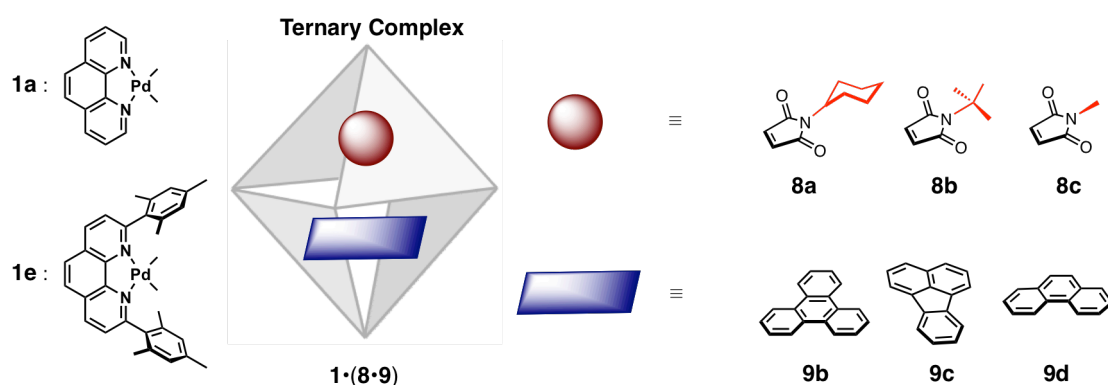


for specific reactions. So maleimide with middle-sized *N*-substituents was expected to be a good dienophile for the reactions. Thus, suitable size of spherical guest is very important for bimolecular recognition of shrunken cavity and it may affect the reactivity of diene.



**Figure 4.** Ternary complex and their host signals of a) **1e·(8c·9a)** and b) **1e·(8b·9a)**.

### 5.3 Diels-Alder Reaction of Small Inert Diene



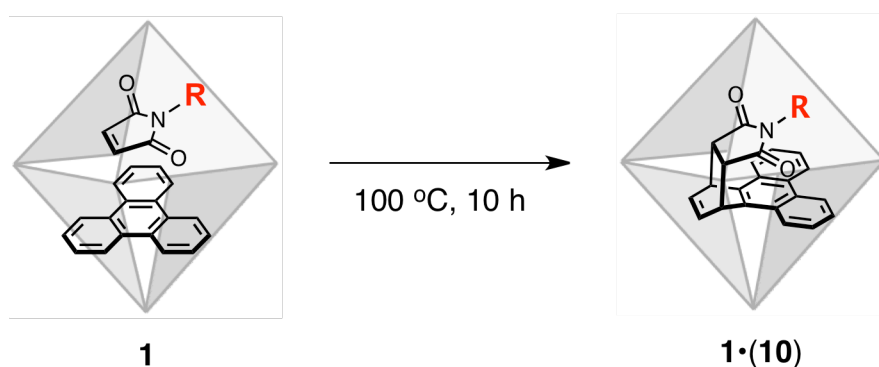
**Figure 5.** Different dienes and dienophiles for Diels-Alder reaction within cage **1**.

Some pericyclic aromatic molecules, such as triphenylene (**9b**), are inert under ordinary thermal conditions. However, we found that the two inert molecules can undergo the Diels-Alder reaction with *N*-cyclohexylmaleimide (**8a**) when trapped inside the conventional cavity of cage **1a**. Although the reaction yield of is moderate (40% based on cage framework), the neat and confined cavity environment apparently accelerated the reaction by putting the two substrates approximate.<sup>[26]</sup> Here, we employed other small dienes as well as tuning the size of dienophile (Figure 5). All these dienes are panel molecules (**9**) and can be pair-wisely encapsulated with the cage **1** when combined with round-shape dienophiles (**8**). The ternary complexes of **1**·(**8**·**9**) have potential to conduct Diels-Alder reaction upon heating. In some cases, stable ternary complex may not be found. But the product is usually strongly bound to the cavity and can be isolated from aqueous phase.

By using smaller dienophile (**8b**), after stirring for 1 h at 60 °C then heating at 100 °C for 10 h, we observed the formation of the Diels-Alder adduct in approximately 21% NMR yield based on cage **1a** (Scheme 3). Because the guest pair packing of smaller dienophile (**8b**) is not as effective as the large dienophile (**8a**), the reaction yield decreased a lot. In contrast, the reaction yield was dramatically improved to 75% by using cage **1e** with shrunken cavity. The product was extracted with chloroform and identified by NMR and MS as compound **10b**, that is, an *endo* Diels-Alder adduct at one of the benzene rings of **10b**. The *syn* stereochemistry of **10b** was confirmed via a NOESY experiment (see “experimental section”). If the dienophile was further

decreased by size, by using dienophile **8c**, no reaction were observed for both cage **1a** and **1e**, probably due to insufficient packing or the “wrong pre-organization” of the guest pair for within the cavity (Table 2). The big difference in reactivity for diene **9b** by different cavity (cage **1a** and **1e**) substantiated the reality: reactivity highly depend on the cavity volume. This inspired me for further investigating more inert compounds

**Scheme 3.** Diels-Alder reaction procedure of triphenylene (**9b**) within cage **1**.



**Table 2.** Diels-Alder reaction yield of triphenylene (**9b**) with different dienophiles within cage **1**.

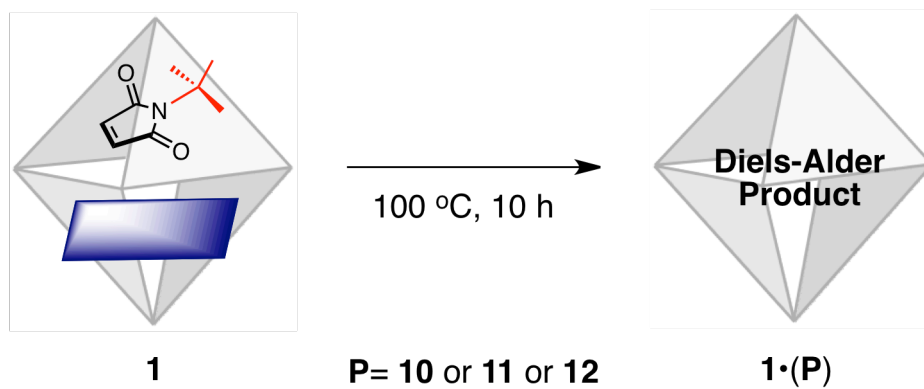
Diels-Alder Product	 <b>8a</b>	 <b>8b</b>	 <b>8c</b>
<b>1a·(10)</b>	40%	21%	0%
<b>1e·(10)</b>	0%	75%	0%

For example, when the size of diene was further decreased, to date, polycyclic reactions involving phenanthrene (**9c**) and fluoranthene (**9d**) have not been reported. The Diels-Alder reaction for the two compounds even cannot proceed within the cavity of **1a**. However, under similar condition (Scheme 4), phenanthrene (**9c**) and fluoranthene (**9d**) can react with dienophile **8b** and afforded the *endo* Diels-Alder adduct (**11b** and **12b**, respectively) within the shrunken cavity of cage **1e** (Table 3). After reaction accomplished, inclusion complex of **1e·11b** and **1e·12b** were fully characterized by <sup>1</sup>H NMR, COSY and NOESY measurements.


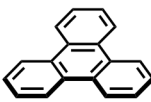
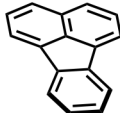
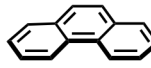
In summary, cage **1b** considerably accelerated the Diels-Alder reaction of small inert diene within its shrunken cavity *via* putting the substrates approximate and

lowering the transition state energy.

**Scheme 4.** Diels-Alder reaction procedure of diene (**9b–d**) with dienophiles (**8b**) within cage **1**.

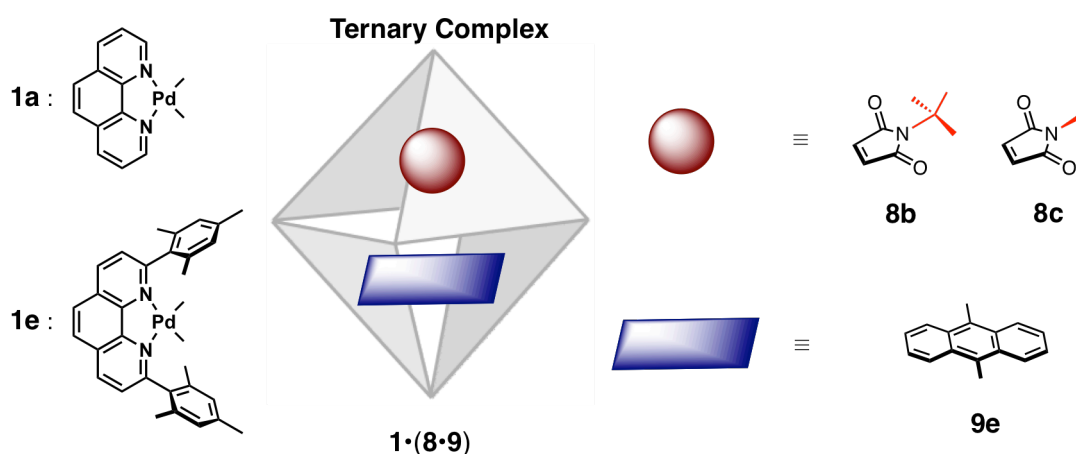


**Table 3.** Diels-Alder reaction yield of diene (**9b–d**) with dienophiles (**8b**) within cage **1**.

Diels-Alder Product	  <b>9b</b>	 <b>9c</b>	 <b>9d</b>
<b>1a·(P)</b>	21%	0%	0%
<b>1e·(P)</b>	75%	41%	37%

## 5.4 Catalytic Diels-Alder Reaction of Anthracene Derivative

Of many aromatic hydrocarbons, anthracene derivatives are the only species used in practical application, despite the utility and wide applicability of the Diels–Alder reaction in organic synthesis.<sup>[28-32]</sup> To date, product inhibition of Diels–Alder reaction limits the potential application of synthetic host in organic synthesis and industry.<sup>[33]</sup> For overcoming this problem, cage with shrunken cavity was introduced and compared with cage with conventional cavity. We applied 9,10-dimethylantracene (**9e**) as diene molecule because the Diels–Alder addition is only proceed at the 9,10-position, which will simplify the product species in our experiments (Figure 6).

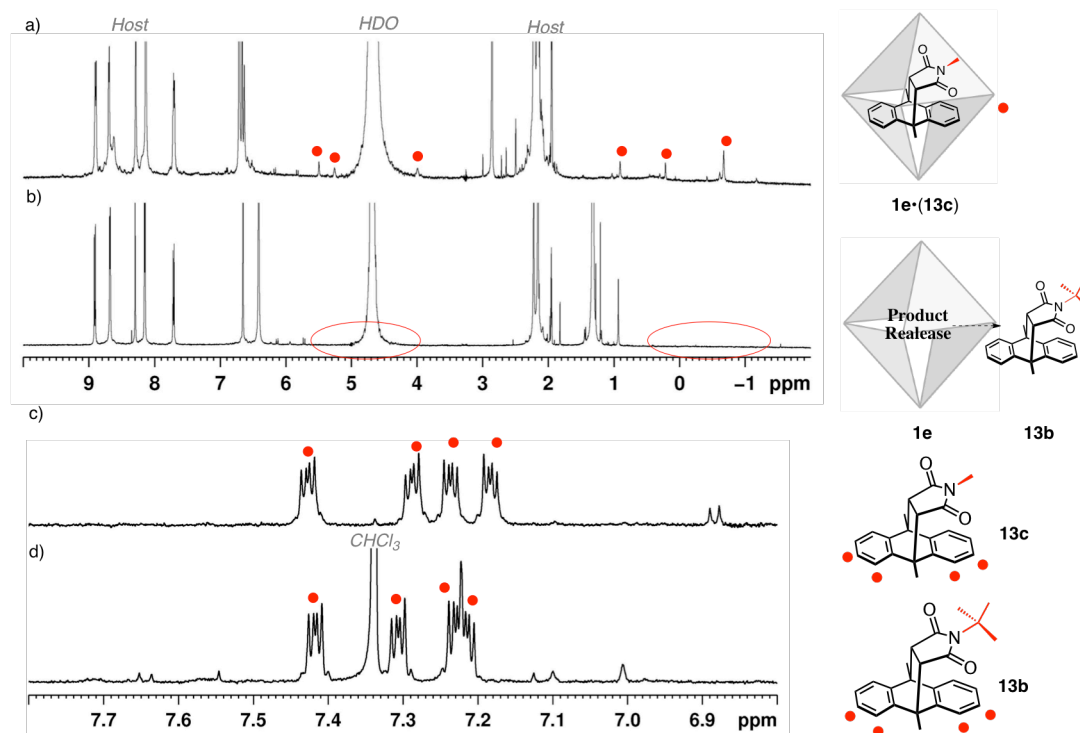


**Figure 6.** Anthracene derivative (**9e**) with different dienophiles for Diels-Alder reaction within cage **1**.

First we investigate the reaction of 9,10-dimethylantracene (**9e**) within the cage **1a** and **1e**. By suspending diene (**9e**) and dienophile (**8a–c**) on the D<sub>2</sub>O solution of cage **1a**, stirring for 1 h at room temperature before filtration of the insoluble compound, then heating the solution at 80 °C for 0.5~1 h, we observed the formation of the Diels-Alder adduct in approximately isolated 95~99% yield based on diene **9e**. By using cage **1e**, dienophile **8b** and **8c** formed the same Diels-Alder adduct but no reaction was observed for the bulky dienophile **8a**. This is because the bulky dienophile **8a** cannot enter the shrunken cavity of **1e** when it was occupied by a panel diene **9e**. The Diels-Alder adduct **13b** and **13c** were isolated and fully characterized by 1D, 2D NMR and MALDI-TOF mass measurements (Figure 7c, d).

Though Diels-Alder adduct **13b** and **13c** were produced in similar yields, however, difference was found for cage **1e** when it produced the two products. After the reaction, aqueous phase were subjected to NMR. Product **13c** was found within

the cavity of cage. In contrast, product **13b** was not encapsulated by but released to the water phase (Figure 7a, b). This unusual phenomenon suggested that cage have potential to catalyze the Diels-Alder reaction of 9,10-dimethylantracene (**9e**).



**Figure 7.** Water phase after Diels-Alder reaction between diene **9e** with dienophile a) **8c** and b) **8b** by cage **1e**; Diels-Alder reaction product of c) **13c** and d) **13b** after extraction by organic solvent.

Then catalytic Diels-Alder reaction was then discussed (Scheme 5). Because Diels-Alder reaction of **8b** and **9e** hardly proceed in organic solution, only 5% product was found after heating at reflux in  $\text{CHCl}_3$  for 2 h. When **8b** and **9e** were suspended in an aqueous solution, the corresponding Diels-Alder products were obtained in 10% isolated yield after heating at 80 °C for 2 h. Indeed, water slightly increases the reaction rate. When in the presence of a catalytic amount of **1a** (2 mol %), reaction rate remains the same as blank water. After extraction by  $\text{CHCl}_3$ , 10% yield of product was confirmed. At the same time,  $^1\text{H}$  NMR of aqueous phase elucidated the inclusion complex **1a**·**13b** which caused product inhibition. However, when in the presence of a catalytic amount of **1e** (2 mol %), the reaction was dramatically accelerated and 90% isolated yield was achieved. Surprisingly, no product was found inside the cavity of **1e** indicating smoothly release of the product after its formation by the shrunken cavity. If smaller dienophile (**8c**) was used, Diels-Alder products (**13c**) were found inside the cavity of cage **1e** and no catalytic reaction was

found (Table 4). This suggested the size of dienophile is very crucial for product release.

**Scheme 5.** Catalytic Diels-Alder reaction procedure with or without cage **1**.



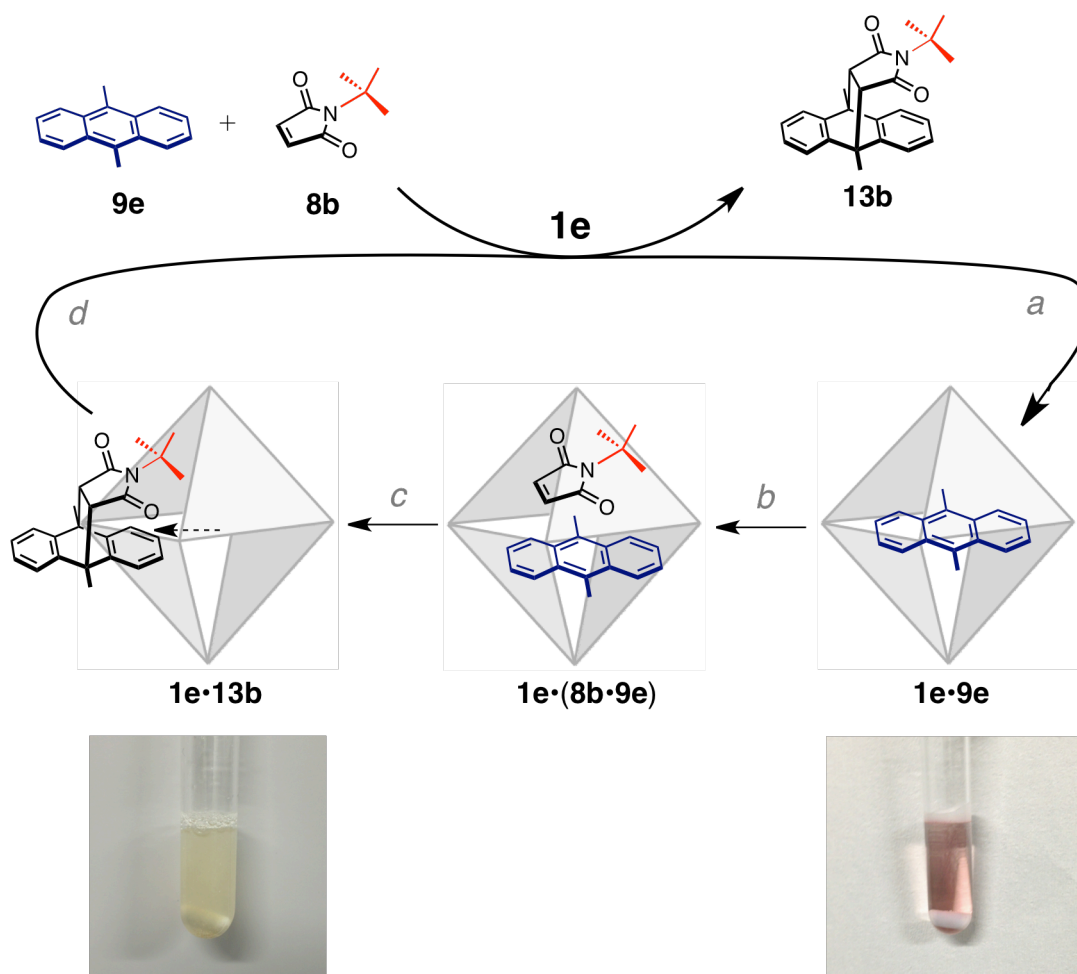
**Table 4.** Isolated Diels-Alder reaction yield of diene (**9e**) with dienophiles (**8b**).

<b>Cage</b>	–	–	<b>Cage 1a</b>	<b>Cage 1e</b>
<b>Solvent</b>	$\text{CHCl}_3$	$\text{D}_2\text{O}$	$\text{D}_2\text{O}$	$\text{D}_2\text{O}$
<b>Yield<sup>a</sup></b>	<b>5%</b>	<b>10%</b>	<b>10%</b>	<b>90%</b>

<sup>a</sup> Isolated yield based on starting material (diene).

The shrunken cavity of cage **1e** overcame the product inhibition by releasing the product as soon as the product was formed. In the initial state of the reaction, diene **9e** can stack onto the triazine ligand of **1e**, gaining considerable stabilization via aromaticaromatic or charge-transfer interactions. This is proved by red color of the solution and formation of inclusion complex of **1e**·**9e** by NMR (Scheme 6a). The reactant-like transition state is similarly stabilized and allowing access by dienophile molecule. Once accessing a dienophile, the diene quickly reacted and the ternary complex was hardly found (Scheme 6b). However, after the formation of product (Scheme 6c), due to the bent geometry of product framework at the 9,10-position, host-guest aromatic stacking interaction was cut off, thus binding affinity of product is much weaker than the substrate. On the other hand, because shrunken cavity is very sensitive for the size of the guest, sudden enlarged product is a very unfavorable guest for shrunken cavity, thus product release was conduct (Scheme 6d). Accordingly, the encapsulated product is considerably destabilized and smoothly replaced by incoming dienes (Scheme 6a). In this fashion, the affinity of the host for reactive substrates and the disaffinity for product is markedly similar to enzymatic behavior.

**Scheme 6.** Catalytic Diels-Alder reaction procedure with or without cage **1**.



Several control experiments were also been done. When presence of only diene, the shrunken cavity encapsulated single molecule of the diene **9e** and formed inclusion complex of **1e-9e** in quantitative form. Heating the solution of this inclusion complex **1e-9e** at high temperature (100 °C) for long time (4 h) will not cause the release of the diene molecule. When treating the isolated product, cage **1e** cannot encapsulated it at all even temperature was elevated to 100 °C. Furthermore, by adding each components (TPT or Pd) of the cage **1e** will not accelerated the reaction at all. All these evidences supported the catalytic reaction proceeded inside the cavity and shrunken cavity released the product when it was formed.

In summary, catalytic Diels-Alder reaction of anthracene derivative has been achieved by cage with shrunken cavity. Owing to different affinity for substrates and products, smooth release of the product from the cavity contributes the most for the catalytic cycle.



## **5.5 Conclusion**

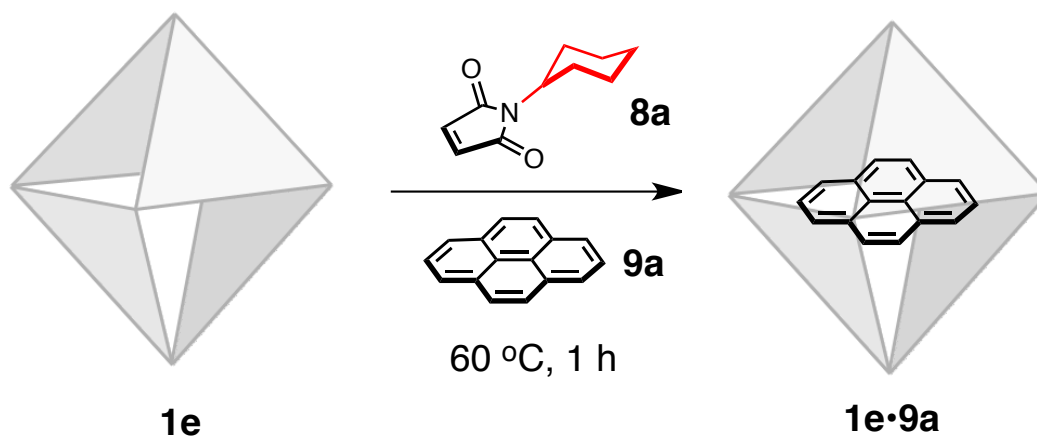
In summary, we successfully activate small inert dienes for Diels-Alder reaction within the shrunken cavity and catalyze the Diels-Alder coupling of the anthracene derivative and the maleimide. The shrunken cavity brings the small diene and dienophile into close proximity and significantly low the entropy costs of Diels-Alder reaction between them. Discriminating the product from substrate furnished the catalytic reaction by the shrunken cavity.

## **5.6 Experiment Section**

### **Materials and Instrumentations:**

<sup>1</sup>H and other NMR spectra were recorded on a Bruker DRX-500 (500 MHz) spectrometer. TMS (CDCl<sub>3</sub> solution) in a capillary served as an external standard ( $\delta = 0$  ppm). MALDI-TOF mass spectra were measured on an Applied Biosystem Voyager DE-STR. Solvents and reagents were purchased from TCI Co., Ltd., WAKO Pure Chemical Industries Ltd., and Sigma-Aldrich Co. Deuterated H<sub>2</sub>O was acquired from Cambridge Isotope Laboratories, Inc. and used as supplied for the complexation reactions and NMR measurements.

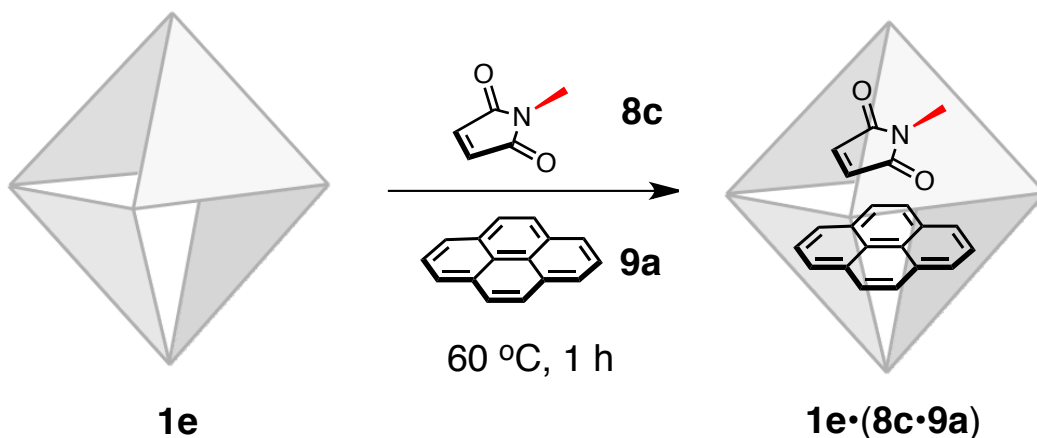
### General Procedure for formation of ternary complex of **1**•(**8**•**9**)



When an excess amount of **8a** and **9a** (10 eq. for cage **1**) was suspended in a D<sub>2</sub>O solution (0.5 mL) of cages **1** (0.5 μmol; 1 mM) and the resulting solution was stirred at 60 °C for 1 h, the solution color turned from colorless to red. After removal of residual guests by filtration, <sup>1</sup>H NMR confirmed the formation of inclusion complexes **1e•9a** in 99% yields. No ternary complex of **1e**•(**8a**•**9a**) was found.

#### Physical Data of Inclusion Complex **1e•9a**

<sup>1</sup>H NMR (500 MHz, D<sub>2</sub>O, 300 K) δ: 9.05 (d, *J* = 8.5 Hz, 12h, **1e**), 8.83 (d, *J* = 6.0 Hz, 24H, **1e**), 8.43 (s, 12h, **1e**), 8.21 (d, *J* = 6.5 Hz, 24H, **1e**), 7.85 (d, *J* = 8.5 Hz, 12h, **1e**), 6.76 (s, 24H, **1e**), 6.23 (br, 4H, **9a**), 6.11 (br, 8H, **9a**), 5.57 (br, 8H, **9a**), 2.32–2.26 (m, 108H, Mes, **1e**). Yield: 99%.

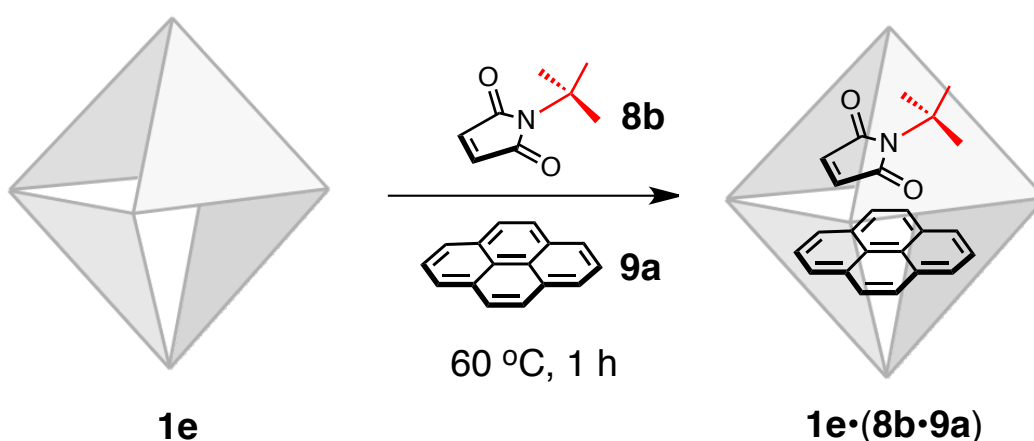


When an excess amount of **8c** and **9a** (10 eq. for cage **1**) was suspended in a D<sub>2</sub>O solution (0.5 mL) of cages **1** (0.5 μmol; 1 mM) and the resulting solution was stirred at

60 °C for 1 h, the solution color turned from colorless to pale red. After removal of residual guests by filtration,  $^1\text{H}$  NMR confirmed the formation of ternary complex of **1e**·(**8c**·**9a**) in 69% yields.

*Physical Data of Inclusion Complex 1e·(8c·9a)*

$^1\text{H}$  NMR (500 MHz,  $\text{D}_2\text{O}$ , 300 K)  $\delta$ : 9.04 (d,  $J = 8.5$  Hz, 12h, **1e**), 8.82 (d,  $J = 6.0$  Hz, 24H, **1e**), 8.42 (s, 12h, **1e**), 8.20 (d,  $J = 6.5$  Hz, 24H, **1e**), 7.84 (d,  $J = 8.5$  Hz, 12h, **1e**), 6.74 (s, 24H, **1e**), 6.26 (br, 4H, **9a**), 6.12 (s, 2H, **8c**), 6.08 (br, 8H, **9a**), 5.57 (br, 8H, **9a**), 2.62 (s, 3H, **8c**), 2.32–2.26 (m, 108H, Mes, **1e**). Yield: 69%.

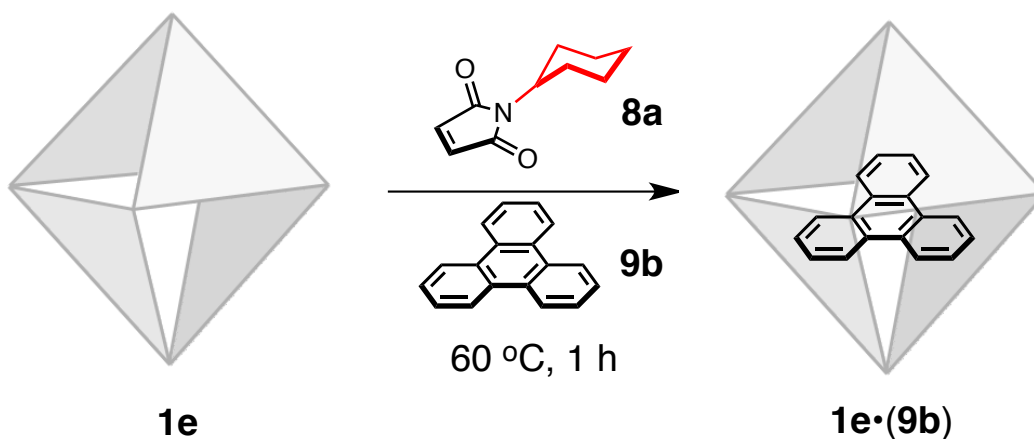


When an excess amount of **8b** and **9a** (10 eq. for cage **1**) was suspended in a  $\text{D}_2\text{O}$  solution (0.5 mL) of cages **1** (0.5  $\mu\text{mol}$ ; 1 mM) and the resulting solution was stirred at 60 °C for 1 h, the solution color turned from colorless to pale red. After removal of residual guests by filtration,  $^1\text{H}$  NMR confirmed the formation of ternary complex of **1e**·(**8b**·**9a**) in 80% yields.

*Physical Data of Inclusion Complex 1e·(8b·9a)*

$^1\text{H}$  NMR (500 MHz,  $\text{D}_2\text{O}$ , 300 K)  $\delta$ : 9.01 (d,  $J = 8.5$  Hz, 12h, **1e**), 8.80 (br, 24H, **1e**), 8.39 (s, 12h, **1e**), 8.25 (br, 24H, **1e**), 7.80 (d,  $J = 8.5$  Hz, 12h, **1e**), 6.57 (br, 24H, **1e**), 6.16 (br, 4H, **9a**), 6.15 (s, 2H, **8b**), 5.96 (br, 8H, **9a**), 5.40 (s, 8H, **9a**), 2.32–2.26 (m, 108H, Mes, **1e**), 1.31 (s, 3H, **8b**). Yield: 80%.

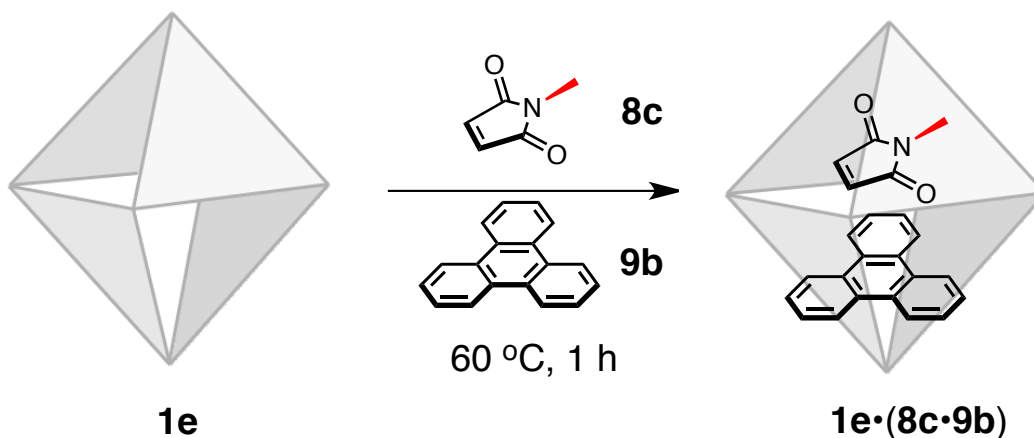
### General Procedure for Diels-Alder Reaction within Cage **1e**



When an excess amount of **8a** and **9b** (10 eq. for cage **1**) was suspended in a D<sub>2</sub>O solution (0.5 mL) of cages **1** (0.5 μmol; 1 mM) and the resulting solution was stirred at 60 °C for 1 h, the solution color turned from colorless to pale yellow. After removal of residual guests by filtration, <sup>1</sup>H NMR confirmed the formation of inclusion complexes **1e·9b** in 66% yields. No ternary complex of **1e·(8a·9b)** was found.

#### Physical Data of Inclusion Complex **1e·9b**

<sup>1</sup>H NMR (500 MHz, D<sub>2</sub>O, 300 K) δ: 9.06 (d, *J* = 8.5 Hz, 12h, **1e**), 8.85 (d, *J* = 6.0 Hz, 24H, **1e**), 8.44 (s, 12h, **1e**), 8.18 (d, *J* = 6.5 Hz, 24H, **1e**), 7.86 (d, *J* = 8.5 Hz, 12h, **1e**), 6.76 (s, 24H, **1e**), 5.66 (br, 6H, **9b**), 5.60 (br, 8H, **9b**), 2.35–2.27 (m, 108H, Mes, **1e**). Yield: 66%.

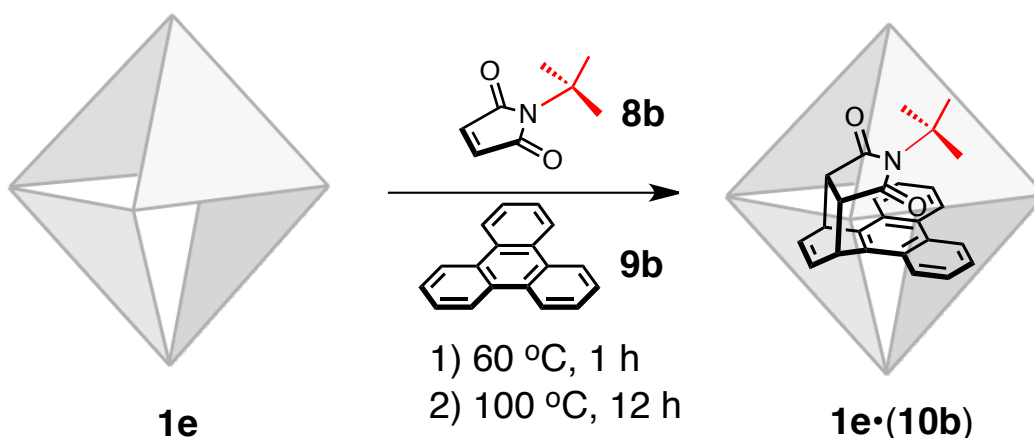


When an excess amount of **8c** and **9b** (10 eq. for cage **1**) was suspended in a D<sub>2</sub>O

solution (0.5 mL) of cages **1** (0.5  $\mu\text{mol}$ ; 1 mM) and the resulting solution was stirred at 60 °C for 1 h, the solution color turned from colorless to pale yellow. After removal of residual guests by filtration, then heating the solution at 100 °C for 12 h,  $^1\text{H}$  NMR confirmed the formation of ternary complex of **1e**·(**8c**·**9b**) in 69% yields. No Diles-Alder adduct was found after extraction by  $\text{CHCl}_3$ .

*Physical Data of Inclusion Complex 1e·(8c·9b)*

$^1\text{H}$  NMR (500 MHz,  $\text{D}_2\text{O}$ , 300 K)  $\delta$ : 9.05 (d,  $J = 8.5$  Hz, 12h, **1e**), 8.84 (d,  $J = 6.0$  Hz, 24H, **1e**), 8.43 (s, 12h, **1e**), 8.18 (d,  $J = 6.5$  Hz, 24H, **1e**), 7.84 (d,  $J = 8.5$  Hz, 12h, **1e**), 6.73 (s, 24H, **1e**), 6.12 (s, 2H, **8c**), 5.64 (br, 6H, **9b**), 5.57 (br, 6H, **9b**), 2.62 (s, 3H, **8c**), 2.32–2.26 (m, 108H, Mes, **1e**). Yield: 69%.

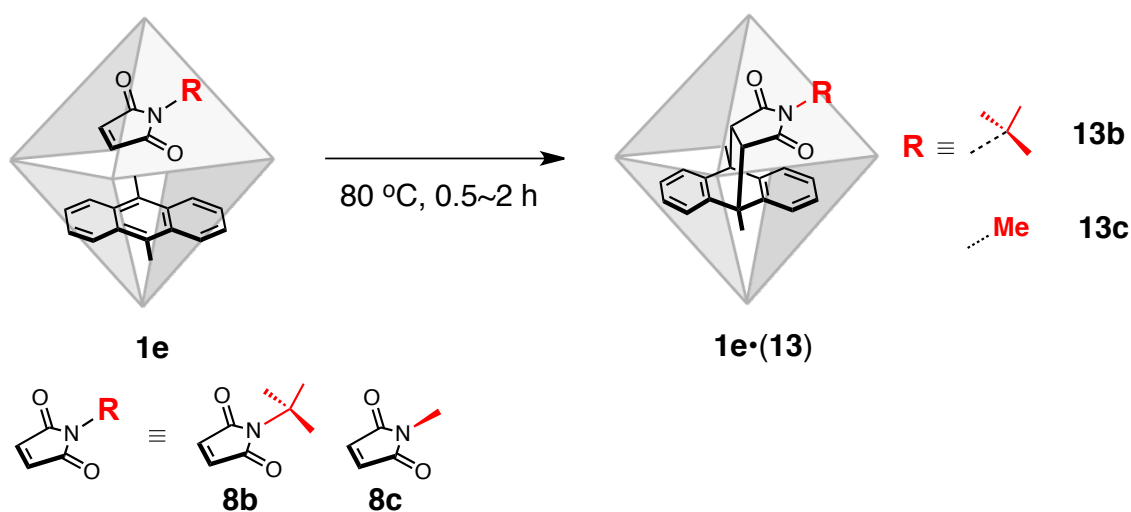


When an excess amount of **8b** and **9b** (10 eq. for cage **1**) was suspended in a  $\text{D}_2\text{O}$  solution (0.5 mL) of cages **1** (0.5  $\mu\text{mol}$ ; 1 mM) and the resulting solution was stirred at 60 °C for 1 h, the solution color turned from colorless to pale red. After removal of residual guests by filtration, then heating the solution at 100 °C for 12 h,  $^1\text{H}$  NMR confirmed the formation of inclusion complex of **1e**·(**10b**) in 75% yields. After filtration, extraction with  $\text{CHCl}_3$ , and purification by column chromatography (Hexane/EtOAc), *syn*-Diels-Alder adduct **10b** was isolated as a white solid.

*Physical Data of Diels-Alder Adduct 10b*

$^1\text{H}$  NMR (500 MHz,  $\text{D}_2\text{O}$ , 300 K)  $\delta$ : 8.73 (d,  $J = 8.0$  Hz, 2H), 8.28 (d,  $J = 8.0$  Hz, 2H), 7.72 (d-d,  $J = 8.5$  Hz, 2H), 7.67 (d-d,  $J = 8.5$  Hz, 2H), 6.86 (t,  $J = 4.0$  Hz, 2h, **1a**), 4.81

(s, overlapped by HDO, 2H), 3.12 (s, 2H), 1.05 (s, 9H), Yield: 75%.



When an excess amount of **9e** (10 eq. for cage **1**) was suspended in a D<sub>2</sub>O solution (0.5 mL) of cages **1** (0.5 μmol; 1 mM) and the resulting solution was stirred at 60 °C for 0.5 h, the solution color turned from colorless to red. Then 1 eq of **8b** was added, the solution was heat at 80 °C for 1 h. After filtration, extraction with CHCl<sub>3</sub>, and purification by column chromatography (CHCl<sub>3</sub>), *syn*-Diels-Alder adduct **13b** was isolated. *syn*-Diels-Alder adduct **13c** was prepared in the same way.

#### Physical Data of Diels-Alder Adduct **13b**

<sup>1</sup>H NMR (500 MHz, CDCl<sub>3</sub>, 300 K) δ: 7.38 (m, 2H), 7.28 (m, 2H), 7.20 (m, 4H), 2.67 (s, 2H), 1.07 (s, 9H), Yield: 95%.

#### Physical Data of Diels-Alder Adduct **13c**

<sup>1</sup>H NMR (500 MHz, CD<sub>2</sub>Cl<sub>2</sub>, 300 K) δ: 7.43 (m, 2H), 7.28 (m, 2H), 7.22 (m, 2H), 7.18 (m, 2H), 2.48 (s, 2H), 0.90 (s, 3H), Yield: 92%.

## 5.7 REFERENCES

- [1] L. Pauling, *Am. Sci.* **1948**, 36, 51.
- [2] W. P. Jencks, *Catalysis in Chemistry and Enzymology* (McGraw-Hill, New York, **1969**).
- [3] D. J. Cram,; J. M. Cram, *Container Molecules and Their Guests* (Royal Society of Chemistry, Cambridge, **1994**).
- [4] J. M. Steed,; J. L. Atwood, *Supramolecular Chemistry* (Wiley, Chichester, UK, **2000**).
- [5] M. Marty,; Z. C. Watson,; L. J. Twyman,; M. Nakash,; J. K. Sanders, *M. Chem. Commun.* **1998**, 2265.
- [6] J. Kang,; J. Rebek Jr., *Nature* **1997**, 385, 50.
- [7] J. Chen,; J. Rebek Jr., *Org. Lett.* **2002**, 4, 327.
- [8] T. Kusukawa,; T. Nakai,; T. Okano,; M. Fujita, *Chem. Lett.* **2003**, 32, 284.
- [9] D. Fiedler,; R. G. Bergman,; K. N. Raymond, *Angew. Chem. Int. Ed. Engl.* **2004**, 43, 6748.
- [10] M. L. Merlau,; M. P. Mejia,; S. T. Nguyen,; J. T. Hupp, *Angew. Chem. Int. Ed. Engl.* **2001**, 40, 4239.
- [11] J. Kang,; J. Santamarfa,; G. Hilmersson,; J. Rebek, Jr., *J. Am. Chem. Soc.* **1998**, 120, 7389.
- [12] M. Yoshizawa,; M. Tamura,; M. Fujita, *Science* **2006**, 312, 251.
- [13] Y. Nishioka,; T. Yamaguchi,; M. Yoshizawa,; M. Fujita, *J. Am. Chem. Soc.* **2007**, 129, 7000.
- [14] E. Fenyvesi,; L. Szenté,; N. R. Russell; M. McNamara, *Comprehensive Supramolecular Chemistry* (Oxford, **1996**, 3, 305.)
- [15] T. Heinz,; D. M. Rudkevich,; J. Rebek, Jr.,; *Nature*, **1998**, 394, 764.
- [16] H.-J. Kim,; J. Heo,; W. S. Jeon,; E. Lee,; J. Kim,; S. Sakamoto,; K. Yamaguchi,; K. Kim,; *Angew. Chem., Int. Ed.*, **2001**, 40, 1526.
- [17] V. Sindelar,; M. A. Cejas,; F. M. Raymo,; W. Chen,; S. E. Parker,; A. E. Kaifer, *Chem.–Eur. J.*, **2005**, 11, 7054.
- [18] S. Liu,; P. Y. Zavalij; L. Isaacs, *J. Am. Chem. Soc.*, **2005**, 127, 16798.
- [19] Y. Ling,; W. Wang,; A. E. Kaifer, *Chem. Commun.*, **2007**, 610.
- [20] S. Liu,; A. D. Shukla,; S. Gadde,; B. D. Wagner,; A. E. Kaifer,; L. Isaacs, *Angew. Chem., Int. Ed.*, **2008**, 47, 2657.
- [21] T. Han,; C.-F. Chen, *Org. Lett.*, **2007**, 9, 4207.



- [22] M. Yoshizawa,; M. Tamura,; M. Fujita, *J. Am. Chem. Soc.*, **2004**, 126, 6846.
- [23] Y. Nishioka,; T. Yamaguchi,; M. Kawano,; M. Fujita, *J. Am. Chem. Soc.*, **2008**, 130, 8160.
- [24] M. Yoshizawa,; J. K. Klosterman,; M. Fujita, *Angew. Chem., Int. Ed.*, **2009**, 48, 3418.
- [25] M. Yoshizawa,; M. Tamura,; M. Fujita, *Science*, **2006**, 312, 251.
- [26] Y. Nishioka,; T. Yamaguchi,; M. Yoshizawa,; M. Fujita, *J. Am. Chem. Soc.* **2007**, 129, 7000.
- [27] T. Murase,; S. Horiuchi,; M. Fujita, *J. Am. Chem. Soc.*, **2010**, 132, 2866.
- [28] J. C. C. Atherton,; S. Jones, *Tetrahedron* **2003**, 59, 9039.
- [29] K. L. Burgess,; M. S. Corbett,; P. Eugenio,; N. J. Lajkiewicz,; X. Liu,; A. Sanyal,; W. Yan,; Q. Yuan,; K. Snyder, *Bioorg. Med. Chem.* **2005**, 13, 5299.
- [30] B. R. Bear,; S. M. Sparks,; K. J. Shea, *Angew. Chem. Int. Ed.* **2001**, 40, 820.
- [31] K. C. Nicolaou,; S. A. Snyder,; T. Montagnon,; G. Vassilikogiannakis, *Angew. Chem. Int. Ed.* **2002**, 41, 1668.
- [32] E. M. Stocking,; R. M. Williams, *Angew. Chem. Int. Ed.* **2003**, 42, 3078.
- [33] S. Horiuchi,; T. Murase,; M. Fujita, *Chem. Asian J.* **2011**, 6, 1839.

## Chapter 6

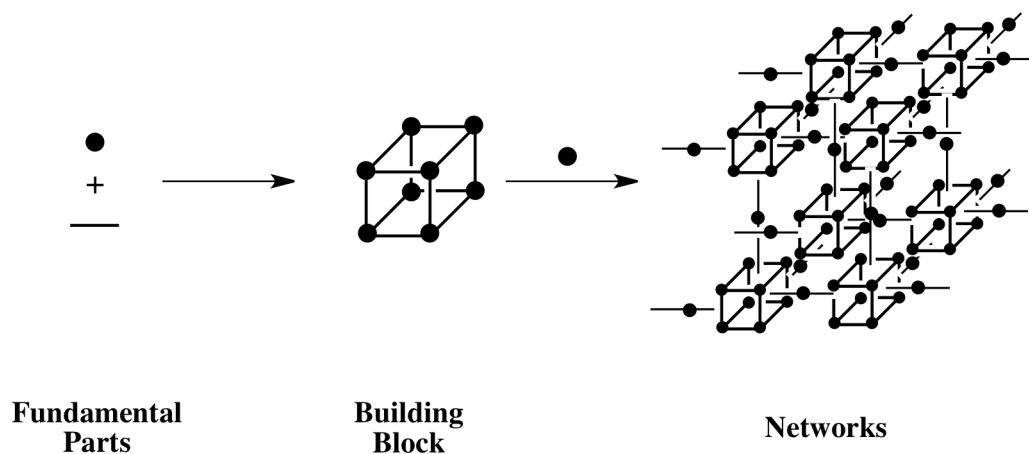
### Bottom-Up Assembly from Helicate to Network through a Remote Binding Site

Bottom-up assembly not only provides a facile way to construct hybrid materials, but also gives an insight into the mechanism of self-assembly. However, ligand design requires hierarchical functional groups in dedicated position. This chapter demonstrated that a homochiral mesoporous network was constructed by a triple stranded helicate through bottom-up assembly.

Inspired by the findings in previous chapters that remote substituents can manipulate the functions of a synthetic host. Pyridine moiety was introduced onto the chiral linear ligand where the pyridyl groups locating far from the major metal-binding site, referring to Schiff base units. Due to the different priorities in coordinating with metal, Schiff base units firstly bind metal ions to form helicate then the network was construct by connecting the remote pyridine moieties. Thus, the remote pyridine substituents changed the structure by bottom-up assembly.

## 6.1 Introduction

Stepwise self-assembly has become a powerful technique to organize modular building blocks into target frameworks, whose topologies and functions were carefully manipulated by the molecular constituents.<sup>[1,2]</sup> Bottom-up approaches refer to methods of building an entire structure from its fundamental parts (Figure 1).



**Figure 1.** Bottom-up approach of self-assembly.

Comparing other different methods, bottom-up approach has its intrinsic advantages, such as monitoring assembly procedure, isolation of intermediate as well as modulating the functionality of the target frameworks.<sup>[3]</sup> However, until now, most metal organic networks were fabricated by a one-pot procedure.<sup>[4-7]</sup>

On the other hand, helical structures, like DNA, are integral to myriad highly sophisticated bioarchitectures, which have motivated chemists to make artificial helical structures.<sup>[8,9]</sup> In general, helicate bears intrinsic chirality, nanometer size, physicochemical properties as well as condensed metal cores.<sup>[10-12]</sup> However, there is rare report for a metal organic network assembled from a helicate.

Here, I found that, by introducing a remote substituent on the linear ligand, discrete helicate can firstly assembled as a building block then constructed coordination networks *via* bottom-up method.

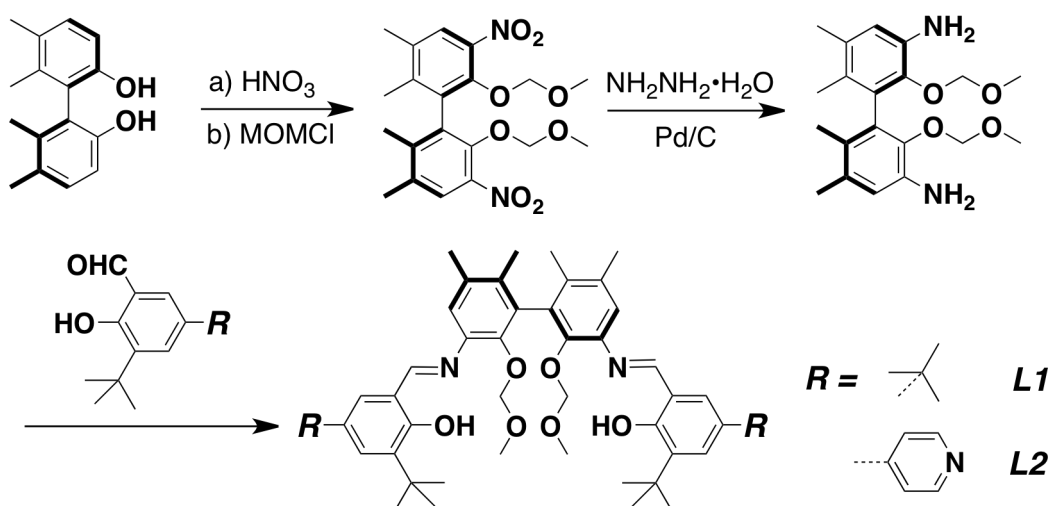
## 6.2 Ligand Design and Synthesis

1,1'-biphenol derivatives with intrinsic  $C_2$ -symmetry are excellent platforms for creating helical species.<sup>[13,14]</sup> My strategy for making helicate consists of using a potential tetraanionic hexadentate 1,1'-biphenol ligand bearing Schiff-base units. On the Schiff-base units, there is a pair of terminal NO donors may chelate metal ions to form linear helicates and the two pendant biphenolic oxygen atoms may entrap more metal ions into the helical cavity, leading to a cluster helicate structure. More importantly, different function groups can be introduced to the *ortho*-positions of the linear ligand, which is far from the major metal binding site (NO pocket). For **L1**, the function group is a *tert*-butyl substituent, which has no metal binding ability. In contrast, when the *tert*-butyl substituent is instead by pyridyl substituent, binding affinity with metal ion is maintained for **L2**. After formation of cluster helicate, the remote free pyridyl groups are expected to point outward from the helicate and further bind metal ions leading to more sophisticated networked structures.<sup>[23]</sup>

The enantiopure Schiff-base ligand **L1** and **L2** were synthesized from 5, 5', 6, 6'-tetramethyl-2, 2'-diol-1, 1'-biphenyl in four steps in an overall ~40% yield (Scheme 1).

These organic compounds were fully characterized by 1D, 2D NMR, IR, thermogravimetric analysis (TGA) and MALDI-TOF mass measurements (see “experimental section”).

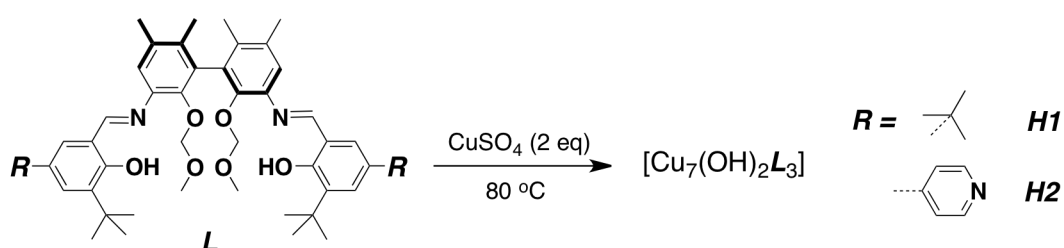
**Scheme 1.** Synthesis of chiral linear ligands **L1** and **L2**.



### 6.3 Self-Assembly of Helicate as Building Block

The solvothermal reaction of (*R*)-**L1** and  $\text{CuSO}_4 \cdot 5\text{H}_2\text{O}$  in a 1:2 molar ratio in DMSO/2-BuOH (2:1 v/v) at  $80^\circ\text{C}$  afforded crystalline single-crystals of  $[\text{Cu}_7(\text{OH})_2(\mathbf{L1})_3] \cdot 2\text{DMSO} \cdot 2\text{H}_2\text{O}$  (**H1**) in 80% yield. The product is soluble in DMSO and practically insoluble in water and other common organic solvents. (*R*)-**L2** also formed the similar compound  $[\text{Cu}_7(\text{OH})_2(\mathbf{L2})_3] \cdot 2\text{DMSO} \cdot 2\text{H}_2\text{O}$  (**H2**) in the same yield (Scheme 2).<sup>[23]</sup>

Scheme 2. Self-assembled of the helicate **H1** and **H2**.



From X-ray single crystallography, both **H1** and **H2** adopt a very similar helical structure and can be viewed as heptanuclear triple-stranded helicate enclosing seven metal ions in its cavity (Figure 2). The only difference between the two helicate is that the outer substituents of helicate **H1** are two *tert*-butyl groups, while of helicate **H2** are one *tert*-butyl and one pyridyl moiety.

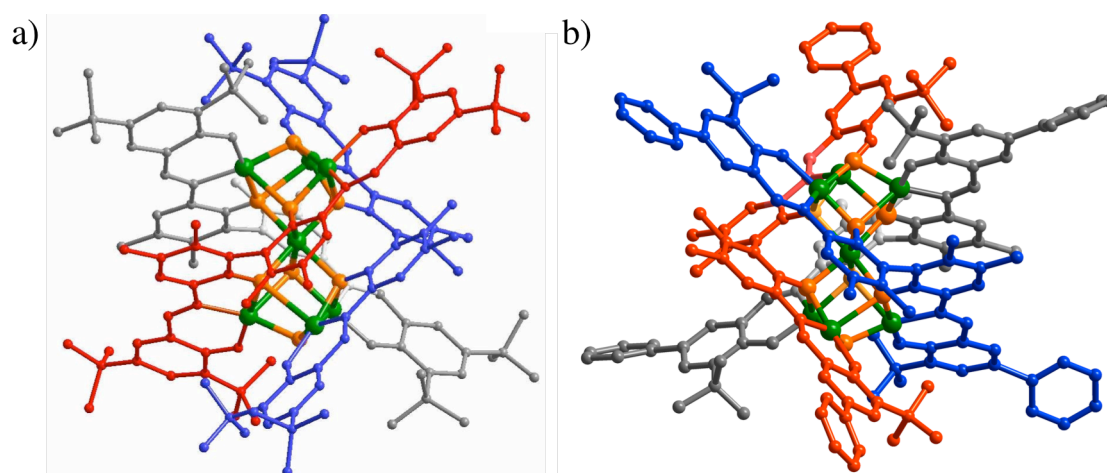
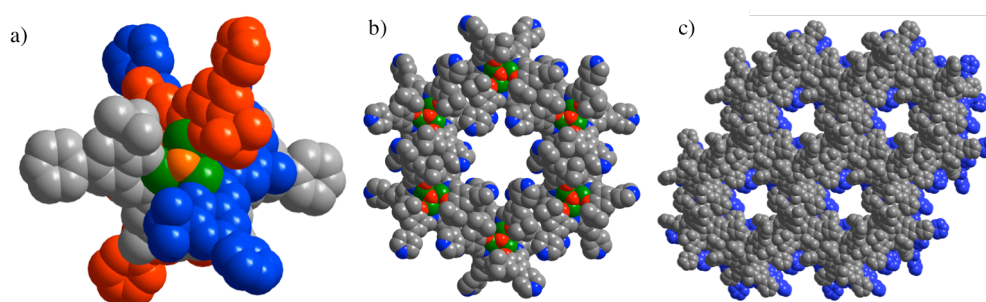


Figure 2. X-ray crystal structure of the helicate a) **H1** and b) **H2** (different color show different molecules of **L** ligand). Reprinted with permission from ref. 23. Copyright 2011 John Wiley and Sons.

For **H1**, seven metal ions are engaged in two  $\text{Cu}_4\text{O}_4$  distorted cubanes by sharing one Cu ion. The six outer Cu ions each are square-pyramidally coordinated by one  $\text{OH}^-$  anion and one N atom and three O atoms from two **L1** ligands, while the central Cu ion is octahedrally coordinated to three N and three O atoms from three **L1** ligands. The MOM groups were completely removed from the starting ligands upon complexation with metal ions, and each **L1** ligand binds to two metal centers through two tridentate  $\text{NO}_2$  donors and to another two metal centers through two biphenolate oxygen atoms. Such an arrangement of the dicubane unit and three **L1** ligands leads to a *P*-configured triple-stranded helicate. With one crystallographic  $C_3$  axis running through a pair of  $\mu_3$ -O atoms and three crystallographic  $C_2$  axes bisecting three pairs of opposite **L1** edges, the  $\text{Cu}_7$  helicate possesses perfect  $D_3$  point group symmetry.

Surprisingly, **H2** adopt a very similar structure with the remote pyridyl moieties intact. Viewing from the two terminal of the helicate (Figure 3a), a snowflake shape structure was clearly observed. The pyridyl moieties are locating outer shell of the helicate pointing to the space. Through packing, strong  $\text{CH}\cdots\pi$  interactions between the methyl group and the conjugated pyridine ring of adjacent helicates ( $\text{C-H}\cdots\pi = 2.65\text{--}3.86 \text{ \AA}$ ) direct packing of helicates along the *c*-axis, making a nanosized tubule with an opening size of  $1.2 \times 1.1 \text{ nm}$  (Figure 3b). The supramolecular structure is reinforced by hydrophobic interactions between *tert*-butyl groups of adjacent helicates and face-to-face intermolecular  $\pi$ - $\pi$  interactions (plane-to-plane separation =  $3.82 \text{ \AA}$ ). Highly directional non-covalent interactions in **H2** thus have clearly steered the packing of helicates to make a homochiral porous 3D nanotubular architecture (Figure 3c). The peripheral free pyridyl groups of **H2** may potentially coordinate additional metal ions to construct extended structures.



**Figure 3.** a) Space filling mode of the helicate **H2**. b) A macrocycle assembled from six helicates of **H2** and c) The 3D porous structure of **H2** viewed along the b-axis. Reprinted with permission from ref. 23.

Copyright 2011 John Wiley and Sons.

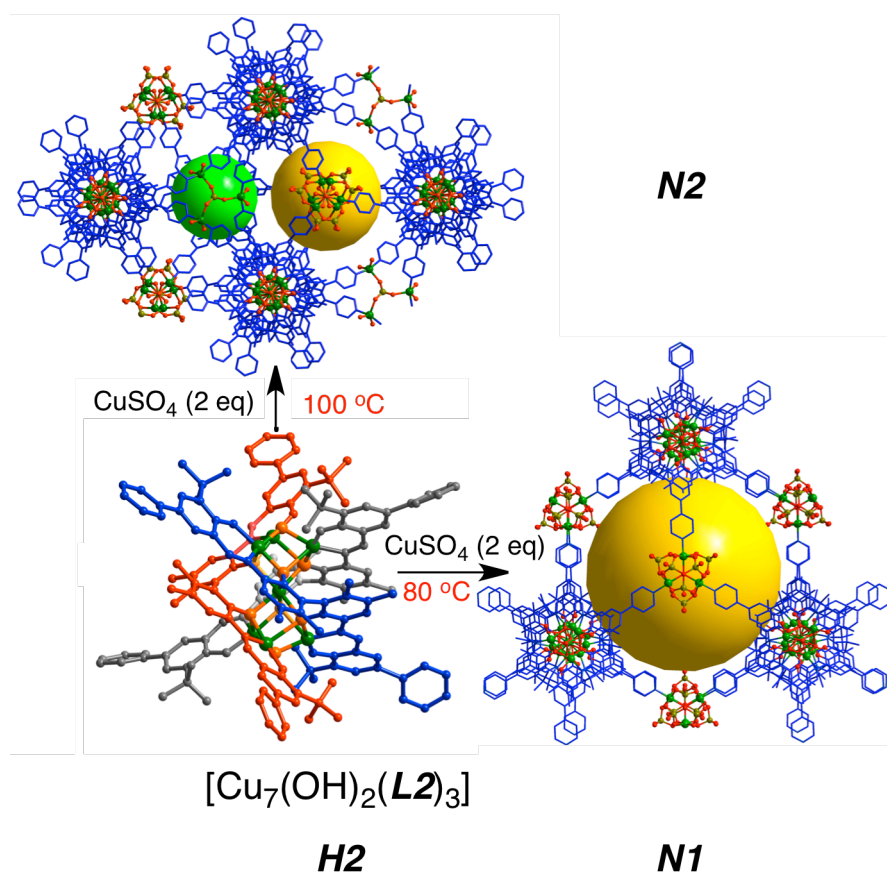
Although The helicate **H1** and **H2** share the same structure in frameworks, the

functionality should be different due to different functional groups. Due to the metal binding affinity of remote pyridyl moiety, helicate **H2** can act as a building block if it is stable in solution state. Finally, the helicate **H2** is proved to be stable in DMSO, as showed by ESI-MS which gave the prominent peak for  $[\text{Cu}_7(\text{OH})_2\text{L}_3 + 7\text{H}]^{7+}$  at  $m/z = 386.9$ . UV-vis spectra of **H2** in DMSO at 25, 80 and 100 °C also gave identical absorption bands at 320, 432, 459 and 605nm. Taking together, these results indicate that the helical structure of **H2** remains intact while allowing it for assembling into 3D frameworks in solution.

## 6.4 Self-assembly of Networks

Because the helicates (**H1** and **H2**) is soluble in organic solvent (e.g. DMSO), **H2** was taken as a building block for further binding metal ions in a homogenous phase. Heating **H2** and  $\text{CuSO}_4 \cdot 5\text{H}_2\text{O}$  (1:2 molar ratio) in DMSO afforded  $[\text{Cu}_7(\text{OH})_2(\text{L2})_3][\text{Cu}_6(\text{OH})_2(\text{SO}_4)_3(\text{S}_3\text{O}_{10})_2] \cdot 10\text{H}_2\text{O}$  (**N1**) in 75% yield at 80 °C and  $[\text{Cu}_7(\text{OH})_2(\text{L2})_3]_2[\text{Cu}_6(\text{OH})_2(\text{SO}_4)_6(\text{S}_2\text{O}_7)] [\text{Cu}_3(\text{SO}_4)(\text{H}_2\text{O})_6] \cdot 18\text{H}_2\text{O}$  (**N2**) in 60% yield at 100 °C (Scheme 3). Both **N1** and **N2** are stable in air and insoluble in water and organic solvents, and are formulated on the basis of elemental analysis, IR and thermogravimetric analysis (TGA). The phase purity of the bulk samples **N1** and **N2** were established by comparison of their observed and simulated powder X-ray diffraction (PXRD) patterns.<sup>[23]</sup>

**Scheme 3.** Self-assembly of a) network **N1** from **H2** at 80 °C and network **N2** from **H2** at 100 °C.

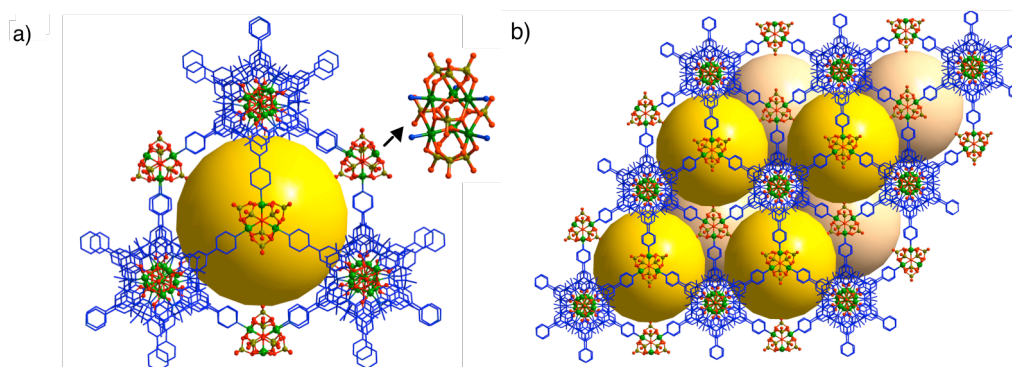


Network **N1** crystallizes in the chiral hexagonal space group  $P6_322$ . As expected, the  $\text{Cu}_7$  helicate binds to six newly generated  $[\text{Cu}_6(\mu_3\text{-OH})_2(\mu_2\text{-SO}_4)_3(\mu_3\text{-S}_3\text{O}_{10})_2]$  ( $\text{Cu}_6\text{-}\alpha$ ) clusters using pyridyl groups. In this  $\text{Cu}_6\text{-}\alpha$  cluster, the metal centers form a  $D_3$



symmetry trigonal prism with top and bottom faces bridged by two  $\mu_3$ -S<sub>3</sub>O<sub>10</sub> anions and the other three faces by three  $\mu_2$ -SO<sub>4</sub> anions; six-coordinate, octahedral geometry at each metal is completed by a  $\mu_3$ -OH unit or a pyridyl group. Therefore, each Cu<sub>6</sub> cluster binds to six pyridyl groups of six Cu<sub>7</sub> helicates, and each Cu<sub>7</sub> helicate connects six Cu<sub>6</sub>- $\alpha$  clusters to form a (6, 6)-connected network.

Six Cu<sub>7</sub> clusters and five Cu<sub>6</sub>- $\alpha$  clusters that are related by C<sub>3</sub> symmetry merge to generate a D<sub>3</sub>-symmetric 4<sup>6</sup>3<sup>6</sup>- $\alpha$  cage (Figure 4a). The cage has an open spherical cavity with an internal diameter of 2.36 nm (considering van der Waals radii) which is occupied by disordered guest molecule, while the quadrilateral aperture on each face

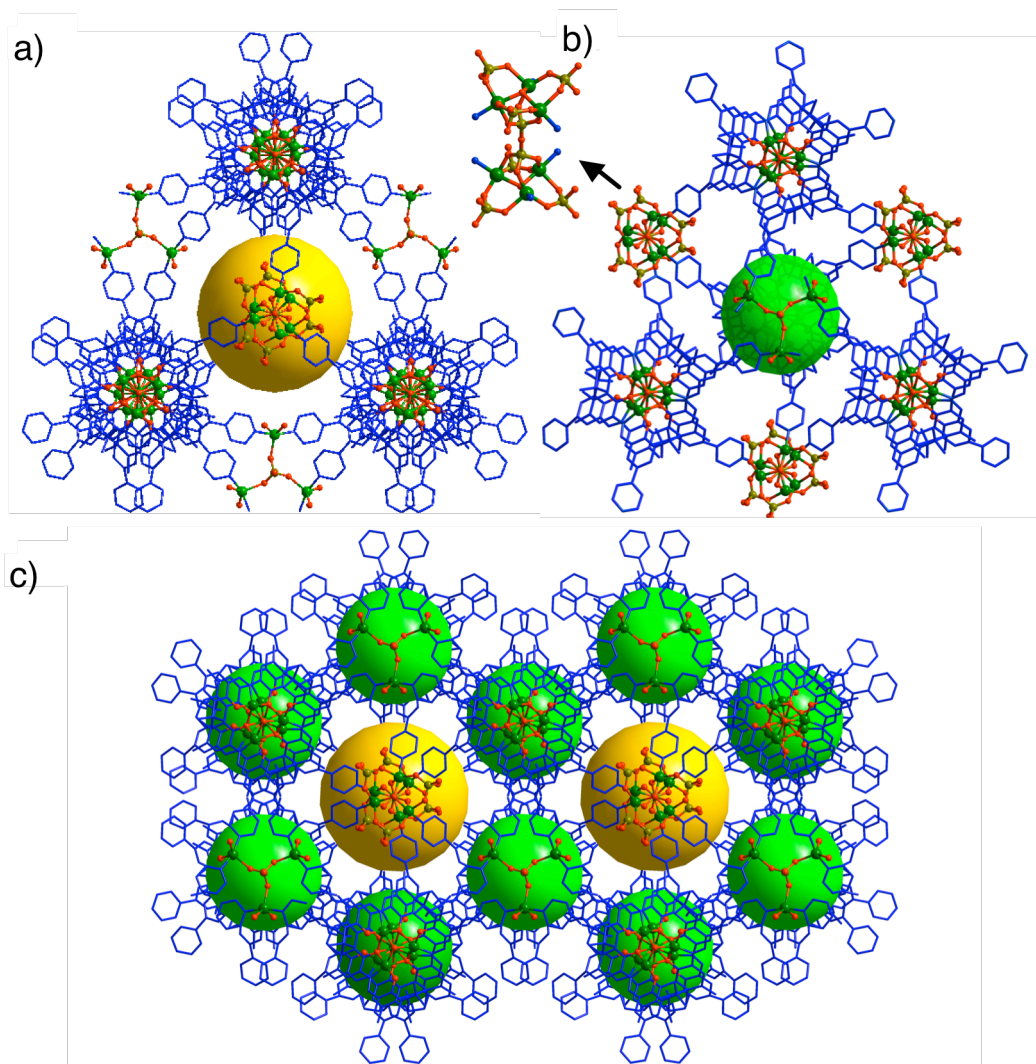


**Figure 4.** a) A mesoporous cage in network **N1** constructed of six helicate **H2**. b) The 3D porous structure of **N1** viewed along the c-axis. Reprinted with permission from ref. 23. Copyright 2011 John Wiley and Sons.

has diagonal distances of  $\sim 1.6 \times 1.6$  nm. The cage shares its quadrilateral and triangular faces with twelve neighboring cages (Figure 4b), while sharing of the square faces gives rise to multidirectional zig-zag channels in the framework of **N1**.

Network **N2** crystallizes in the chiral hexagonal space group *P6<sub>3</sub>22* as well. However, the six pyridines of each helicate are alternatively linked by two types of D<sub>3</sub> symmetry metal clusters, namely, a SO<sub>4</sub><sup>2-</sup>-bridged trimetal cluster [Cu<sub>3</sub>( $\mu_3$ -SO<sub>4</sub>)(H<sub>2</sub>O)<sub>3</sub>] and a hexanuclear cluster [(Cu<sub>3</sub>( $\mu_3$ -OH)( $\mu$ -SO<sub>4</sub>)<sub>2</sub>)( $\mu_6$ -S<sub>2</sub>O<sub>7</sub>)] (Cu<sub>6</sub>- $\beta$ ) with two triangular [Cu<sub>3</sub>( $\mu_3$ -OH)] units bonded by three  $\mu$ -SO<sub>4</sub><sup>2-</sup> anions and linked through one  $\mu_6$ -S<sub>2</sub>O<sub>7</sub><sup>2-</sup> anion. In both cases, five-coordinate trigonal-bipyramidal geometry at each metal is further completed by two pyridine and two water molecules and by one pyridine, respectively. Both hexa- and tricopper clusters are six-connected nodes linked by six pyridyl groups of helicate **L2**, and each helicate **L2** bridges three Cu<sub>3</sub> clusters and three Cu<sub>6</sub>- $\beta$  clusters in a hexadentate fashion, thereby generating a (6, 6)-connected framework.

The framework of **N2** consists of two types of  $D_3$  symmetry cages, namely a larger  $4^{63^6}-\beta$  cage (Figure 5a), similar to that in **N1**, encapsulated by six  $\text{Cu}_7$  clusters, three  $[\text{Cu}_3(\text{SO}_4)(\text{H}_2\text{O})_6]$  and two  $\text{Cu}_6-\beta$  clusters and a smaller  $4^6$  cage (Figure 5b) enclosed by four  $\text{Cu}_7$  helicates, one  $[\text{Cu}_3(\text{SO}_4)(\text{H}_2\text{O})_6]$  and three  $\text{Cu}_6-\beta$  clusters. Each type of cages has an irregular open cavity that has a maximum inner width of  $\sim 2.3$  and  $1.8$  nm, respectively, and is occupied by disordered guest molecules. The quadrilateral aperture on each faces has a diagonal distance of  $\sim 1.6 \times 1.4$  nm. The  $4^{63^6}-\beta$  cage shares its square and triangular faces with six  $4^6$  cages and six  $4^{63^6}-\beta$  cages, respectively, while the  $4^6$  cage shares its quadrilateral faces with three  $4^6$  cages



**Figure 5.** a) A mesoporous cage (yellow sphere) in network **N2** constructed of six helicate **H2**. b) A mesoporous cage (green sphere) in network **N2** constructed of four helicate **H2**. c) The 3D porous structure of **N2** viewed along the c-axis. Reprinted with permission from ref. 23. Copyright 2011 John Wiley and Sons.

and three  $4^63^6$ - $\beta$  cages. Sharing of the quadrilateral windows with neighboring cages leads to multidirectional zig-zag channels in the framework of **N2**.

To our knowledge, until 2011, this is the first example of a truly stepwise construction of MOFs using a helicate. The self-assembly and amplification of intrinsic information encoded in the  $\text{Cu}_7$  helicate is expressed by the formation of the  $\text{Cu}_6$ - $\alpha$  and  $-\beta$  and  $\text{Cu}_3$  clusters, and finally the three types of assembled  $4^63^6$ - $\alpha$  and  $-\beta$  and  $4^6$  cages in **N1** and **N2**, bearing the same handedness of chirality and  $D_3$  symmetry as the helicate precursor. Therefore, the coordination-driven stepwise assembly of the helicate **H2** enabled its geometry, symmetry and enantiopurity to be high efficiently amplified in the infinite frameworks.

Interestingly, networks **N1** and **N2** could readily adsorb 4.32 and 4.97 Rhodamin 6G molecules ( $\sim 1.4 \text{ nm} \times 1.6 \text{ nm}$  in size) and 1.12 and 1.25 Brilliant Blue R-250 molecules ( $1.8 \text{ nm} \times 2.2 \text{ nm}$  in size) per formula unit, respectively. The inclusion solids exhibited the same PXRD patterns as the pristine **N1** and **N2**. These results indicate that the structural integrity and open channels of these mesoporous MOFs are maintained in solution. The synthesis of mesoporous MOFs remains a great challenge because such crystals tend to disintegrate upon guest removal, and only several examples of mesoporous MOFs have thus far been reported.<sup>[15-21]</sup> **N1** and **N2** represent the rare examples of homochiral mesoporous crystalline frameworks including both MOFs and zeolites.<sup>[21, 22]</sup>

## **6.5 Conclusion**

In conclusion, this chapter describes the remote pyridyl moieties totally changed the final structure through the bottom-up assembly. Due to the hierarchical functional groups on pre-designed linear ligands, step-by-step assembly of two homochiral mesoporous coordination networks (**N1** and **N2**) from a triple-stranded cluster helicate was obtained. Until 2011, coordination networks **N1** and **N2** represent the first two mesoporous zeolite-like MOFs to be reported.

The initial gas and liquid adsorption results provide an insight into the potential of these materials in inclusion chemistry. Work is in progress to explore the potential of constructed coordination networks as hosts for molecules with applications in enantioselective catalysis and/or separation. Given the high structural diversity of helicates, this work opens new perspectives for the hierarchical assembly of fascinating chiral networks.

Combining with previous chapters, remote substituents not only can manipulate the functionality of a host without changing frameworks, but also can totally change the final structures by offering extra metal binding ability.

## 6.6 Experimental Section

### Materials and General Procedures.

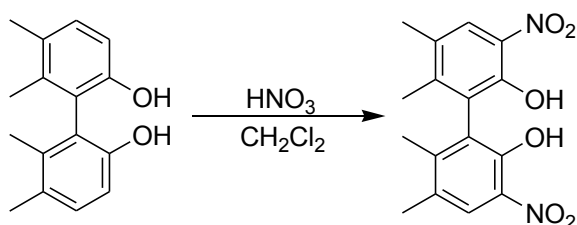
All of the chemicals are commercial available, and used without further purification. Elemental analyses of C, H and N were performed with an EA1110 CHNS-0 CE elemental analyzer. The IR (KBr pellet) spectrum was recorded (400-4000  $\text{cm}^{-1}$  region) on a Nicolet Magna 750 FT-IR spectrometer.  $^1\text{H}$  and  $^{13}\text{C}$  NMR experiments were carried out on a MERCURYplus 400 spectrometer operating at resonance frequencies of 100.63 MHz. Electrospray ionization mass spectra (ES-MS) were recorded on a Finnigan LCQ mass spectrometer using dichloromethane-methanol as mobile phase.

**X-ray Crystallography.** Single-crystal XRD data for the compounds was collected on a Bruker Smart 1000 CCD diffractometer with Mo- $K\alpha$  radiation ( $\lambda = 0.71073 \text{ \AA}$ ) at room temperature. The empirical absorption correction was applied by using the SADABS program (G. M. Sheldrick, SADABS, program for empirical absorption correction of area detector data; University of Göttingen, Göttingen, Germany, 1996). The structure was solved using direct method, and refined by full-matrix least-squares on *F*<sup>2</sup> (G. M. Sheldrick, SHELXTL97, program for crystal structure refinement, University of Göttingen, Germany, 1997). All non-H atoms were refined anisotropically. Crystal data and details of the data collection are given in **Table S1**.

For figures and tables: Reprinted with permission from ref. 23. Copyright 2011 John Wiley and Sons.

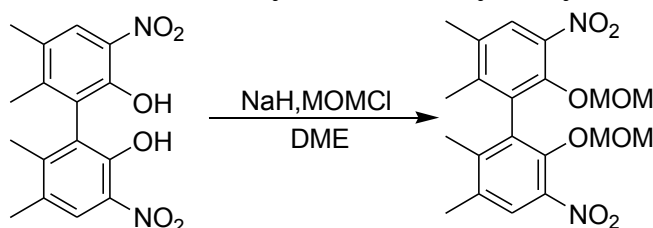
## Synthesis of the L ligand

### (*R*)-3,3'-Dinitryl-5,5',6,6'-Tetramethyl-1,1'-biphenyl-2,2'-diol:



5,5',6,6'-Tetramethyl-1,1'-biphenyl-2,2'-diol (1.5 g, 6.18 mmol) was dissolved in dichloromethane (140 mL) in a 250 ml round bottomed flask. 1 mL of concentrated nitric acid (24.6 mmol, 65%) was added dropwise to the solution and the reaction mixture was stirred 5h, while keeping the temperature below 30 °C. Then the solvent was evaporated in vacuo, the residue was purified by flash chromatography (silica gel, hexane: ethyl acetate=40:1) to yield the product (1.6 g, 78% yield) as a yellow solid after evaporation of the solvent; <sup>1</sup>H NMR (CDCl<sub>3</sub>, TMS, 400MHz): 10.764(s, 2H, OH), 7.994(s, 2H, ArH), 2.348(s, 6H, Me), 2.001(s, 6H, Me); <sup>13</sup>C NMR (CDCl<sub>3</sub>, TMS, 400MHz): 151.245, 148.142, 131.717, 129.622, 126.115, 124.870, 20.092, 17.677.

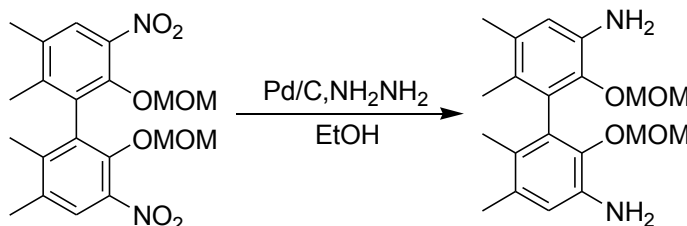
### (*R*)-3,3'-Dinitryl-5,5',6,6'-tetramethyl-2,2'-methoxymethyl-1,1'-biphenyl:



Under a nitrogen atmosphere, 3,3'-Dinitryl-5,5',6,6'-Tetramethyl-1,1'-biphenyl-2,2'-diol (1.45 g, 4.37 mmol) was added to a suspension of NaH (1.75 g, 72.9 mmol) dropwise in anhydrous DME (100 mL) at room temperature with stirring. The resulting solution was stirred for 30 min, and heated to 55 °C. After the solution turned to dark red, methoxymethyl chloride (13.6 mL, 48 mmol) was slowly added. The mixture was allowed to stay at this temperature and stirred for 2 h. Then the reaction was quenched by water. After evaporation of the DME, the aqueous layer was extracted with ethyl acetate (2×100 mL). The combined organic layers were washed with brine and dried over MgSO<sub>4</sub>. After removal of the solvent, the product as a white solid was obtained (1.5 g, 81.7% yield), which was pure enough for the next

step.  $^1\text{H}$  NMR ( $\text{CDCl}_3$ , TMS, 400 MHz): 7.762(s, 2H, ArH), 4.836(s, 4H,  $\text{CH}_2$ ), 2.893(s, 6H, Me), 2.363(s, 6H, Me), 1.990(s, 6H, Me);  $^{13}\text{C}$  NMR ( $\text{CDCl}_3$ , TMS, 400MHz): 147.591, 143.952, 141.890, 133.834, 133.689, 125.862, 101.158, 56.731, 20.284, 17.915

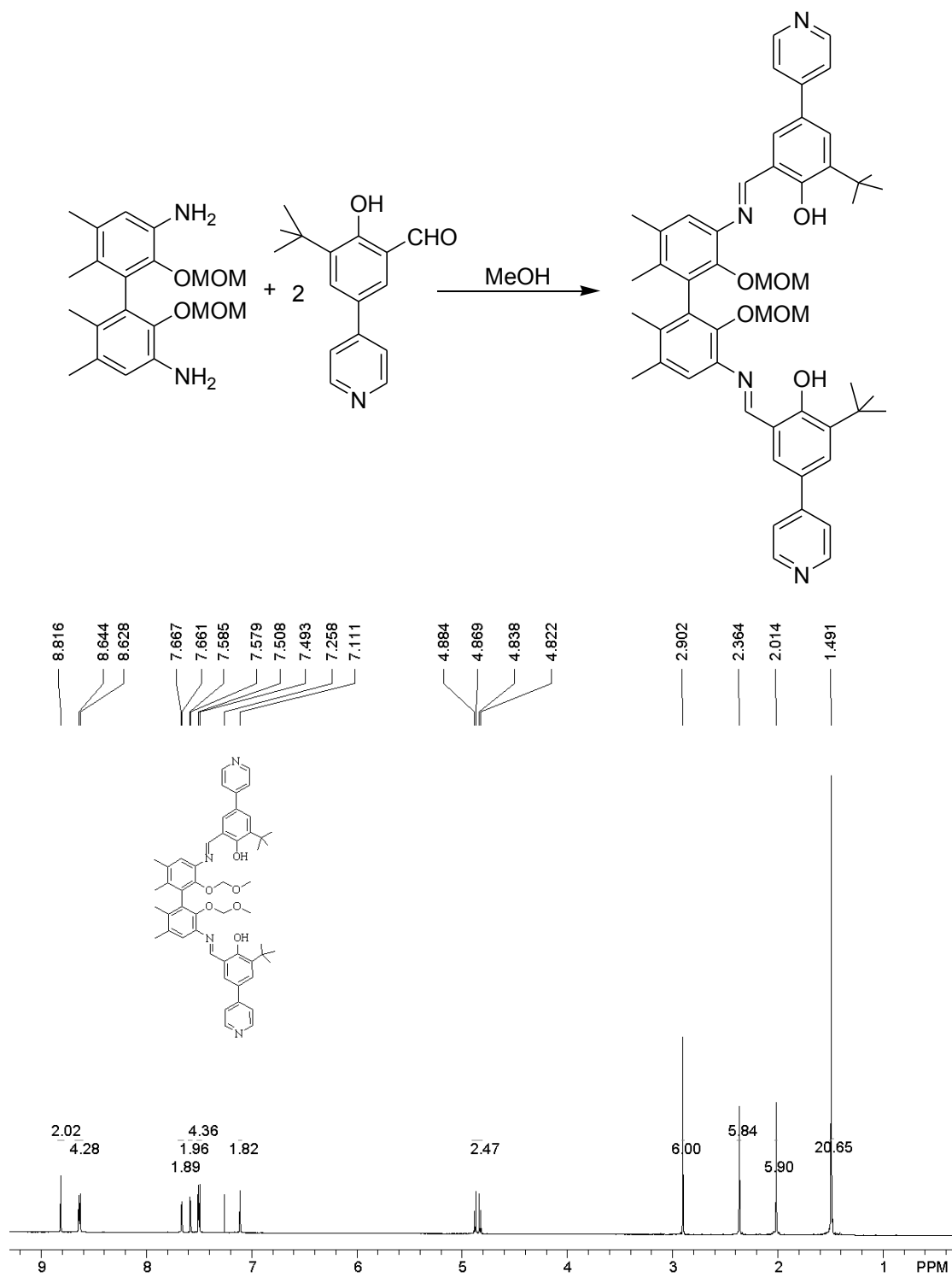
**(R)-3,3'-diamino-5,5',6,6'-tetramethyl-2,2'-methoxymethyl-1,1'-biphenyl:**



A 250ml round bottom flask was placed under a nitrogen atmosphere and charged with the 3,3'-Dinitryl-5,5',6,6'-tetramethyl-2,2'-methoxymethyl-1,1'-biphenyl (2.12 g, 5.03 mmol), Palladium on charcoal (10%, 462 mg), hydrazine hydrate (128.3 mL, 1.69 mol) and EtOH(250 mL), the reaction mixture was refluxed and stirred 12h. The cooled mixture was filtered off and the filtrate was concentrated to give product as colorless liquid (1.37 g, 75.7%);  $^1\text{H}$  NMR ( $\text{CDCl}_3$ , TMS, 400MHz): 6.605(s, 2H, ArH), 4.587(s, 4H,  $\text{CH}_2$ ), 3.142(s, 6H, Me), 2.185(s, 6H, Me), 1.819(s, 6H, Me);  $^{13}\text{C}$  NMR ( $\text{CDCl}_3$ , TMS, 400MHz): 140.785, 137.618, 132.988, 132.342, 125.604, 117.224, 98.465, 56.832, 20.356, 16.141

**(R)-N,N'-Bis(3-tert-butyl-5-(4-pyridyl) salicylidene)-3,3'-diamino-5,5',6,6'-tetramethyl-2,2'-methoxymethyl-1,1'-biphenyl [L2]:**

A mixture of 3,3'-diamino-5,5',6,6'-tetramethyl-2,2'-methoxymethyl-1,1'-biphenyl (2.6 g, 10 mmol) and 3-tert-butyl-5-(4-pyridyl) salicylaldehyde (5.13g, 20.1 mmol) in MeOH (80 mL) was refluxed and stirred for 24 h, and the reaction mixture was then filtered to collect the product as an orange solid (6.6 g, 80%);  $^1\text{H}$ NMR ( $\text{CDCl}_3$ )  $\delta$ : 8.82 (s, 2H,  $\text{HC}=\text{N}$ ), 8.36 (d, 4H, pyridylH), 7.66 (s, 2H, ArH), 7.58 (d, 2H, ArH), 7.50 (d, 4H, pyridylH), 7.11 (s, 2H, ArH), 4.85 (dd, 4H,  $\text{CH}_2$ ), 2.90 (s, 6H, Me), 2.36 (s, 6H, Me), 2.01 (s, 6H, Me), 1.49 (s, 18H,  $\text{CMe}_3$ ).  $^{13}\text{C}$ NMR ( $\text{CDCl}_3$ )  $\delta$ : 162.86, 161.88, 150.42, 148.20, 147.47, 139.03, 138.76, 136.31, 133.58, 133.32, 129.06, 128.93, 121.17, 120.22, 119.72, 99.71, 56.50, 35.38, 29.47, 20.56, 17.24. MALDI-TOF: m/z 834.4 (Calcd m/z 835.5 for  $[\text{M}+\text{H}]^+$ )



**Figure S1.**  $^1\text{H NMR}$  spectrum (400 MHz,  $\text{CDCl}_3$ , 300 K) of ligand **L2**.



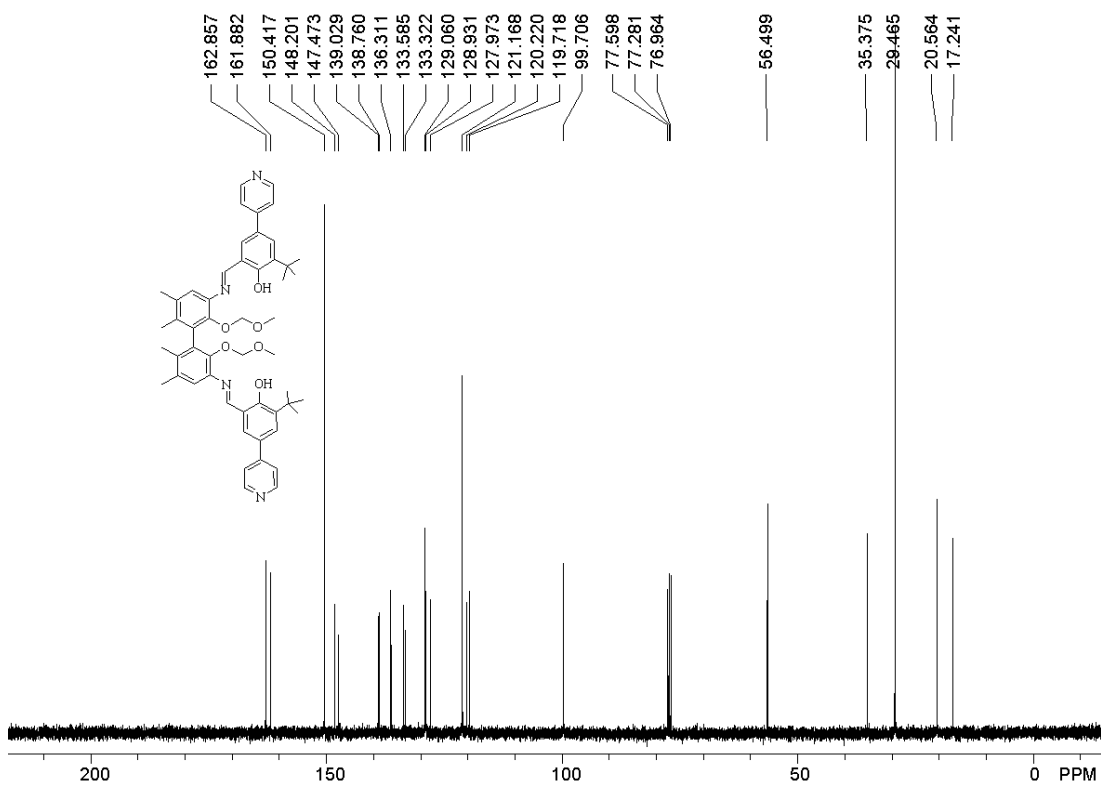


Figure S2. <sup>13</sup>C NMR spectrum (100 MHz, CDCl<sub>3</sub>, 300 K) of ligand L2.

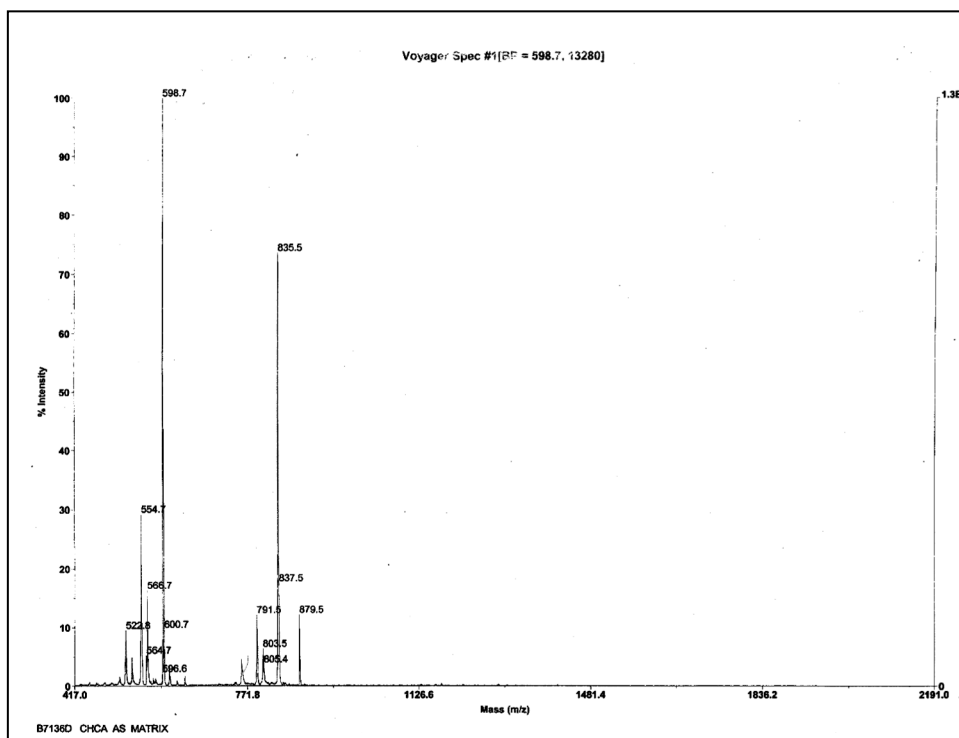


Figure S3. MALDI-TOF Mass spectrum of ligand L2.

## Self-assembly of the helicate **H2** and coordination networks **N1** and **N2**

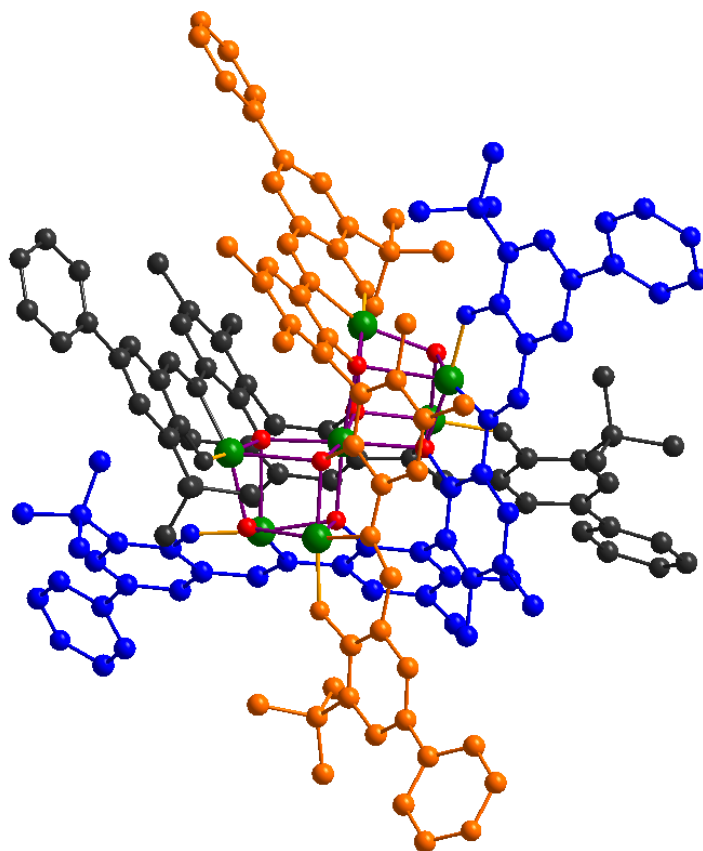
**H2**: A mixture of  $\text{CuSO}_4 \cdot 5\text{H}_2\text{O}$  (25 mg, 0.1 mmol) and **L2** (41.7 mg, 0.05 mmol) was placed in a small vial containing DMSO (1 mL),  $\text{H}_2\text{O}$  (0.1 mL), and sBuOH (1 mL). The vial was sealed and heated at 80 °C for one day. Turquoise rodlike crystals of **1** were collected, washed with diethyl ether, and dried in air. Yield: 33.9 mg (80% based on Cu). Elemental analysis (%): calcd for  $\text{C}_{148}\text{H}_{156}\text{Cu}_7\text{N}_{12}\text{O}_{18}\text{S}_2$ : C 61.30, H 5.42, Cu 15.34, N 5.80, S 2.21; found: C 60.20, H 5.39, Cu 15.24, N 5.76, S 2.20. ESI-MS:  $m/z$  2707.5 (calcd  $m/z$  2708.6 for  $[\text{M} + \text{H}]^+$ ). IR (KBr): 3423 (w), 2994 (m), 2918 (w), 2858 (w), 2326 (s), 1592 (s), 1503 (m), 1460 (m), 1384 (w), 1286 (m), 1259 (w), 1228 (m), 1025 (w), 897 (w), 829 (w), 790 (w), 705 (w), 616 (w), 531  $\text{cm}^{-1}$  (w).

**N1**: A mixture of  $\text{CuSO}_4 \cdot 5\text{H}_2\text{O}$  (25 mg, 0.1 mmol) and **H2** (135 mg, 0.05 mmol) was placed in a small vial containing DMSO (1 mL),  $\text{H}_2\text{O}$  (0.1 mL), and sBuOH (1 mL). The vial was sealed, heated at 80 °C for one day, and the turquoise block-like crystals of **2** were collected, washed with diethyl ether, and dried in air. Yield : 57.0 mg, 75 % based on Cu. Elemental analysis (%): calcd for  $\text{C}_{144}\text{H}_{162}\text{Cu}_{13}\text{N}_{12}\text{O}_{58}\text{S}_9$ : C 42.15, H 3.98, Cu 20.13, N 4.10, S 7.03; found: C 41.97, H 3.91, Cu 20.02, N 4.05, S 6.97. IR (KBr): 3418 (w), 2950 (m), 2862 (w), 2364 (w), 1627 (s), 1599 (s), 1524 (m), 1443 (m), 1389 (w), 1362 (m), 1290 (w), 1219 (m), 1134 (w), 1020 (w), 973 (w), 864 (w), 778 (w), 729 (w), 524  $\text{cm}^{-1}$  (w).

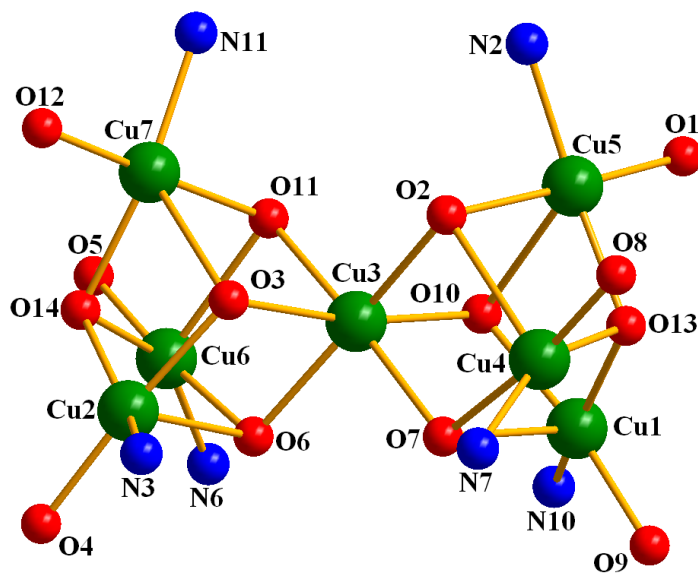
**N2**: The procedure was as for **N1**, and the vial was sealed, heated at 100 °C for one day. The turquoise block-like crystals of **N2** were collected, washed with diethyl ether, and dried in air. Yield: 56.4 mg, 60% based on Cu. Elemental analysis (%): calcd for  $\text{C}_{288}\text{H}_{330}\text{Cu}_{23}\text{N}_{24}\text{O}_{89}\text{S}_9$ : C 47.37, H 4.56, Cu 20.02 ; N 4.60, S 3.95 ; found: C 47.24, H 4.49, Cu 19.97, N 4.56, S 4.00. IR (KBr): 3510 (w), 2994 (m), 2910 (w), 2356 (w), 2334 (s), 1593 (s), 1503 (m), 1443 (m), 1381 (w), 1360 (m), 1257 (w), 1224 (m), 1109 (w), 1027 (w), 895 (w), 855 (w), 644 (w), 616 (w), 500  $\text{cm}^{-1}$  (w).

**Table S1.** Crystal data and structure refinement for **H2**, **N1** and **N2**.

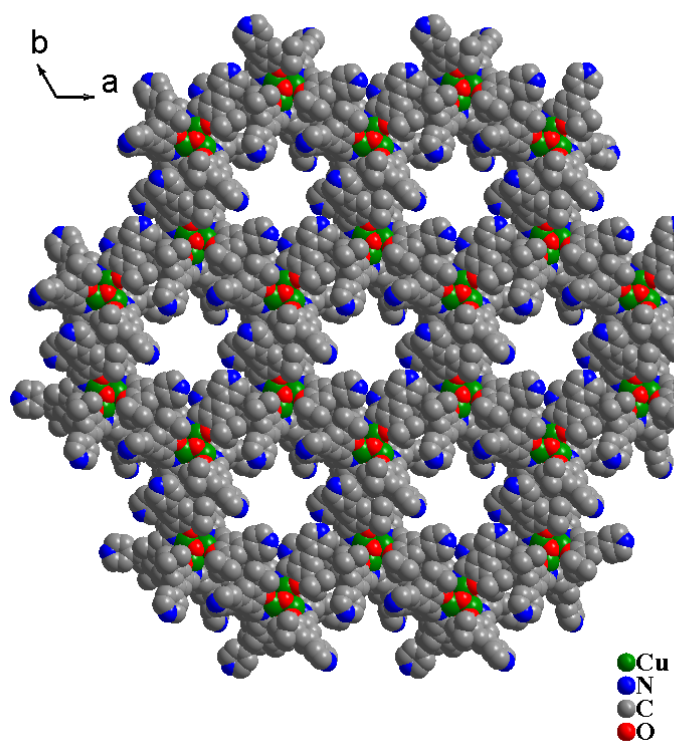
Identification code	<b>H2</b>	<b>N1</b>	<b>N2</b>
formula	C <sub>148</sub> H <sub>164</sub> Cu <sub>7</sub> N <sub>12</sub> O <sub>22</sub> S <sub>2</sub>	C <sub>144</sub> H <sub>210</sub> Cu <sub>13</sub> N <sub>12</sub> O <sub>82</sub> S <sub>9</sub>	C <sub>144</sub> H <sub>189</sub> Cu <sub>11.5</sub> N <sub>12</sub> O <sub>50.5</sub> S <sub>4.5</sub>
crystal system	trigonal	hexgonal	hexgonal
space group	P3 <sub>2</sub> 21	P6 <sub>3</sub> 22	P6 <sub>3</sub> 22
unit cell dimensions	a = 26.1935(2) Å b = 26.1935(2) Å c = 46.0311(6) Å	a = 26.2486(5) Å b = 26.2486(5) Å c = 25.2139(6) Å	a = 24.0343(2) Å b = 24.0343(2) Å c = 43.8206(7) Å
	α = 90°	α = 90°	α = 90°
	β = 90°	β = 90°	β = 90°
	γ = 120°	γ = 120°	γ = 120°
volume (Å <sup>3</sup> )	27350.7(5)	15044.7(5)	21921.6(4)
T, K	123	296(2)	296(2)
wavelength (Å)	1.54178	1.54178	1.54178
reflns measured	82969	61273	43277
Data / restraints / parameters	21830 / 21 / 1390	8792 / 7 / 304	7945 / 18 / 500
Independent reflns	21830	8792	7945
[R(int)]	[R(int) = 0.0770]	[R(int) = 0.0682]	[R(int) = 0.0422]
Final R indices [I > 2σ(I)]	R1 = 0.0872, wR2 = 0.2279	R1 = 0.0881, wR2 = 0.2184	R1 = 0.0883, wR2 = 0.2298
R indices (all data, F <sup>2</sup> refinement)	R1 = 0.01196, wR2 = 0.2558	R1 = 0.1081, wR2 = 0.2522	R1 = 0.1008, wR2 = 0.2445
GOF on F <sup>2</sup>	1.105	1.146	1.147
Largest diff. peak and hole, e/Å <sup>3</sup>	0.738 and -0.618	0.982 and -0.884	0.943 and -0.762
flack parameter	0.03(4)	0.01(5)	-0.01(6)



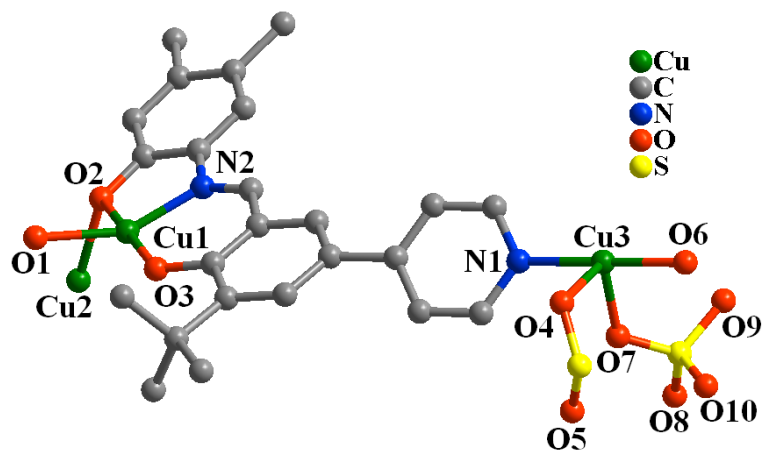
**Figure S4.** X-ray crystal structure of triple-stranded helicate **H2**. (three colors indicate three molecule of **L2**)



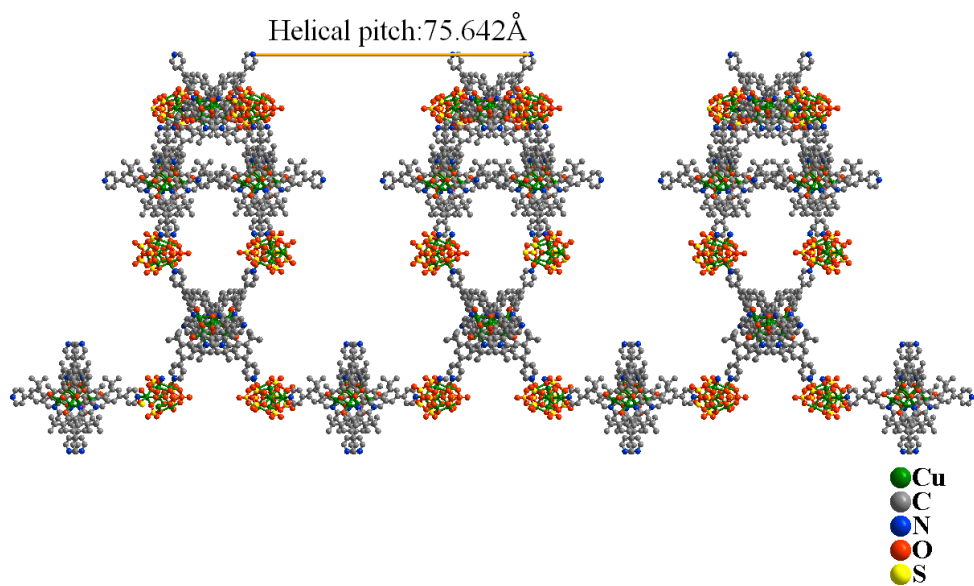
**Figure S5.** Metal cluster of triple-stranded helicate **H2**. (seven Cu metal ions show as green color)



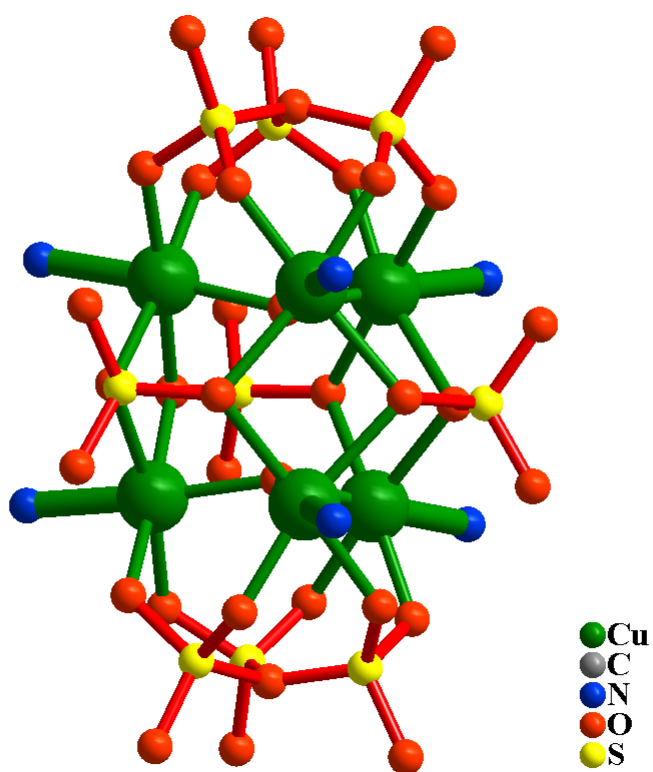
**Figure S6.** Packing mode of **H2**. (view from the c-axis)



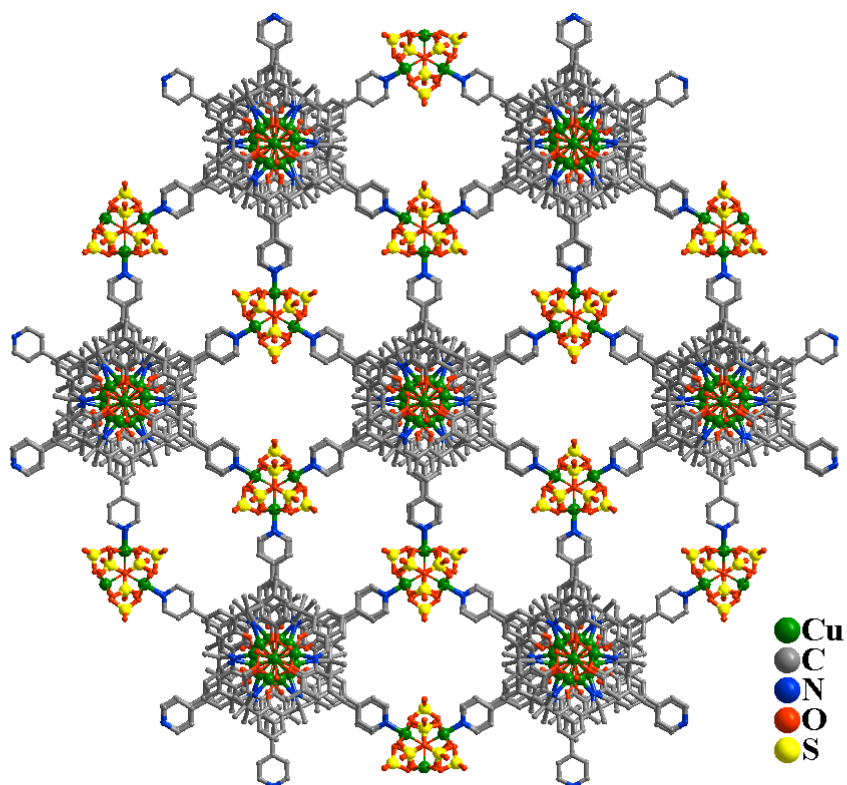
**Figure S7.** Asymmetric unit of **N1**. (the solvent molecule was omitted)



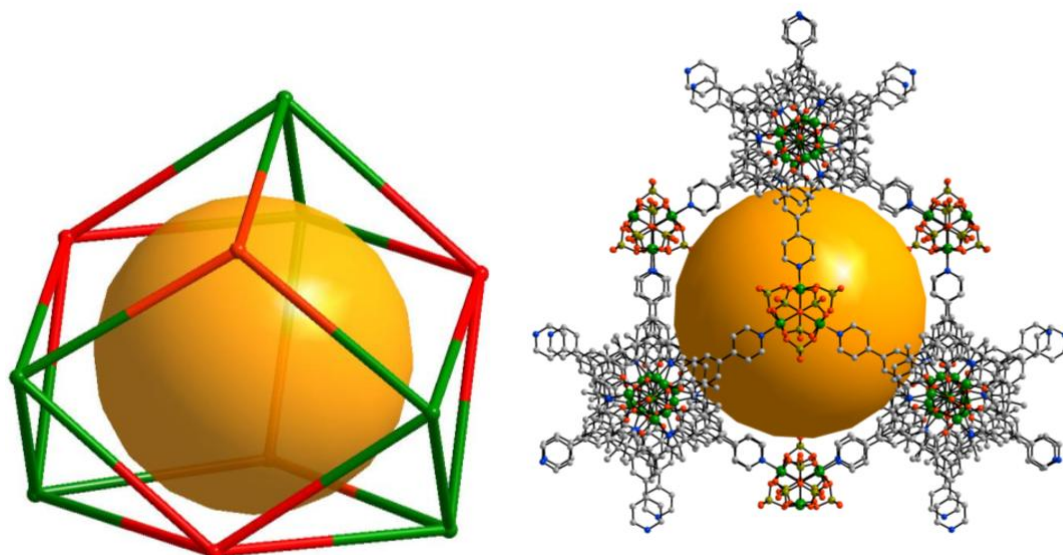
**Figure S8.** View of 1D single-strand  $6_3$  axis helical polymeric chain in networks N1.



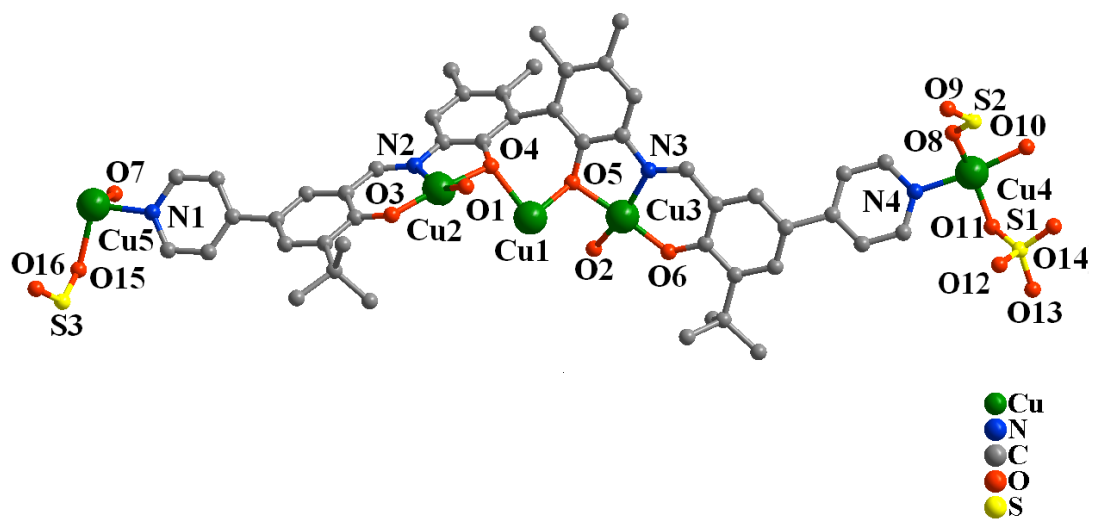
**Figure S9.** View of the heptanuclear copper (II) cluster of networks N1.



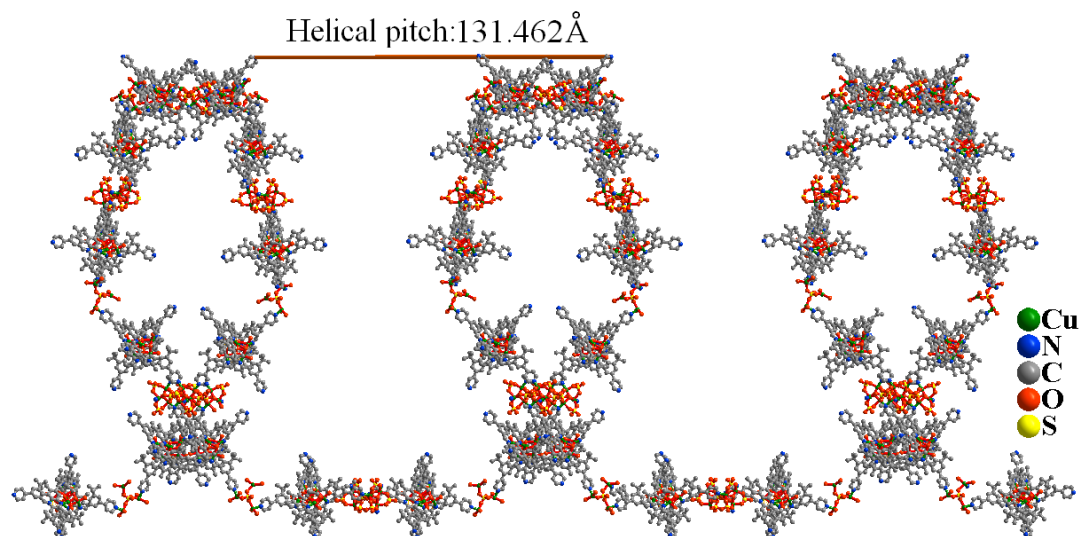
**Figure S10.** View of 3D networks N1.



**Figure S11.** The  $4^6_36$  cage in networks N1.

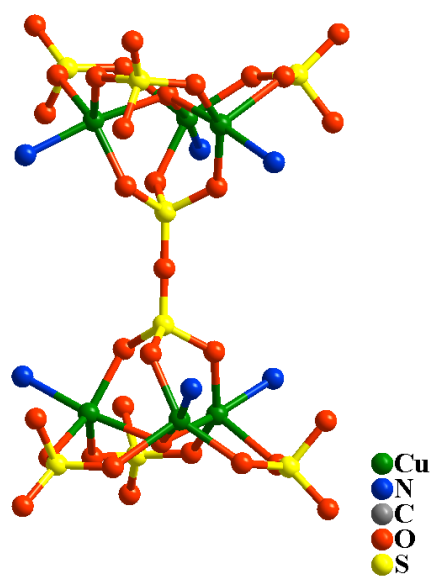


**Figure S12.** Asymmetric unit of N2. (the solvent molecule was omitted)

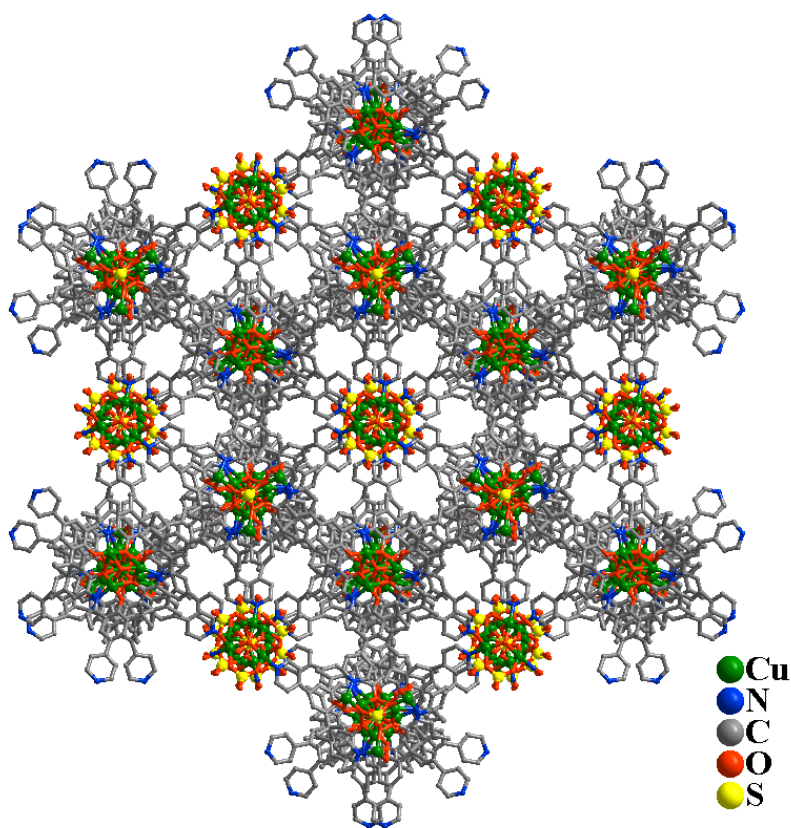


**Figure S13.** View of 1D single-strand  $6_3$  axis helical polymeric chain in networks N2.

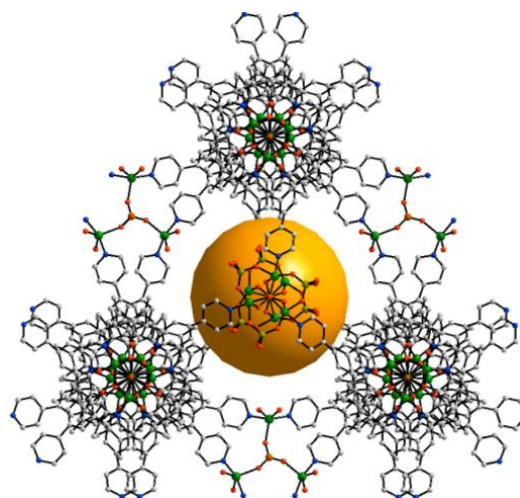
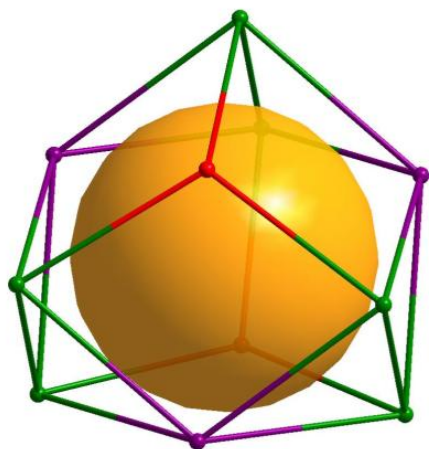




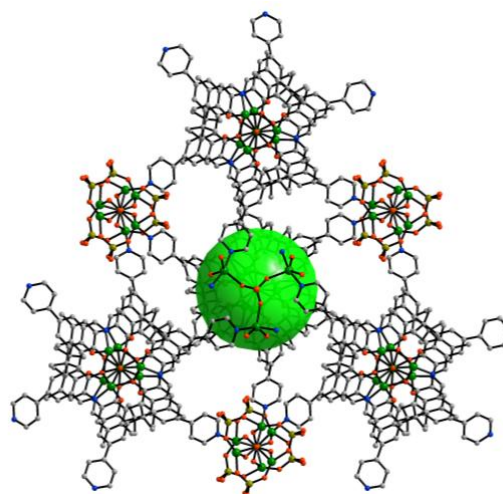
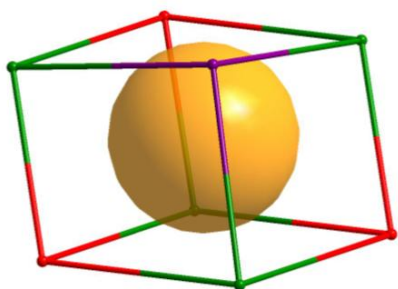
**Figure S14.** View of the dumbbell-like two planar tricopper (II) cluster of networks N2.



**Figure S15.** View of 3D networks N2.



**Figure S16.** The  $4^6_3^6$  cage in networks N2.



**Figure S17.** The  $4^6$  cage in networks N2.

## 6.7 Reference

- [1] Lehn, J. M., *Proc. Natl. Acad. Sci USA*, **2002**, *99*, 4763.
- [2] Reinhoudt, D. N.; Crego-Calama M. *Science*, **2002**, *295*, 2403.
- [3] Chris Ritchie, C.; Cooper, G. J. T.; Song, Y.; Streb, C.; Yin, H.; Parenty, A. D. C., MacLaren, D. A.; Cronin, L. *Nat. Chem.* **2009**, *1*, 47.
- [4] Moulton, B.; Zaworotko, M. J. *Chem. Rev.* **2001**, *101*, 1629.
- [5] Yaghi, O. M.; O’Keeffe, M.; Ockwig, N. W.; Chae, H. K.; Eddaoudi, M.; Kim, J. *Nature* **2003**, *423*, 705.
- [6] Kitagawa, S.; Kitaura, R.; Noro, S. *Angew. Chem., Int. Ed.* **2004**, *43*, 2334.
- [7] Lee, J.; Farha, O. K.; Roberts, J.; Scheidt, K. A.; Nguyen, S. T.; Hupp, J. T. *Chem. Soc. Rev.* **2009**, *38*, 1450.
- [8] Bonner, W. A. *Top. Stereochem.* **1988**, *18*, 1.
- [9] Cornelissen, J. J. L. M.; Rowan, A. E.; Nolte, R. J. M.; Sommerdijk, N. A. J. M. *Chem. Rev.* **2001**, *101*, 4039.
- [10] Piguet, C.; Bernardinelli, G.; Hopfgartner, G. *Chem. Rev.* **1997**, *97*, 2005.
- [11] Albrecht, M. *Chem. Rev.* **2001**, *101*, 3457.
- [12] Tanaka, K.; Tengeiji, A.; Kato, T.; Toyama, N.; Shionoya, M. *Science* **2003**, *299*, 121.
- [13] Yuan, G.; Zhu, C.; Liu, Y.; Xuan, W.; Cui, Y. *J. Am. Chem. Soc.* **2009**, *131*, 10452.
- [14] Liu, T.; Liu, Y.; Xuan, W.; Cui, Y. *Angew. Chem., Int. Ed.* **2010**, *49*, 4121.
- [15] Koh, K.; Wong-Foy, A. G.; Matzger, A. J. *Angew. Chem., Int. Ed.* **2008**, *47*, 677.
- [16] Park, Y. K.; et al. *Angew. Chem., Int. Ed.* **2007**, *46*, 8230.
- [17] Fang, Q. R.; Zhu, G. S.; Jin, Z.; Ji, Y. Y.; Ye, J. W.; Xue, M.; Yang, H.; Wang, Y.; Qiu, S. L. *Angew. Chem., Int. Ed.* **2007**, *46*, 6638.
- [18] Klein, N.; Senkowska, I.; Gedrich, K.; Stoeck, U.; Henschel, A.; Mueller, U.; Kaskel, S. *Angew. Chem., Int. Ed.* **2009**, *48*, 9954.
- [19] Wang, X.; Ma, S.; Sun, D.; Parkin, S.; Zhou, H. *J. Am. Chem. Soc.* **2006**, *128*, 16474.
- [20] Jiang, H.; Tatsu, Y.; Lu, Z.; Xu, Q. *J. Am. Chem. Soc.* **2010**, *132*, 5586.
- [21] Ma, L.; Lin, W. *J. Am. Chem. Soc.* **2008**, *130*, 13834.
- [22] Sun, J.; Bonneau, C.; Cantin, A.; Corma, A.; Diaz-Cabanas, M. J.; Moliner, M.; Zhang, D.; Li, M.; Zou, X. *Nature*, **2009**, *458*, 1154.
- [23] Xi, X.; Fang, Y.; Dong, T.; Cui, Y. *Angew. Chem., Int. Ed.* **2011**, *50*, 1154.



# Chapter 7

## Summary and Perspective

### 7.1 Research Summary

In nature, the functionality of enzymes and proteins can be controlled by amino acid loops or single amino residue that locate, not at the interior, but at the exterior of the pocket. This unique feature of natural enzymes and protein makes people a “puzzle” to study the protein because it is difficult to find the dominant factor that is governing the function of protein.

In coordination chemistry, the synthetic host was designed to mimic the function of enzyme. The synthetic host usually contains framework and cavity. It can be regarded as a simplified enzyme. Thus, it is relatively easy to replay the natural behavior and monitor the process of enzyme function in synthetic host. Such research can help us understand how enzyme works! The research on enzyme and protein direct the orientation of chemistry. The enzyme-mimic in chemistry way feed back for biology and shed light for finding mechanism of enzyme in a facial manner.

The research of this thesis is to answer: “Can we remotely control the property of synthetic host?” “How can we remotely tune the property of synthetic host like enzyme?” “What is the dominant factor for tuning property?” “How tiny difference in structure can be distinguish in functionality?”.

By the content of this thesis, we can answer as follows:

(1) Cavity of synthetic cage can be “remotely controlled” by remote groups

Synthetic host **1** with different remote groups on ancillary ligand has been investigated. After introducing bulky remote groups (mesityl), the cavity volume of synthetic host was reduced around 20% (Figure 1).

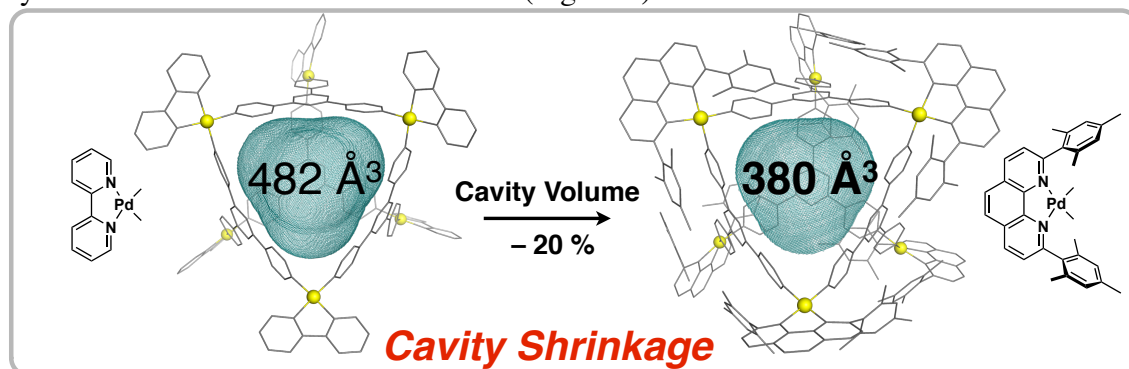


Figure 1. Cavity comparison.

(2) Guest binding was tuned by single remote methyl group

The inclusion yields of rigid probe molecule (**4b**) depends on the different modification of the cavity through remote groups were elucidated. For cage **1b** without remote groups, probe guest was not encapsulated due to its too large cavity. For cage **1c** with methyl remote groups, probe guest was encapsulated due to its medium cavity. For cage **1e** with bulky remote groups, probe guest was firmly encapsulated due to its shrunken cavity (Figure 2).

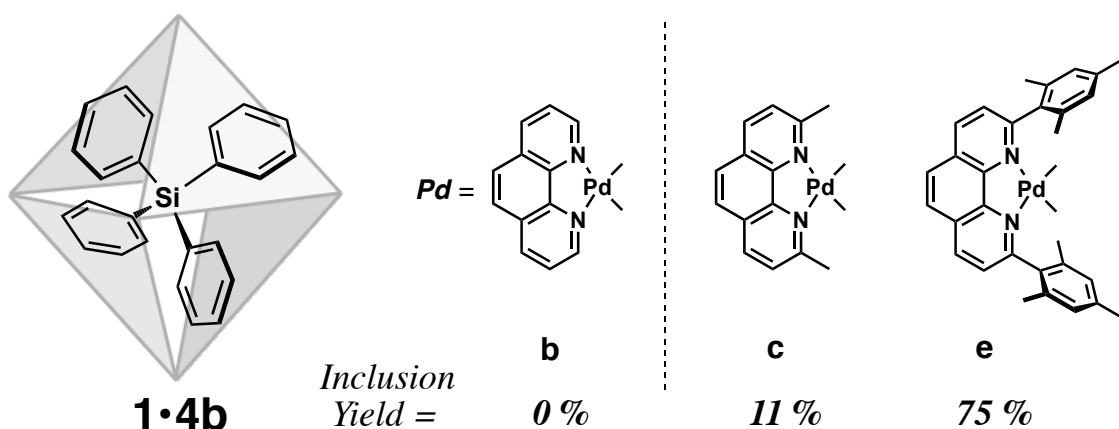


Figure 2 Encapsulation of guest **4b** by different cages.

(3) Guest motion was governed by a remote *para*-methyl group

The restraint degree for the guest **4g** is gradually increasing with the increasing of pendant groups from **1b** to **1d**. Even a *para*-methyl group difference between **1d** and **1e** can be distinguished in NMR spectra. Only the cage **1d** with *para*-methyl groups can efficiently stop guest motion of guest **7** in high temperature (Figure 3). Thus, dominant factor for tuning guest-motion property of the cavity is just a *para*-methyl remote group.

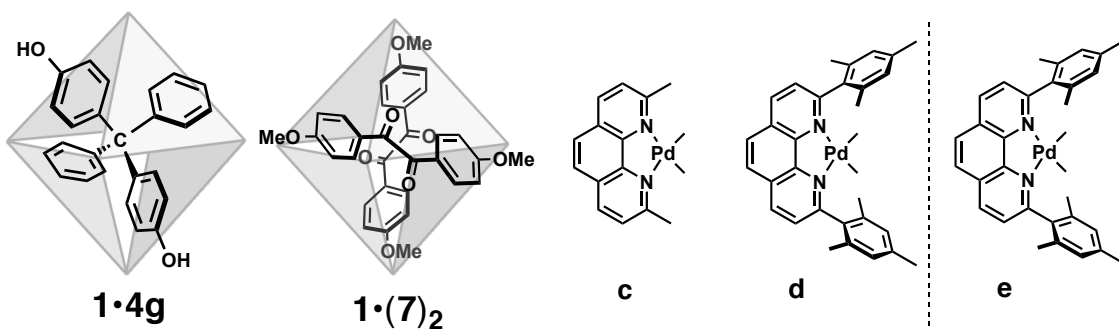
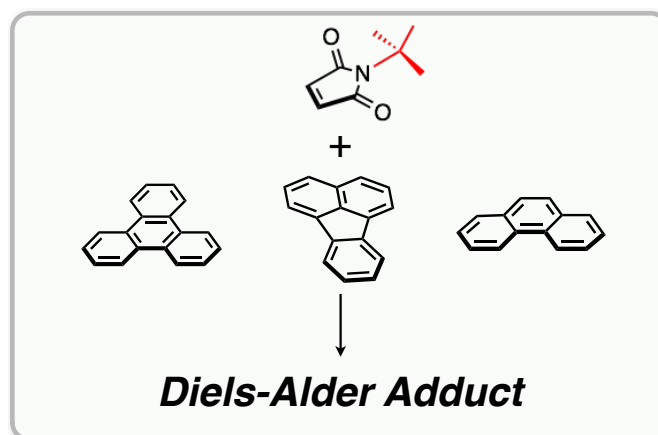


Figure 3. Guest motion inside cages.

(4) Diels-Alder reaction was promoted by “shrunkn caity”

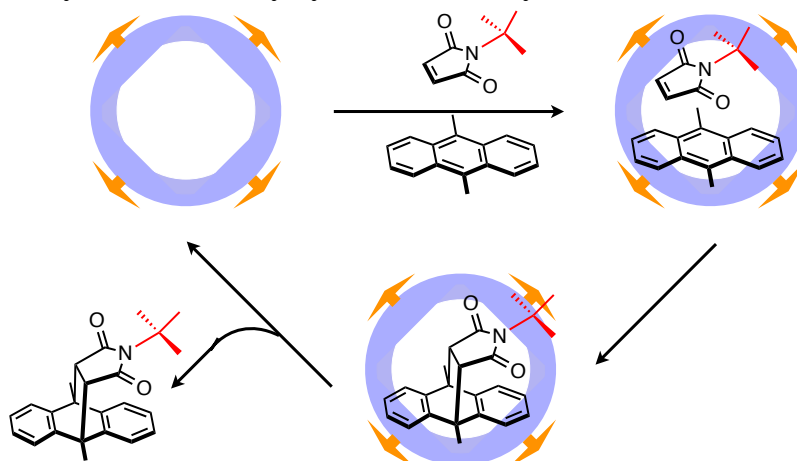
By introducing remote bulky substituents, a cage with shrunkn cavity was obtained. The smaller inner space put substrates close then dramatically improved the reactivity for small diene undergoing Diels-Alder reactions (Figure 4.).



**Figure 4.**Diels-Alder reactions of small dienes were promoted by shrunkn cavity.

(5) Catalytic Diels-Alder reaction of anthracene derivative was found by “shrunkn cavity”

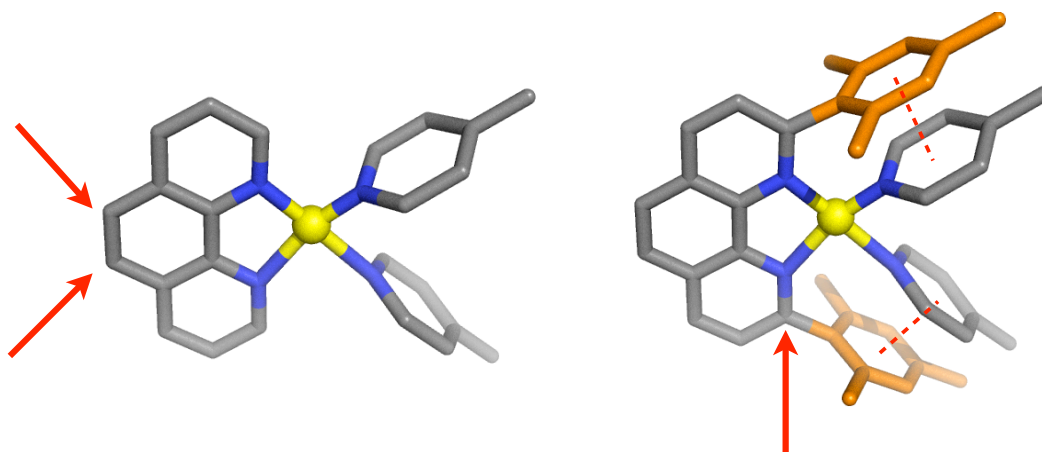
The small inner cavity of shrunkn cavity serves as discriminational environment for substrates and products. Once the Diels-Alder adduct was formed inside the shrunkn cavity, the product was smoothly released from cavity, due to the large size of guest and weak packing of host-guest. Further encapsulating the substrates furnished the catalytic reaction only by shrunkn cavity.



**Figure 5.**Catalytic cycle of Diels-Alder reaction of anthracene derivative by shrunkn cavity.

## 7.2 Perspective

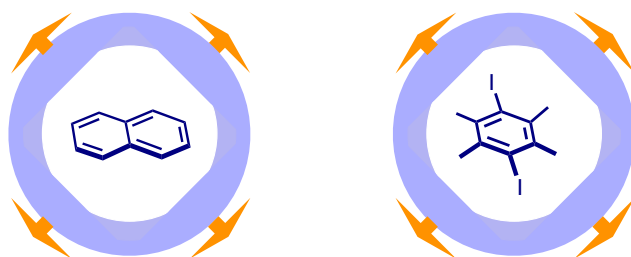
(1) “Remote Control” requires specific noncovalent interactions between remote groups and host framework. The shrinkage degree of the cavity depends on the strength of the noncovalent interactions. In this study, once remote substituents were introduced on 2,9-position of phenanthroline, reformation of the cavity is size and shape was observed. Substitution on other positions does not change the property because of the lack of noncovalent interactions between remote groups and the host framework (Figure 6).



**Figure 6.** Modification position of ancillary ligand.

(2) Extrem inert compound, such as substituted benzene, can be activated for Diels-Alder reaction by well- designed shrunken cavity.

Until now, several small dienes were activated by shrunken cavity. The shrunken cavity was also proved to have affinity for smaller and more inert diene, such as naphthalene and substituted benzene (Figure 7). If the well-designed cavity can put these small molecule close enough, Diels-Alder reaction can be proceed inside the cavity, thus new reaction and product can be obtained.



**Figure 7.** Small and extreme inert diene within the shrunken cavity.



## Acknowledgements

First of all, my deepest gratitude goes first and foremost to my supervisor, Prof. Makoto Fujita for his wise guidance, constructive encouragement, constant patience and support. As a foreign student, I have received his kindness and care both academically and personally during every moment of the three years.

Second, I would like to express my deepest gratitude to Dr. Takashi Murase. He has walked me through all the stages of the writing of this thesis. Without his consistent and illuminating instruction, this thesis could not have reached its present form. His professional knowledge and serious attitude in both science and life has provided me a perfect guidance for my future research work and daily life. Soon he will move to and take a Yamagata University and take an Associate Prof. position. I will sincerely express my best wishes for his happiness and success in the near future.

Big thanks also give to Associate Prof. Sota Sato of Tohoku University for his kindhearted management and support in the synchrotron X-ray diffraction measurements and analyses. Assistant Prof. Yasuhide Inokuma, Assistant Prof. Tomohisa Sawada, Assistant Prof. Daishi Fujita and other staff members of Fujita lab helped me so much in my daily research and gave a lot of valuable suggestions for becoming a qualified researcher.

Thanks go to current and former members of Fujita lab for their help and discussions. It has been a pleasure to work with these friends: Dr. Shinosuke Horiuchi, Dr. Qing-Fu Sun, Dr. Harris Kate, Mr. Takafumi Osuga, Dr. Yuh Kohyama, Dr. Koki Ikemoto, Mr. Hiroki Takezawa, Dr. Guo-Hong Ning, Mr. Shi-Tao Wang, Dr. Yoshihiro Ueda, Mr. Tatsuhiko Arai and Mr. Shota Yoshioka.

Special thanks go to the secretaries of Fujita lab. I have been well taken care of by Miss Yukari Ara, Miss Ayano Oishi and Noriko Yamaguchi during the three years.

Last my thanks would go to my beloved family for their loving considerations and great confidence in me all through these years. I also owe my sincere gratitude to my friends and my fellow classmates who gave me their help and time in listening to me and helping me work out my problems during the difficult course of the thesis.

Financial support of Global COE program as well as SEUT fellowship is gratefully acknowledged.

Yu Fang

Mar. 2014

## Publication List

(6) **Yu Fang**, Takashi Murase and Makoto Fujita. Acceleration of Unique Diels-Alder Reaction within Shrunk Cavities. *in preparation*. [Chapter 5]

(5) **Yu Fang**, Takashi Murase and Makoto Fujita. Remote Impacts of Methyl Substituents upon the Guest-Binding Abilities of Self-Assembled Cages. *Chem. Asian J.* (full paper) *in press*. (DOI: 10.1002/asia.201301642) [Chapter 3, 4]

(4) **Yu Fang**, Takashi Murase, Sota Sato and Makoto Fujita. Noncovalent Tailoring of the Binding Pocket of Self-Assembled Coordination Cages by Remote Bulky Ancillary Groups. *J. Am. Chem. Soc.*, **2013**, *135*, 613-615. [Chapter 2, 3]

(3) Xiaobing Xi, **Yu Fang**, Taiwei Dong, and Yong Cui. Bottom-Up Assembly from a Helicate to Homochiral Micro- and Mesoporous Metal–Organic Frameworks. *Angewant. Chem. Int. Ed.*, **2011**, *50*, 1154-1158. [Chapter 6]  
(Monthly “Hot Paper”, highlighted by *Nature Chemistry*, *Nature Chemistry*, 2011, *3*, 186–187)

(2) **Yu Fang**, Weimin Xuan, Chengfeng Zhu, Guozan Yuan and Yong Cui. Synthesis and Characterization of Chiral Mercury (II) and Cadmium (II) complexes with 3,3'-bipyridine-5,5',6,6'-tetramethyl-2,2'-dimethoxy-1,1'-biphenyl. *Chinese J. Struct. Chem.*, **2011**, *30*, 1147-1153.

(1) Guozan Yuan, Chengfeng Zhu, Yan Liu, **Yu Fang** and Yong Cui. Water clusters induced assembly of chiral organic microstructures showing reversible phase transformations and luminescence switching. *Chem. Commun.*, **2010**, *46*, 2307-2309.